INFORMATION TO USERS

This manuscript has been reproduced from the microfilm master. UMI films the text directly from the original or copy submitted. Thus, some thesis and dissertation copies are in typewriter face, while others may be from any type of computer printer.

The quality of this reproduction is dependent upon the quality of the copy submitted. Broken or indistinct print, colored or poor quality illustrations and photographs, print bleedthrough, substandard margins, and improper alignment can adversely affect reproduction.

In the unlikely event that the author did not send UMI a complete manuscript and there are missing pages, these will be noted. Also, if unauthorized copyright material had to be removed, a note will indicate the deletion.

Oversize materials (e.g., maps, drawings, charts) are reproduced by sectioning the original, beginning at the upper left-hand corner and continuing from left to right in equal sections with small overlaps. Each original is also photographed in one exposure and is included in reduced form at the back of the book.

Photographs included in the original manuscript have been reproduced xerographically in this copy. Higher quality 6" x 9" black and white photographic prints are available for any photographs or illustrations appearing in this copy for an additional charge. Contact UMI directly to order.

UMI

A Bell & Howell Information Company
300 North Zeeb Road, Ann Arbor MI 48106-1346 USA
313/761-4700 800/521-0600

NOTE TO USERS

The original manuscript received by UMI contains pages with slanted print. Pages were microfilmed as received.

This reproduction is the best copy available

UMI

Université d'Ottawa · University of Ottawa

FACULTY OF SCIENCES

DYNAMICAL INVARIANTS, MULTISTABILITY, CONTROLLABILITY AND SYNCHRONIZATION IN DELAY-DIFFERENTIAL AND DIFFERENCE EQUATIONS

BOUALEM MENSOUR

Thesis
submitted to the University of Ottawa
in partial fulfillment of the
requirements for the degree of
Philosophy Doctorat (Ph.D.) in Physics

Ottawa-Carleton Institute for Physics
University of Ottawa
Ottawa, Canada

November 1997

©Boualem Mensour, Ottawa, Canada, 1997

National Library of Canada

Bibliothèque nationale du Canada

Acquisitions and Bibliographic Services

Acquisitions et services bibliographiques

395 Wellington Street
Ottawa ON K1A 0N4
Canada

395, rue Wellington
Ottawa ON K1A 0N4
Canada

Your file Votre référence

Our file Notre référence

The author has granted a non-exclusive licence allowing the National Library of Canada to reproduce, loan, distribute or sell copies of this thesis in microform, paper or electronic formats.

L'auteur a accordé une licence non exclusive permettant à la Bibliothèque nationale du Canada de reproduire, prêter, distribuer ou vendre des copies de cette thèse sous la forme de microfiche/film, de reproduction sur papier ou sur format électronique.

The author retains ownership of the copyright in this thesis. Neither the thesis nor substantial extracts from it may be printed or otherwise reproduced without the author's permission.

L'auteur conserve la propriété du droit d'auteur qui protège cette thèse. Ni la thèse ni des extraits substantiels de celle-ci ne doivent être imprimés ou autrement reproduits sans son autorisation.

0-612-28360-7

Canada

Acknowledgments

I would like to thank my supervisor André Longtin for giving me the opportunity to work with him. I am grateful to André for his helpful guidance and discussion, encouragement and patience throughout the course of this work. I also thank him for his financial support.

I thank the faculty members of the Physics Department: secretaries, professors, students, and staff for their friendship.

My thanks also go to the different people who contributed with their suggestions and effort to make this thesis possible: the Department of Physics and the Graduate School of the University of Ottawa.

Finally, I would like to thank the Canadian International Development Agency (CIDA) and the University of Ottawa (UO) for their finantial support.

Contents

List of Figures

List of Tables

Chapter 1

Introduction

The research presented in this thesis is multidisciplinary: it is at the intersection of physics, engineering and neurobiology. It uses concepts from nonlinear dynamics and control theory to study a class of neural and optical circuits characterized by the intrinsic nonlinearity of their components and by their interaction delays. Nonlinearity and delay underly the different dynamical behaviors that these systems exhibit when some parameters are varied, ranging from a stable fixed point, through simple and complex oscillations, to chaotic oscillations.

It is natural to model these systems by nonlinear delay-differential equations (DDE's) in which the time evolution depends not only on the present states but also on the states at a given time in the past. Nonlinear DDE's have been applied to problems in many scientific disciplines. In optics for example, the Ikeda equation models the laser ring cavity [1]. In physiology, the Mackey-Glass equation models white blood cell production [2]. In human physiological control, DDE's model the pupil light reflex [3], and recurrent inhibition or excitation in the spinal cord and the hippocampus [4, 5]. The dynamics of electronic or optical neural networks also can involve DDE's [6].

Delay-differential equations are infinite-dimensional dynamical systems. However, their phase space attractors have a finite fractal dimension proportional to the delay [7]. These systems combine properties of ordinary differential and difference equations. They can have a large variety of self-oscillatory modes, exhibit bifurcation routes such as period-doubling and can also exhibit multistability [8]. The latter, which arises from the combination of nonlinearity and delay, is the coexistence of multiple attractors. This property is very difficult to study analytically in DDE's [9, 10]; it is also difficult to study numerically due to the presence of long transients, and the difficulty of forcing the system to oscillate in prescribed periodic or chaotic patterns through the choice of special initial conditions, which are in fact "initial functions".

This thesis is concerned with the study of dynamical invariants and multistability in nonlinear DDE's such as the Mackey-Glass or the Ikeda equations [1, 2]. In particular, it focusses on special properties which are potentially important for practical applications: storage and transmission of finite or infinite patterns or messages, using stable periodic orbits or unstable periodic orbits stabilized by delayed feedback-based chaos-control techniques. The storage property originates in the multistability that these systems exhibit when the delay τ in the feedback loop is much greater than the response time τ_r of the system (i.e. $R = \tau/\tau_r >> 1$), as first suggested by Ikeda and Matsumoto [8] and implemented on a hybrid laser diode by Aida and Davis [11]. The message is encoded into the multistable solutions obtained with special initial functions.

We have applied the idea of storage to physiologically-based models of neural recurrent feedback, with either non-spiking neurons such as in the Mackey-an der Heiden model [5], or with spiking neurons such as in the Plant model [4] based on the Fitzhugh-Nagumo equations, or the Hodgkin-Huxley model [12, 13]. The information is stored into multistable periodic patterns of voltage, and thus of spikes. Our approach offers a simple mechanism for active short-term memory [14, 15, 16] based on the temporal patterns of firing in a simple neural system rather than on the spatial properties of a neural network. A variety of different patterns can be stored in these recurrent circuits depending on their initial conditions and on the perturbations which they receive.

The memory storage strategy discussed above doesn't work for multistable chaotic patterns because of the exponential divergence of trajectories. Any message stored in the initial function will be lost after a few delays and will never be recovered. We have thus applied the chaos-control technique proposed by Pyragas [17] to stabilize unstable periodic orbits (UPO's) of the Mackey-Glass equation, and then store information in their waveforms. We show that the chaotic regime yields a more versatile memory system than the periodic regime because of the large number of UPO's that coexist with one or more attractors. We show that a binary signal can be encoded directly into the initial function from which the controlled DDE evolves. There are l^n different initial functions or "messages" which can be stored (one at a time), where l represents the number of different "plateaus" in the controlled UPO solution, and n is the number of plateaus in one delay. The storage capacity is found to increase with the delay and is maximum when n reaches its maximum value, corresponding to the multistable solution with the highest possible frequency. Further, the number of possible multistable solutions that can be used for encoding finite messages is found to be related to the unstable modes of the linearized system. Hence, the maximum storage capacity can be estimated from the number of unstable modes.

The number of UPO's that can be stabilized by Pyragas method [17] for storage purposes is very limited. This is due to the fact that higher periodic orbits are very difficult to control. It is important to realize that the systems considered here have two feedback terms: one is due to the basic control involved in the normal operation of the system; the other contains only one state in the past and serves to control the resulting dynamics of the basic control system. We have also applied the extended control technique proposed by Socolar *et al.* [18], which contains an infinite number of states at given times in the past, to control orbits with higher periodicity, and to increase the storage capacity and the range of controllability of orbits with lower periodicity. In this case, the system has one or many more extra feedback terms which depend on other states further in the past.

At large delay, the controllability of UPO's is shown to be predictable by the Lyapunov exponents and the dispersion (see Chap.6) of the map obtained by discretizing the time in units of the delay in the singular limit of the DDE ($R \to \infty$). The form of the map provides an improved method of controlling UPO's in discrete systems such as the Logistic map, the Mackey-Glass map, the Hénon map, and in neural networks such as the Nagumo-Sato model [19, 20].

In this thesis, we have also investigated the use of DDE's as broadband carriers for secure communication. The multistability and the high-dimensional chaos they exhibit when R is large make them very useful for masking information. Besides, they are very easy to implement experimentally. The message can, for example, be encoded onto a controlled UPO, transmitted using a high-dimensional chaotic carrier from another similar DDE, and then recovered at the receiver end using chaotic synchronization. This method of masking information with a DDE carrier is certainly more efficient and more secure than with low-dimensional systems [21, 22, 23].

Finally, many properties of DDE's such as dynamical invariants, multistability, and controllability can be studied using power spectra, linear stability analysis, and the map obtained in the singular perturbation limit of the DDE. These numerical techniques are far simpler for estimating dynamical invariants such as attractor dimension (D) and Lyapunov exponents in comparison with usual methods (such as the correlation integral), especially when the attractors are high-dimensional (e.g. $D > 10$). These are the kinds of attractor dynamics that are useful for storage purposes.

When R is large ($R > 5$), a curious modulation, superimposed on an exponentially decaying background, was observed by Farmer [7] in the power spectra of the Mackey-Glass DDE. We found that the peaks of this modulation correspond to the modes of oscillations predicted by linear stability analysis of the dynamics around the fixed point. Also, the number of such modes below a characteristic frequency (the inverse of the autocorrelation time of the feedback term) agrees with the Lyapunov dimension of the attractor. Further, the inverse of the decay rate of the spectrum at mid-frequencies is found to agree with the sum of the positive Lyapunov exponents, and is proportional to the sum of the real parts of the unstable linear modes. Our results suggest that for this class of dynamical systems, connections between spectral properties and dynamical invariants occur at mid-frequencies, rather than in the asymptotic frequency range as suggested by Sigeti [24]. The spectral properties of the continuous-time difference equation (CTDE) obtained when R goes to infinity can also be used to explain many properties of the DDE such as multistability, which is important for memory storage and pattern recognition, and controllability of orbits. It can also explain the shape of the spectrum at low frequencies, and be used to estimate the attractor dimension. The advantage of working with the CTDE is that it is easy to simulate numerically and its spectrum can be calculated analytically once the spectrum of the map is determined.

This thesis is organized as follows:

In Chapter 2, we present the necessary tools from nonlinear dynamic and bifurcation theory that help us understand the work in this thesis. First, we give an overview on dynamical systems, bifurcation theory, and the different transitions to chaos that occur in DDE's with an emphasis on the period-doubling cascade, which is our main interest here. Finally, we introduce dynamical invariants such as Lyapunov exponents and dimensions to characterize the chaotic attractors of DDE's at large R values.

In Chapter 3, we study in more detail the properties of DDE's such as stability of the fixed point, multistability and the singular perturbation limit ($R \to \infty$). We also look at the more realistic case of distributed delays and its limiting case of a single fixed delay.

In Chapter 4, we show that certain properties of DDE's at large delay such as power spectra and dynamical invariants can be studied using linear stability analysis and the one-dimensional map obtained in the singular limit of the DDE ($R \rightarrow \infty$). Linear stability analysis explains the oscillations in power spectra, which in turn are useful to estimate attractor dimension. The unstable modes or the decay rate of power spectra in the mid-to-high frequency range are used to estimate the metric entropy, which is related to the Lyapunov exponents spectrum.

In Chapter 5, we show how multistability is used for storing memories in neural feedback systems with recurrent inhibition and excitation. The storage strategy is explained using the Mackey-Glass equation in the periodic regime. We show how recurrent inhibition circuits with non-spiking neurons such as the Mackey-an der Heiden model and spiking neurons such as the Plant model can store information in their patterns of voltages and of spikes.

In Chapter 6, we study the storage of information in the chaotic regime, using unstable periodic orbits of the Mackey-Glass equation which are stabilized with a delayed-feedback control technique [17]. The controlled solutions are found to be multistable to initial functions, i.e. the space of initial functions is divided into subspaces, with initial functions in one subspace leading to the same asymptotic motion. We also look at the relation between the power spectrum and the linear stability analysis on one hand, and the dispersion on the other hand in a set of two-nonlinear delay-differential equations used to model cortical oscillations [25].

In Chapter 7, we discuss the controllability of discrete systems such as the Logistic map, the Mackey-Glass map, and the Nagumo-Sato network, using a new control technique which is obtained in the singular limit of the DDE ($R \rightarrow \infty$). We also show how the storage capacity in DDE's is increased when combining our new method with the extended control technique in [18], enabling us to control higher periodic orbits.

In Chapter 8, we show that multistability and high-dimensional chaos exhibited by DDE's can make them very useful for secure communication purposes. The context here is synchronization of two delayed-feedback systems. When a message is masked or modulated with a high-dimensional chaotic carrier, its probability of detection is very low compared to the low-dimensional chaos case, especially when the message is encoded onto UPO's of the DDE. The results on synchronization here are also relevant to understanding the dynamics of multi-loop feedback systems with delays, such as those occuring in physiology [26].

In Chapter 9, we conclude the thesis and discuss open problems and future work.

Publication Notes

The following sections of this thesis have appeared or have been submitted for publication:

- Section 3.4 and Chapter 7 contain work under review in *Phys. Rev. E* (A. Longtin, second author).

- Chapter 4 has appeared in *Physica D* 1786, 1 (1997) (A. Longtin, second author).

- Chapter 5 contains the results from two publications: the first one has appeared in IEEE 17^{th} Ann. Intern. Conf. of the Engineering in Medecine and Biology Society & 21^{st} Canadian Medical and Biological Engineering Conference, Montreal, Canada (Sept. 1995). The second one is joint work with J. Foss, A. Longtin, and J. Milton and has appeared in *Phys. Rev. Lett.* **76**, 708 (1996). In the latter, J. Foss and J. Milton did computations for repetitively firing neurons while we did them for the excitable neurons.

- Chapter 6 has appeared in *Phys. Lett. A* **205**, 18 (1995) (A. Longtin, second author).

- The work in Chapter 8 is under review in *Phys. Lett. A* (A. Longtin, second author).

Chapter 2

Nonlinear dynamics

A violent order is disorder; and a great disorder is an order. These two things are one (Wallace Stevens, "Connoisseur of chaos").

2.1 Introduction

Nonlinear dynamic is a branch of mechanics that deals with instabilities in nonlinear systems. In such systems, a small change in a parameter can lead to sudden and dramatic changes in both the qualitative and quantitative behavior of the system. The solutions may exhibit behaviors ranging from a globally stable fixed point, through stable limit cycle behavior, to complex or irregular behavior. In recent years, the theory of nonlinear dynamics has considerably improved our understanding of these changes and of this irregular behavior in physical, chemical, biological, and other natural phenomena. It has allowed us to describe and classify the complex behavior of nonlinear systems, and to see an order and universality that underlies these complexities. In this Chapter we introduce the mathematical tools such as linear stability analysis and bifurcation theory to describe the behavior of a nonlinear dynamical system. We show how a fixed point or a limit cycle loses its stability when a parameter of the system is changed. This stability of a fixed point or limit cycle is crucial to understand the dynamics of the nonlinear system near that fixed point or limit cycle.

This Chapter is organized as follows: in Section 2.2 and 2.3, we give a description of conservative and dissipative dynamical systems, and the Poincaré section technique used to reduce the dimensionality of high-dimensional systems. In Section 2.4, we introduce bifurcation theory and chaos observed in nonlinear systems. In Section 2.5, we present the different transitions to chaos such as period-doubling, intermittency, crises and quasi-periodicity. Section 2.6 characterizes motion on an attractor using dynamical invariants such as the dimension and the Lyapunov exponents. The Chapter concludes in Section 2.7.

2.2 Dynamical systems

A dynamical system is a mathematical entity that describes the time-evolution of the state of the system using differential or difference equations, depending whether the time is continuous or discrete. The system evolves in the *phase space* spanned by its state variables. The path followed by the system in phase space is called an *orbit* or *trajectory*. If the time is continuous, then the evolution of paths starting from all initial conditions is called the *flow* of the system. There are two types of dynamical systems: *conservative* systems or *Hamiltonian* systems, for which a volume element in phase space is preserved when evolving in time, and *nonconservative* or *dissipative* dynamical systems, for which a volume element shrinks to zero as time increases. For continuous dynamical systems

$$d\mathbf{x}/dt = \mathbf{f}(\mathbf{x})\,, \tag{2.1}$$

the time-evolution of a volume element V in N-dimensional phase space is given by the divergence theorem

$$\frac{dV}{dt} = \int_V \nabla \cdot \mathbf{f} d^N x\,, \tag{2.2}$$

where $\nabla \cdot \mathbf{f} \equiv \sum_{i=1}^{N} \partial f_i(x^{(1)}, \cdots, x^{(N)})/\partial x^{(i)}$ is the divergence of $\mathbf{f}$. If $\nabla \cdot \mathbf{f} = 0$, then the phase space volume is preserved and the system is *conservative*. However, if $\nabla \cdot \mathbf{f} < 0$, then there is contraction of the phase space volume and the system is *dissipative*. We will see in Section 2.6.2 that this notion of dissipation can be related to the sum of Lyapunov exponents, which are characteristic rates of contraction and expansion of the phase space motion. In this study, we shall be mainly interested in dissipative systems, which are characterized by the presence of attracting sets (for example points, curves, areas) in phase space called *attractors* as shown in figure 2.1. The trajectories all converge to such subsets of phase space as $t \to \infty$. The geometric dimension of these attrators is in general less than that of the original phase space. The set of initial conditions leading to those trajectories that approach a given attractor is called the *basin of attraction* for that attractor.

In the case of discrete-time systems such as maps, defined in N-dimensional space by $\mathbf{x}_{n+1} = \mathbf{F}(\mathbf{x}_n)$, conservation and dissipation is expressed as a function of the magnitude of the determinant of its Jacobian matrix of partial derivatives, that is $J(\mathbf{x}) \equiv |det[\partial \mathbf{F}(\mathbf{x})/\partial \mathbf{x}]|$. If $J(\mathbf{x}) = 1$, the map is conservative. On the other hand, if $J(\mathbf{x}) < 1$, the map is dissipative. Examples of dissipative maps are: the Logistic map $x_{n+1} = \mu x_n(1 - x_n)$, the Hénon map $(x_{n+1}, y_{n+1}) = (1 - ax_n^2 + y_n, bx_n)$ $(|b| < 1)$, and the Mackey-Glass map $x_{n+1} = ab^{-1}x_n/(1+x_n^{10})$ obtained in the singular limit of the Mackey-Glass delay-differential equation (see Sect.3.6). This map and this limit (see Sect.3.6) will be of great interest in this thesis.

The evolution of a trajectory is phase space is confined by the following No-intersection theorem [27]:

Theorem 2.1 *Two distinct state space trajectories cannot intersect (in a finite period of time). Nor can a single trajectory cross itself at a later time.*

We cannot have two trajectories intersect in phase space. If they do, they will have the same values even though they evolve in different ways from that point. This is not possible in *deterministic* systems, where the time-evolution equations, the parameters that describe the system, and the initial conditions, completely determine the future behavior of the system. This theorem can be violated when a 3-dimensional phase space trajectory for example is projected onto a 2-dimensional phase space. The trajectory in 2-dimensional phase space may then cross itself.

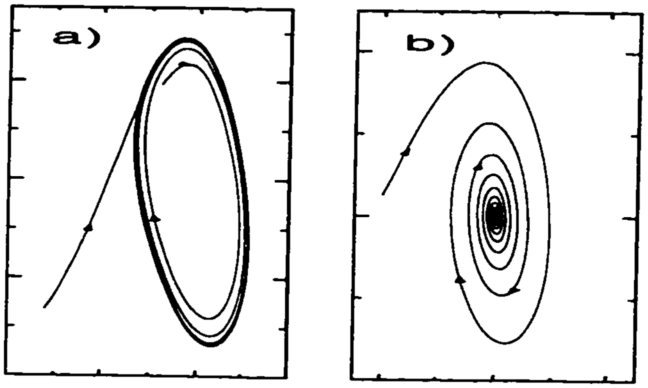

Figure 2.1: Attractors of Mackey-Glass delay-differential equation (see Sect.3.3). a) The trajectory approaches a limit cycle attractor. b) The trajectory approaches a fixed point attractor.

2.3 Poincaré section

It is often useful to reduce a continuous time system (or "flow") of dimensionality N to a discrete time map of dimensionality $N-1$ using the Poincaré section technique. A "Poincaré map" is generated by choosing a two-dimensional surface and recording on that surface the points at which a given trajectory cuts transversely through that surface. Figure 2.2 illustrates the Poincaré surface of section in a three-dimensional flow. In this case, a Poincaré map is generated using a plane parallel to the xy-plane. The Poincaré map obtained represents an invertible two-dimensional map transforming the coordinates (x_n, y_n) of the nth piercing of the surface of section to the coordinates (x_{n+1}, y_{n+1}) at piercing $n+1$ (see Sect.2.4). This transformation can mathematically be represented as $\mathbf{x}_{n+1} = \mathbf{F}(\mathbf{x}_n)$, where $\mathbf{F}$ is the Poincaré map function. This technique is very important for studying the stability and controllability of orbits. For example, in phase space a period-2 limit cycle is represented by 1 point on the Poincaré section, a period-4 limit cycle by 2 points on the Poincaré section, and so on.

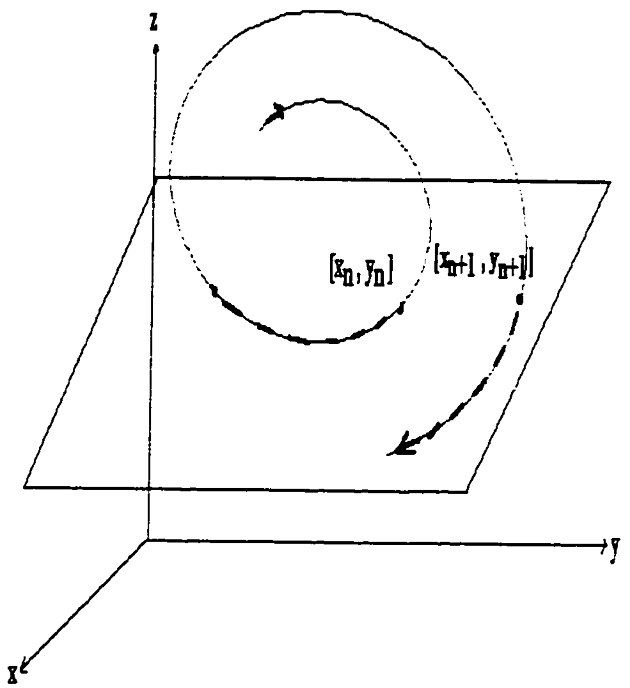

Figure 2.2: A Poincaré map of a trajectory in three-dimensional phase space, generated using a plane parallel to the xy plane. The trajectory intersects this plane transversely (i.e. in any direction other than parallel) and in the same direction. The intersections in the plane are represented by a two-dimensional map function $(x_{n+1}, y_{n+1}) = (F_1(x_n, y_n), F_2(x_n, y_n))$.

2.4 Bifurcation and chaos

Linear systems don't show qualitative changes when some parameters are varied. For example, the amplitude and the frequency of oscillations in a simple harmonic oscillator will change when varying the spring constant, but the qualitative nature of the behavior remains the same. We can always make the oscillations look similar to the original ones by appropriately rescaling the amplitude and time axes. Nonlinear systems however, show sudden and dramatic changes in both qualitative and quantitative changes as some parameters are varied. The behavior of nonlinear systems can range from simple oscillations to complex and chaotic oscillations as the parameters are slightly changed. The changes allow us to classify the complex behavior of these systems, and to see the order and universalities that underly these complexities. Any qualitative change in the dynamic of the system in N-dimensional space which occurs as some parameter is varied is called *bifurcation*. As the parameter increases through successive bifurcations, the asymptotic motion of the system typically gets more complicated. One such complex motion is called *chaos*, and can be observed only in systems with phase space dimension $N \geq 3$, a consequence of the Poincaré-Bendixson theorem [28]:

Theorem 2.2 *In a two-dimensional flow, the trajectory can only approach a fixed point or a limit cycle.*

Thus, chaotic trajectories cannot occur in a two-dimensional space. This result can also be used to establish the existence of limit cycles in two-dimensional flows. The Poincaré-Bendixson theorem doesn't hold for maps and therefore chaos can be observed even in a one-dimensional map, if it is noninvertible (see below) as in the Logistic or the Mackey-Glass maps. However, if the map is invertible, then chaos can be observed only if $N \geq 2$ [29].

Definition 2.1 *We say that the map* $\mathbf{F}$ *is invertible if we can solve* $\mathbf{x}_{n+1} = \mathbf{F}(\mathbf{x}_n)$ *uniquely for* $\mathbf{x}_n$, *that is* $\mathbf{x}_n = \mathbf{F}^{-1}(\mathbf{x}_{n+1})$, *where* $\mathbf{F}^{-1}$ *is the inverse of* $\mathbf{F}$.

Deterministic chaos may be a useful description of the time behavior of a real physical system when that behavior is aperiodic or irregular [30]. In general this aperiodic behavior doesn't necessarily mean *chaos*, which is a deterministic process; it can also mean *noise*, which is a random process. Several means of distinguishing these two processes have been developed and used successfully both in theoretical calculations and experimental studies (see e.g. [31] and references therein). The easiest to use experimentally is called *divergence of nearby trajectories.* Chaotic systems are characterized by their strong dependence on initial conditions [32]. Figure 2.3 shows two trajectories with very close initial conditions $\mathbf{x}_1(0)$ and $\mathbf{x}_2(0)$ evolving forward in time under the action of continuous-time dynamical system. As time increases, their separation $\mathbf{d}(t) = \mathbf{x}_2(t) - \mathbf{x}_1(t)$ grows exponentially as $\mathbf{d}(t) = \mathbf{d}(0)e^{\lambda t}$, where λ is a positive constant. We say that the system displays "sensitive dependence on initial conditions" and therefore is chaotic.

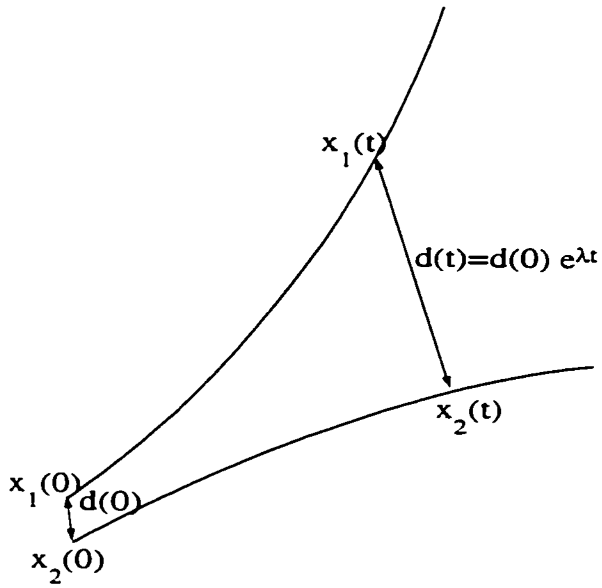

Figure 2.3: Sensitive dependence on initial conditions in chaotic systems. The trajectories $\mathbf{x}_1(t)$ and $\mathbf{x}_2(t)$ diverge as time increases. The rate of divergence λ is called the positive Lyapunov exponent (see Sect.2.6.2).

Deterministic chaos is observed in both dissipative and conservative systems such as classical systems and quantum systems. An example of a dissipative dynamical system is the Lorenz model [33]

$$\begin{aligned}\dot{x} &= -\sigma x + \sigma y \\ \dot{y} &= -xz + rx - y \\ \dot{z} &= xy - bz\end{aligned} \tag{2.3}$$

for which the volume element contracts exponentially in time as

$$V(t) = V(0)e^{-(\sigma+1+b)t}, \quad (\sigma > 0, b > 0). \tag{2.4}$$

where $(-\sigma - 1 - b) = \nabla \cdot \mathrm{f}$. With parameters $r = 28$, $\sigma = 10$ and $b = 8/3$, the trajectory is attracted to a bounded region in phase space, the motion is chaotic, and there is a sensitive dependence of the trajectory on the initial conditions as shown in Figure 2.4. Since the Lorenz model displays divergence of nearby trajectories for some range of its parameter values, then its behavior is *unpredictable* in the long-term even though the system is still deterministic. If we knew the initial conditions of a trajectory with infinite accuracy, then we could predict the future behavior of that trajectory by integrating (with infinite accuracy) the time-evolution equation (Eq.2.3). But since in a real or computer experiment initial states can only be known with finite precision, and that physical noise or truncation error are part of the dynamics, then it is impossible to predict its long-term behavior.

The Lorenz attractor has a Hausdorff dimension $D = 2.6$, which is noninteger. We call this type of attractor that has a noninteger value for the dimension, a *strange attractor*. This strange attractor arises because the flow contracts the phase space along some directions, but stretches it along others. This stretching and folding process produces a chaotic motion of the trajectory on that strange attractor [32].

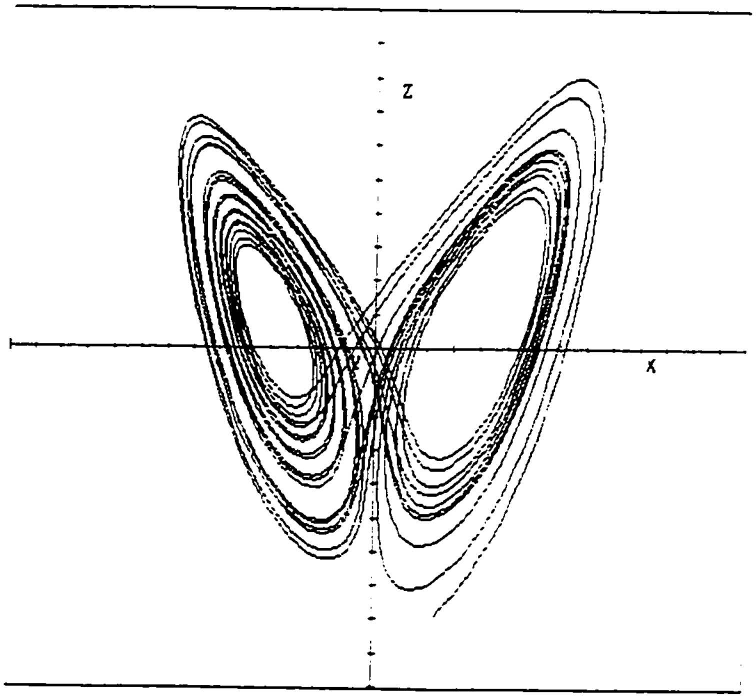

Figure 2.4: The chaotic Lorenz attractor projected in the xz plane (Eq.2.3). The parameters are $r = 28$, $\sigma = 10$, and $b = 8/3$.

2.5 Transitions to chaos

Different types of transitions to chaos have been observed in nonlinear dynamics as the control parameter of the system is changed: period-doubling bifurcation, quasi-periodicity, intermittency and the crisis. A lot is known about period-doubling cascades ("Feigenbaum scenario"), and one can even predict features of this transition quantitatively. We do not, however, have a complete classification of the possible transitions in dynamical systems, leading to more complicated behavior such as turbulence in the context of fluid dynamics. This thesis will be mainly concerned with period-doubling bifurcation, so only a brief discussion will be given about the other transitions.

2.5.1 Period-doubling bifurcation

In the flow, the period-doubling scenario begins with a limit cycle that may have been born from a bifurcation involving a fixed point. As the control parameter changes. this limit cycle becomes unstable and a new limit cycle with twice the period is created. As the control parameter is changed further, this new limit cycle becomes unstable and gives birth to another limit cycle with four times the period of the original limit cycle. The period-doubling process continues until the period becomes infinite. The trajectory is then chaotic. In the map, the period-doubling process starts with a fixed point, which becomes unstable and gives birth to period-2 orbit. This period-2 orbit becomes unstable and gives birth to period-4 orbit, and so on (see below). For simplicity, let us illustrate this process on a one-dimensional map of the form $x_{n+1} = F(x_n)$. One-dimensional maps are simple, numerically not very time consuming, and they can show many universal properties of chaotic transitions observed in higher-dimensional systems such as delay-differential equations (see Chapter 3). As an example, we will use the map of the Mackey-Glass equation [2] obtained in the singular limit of the delay-differential equation (see Sect.3.6).

$$x_{n+1} = F(x_n) = \frac{ax_n}{b(1 + x_n^{10})} \tag{2.5}$$

where a is the control parameter, b is a constant equals to 0.1.

Stability of the fixed points

The fixed points x^* of the map are the solutions of the equation $x^* = F(x^*)$. Their stability can be found from the linear stability analysis based on the first order of a Taylor series expansion:

$$x_{n+1} = F(x^*) + (x_n - x^*)F'(x^*) + \cdots \tag{2.6}$$

where $F'(x^*)$ is the derivative evaluated at the fixed point. If we keep the linear term only, the above equation can be rewritten as

$$x_{n+1} - x^* = (x_n - x^*)F'(x^*) \tag{2.7}$$

The criteria for the stability of the fixed point of the one-dimensional map is $|F'(x^*)| < 1$. In the Mackey-Glass map and for $a < 0.1$, we have only one fixed point $x^* = 0$. This fixed point is stable, so all the trajectories are attracted to it as shown in Figure 2.5a. This fixed point is an *attractor* and the set of initial conditions in the interval $[0, \infty[$ leading to this attractor is its *basin of attraction.*

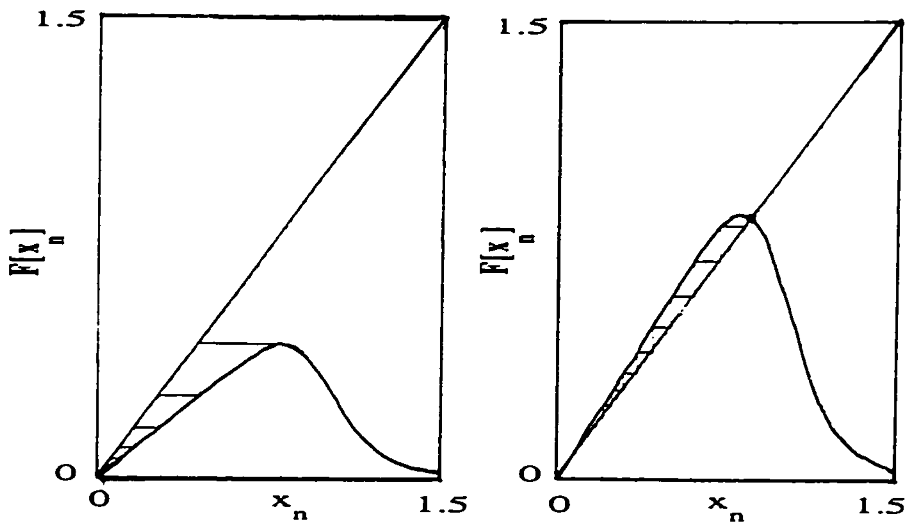

Figure 2.5: The fixed points in the Mackey-Glass map (Eq.2.5). a) There is only one fixed point at $x^* = 0$, which is stable for $a = 0.06$. The initial condition is $x_0 = 0.8$. b) There are two fixed points for $a = 0.12$: the stable fixed point is at $x^* = (a/b - 1)^{0.1}$, and the unstable one is at $x^* = 0$. The initial condition is $x_0 = 0.2$.

If $a > 0.1$, this fixed point becomes unstable in favour of the second fixed point $x^* = (a/b - 1)^{0.1}$ as shown in Figure 2.5b. If we further increase the control parameter a, this second fixed point also becomes unstable. Let us examine closely what happens when $0.125 < a < 0.134$ using the second iterate of $F(x_n)$, $F^2(x_n) = F[F(x_n)]$, shown in Figure 2.6. At $a = 0.13$, this fixed point becomes unstable in both $F(x_n)$ and $F^2(x_n)$, and two new stable fixed points $x_1^* = F^2(x_1^*)$ and $x_2^* = F^2(x_2^*)$ are created in $F^2(x_n)$ (see Fig.2.6b). These new fixed points are mapped onto each other by $F(x_n)$ as $F(x_1^*) = x_2^*$ and $F(x_2^*) = x_1^*$, and constitute an attractor of $F(x_n)$ of period-2 (see Fig.2.7a). At $a = 0.125$ (see Fig.2.6a) we say that the Mackey-Glass map trajectories undergo a *period-doubling bifurcation.* If we now further increase a , the fixed points of $F^2(x_n)$ become simultaneously unstable, and four stable fixed points of the fourth iterate $F^4(x_n) = F^2(x_n)F^2(x_n)$ are born (see Fig.2.8), which leads to an attractor of period-4. The trajectory cycles between four points in the following order: the largest, the smallest, next to the largest, next to the smallest, then back to the largest, and so on (see Fig.2.7b). The system has changed from a period-2 orbit to period-4 orbit at the transition point $a = 0.134$ (see Fig.2.8a). At this point we say that the system undergoes a second period-doubling bifurcation. This process of period-doublings continues as a increases, producing an infinite cascade of period-doublings, which accumulate at a finite a value denoted by $a_\infty \approx 0.138$ (see Fig.2.10a). The period of the trajectory becomes infinite. The trajectory is then chaotic (see Fig.2.9). In order to observe such a behavior, the map has to be unimodal, that is, a continuously differentiable function with a single maximum in the unit interval [0,1]. The Mackey-Glass map (Eq.2.5), which has a single maximum $x_0 \approx 0.8$ in the interval $[0, +\infty[$, verifies this property if the following rescaling is used: $x_n \longrightarrow x_n/(1-x_n)$. In general not all unimodal functions display an infinite sequence of period-doubling bifurcations, but only those with a negative Schwarzian derivative [34, 35].

$$SF(x) = \frac{F'''}{F'} - \frac{3}{2}(\frac{F''}{F'})^2 < 0 \tag{2.8}$$

The period-doubling cascade route to chaos has some important universal features, the Feigenbaum constants δ and α [36]. The constant δ is given by

$$\delta = \lim_{n\to\infty} \frac{a_n - a_{n-1}}{a_{n+1} - a_n} = 4.66920161... \tag{2.9}$$

where a_n is the parameter value at which a stable period-2^n is created as shown in Figure 2.11.

The Feigenbaum size scaling α is given by

$$\alpha = \lim_{n\to\infty} \frac{d_n}{d_{n+1}} = 2.5029... \tag{2.10}$$

where d_n is the distance between the *superstable* 2^n-cycle element x_0, defined by

$$\frac{dF^{2n}(x_0)}{dx_0} = 0\,, \tag{2.11}$$

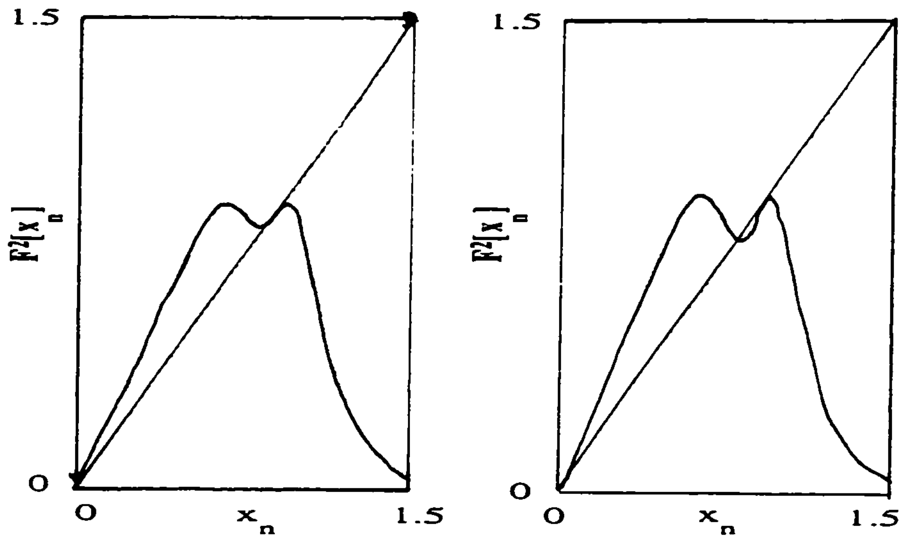

Figure 2.6: The second iterate $F^2(x_n)$ of the Mackey-Glass map function $F(x_n)$ (Eq.2.5). a) The function $F^2(x_n)$ becomes tangent to the 45^0 line at the first period-doubling bifurcation $a = 0.125$. b) Two new stable fixed points with $|slope| < 1$ are created in $F^2(x_n)$ for $a = 0.13$, and constitute an attractor of period-2 (see Fig.2.7a).

and the nearest to it of the other $2^n - 1$ points in the cycle, $x_1 = F^{2n-1}(x_0)$ (see Fig.2.11), i.e.

$$d_n = |F^{2n-1}(x_0) - x_0| \; . \tag{2.12}$$

In addition to chaotic orbits, Figure 2.10 also shows narrow ranges within $a_\infty < a < 0.16$ in which the attracting orbit is periodic. For example, the widest such range is occupied by the period-3 occuring to the right of period-5, which occurs to the right of period-7, and so on. Because there are multiple chaotic bands, however, these windows are known as higher periodicity windows. For example, at $a = 0.139$, where there are two chaotic bands, each subband shows a period-3 window, which together form a period-6 window (see Fig.2.10a). This ordering of periodic orbits was proved by the Russian mathematician A. N. Sarkovskii in 1964 in his remarkable theorem [37]:

Theorem 2.3 *Consider a continuous one-dimensional map function $F(x)$. Then if for*

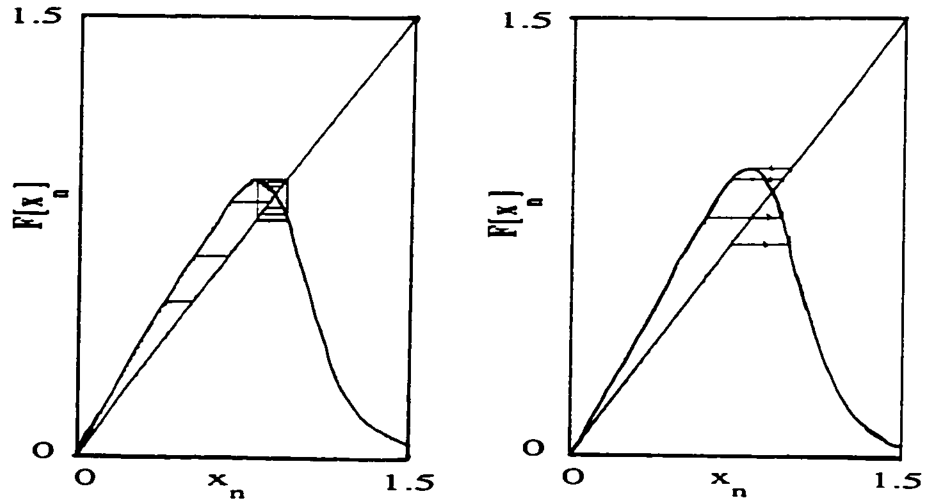

Figure 2.7: a) A stable period-2 orbit, cycling between two points on the map, is obtained after the first period-doubling bifurcation for $a = 0.13$. The initial condition is $x_0 = 0.4$. b) A stable period-4, orbit cycling between four points on the map, is obtained after the second period-doubling bifurcation for $a = 0.1365$. The initial condition is $x_0 = 0.6$.

some parameter value, F has a periodic point with prime period m, then F also has (for the same parameter value) a periodic point of period n, where n occurs to the right of m in the following ordered set:

$$3 \rightarrow 5 \rightarrow 7 \rightarrow \cdots 2 \cdot 3 \rightarrow 2 \cdot 5 \rightarrow \ldots 2^2 \cdot 3 \rightarrow 2^2 \cdot 5 \rightarrow \cdots \rightarrow 2^3 \rightarrow 2^2 \rightarrow 2 \rightarrow 1. \tag{2.13}$$

First we list all the odd positive integers starting with 3 in increasing order. Then we list the positive integers that are two times the odd integers starting again with 3 in increasing order, then the positive integers that are four times the odd integers, and so on. Finally, we list in decreasing order the powers of 2.

If a is further increased, other periodic windows are observed such as period-4 and period-5 (see Fig.2.10).

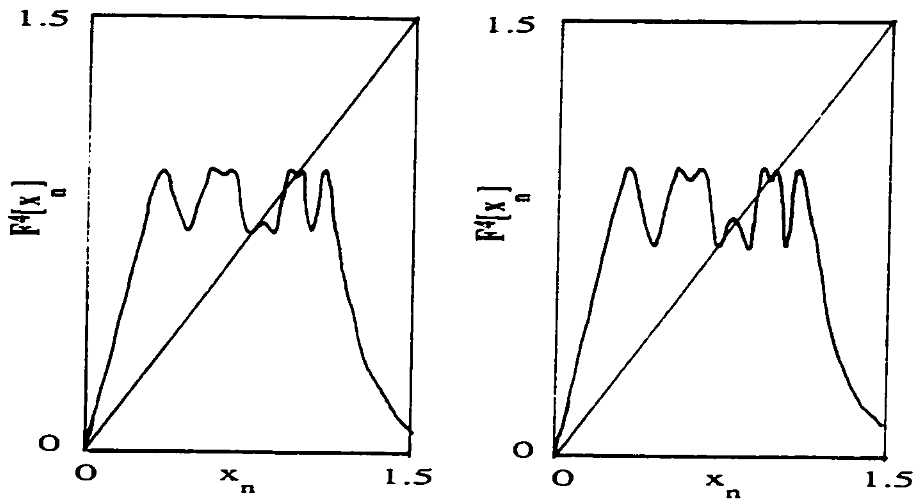

Figure 2.8: The forth iterate $F^4(x_n)$ of the Mackey-Glass map function $F(x_n)$ (Eq.2.5). a) The function $F^4(x_n)$ becomes tangent to the 45^0 line at the second period-doubling bifurcation $a = 0.134$. b) Four new stable fixed points are created in $F^4(x_n)$ for $a = 0.1365$, and constitute an attractor of period-4 (see Fig.2.7b).

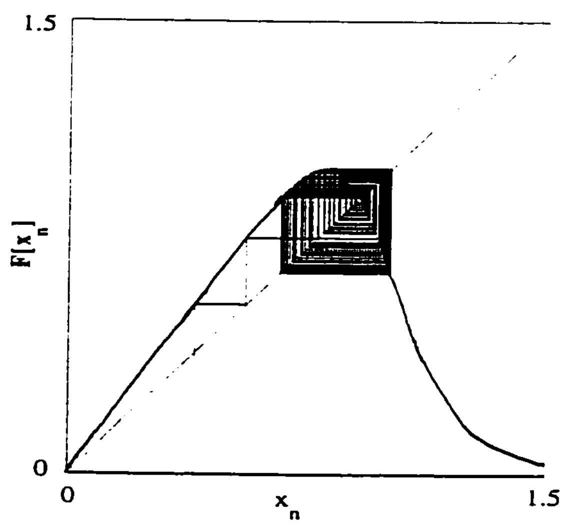

Figure 2.9: The chaotic trajectory is represented on the Mackey-Glass map for $a = 0.14$ and $x_0 = 0.4$.

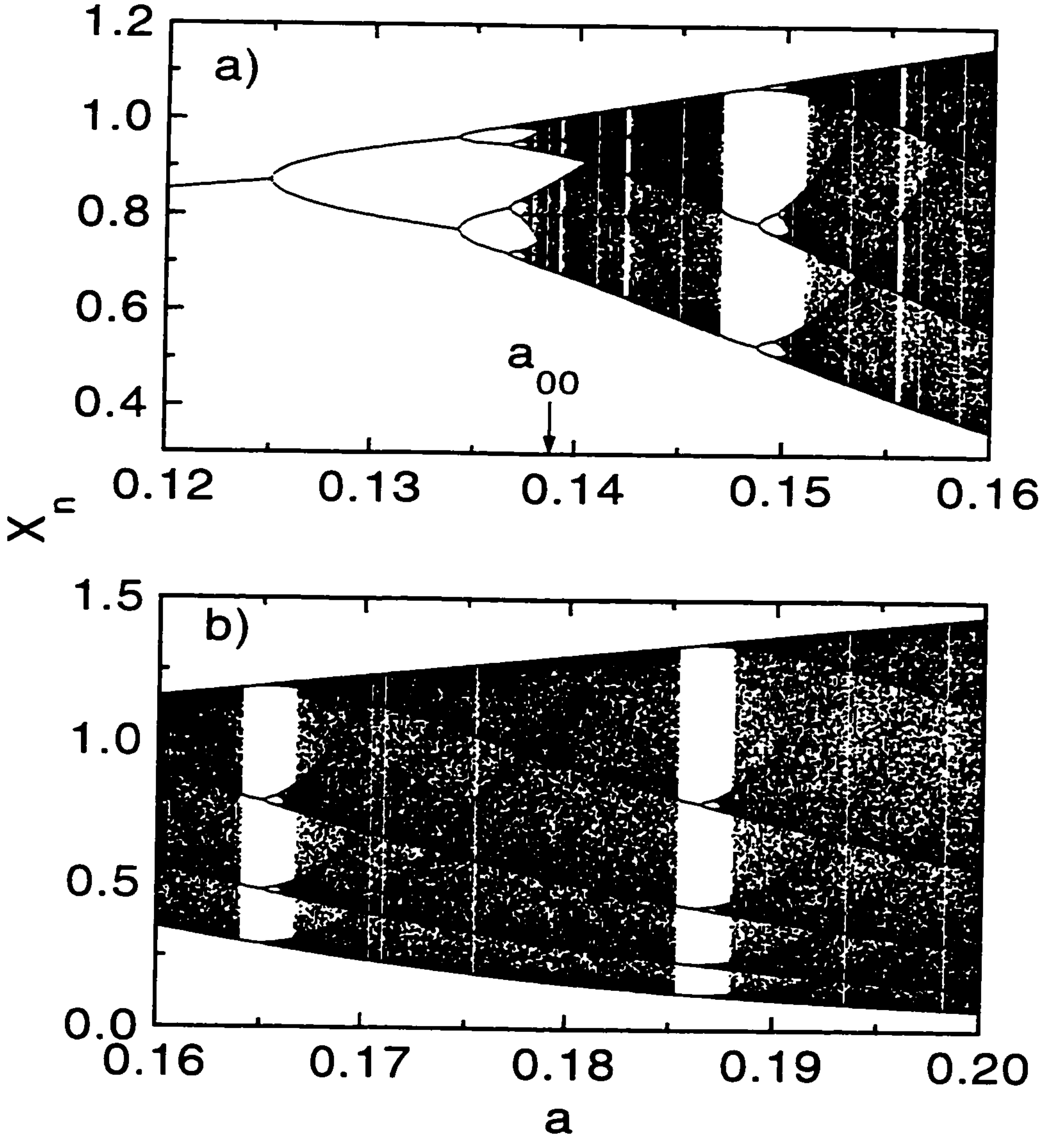

Figure 2.10: Bifurcation diagram showing a period-doubling cascade in the Mackey-Glass map (Eq.2.5). a) The parameter a spans between 0.12 and 0.16. b) The parameter a spans between 0.16 and 0.2.

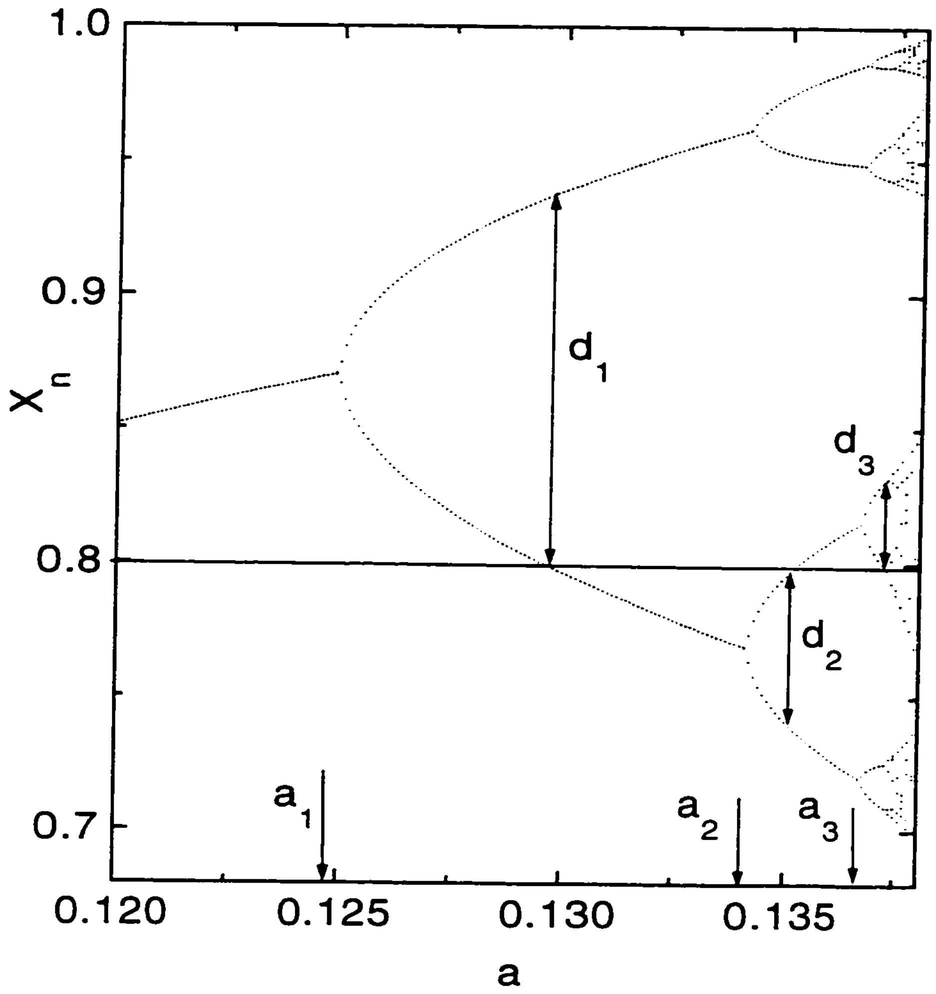

Figure 2.11: The distances $(d_n)'s$ and their correspondence $(a_n)'s$ for superstable 2^n-orbits. The abscissa $x_0 \approx 0.8$ (solid line), at which the Mackey-Glass map function is maximum, is part of the superstable orbits, and is responsible for producing a null characteristic multiplier (Eq.2.11).

2.5.2 Intermittency

This transition to chaos in flows was described by Pomeau and Manneville [38](see also [27, 29]). It occurs when the periodic behavior is interrupted by a finite duration of bursts (see Fig.2.13 for the map). As the control parameter is changed the bursts become more frequent so that the periodic behavior can no longer be distinguished. The stable periodic orbit either becomes unstable or is destroyed, and is not replaced by a new stable orbit as in the period-doubling bifurcations. Based on the type of stability of the orbit, we can distinguish three types of intermittency as shown in Figure 2.12:

Type I: saddle-node bifurcation (in a one-dimensional map this is called a *tangent bifurcation*).
Type II: Hopf-bifurcation.
Type III: inverse period-doubling.

In the saddle-node bifurcation, the stable and unstable eigenvalues of the linearized Poincaré map of the flow come together and annihilate each other at point $+1$ on the unit circle. This leads to merging of the stable and unstable orbits, and the periodic behavior is then interrupted by the chaotic bursts. As the control parameter of the system is changed, the chaotic burst becomes longer and occurs more frequently until the entire behavior is chaotic. In the Hopf bifurcation, the periodic orbit goes unstable by having a complex conjugate pair of eigenvalues that cross the unit circle simultaneously. In this type of intermittency, the system's behavior switches between periodic and quasi-periodic behavior. In the inverse period-doubling bifurcation a real eigenvalue crosses the unit circle at -1. The unstable periodic orbit collapses onto a stable periodic orbit, which becomes unstable at the bifurcation point. Type I intermittency is probably the most important since it has been observed in many experiments, particularly in systems that also show period-doubling bifurcations. So we will describe this transition in detail.

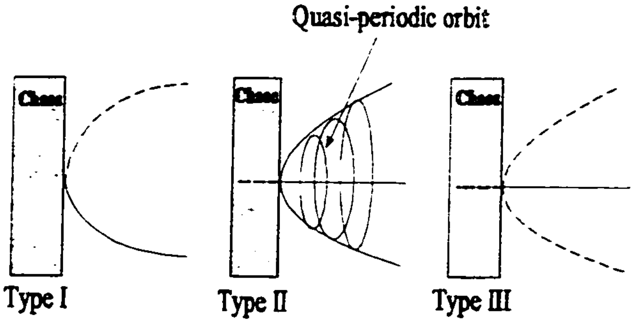

Figure 2.12: Three types of intermittency transitions to chaos can be distinghished: type I is the saddle-node bifurcation, type II is the Hopf-bifurcation, and type III is the inverse period-doubling. The stable and unstable orbits are represented by solid and dashed lines, respectively. In all cases, the abscissa (not shown) corresponds to the parameter.

Type I intermittency

This type of transition is observed in continuous-time systems such as Lorenz system of ordinary differential equations and also in discrete-time systems such as the Logistic and the Mackey-Glass maps. In this Section we describe in details how this transition to chaos occurs in Mackey-Glass one-dimensional map (Eq.2.5). At the critical point $a_c = 0.147$ this map exhibits a periodic window of period three in the chaotic regime as shown in Figure 2.10. As a is decreased slightly below a_c, the periodic behavior is interrupted by chaos. This behavior can be explained using the third iterate $F^3(x_n)$ of $F(x_n)$. At $a = a_c$, $F^3(x_n)$ has three stable fixed points, and becomes tangent to the 45^0 line at these fixed points. At this point we are in presence of a *tangent bifurcation* (see Fig.2.14a). If a is decreased slightly below a_c, the stable fixed points disappear as shown in Figure 2.14b, and the trajectories take many iterates to go through the gaps between the map function and the 45^0 line as shown in Figure 2.15. Since the previous stable fixed points are not replaced by new stable fixed points as in the period-doubling scenario, the motion becomes chaotic. As the gap size decreases, i.e. as $a \rightarrow a_c$ from below, the trajectory spends more time on the average in the gap and the system's behavior becomes more and more periodic until the gap size vanishes,

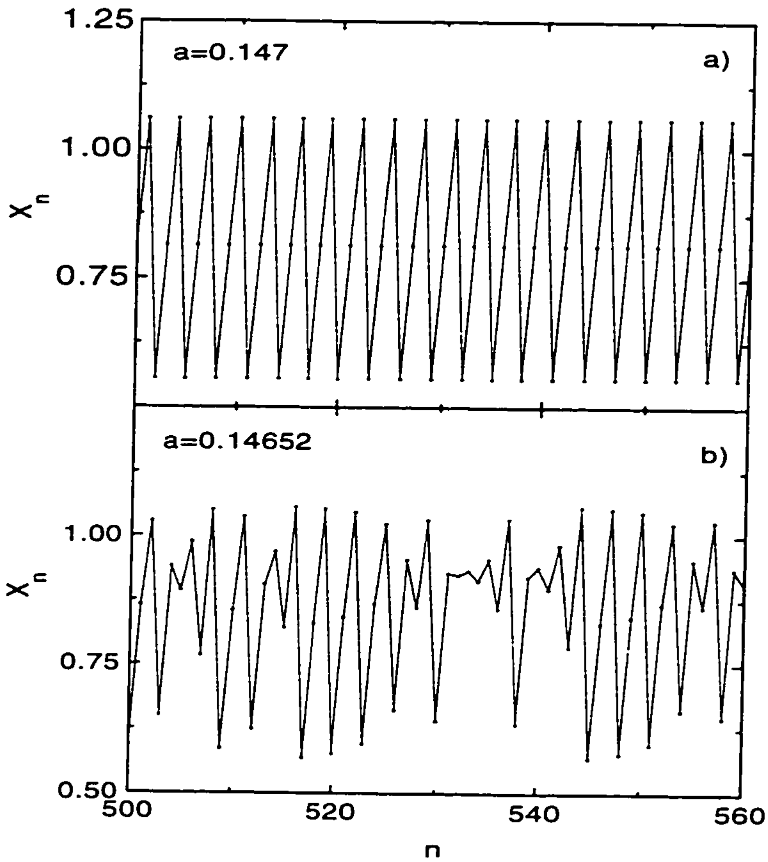

Figure 2.13: Intermittency in the MG map. a) The period-3 window in the chaotic regime at $a = 0.147$ (see Fig.2.10). b) The periodic behavior in (a) is interrupted by chaotic burts when a is decreased slightly towards 0.14652.

and then the system is completely periodic.

2.5.3 Crises

A crisis is defined as the sudden change in the chaotic attractor when it collides with an unstable periodic orbit [39, 40] . According to the nature of changes that can result from that collision, we can distinguish three different types of crisis:

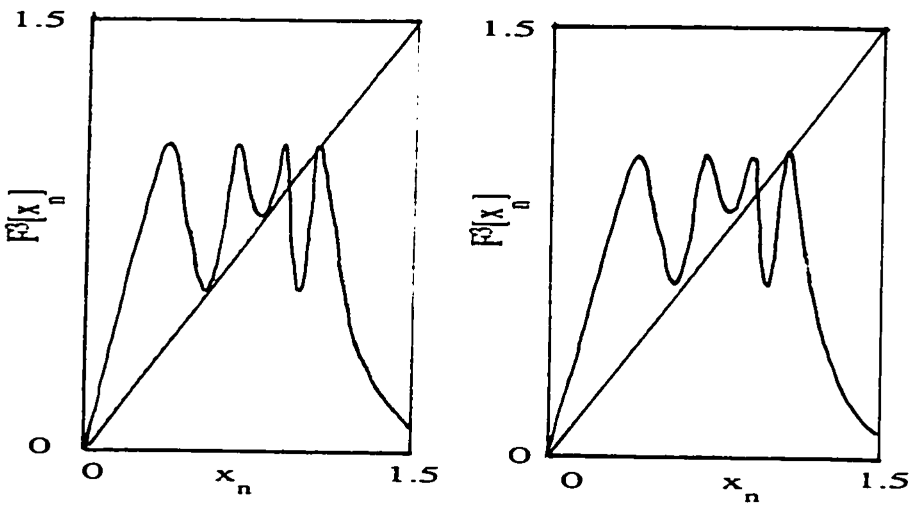

Figure 2.14: The transition to intermittency type I via the tangent-bifurcation in the Mackey-Glass map. a) The function $F^3(x_n)$ is tangent to the 45^0 line at $a = 0.147$. b) A gap between the function $F^3(x_n)$ and the 45^0 line is created when a is decreased to 0.145.

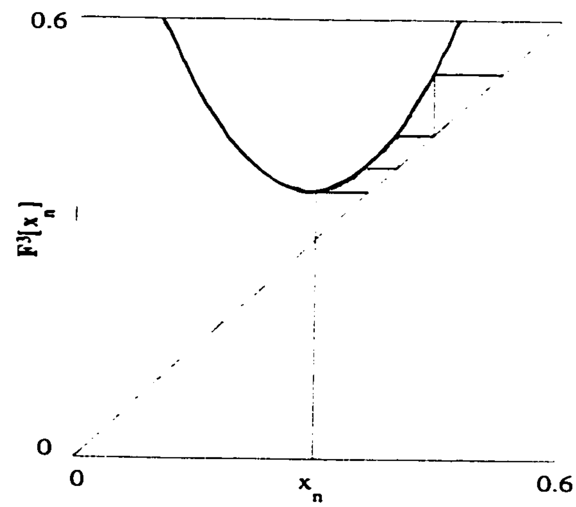

Figure 2.15: The third iterate of $F(x_n)$ in the Mackey-Glass map. The trajectory spends some time to go through the gap for $a = 0.14652$ and $x_0 = 0.55$. Then, the periodic behavior is interrupted by chaotic bursts (see Fig.2.13).

a) **Boundary crisis**

The chaotic attractor is suddenly destroyed by a collision with the periodic orbit on its basin boundary. This type of crisis is observed in the Logistic map and also in the Hénon map. For example in the Logistic map $x_{n+1} = F(x_n) = rx_n(1 - x_n)$ at $r = 4$ the chaotic attractor collides with the unstable fixed point $x^* = 0$, and then disappears completely without replacement with another attractor. For $r > 4$, there is a region of space called the *escape region* centered near $x = 1/2$, in which all trajectories, going through this region go to $-\infty$. The boundary of this region is found by solving the map equation that leads to $F(x_n) = 1$. The solutions are

$$x_1 = \frac{1}{2}\left(1 - \sqrt{\frac{r-4}{r}}\right), \quad x_2 = \frac{1}{2}\left(1 + \sqrt{\frac{r-4}{r}}\right) \tag{2.14}$$

the witdh of the *escape region* is then $W = x_2 - x_1 = \sqrt{(r-4)/r}$ as shown in figure 2.16. Trajectories starting outside the escape region will wander chaotically until they hit this region and escape.

b) **Interior crisis**

This type of crisis occurs when the size of the attractor suddenly increases due to a collision with the periodic orbit in the interior of its basin. An example of this crisis is illustrated in Figure 2.17 on the Mackey-Glass map for the period-3 window. The chaotic attractor collides with an unstable fixed point, which is created at the tangent bifurcation (dashed lines), and suddenly increases in size at $a = 0.1512$. This type of behavior is also known as *crisis-induced intermittency* [41].

c) **Attractor merging crisis**

In this case, two or more chaotic attractors simultaneously collide with a periodic orbit (or orbits) on the basin boundary, and then merge to form one chaotic attractor(see [29]).

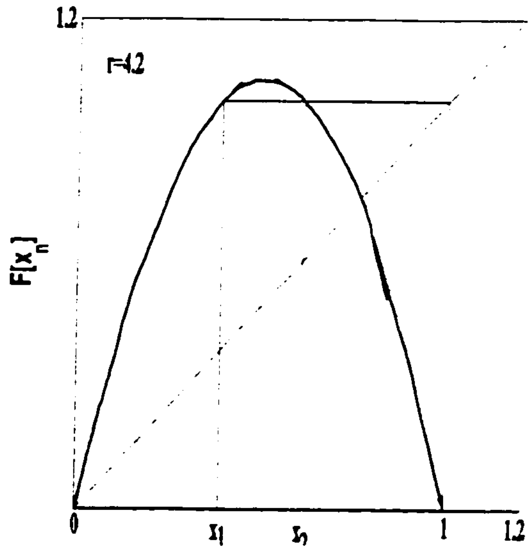

Figure 2.16: The crisis scenario in the Logistic map observed for $r = 4.2$. The chaotic attractor is destroyed after the collision with the unstable fixed point $x^* = 0$. All trajectories landing in the escape region $[x_1, x_2]$ go to $-\infty$.

2.5.4 Quasi-periodicity route to chaos

The route to chaos via quasi-periodicity was first observed by Ruelle and Takens [42] and remains less understood theoretically in comparison with the period-doubling and intermittency routes. The quasi-periodic scenario involves competition between two or more independent frequencies characterizing the dynamics of the system. If the ratio of two frequencies f_2/f_1 is irrational, then we say that the behavior is quasi-periodic, where f_1 and f_2 are associated with the motion of the trajectories around a large and small cycle, respectively [27].

2.6 Characterizing the attractors

It is often difficult to distinguish a purely chaotic motion from a quasiperiodic one or from a motion perturbed by external noise by simply looking at a finite sequence of data. We need

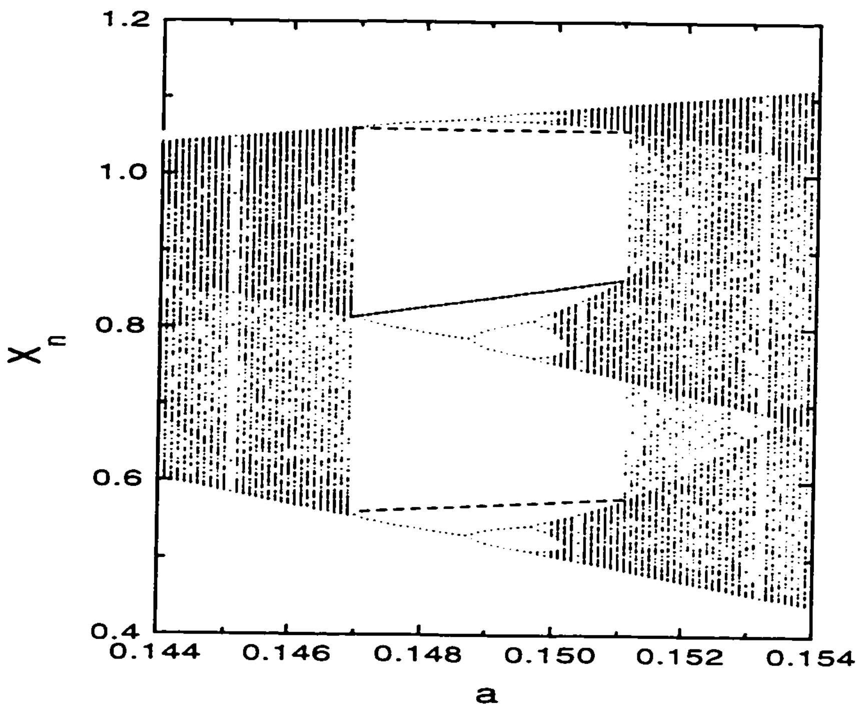

Figure 2.17: Interior crisis in the Mackey-Glass map for period-3 window: the stable (dotted lines) and unstable (dashed lines) fixed points annihilate each other at the tangent bifurcation. The chaotic attractor increases in size when it collides with an unstable fixed point, created at the tangent-bifurcation.

some quantitative means to recognize, characterize and classify attractors from the available data, and in particular, from a single time series of sampled points.

Power spectrum analysis is useful in telling quasiperiodic motion from periodic motion, and in identifying high-order periodicities embedded in chaotic bands (they appear as fine structure in the spectra). Power spectra of chaotic attractors associated with period-doubling distinguish themselves by sharp peaks on a broadband background, but this is also a feature of other types of chaotic attractors. There are sophisticated ways of characterizing attractors, among which Lyapunov exponents and various definitions for the dimension of the set of points constituting the attractor [32].

2.6.1 Dimension

In the phase space, the number of variables needed to describe a trajectory is N, but for trajectories on the attractor this number may be less than N. The dimension of an attractor represents the number of "active" degrees of freedom for a dynamical system. The dimension of trivial attractors can be easily calculated to be integers: $d = 0$ for fixed points, $d = 1$ for limit cycles, $d = 2$ for 2-tori (such as for quasi-periodic motion with two frequencies), etc. However, the dimension of strange attractors often turns out to have a noninteger value. There are several different dimensions that can be used to describe dynamical systems and their attractors: examples are the box-counting dimension, the information dimension, the correlation dimension, and Lyapunov dimension [32, 43].

a) Box-counting dimension

The box-counting dimension (often called the Hausdorff dimension or the capacity dimension) of a geometric object is determined by the following: construct boxes of side length ϵ to cover the space occupied by the geometric object, namely in our case, the attractor. We then count the number of boxes $N(\epsilon)$ needed to cover the object. We do this for successively smaller ϵ values. The box-counting dimension is defined to be the number d_b that satisfies

$$N(\epsilon) = \lim_{\epsilon \to 0} k\epsilon^{-d_b} \tag{2.15}$$

where k is a proportionality constant. By taking the logarithm of both sides and in the limit of very small ϵ, the term with the constant k goes to zero and the dimension becomes

$$d_b = \lim_{\epsilon \to 0} \frac{\ln(N(\epsilon))}{\ln(1/\epsilon)} \tag{2.16}$$

The box-counting dimension is 0 for a point, 1 for a line segment, 2 for a square, etc. Let us apply the above formula to the case of strange attractors such as the Cantor set.

b) Cantor set

We illustrate the concept of box-counting dimension using a simple Cantor set, created as follows: we start with a line segment of length 1, we delete the middle third of that segment. Two segments are left each of length 1/3. Now, we delete the middle third of each of those segments, resulting in four segments, each of length 1/9 (see Fig.2.18). If we repeat this procedure $n+1$ times, we produce 2^n segments, each of length $(1/3)^n$. As $n \to \infty$, resulting segments form a "Cantor set". Equation 2.16 then becomes

$$d_b = \lim_{n \to \infty} \frac{\ln(N(\epsilon_n))}{\ln(1/\epsilon_n)} \tag{2.17}$$

The dimension of this set is then obtained by putting $\epsilon_n = (1/3)^n$ and $N(\epsilon_n) = 2^n$,

$$d_b = \ln 2 / \ln 3 = 0.63... \tag{2.18}$$

Since this dimension is a noninteger number between zero and one, we say that the Cantor set is a fractal object [44].

When counting the number of boxes to cover the attractor $N(\epsilon)$, no attention has been paid to the possible inhomogeneity of the attractor. A box is counted only once no matter how many times an orbit goes through it. To take this inhomogeneity into account,

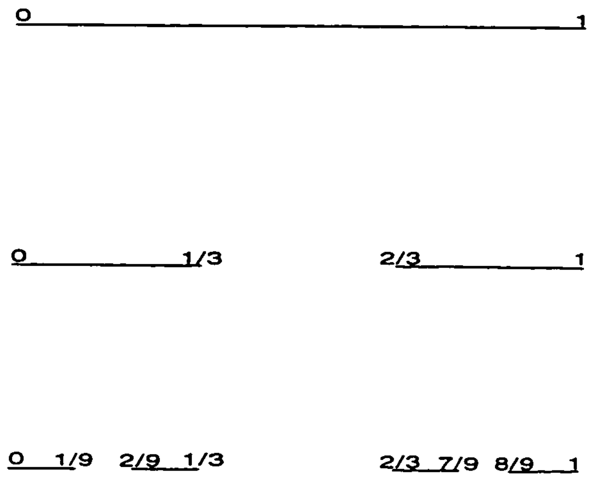

Figure 2.18: Calculating the box-counting dimension using the Cantor set.

one introduces a dimension that uses information on how frequently a box is visited. The corresponding dimension is called the information dimension.

c) Information dimension

This dimension is introduced in order to correct the box-counting dimension specially when the attractor is inhomogeneous and is given by

$$d_I = \lim_{\epsilon \to 0} \frac{I(\epsilon)}{\ln(1/\epsilon)} \tag{2.19}$$

where

$$I(\epsilon) = -\sum_{i=1}^{N(\epsilon)} P_i \ln P_i \tag{2.20}$$

$N(\epsilon)$ being the total number of boxes visited. If every box is visited with equal probability $P_i = 1/N(\epsilon)$, then $d_I = d_b$. In general $d_I \leq d_b$.

The box-counting algorithm has its limitations, particularly for higher-dimensional systems such as delay-differential equations studied in this thesis. The number of computations required increases exponentially with the phase space dimension, so it is a time-consuming process. A computationally simpler dimension for an attractor, is the correlation dimension, introduced by Grassberger and Procaccia [45].

d) Correlation dimension

The correlation dimension is widely used to characterize chaotic attractors. It is easy to implement and has a computational advantage because it uses the trajectory points directly and does not require a separate partitioning of the phase space. It is given by

$$d_c = \lim_{r \to 0} \frac{\ln C(r)}{\ln r} \tag{2.21}$$

where $C(r)$ is called the correlation integral and is computed by counting distances between point pairs on the attractor:

$$C(r) = \frac{number\ \ of\ \ distances\ \ less\ \ than\ \ r}{total\ \ number\ \ of\ \ distances} \tag{2.22}$$

Extracting the dimension directly from Eq.2.21 is inefficient, since it is not possible to take the limit $r \to 0$. In practice we plot $\ln C(r)$ versus $\ln r$ for a set of increasing embedding dimensions [43]. As the embedding dimension increases, the slope of the $\ln C(r)$ versus $\ln r$ plot should, over a certain range of r values (the "scaling range"), saturate at a value equal to the attractor's dimension.

In dissipative dynamics, the correlation dimension reflects only the density of points in phase space and doesn't reflect the stretching or folding of the attractor. Kaplan and Yorke introduced a useful conjecture [46] that relates the fractal dimension of a strange attractor to the Lyapunov exponents (see Sect.2.6.2). The corresponding dimension is called the Lyapunov dimension.

e) Lyapunov dimension

The Lyapunov dimension, compared to the box-counting method, converges fairly rapidely as a function of time. It is given by

$$d_L = j + \frac{\sum_{i=1}^{j} \lambda_i}{|\lambda_{j+1}|} \tag{2.23}$$

where $\{\lambda_1 > \lambda_2 > \cdots\}$ are the Lyapunov exponents in decreasing order and j is the largest integer such that $\sum_{i=1}^{j} \lambda_i > 0$.

2.6.2 Lyapunov spectrum

The *Lyapunov exponents* measure the rate of exponential divergence of nearby trajectories [30]. If two nearby trajectories on a chaotic attractor start off an infinitesimal distance ϵ apart, then their trajectories diverge and their separation at time t satisfies $\epsilon e^{\lambda t}$. The parameter λ is called the Lyapunov exponent. To define the spectrum of Lyapunov exponents, consider a sphere of radius $r(0)$ in the phase space. Under the dynamics this sphere evolves to an ellipsoid, with some directions being stretched and others contracted. The longest axis of this ellipsoid corresponds to the most unstable direction of the flow, and the asymptotic rate of expansion of this axis corresponds to the largest Lyapunov exponent. At time t the length of the ith principal axis will be $l_i(t)$, and then the ith Lyapunov exponent is defined by

$$\lambda_i = \lim_{t \to \infty} \frac{1}{t} \ln \frac{l_i(t)}{r(0)} \tag{2.24}$$

By convention, the Lyapunov exponents are always ordered so that $\{\lambda_1 > \lambda_2 > \cdots\}$. If any of the λ_i is positive, then the system is chaotic. If all the λ_i are negative, then all orbits are stable. In a dissipative system, the sum of the λ_i must be negative. If the dynamics is governed by differential equations, there will be a zero Lyapunov exponent which corresponds to the motion along the vector field.

There is an interesting result by Pesin [47] (see also [48]) that relates the sum of the positive Lyapunov exponents to metric entropy of Kolmogorov and Sinai

$$h(\mathbf{X}) = \sum_{\lambda_i > 0} \lambda_i \tag{2.25}$$

The metric entropy is a measure of the time rate of creation of information as a chaotic orbit evolves. We will see in chapter 4 that this result is also related to the decay constant of power spectra in delay-differential equations.

Besides the characterization of chaotic attractors, Lyapunov exponents are used to classify attractors. For example, in three-dimensional systems, the spectra $(-,-,-)$, $(0,-,-)$, $(0,0,-)$ and $(+,0,-)$ correspond respectively to a fixed point, a limit cycle, a 2-tori, and a strange attractor.

The spectrum of Lyapunov exponents is determined by following the evolution of small perturbations to an orbit under the linearized dynamics of the system. Suppose the system is described by a discrete-time dynamic in R^d:

$$\mathbf{y}_{n+1} = \mathbf{F}(\mathbf{y}_n) \tag{2.26}$$

where $\mathbf{F} : R^d \rightarrow R^d$ is a map. This map can result, for example, from a difference scheme used to integrate equations of motion in continuous-time. A small perturbation $\mathbf{z}_n$ to the orbit $\mathbf{y}_n$ evolves according to the linearized dynamics given by

$$\mathbf{z}_{n+1} = \mathbf{DF}(\mathbf{y}_n) \cdot \mathbf{z}_n \tag{2.27}$$

where $\mathbf{DF}(\mathbf{y}_n)$ is the Jacobian matrix of the map $\mathbf{F}(\mathbf{x})$

$$\mathbf{DF}(\mathbf{x})_{\alpha\beta} = \frac{\partial F_\alpha(\mathbf{x})}{\partial x_\beta}; \quad \alpha, \beta = 1, 2, \cdots, d \tag{2.28}$$

evaluated along the orbit at $\mathbf{x} = \mathbf{y}_n$. If we advance L time steps forward from the point $\mathbf{y}_n$, we find that the perturbation has evolved to

$$\begin{aligned} \mathbf{z}_{n+L} &= \mathbf{DF}(\mathbf{y}_{n+L-1}) \cdot \mathbf{DF}(\mathbf{y}_{n+L-2}) \cdots \mathbf{DF}(\mathbf{y}_n) \cdot \mathbf{z}_n \\ &\equiv \mathbf{DF}^L(\mathbf{y}_n) \cdot \mathbf{z}_n \end{aligned} \tag{2.29}$$

We wish to compute the eigenvalues of the so-called "Oseledec" matrices:

$$OSL(\mathbf{x}, L) = [(\mathbf{DF}^L(\mathbf{x}))^T \cdot \mathbf{DF}^L(\mathbf{x})]^{1/2L} \tag{2.30}$$

$$OSL(\mathbf{x}) = \lim_{L\to\infty} OSL(\mathbf{x}, L). \tag{2.31}$$

where $(\mathbf{DF}^L(\mathbf{x}))^T$ is the transpose matrix of $\mathbf{DF}^L(\mathbf{x})$. The *multiplicative ergodic* theorem of Oseledec [49] states that in the limit $L \to \infty$, the matrix $OSL(\mathbf{x})$ is well-defined and its eigenvalues are independent of the initial conditions that lead to the orbit of the attractor. The matrix $OSL(\mathbf{x}, L)$ is real and symmetric, so the $1/2L$ power is well-defined. and the resulting eigenvalues are real and positive. These eigenvalues $e^{\lambda_1}, e^{\lambda_2}, ..., e^{\lambda_d}$ are independant of $\mathbf{x}$ within the basin of attraction of the attractor. In practice, when L becomes large, the matrix $OSL(\mathbf{x})$ is very ill-conditioned and the diagonalization of such a matrix poses serious problems. We will use a recursive QR decomposition method due to Eckmann and Ruelle [32] in the implementation of Abarbanel [50]. Any arbitrary matrix M can be decomposed into a product of an orthogonal matrix Q and an upper-triangular matrix R with non-negative diagonal elements so that $M = Q \cdot R$. Applying the recursive QR decomposition on the matrix $M_1 = (\mathbf{DF}^L)^T \cdot \mathbf{DF}^L$ yields

$$M_1(i).Q_1(i-1) = Q_1(i).R_1(i)\,. \tag{2.32}$$

where $Q(0)$ is initialized to the identity matrix. By performing the above equation $2L$ times, the matrix M_1 then becomes

$$M_1 = Q_1(2L).R_1(2L).R_1(2L-1)\cdots R_1(1)\,. \tag{2.33}$$

If $Q_1(2L)$ is the identity matrix, the eigenvalues of $OSL(\mathbf{x}, L)$ will all lie in the upper triangular matrix M_1. In general, $Q_1(2L)$ is not the identity. So we shuffle it over to the right of Eq.2.33 and start the QR decomposition again. This yields the matrix M_2 defined as follows:

$$\begin{aligned} M_2 &= R_1(2L).R_1(2L-1)\cdots R_1(1)\cdot Q_1(2L) \\ &= Q_2(2L).R_2(2L).R_2(2L-1)\cdots R_2(1)\,. \end{aligned} \tag{2.34}$$

Since $M_2 = Q_1^T(2L)\cdot M_1 \cdot Q_1(2L)$, M_1 and M_2 have the same eigenvalues. We continue this operation of shuffling creating respectively $M_3, M_4, ..., M_k$:

$$M_k = Q_k(2L).R_k(2L).R_k(2L-1)\cdots R_k(1)\,. \tag{2.35}$$

As k increases, $Q_k(2L)$ converges to the identity matrix [51]. In practice, this convergence is obtained after 2 or 3 shufflings only, and one can obtain the Lyapunov exponents λ_i from the diagonal elements of the $R_k(j)'s$[1]:

$$\lambda_i = \frac{1}{2L}\sum_{j=1}^{2L} \ln[R_k(j)_{ii}] \tag{2.36}$$

The recursive QR decomposition method can also be applied to continuous-time systems such as differential equations. One can simultaneously solve the differential equation and the variational equation for the perturbation around the computed orbit and then apply the QR decomposition procedure in the same fashion to find the Lyapunov exponents.

2.7 Conclusion

We have introduced the necessary mathematical tools used in this thesis such as stability analysis and bifurcation theory. We focussed mostly on the Mackey-Glass map, which is of great interest in this thesis. This map will be used to study certain properties of first order delay-differential equations such as stability, controllability, and synchronization. We gave an overview of the different transitions that can occur in chaotic dynamical systems and the different quantities that characterize and classify an attractor, such as its dimension and its Lyapunov exponent spectrum.

[1]The eigenvalues of a product of upper-triangular matrices are the product of the eigenvalues of the individual matrices

Chapter 3

Delay-differential equations

3.1 Introduction

Delay-differential equations (DDE's) are used to model a large variety of nonlinear phenomena in which the time evolution depends not only on present states but also on states at or near a given time in the past (see e.g. [52] and references therein). From the point of view of nonlinear dynamics, these infinite-dimensional dynamical systems are interesting because their chaotic attractors have a finite dimension proportional to the delay [7, 53, 54, 55], making them useful to study general properties of high-dimensional chaos (Fig.1). The large delay case, or more precisely, the large delay-to-response time case, has received a lot of attention because it is in this limit that certain properties of the DDE can be studied using a discrete-time map [8, 9]. Other recent studies have approached the problem of high-dimensional chaos in DDE's through the use of interval maps [10] and iterative delay maps [56, 57]. Further, there has been recent interest in DDE's at large delay in the context of phase defects and phase turbulence in lasers, which can be studied by arranging temporal solutions in a two-dimensional space-time representation [59].

DDE's at large delay are also of interest because they exhibit multistability, i.e. different initial conditions lead to different asymptotic periodic solutions, chaotic solutions or both [60]. This means that, while a given initial function uniquely specifies the solution, the functional space in which these equations evolve has more than one basin of attraction. For example, the asymptotic solution depends on the choice of the initial function when the strength of the feedback is such that the system's behavior is periodic. However if the system's behavior is chaotic, the precise form of the initial function from which the DDE evolves is lost but the multistability still exists at large delay. This property makes delay-differential systems attractive for memory storage purposes, as first suggested by Ikeda [8]. In fact, it has been shown [11, 13, 61] that finite bit strings can be stored as specific periodic solutions of DDE's through judicious choices of initial conditions. The procedure works also for unstable periodic solutions stabilized by chaos-control techniques [62] (Chap.6 of this thesis).

There has been much progress in our understanding of multistability and chaos in DDE's (see e.g. [8]), despite two main difficulties that hamper such studies. The first is that initial conditions for DDE's are functions on the delay interval $(-\tau, 0)$, where τ is the delay; evolution in functional spaces is more difficult to study than in finite-dimensional phase spaces. Further, calculating dynamical invariants for high-dimensional chaos is numerically very involved.

Nonlinear phenomena induced by the delay in the feedback loop have many applications in laser systems [60], in physiological systems [2, 4, 5, 63], and in artificial neural network models [6].

We present first some important properties of delay-differential equations in Section 3.2. In Section 3.3, we discuss linear stability of fixed points, and show how periodic and chaotic solutions appear with increasing delay. In Section 3.4 we discuss multistability of periodic and chaotic solutions, and present some new results that relate this multistability to the unstable modes in the linearized system. In Section 3.5, we study the more general case of distributed delays. In Section 3.6, we show how the continuous-time difference equation

(CTDE), which is obtained in the singular perturbation limit, can predict the asymptotic solution of the DDE at large delay. The Chapter concludes in Section 3.7.

3.2 Properties of delay-differential equations(DDE's)

First order nonlinear delay-differential equations such as the Mackey-Glass (MG) [2] or the Ikeda equation [1] have the form

$$\frac{dx(t)}{dt} = -bx(t) + F(x(t-\tau)) \tag{3.1}$$

where x is a state variable which is destroyed at a constant rate b and produced at a rate F that depends on the value of the state variable x at time τ in the past. The feedback function F can be of the positive feedback-type if F is monotone increasing, or negative feedback-type if it is monotone decreasing, or mixed feedback-type if it is monotone increasing over some portions of its domain, and decreasing over other portions. This thesis is mainly concerned with this last case, which is responsible for the chaotic behavior observed in the Ikeda model of the laser ring cavity and the Mackey-Glass model of white blood cell production.

To solve Eq.3.1, it is necessary to specify the initial condition of x over one delay interval τ, i.e. one must specify an initial function. Since a function corresponds to an infinite number of initial conditions, these dynamical systems are infinite-dimensional. In numerical simulations, we partition this delay interval into M subintervals. Thus the behavior of the infinite-dimensional DDE is approximated by that of an M-dimensional discrete dynamical system [7], which maps the values of x over one delay interval into those over the following delay interval. The limit $M \to \infty$ recovers the infinite-dimensional state space. For large delay, the integration of this equation is time-consuming. We rescale this equation by the singular perturbation parameter ϵ as follows:

$$\tau \quad \longrightarrow \quad \tau'/\epsilon$$

$$\begin{aligned} t &\rightarrow t'/\epsilon \\ x(t) &\rightarrow y(t') \end{aligned} \tag{3.2}$$

where ϵ is a small positive number and τ' is a finite delay. Eq.3.1 then becomes

$$\epsilon \frac{dy(t')}{dt'} = -by(t') + F(y(t' - \tau')) \tag{3.3}$$

With this transformation, we can study numerically a DDE at large delay (i.e. small ϵ) in terms of an equivalent DDE at smaller delay.

Delay-differential equations have very interesting properties that make them appealing for information storage purposes [8, 11, 13, 62], as we will see in later chapters. These properties can be summarized as follows:

- They are infinite-dimensional dynamical systems because we need to specify a function over one delay interval as the initial condition.
- They are multistable at large delays, i.e. different initial functions lead to different attractors.
- In the chaotic regime, their attractors have a finite fractal dimension proportional to the delay.
- The solutions exhibit series of connected plateaus in the singular limit, where the delay is much greater than the response time $\tau_r = 1/b$. In this limit, certain properties of the DDE can be studied using a discrete-time map.

3.3 Solutions of the Mackey-Glass (MG) equation

This thesis focusses on numerical simulations of the Mackey-Glass DDE

$$\frac{dx(t)}{dt} = -bx(t) + \frac{ax(t-\tau)}{1 + x^{10}(t-\tau)}, \tag{3.4}$$

where b is kept fixed at 0.1 throughout this thesis (as in [7]), and a and τ are parameters that can be varied from one simulation to the next.

3.3.1 Fixed points

If the parameter $a < 0.125$, numerical solutions show only stable fixed points no matter what the value of the delay is. This result agrees with the Mackey-Glass one-dimensional map, studied in Chapter 2. We will see the reason for this later in this Chapter. What is a fixed point?

The fixed points of equation 3.1 are defined by the fact that the system is not changing with time, i.e.

$$x(t) = x(t-\tau) = x^* = constant, \tag{3.5}$$

and

$$\frac{dx(t)}{dt} = 0, \quad F(x^*) = bx^*. \tag{3.6}$$

In general we can't solve Eq.3.6 analytically, but if we plot the graph of $F(x^*)$ and bx^*, the fixed point will be at their intersection. In the MG equation (Eq.3.4) the fixed points are straightforward: $x_1^* = 0$ and $x_2^* = (a/b - 1)^{0.1}$. This thesis is concerned with the loss of stability of the latter, which can lead to period-doubling cascades and chaos when the delay "τ" and/or the feedback parameter "a" are increased. Since DDE's are high-dimensional systems, and in general cannot be solved analytically, we use a linear approximation near the steady states to find the stability of the solutions.

Linear stability analysis is used extensively in order to understand the dynamics of nonlinear systems near fixed points. We expand the nonlinear function to first order approximation in the neighborhood of the fixed point $x^* = x_2^*$ using a Taylor series expansion. Equation 3.1 becomes a linear differential equation

$$\frac{dx(t)}{dt} = -b[x(t) - x^*] + \beta[x(t-\tau) - x^*] + \cdots \tag{3.7}$$

where $\beta = F'(x^*) = b(10b/a - 9)$ is the derivative at the fixed point. Now if we set $u(t) \equiv x(t) - x^*$, the above equation can be rewritten as,

$$\frac{du(t)}{dt} = -bu(t) + \beta u(t - \tau). \tag{3.8}$$

If we take trial solutions of the form $u(t) = u(0)e^{st}$, the characteristic equation becomes

$$s + b - \beta e^{-s\tau} = 0 \tag{3.9}$$

Equation 3.9 has an infinite number of complex conjugate roots $s_n = \lambda_n \pm i\omega_n$, with ω_n satisfying (see also [53, 65])

$$\frac{(n - 1/2)\pi}{\tau} < \omega_n < \frac{n\pi}{\tau} \quad n = 1, 3, 5, \cdots \tag{3.10}$$

We associate to each pair of complex conjugate eigenvalues s_n a "mode". This mode goes unstable at $\lambda_n = 0$. If the delay τ or the feedback parameter a is increased, many modes cross the imaginary axis and thus become unstable with period close to $2\tau/n$. The stability of the fixed point is determined by the value of λ_1 of the first mode. If $\lambda_1 < 0$, then the solution approaches x^* asymptotically in time by spiraling in phase space $x(t)$ vs $x(t - \tau)$, due to the nonzero imaginary part of s_1. In this case, the fixed point is stable and attracts all initial conditions towards itself (see Fig.3.1a). If $\lambda_1 > 0$ on the other hand, then the solution diverges from x^* exponentially in time by spiraling in phase space $x(t)$ vs $x(t - \tau)$, so the fixed point is unstable and repels all nearby trajectories. If $\lambda = 0$, there is an eigenvalue pair on the imaginary axis. The condition of stability of the fixed point is obtained by separating the real and imaginary parts in Eq. 3.9:

$$\begin{aligned} \lambda_1 + b - \beta e^{-\lambda_1\tau}\cos(\omega_1\tau) &= 0 \\ \omega_1 + \beta e^{-\lambda_1\tau}\sin(\omega_1\tau) &= 0 \end{aligned} \tag{3.11}$$

or equivalently,

$$\begin{aligned} (\lambda_1 + b)^2 + \omega_1^2 &= \beta^2 e^{-2\lambda_1\tau} \\ \tan(\omega_1\tau) &= -\frac{\omega_1}{\lambda_1 + b}. \end{aligned} \tag{3.12}$$

We can compare Eq.3.12 with λ_1 positive, corresponding to an unstable solution, to the case where $\lambda_1 = 0$, and obtain the following inequalities:

$$
\begin{aligned}
\beta^2 = e^{2\lambda_1\tau}[(\lambda_1 + b)^2 + \omega_1^2] &> b^2 + \omega_1^2 \\
0 > \tan(\omega_1\tau) &> -\omega_1/b
\end{aligned}
\tag{3.13}
$$

The above equations can be grouped together, leading to

$$
0 > \tan(\omega_1\tau) > -\sqrt{\beta^2/b^2 - 1}, \tag{3.14}
$$

and the condition of unstability of the fixed point is then

$$
\tau > \frac{\tan^{-1}(-\sqrt{\beta^2/b^2 - 1}) + \pi}{\omega_1} > \frac{\tan^{-1}(-\sqrt{\beta^2/b^2 - 1}) + \pi}{b\sqrt{\beta^2/b^2 - 1}} \tag{3.15}
$$

Thus the linear Equation 3.8 has a locally stable fixed point, if and only if

$$
\tau < \tau_{Hopf} = \frac{\tan^{-1}(-\sqrt{\beta^2/b^2 - 1}) + \pi}{b\sqrt{\beta^2/b^2 - 1}} \tag{3.16}
$$

where τ_{Hopf} (we will define Hopf bifurcation below) is the delay time for which the eigenvalue value s_1 has zero real part. In the Mackey-Glass DDE, if $a = 0.13$ and other parameters as in Eq.3.4, the fixed point x^* is stable when $\tau < \tau_{Hopf} = 28.97$ and all the eigenvalues have negative real parts ($\lambda_n < 0$) (see Fig.3.1b). If the delay is increased beyond τ_{Hopf}, the first mode associated with ω_1 goes unstable at $\lambda_1 = 0$ and a periodic solution appears.

Linear stability analysis tells us whether solutions converge to a fixed point, to infinity, or oscillate. This latter case occurs when an eigenvalue pair is on the imaginary axis. It does not tell us what happens in the nonlinear system once a linearized solution goes unstable.

3.3.2 Periodic solutions

When the fixed point of a DDE loses stability, its neighbourhood may become repelling, but typically remains attracting with respect to regions located far away. Local repulsion and

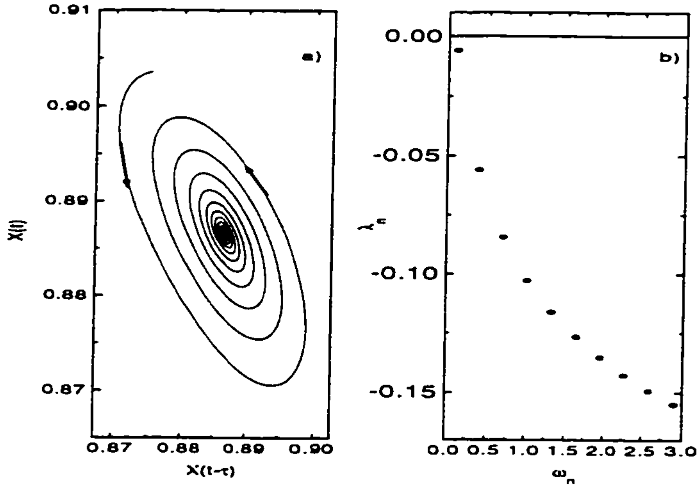

Figure 3.1: A stable fixed point and its corresponding modes for the MG DDE (Eq.3.4) The parameters are $a = 0.13$ and $\tau = 20$. a) Numerical solution of Eq.3.4; the trajectory approaches the fixed point by spiraling, due to the nonzero imaginary part of the first stable pair of complex conjugate eigenvalues. b) Linear modes, solutions of Eq.3.9, are represented only for $\omega_n > 0$. The modes with $\omega_n < 0$ are symmetric to these ones, and there is no need to represent them. All the modes have negative real parts, so they are stable. Note that the imaginary axis is the abscissa here, while the real axis forms the ordinate.

global attraction of the flow implies the formation of a closed curve around the unstable fixed point and the curve attracts all nearby trajectories. This closed curve is called a *limit cycle* and corresponds to a periodic motion of the system. The transition from a fixed point to a stable limit cycle at $\tau = \tau_{Hopf}$ is called a *Hopf bifurcation*. At the Hopf bifurcation we have

$$\omega_1 = \frac{\tan^{-1}(-\sqrt{\beta^2/b^2 - 1}) + \pi}{\tau}, \tag{3.17}$$

with $-\pi/2 < \tan^{-1}(-\sqrt{\beta^2/b^2 - 1}) < 0$. At that bifurcation point, the period of the zero-amplitude limit cycle is $T_1 = 2\pi/\omega_1$, and by looking at both limits of this inequality we find that $2\tau < T_1 < 4\tau$. Near the bifurcation, the amplitude of the limit cycle varies as $\sqrt{\tau - \tau_{Hopf}}$. Nonlinear terms become increasingly important in determining the solution shape as τ increases, and thus the solution evolves from a pure sinusoid (of zero amplitude) to a nonsinusoidal periodic solution. This type of bifurcation is called *supercritical Hopf bifurcation.* Figure 3.2a, and b show a limit cycle with period T_1 corresponding to the most unstable mode of frequency ω_1. If the delay is much greater than the response time $t_r = b^{-1}$, many modes cross the imaginary axis and become unstable (see Fig.3.2d). The solution corresponding to the most unstable mode of frequency ω_1 then rapidly evolves as τ increases past τ_{Hopf}, from a quasi-sinusoid to a solution with plateaus linked together by short transitions of width proportional to t_r [9, 66] (see Fig.3.2c). The other unstable modes ω_3, ω_5, and ω_7 correspond to the possible harmonic solutions of the fundamental for $\tau = 300$, as we will see in Section 3.4.

3.3.3 Chaotic solutions

When the feedback parameter a in MG is greater than the Feigenbaum point of accumulation of the period-doubling cascade, $a_\infty > 0.138$, not only periodic solutions but also chaotic solutions are observed when the delay is increased [7]. For example, if $a = 0.2$, the system goes through the first Hopf bifurcation at $\tau = 4.71$, then through a period-doubling bifurcation at $\tau = 12.82$, and so on. Chaotic behavior is observed at $\tau > 16.5$. Figure 3.3 shows three different behaviors obtained by varying the delay: a period-2 solution, a period-4 solution, and chaos for $\tau = 10$, 15, and 300 respectively.

In this chaotic regime, many different motions simultaneously exist in the system. So there are typically an infinite number of unstable periodic orbits (UPO's) that co-exist with one or more chaotic attractors. If the system is exactly on an unstable periodic orbit, it will stay on that orbit forever. However, any small deviation from that unstable orbit (due to noise for example) will grow in time, and will cause the system to quickly move away from it. In other words, the unstable orbit is repelling. Such unstable periodic solutions are not visible for an arbitrary initial function, although chaotic trajectories can spend time near them before being repelled away.

Under certain conditions, the chaotic dynamics can exhibit multistability, which is the coexistence of different solutions (some may be periodic, others chaotic) which are stable. i.e. which are attracting. This property is important, for example, for coding information in time-delayed feedback systems as we will see in Chapter 5 and 6. We will see in Section 3.4 how the initial function, from which a chaotic solution evolves, leaves little or no signature of itself in the solutions; yet, multistability can still exist, especially when the delay is large.

3.4 Multistability

Multistability in a dynamical system is the coexistence of multiple attractors. In such a system, qualitative changes in dynamics can result from changes in the initial conditions. A well-studied case is the bistability associated with a subcritical Hopf bifurcation [67] between a fixed point and a limit cycle. Multistable modes of oscillation can arise in delayed feedback systems when the delay is larger than the response time of the system [60, 8]. Multistability of this type has been demonstrated in experiments involving electronic circuits [58] and laser devices [1, 64, 11].

In the MG system at large delay $\tau = 300$, one can vary the feedback parameter a in order to see the coexistence of periodic and chaotic solutions (see also [60]). If the parameter a is increased, a square-wave solution of period $T_1 \approx 2\tau$ appears after the first Hopf bifurcation $a = 0.125$. For further increase of a, this square wave solution undergoes a period-doubling cascade predicted by the map (Eq.3.34). As a reaches the Feigenbaum point $a_\infty \approx 0.138$, this solution becomes chaotic, but it still has a square-wave-like shape (see Fig.3.5a) If a is further increased, this square-wave solution becomes unstable and successive harmonics of period close to T_1/n (n: odd integer representing the harmonic order) are observed. The solution jumps first to the third harmonic of period $T_1/3$ at $a = 0.1412$, then to the fifth

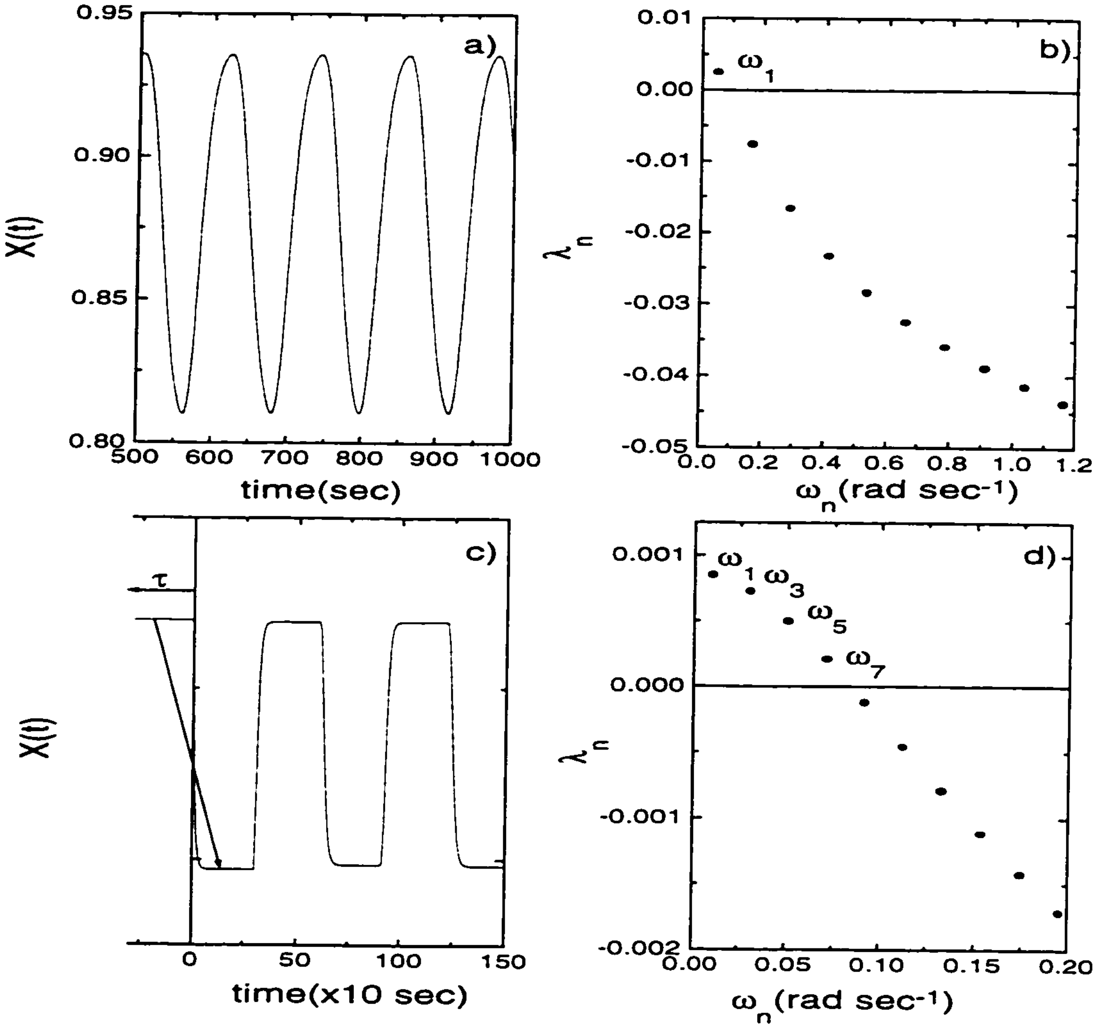

Figure 3.2: A stable limit cycle is observed for $a = 0.13$ in the Mackey-Glass DDE. a) Numerical solution of Eq.3.4 for $\tau = 50$ using a fourth-order Runge-Kutta integration algorithm with fixed time step 0.01. b) Solutions of Eq. 3.9 for the first 10 roots. The first mode is unstable and its imaginary part corresponds to the angular frequency of oscillation seen in (a). c) Same as in (a), but using Eq.3.3. This enables us to solve numerically the DDE (Eq.3.1) for $\tau = 300$ with an equivalent DDE (Eq.3.3) for $\tau' = 30$ and $\epsilon = 1/10$; clear plateaus are observed in the solution. d) Same as in (b) but for $\tau = 300$. The modes with frequencies ω_3, ω_5, and ω_7 are the harmonic solutions of the fundamental solution of frequency ω_1.

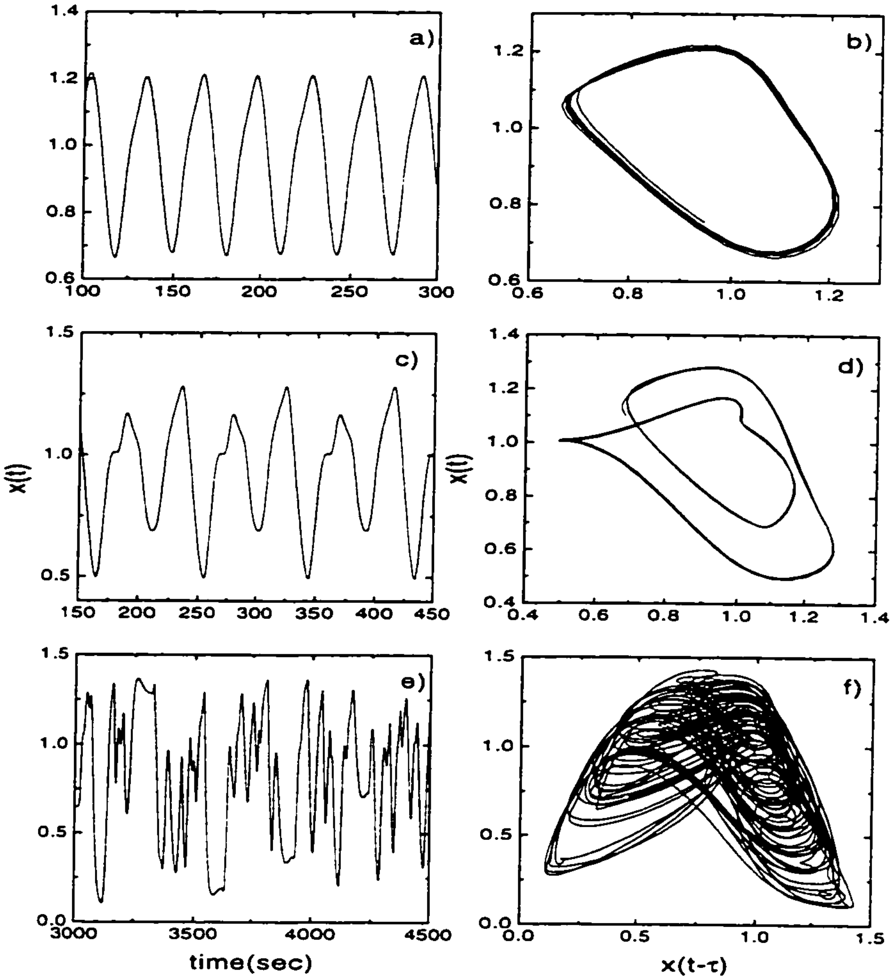

Figure 3.3: Numerical solutions of the MG DDE for $a = 0.2$ and different delays after 10 delay transients have died out. a-b) X vs t and a phase plot $x(t)$ vs $x(t-\tau)$ for a limit cycle solution with $\tau = 10$. c-d) X vs t and a phase plot $x(t)$ vs $x(t-\tau)$ for a solution which has period-doubled (compared to (a-b)) with $\tau = 15$. e-f) X vs t and a phase plot $x(t)$ vs $x(t-\tau)$ for a chaotic solution with $\tau = 300$.

harmonic of period $T_1/5$ at $a = 0.1415$, then to the seventh harmonic of period $T_1/7$ at $a = 0.1467$, and finally to developed chaos at $a = 0.149$. The transitions between harmonics form hysteresis loops, as shown in Fig.3.4.

Figure 3.5 shows the different chaotic solutions observed when a is varied using piecewice constant initial functions[1]. The range of stability of an harmonic of order n is obtained by choosing a special initial function. This latter is obtained by first dividing the delay interval into n equal subintervals. The values of the initial condition in each subinterval is chosen as a constant equal to one of the plateau values in the fundamental square-wave solution. Figure 3.4 shows the coexistence of several harmonic solutions for the same value of a: the initial function determines which one is seen. This coexistence of solutions can be between, for example, 1) a chaotic and a periodic orbit such as the fundamental, and the third and the fifth harmonics at $a = 0.141$, or the fifth and the seventh harmonic at $a = 0.1425$; 2) periodic orbits at $a = 0.1376$ as shown in Figure 3.6; 3) chaotic orbits as in the Ikeda model [60].

To our knowledge the following result is new and hasn't been discussed neither in [8, 60] nor in [11]. For a fixed large delay, we have found that there is a limit to the number of harmonic solutions that can be observed when a is varied. In other words there is a limit to the number of plateaus n in the initial function that can evolve in time without merging. If $\tau = 300$ for example, the number of possible harmonic solutions is 4, so the maximum number of plateaus is 7, which corresponds to the seventh harmonics (the highest harmonic that can be observed). Solutions with more than 7 plateaus will merge to one of the stable solutions in Figure 3.4 (not shown).

The number of harmonic solutions is found to be related to the number of unstable modes, solutions of Eq.3.9. This one-to-one correspondence is obtained when the parameter a is chosen such that the fundamental solution is a perfect square wave, i.e. the plateaus are

[1] The initial functions are carefully chosen to lead to different coexistent stable attractors.

free from any spurious structure such as spikes. For the Mackey-Glass equation, this value of a is found to be equal to 0.13 for $\tau = 300$. If a is slightly larger than 0.13, the plateaus end with sharp spikes, and the square wave nature of the solutions is diminished. Hence the unstable modes shown in Figure 3.2d correspond to the harmonic solutions in Figure 3.5.

We have also checked the Ikeda model of the laser ring cavity [60] and found that our result still holds for this one-to-one correspondence. Further, we found by numerical simulations of the Ikeda equation that the ninth harmonic also exists. This latter wasn't mentioned by Ikeda [60].

At this large delay, the frequency of these observed solutions can be approximated by expanding $\tan(\omega\tau)$ around $\omega_n = n\pi/\tau$:

$$\tan(\omega\tau) \simeq \tan(n\pi) + (\omega\tau - n\pi) \tag{3.18}$$

The modes have frequencies ω_n that can be written as:

$$\omega_n = \frac{n\pi}{\tau}(1 - \frac{1}{b\tau}) \approx \frac{n\pi}{\tau}, \quad n = 1, 3, 5, \cdots \tag{3.19}$$

For n large, these real parts are

$$\lambda_n = -\frac{\ln(-\omega_n/\beta)}{\tau} = -\frac{\ln(-n\pi/\beta\tau)}{\tau}. \tag{3.20}$$

We will see in Chapter 4 that this decay with n is related to the decay of Lyapunov exponents of the full solutions of the DDE.

3.5 Distributed delays

We have extended our study to the more realistic case of distributed delays [68, 69] rather than single fixed delays. Unlike the equations with fixed delays, which possess an infinite number of degrees of freedom("modes"), those with "memory kernels " such as those given by Eq. 3.22, are characterized by a finite but arbitrarily large number of modes, depending

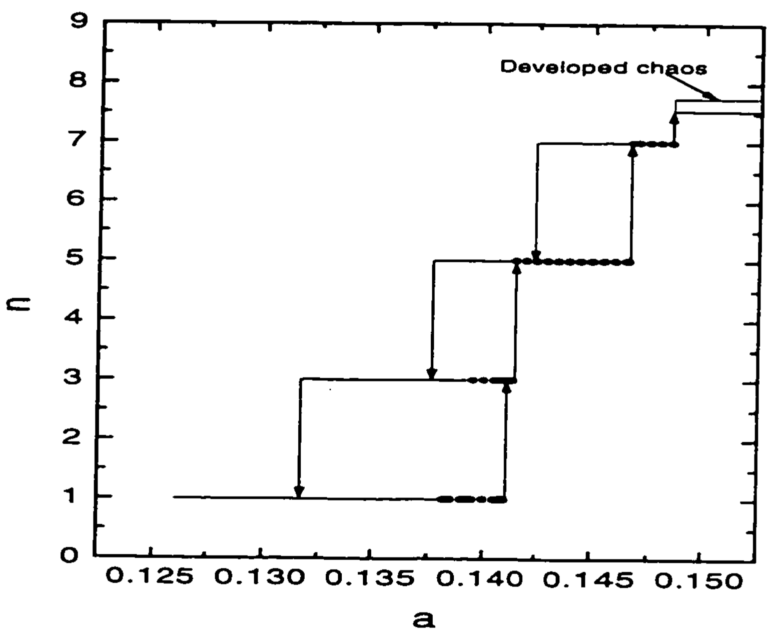

Figure 3.4: Domains of coexistence of harmonics and the transitions between them in the MG equation (Eq.3.3) for $\tau = 300$. The solid lines and the dotted lines indicate the periodic and chaotic solutions, respectively. The initial conditions are chosen from the plateaus of the square wave solutions of period-2 and period-4 orbits. We note here that for $R = \tau/t_r$ large, the limit cycles appearing at the Hopf bifurcation and the first period-doubling thereafter can be called period-2 (2 plateau values) and period-4 (4 plateau values), respectively. Some solutions seem to be stable at the beginning, but after a while, they merge to lower order solutions. For this reason, transients of about 7000 delays have been discarded in order to see the real stable solutions.

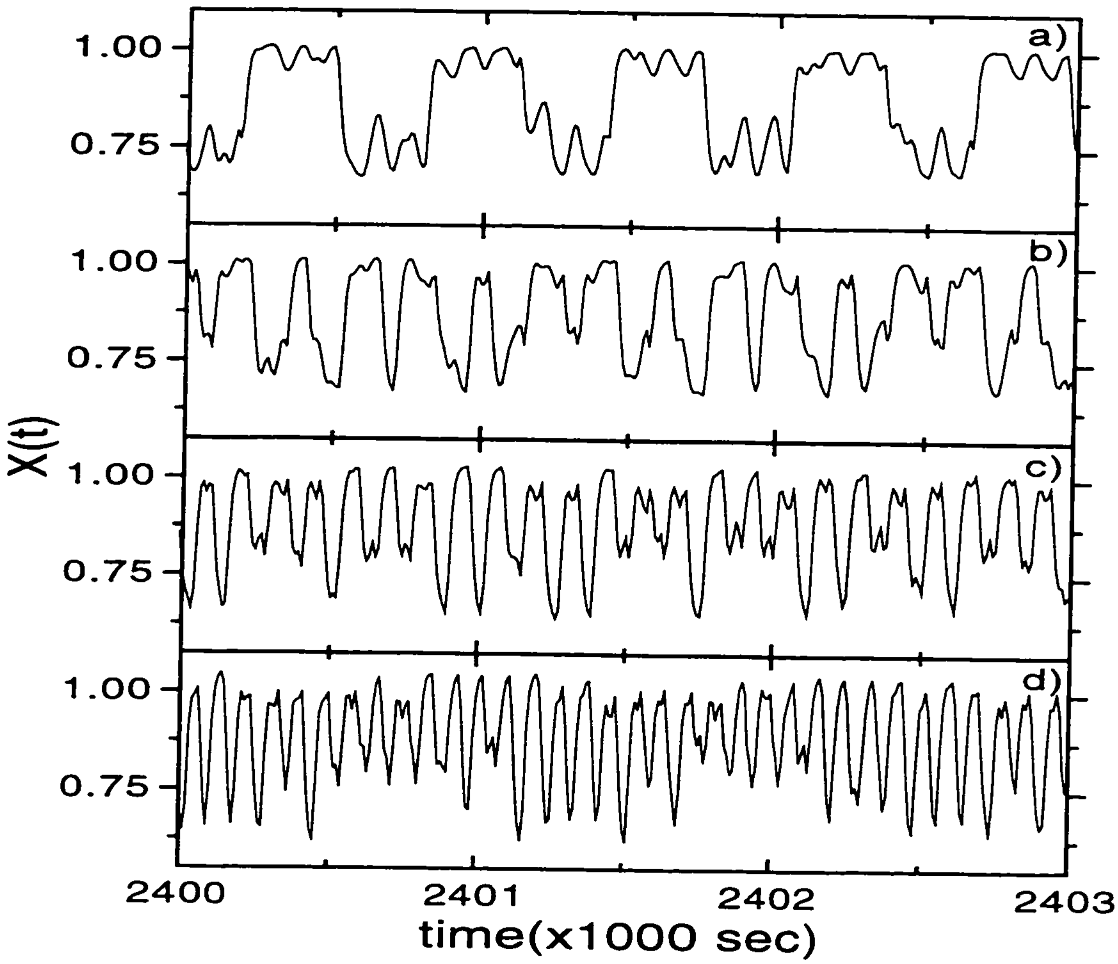

Figure 3.5: The differents solutions of Eq.3.3 corresponding to the different harmonics in Fig.3.4 for $\tau = 300$. We used the same constant initial function $x_0 = 0.95$ on $(-\tau, 0)$. Other initial conditions can also be used to obtain the same result. a) Fundamental ($a = 0.14$), b) Third harmonic ($a = 0.141$), c) Fifth harmonic ($a = 0.143$), d) Seventh harmonic ($a = 0.1467$).

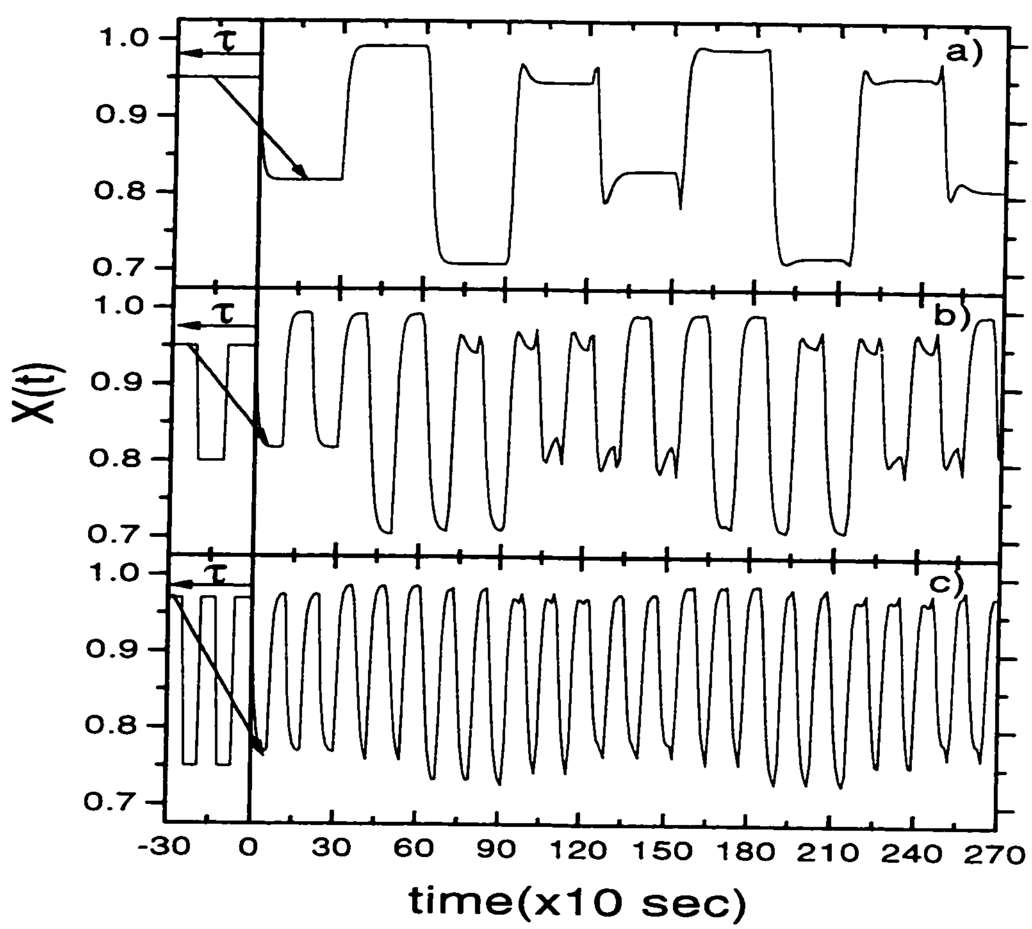

Figure 3.6: Three multistable periodic solutions of Eq.3.3 coexist for $a = 0.1376$ and $\tau = 300$: a) The fundamental. b) The third harmonic. c) The fifth harmonic. These solutions are obtained with three different piecewise constant initial functions, using Eq.3.3. The delay τ is subdivided into 1, 3 and 5 small plateaus of equal width.

on how well the DDE is approximated. In distributed delay equations, the system state in the present is affected by the system state in the whole past via a memory kernel $K(t)$:

$$\frac{dx}{dt} = f(x(t), z(t)), \quad z(t) = \int_{-\infty}^{t} K(t-u)x(u)du \tag{3.21}$$

The kernel $K(t)$ can preferentially select a time domain in the past that can affect the present dynamics. If this delay kernel is chosen as a delta function, the integro-differential dynamics in Eq.3.21 become equivalent to those of the original DDE, as we will see below. An example of a distributed delay occurs in the transmission of electrical activity along a nerve in which there is a distribution of axonal diameters, and thus of conduction velocities or of synaptic transmission times, both of which can be modeled by the kernel $K(t)$ [5]. If the kernel $K(t)$ is chosen to be a Gamma distribution function, we have:

$$G_{\alpha}^{m}(q) = \frac{\alpha^{m+1}}{m!} q^{m} e^{-\alpha q}, \quad \alpha, m \geq 0 \tag{3.22}$$

where m is an integer. One limit of the kernel is given by

$$\lim_{m \to +\infty, \alpha \to +\infty} G_{\alpha}^{m}(t) = \delta(t - \overline{\tau}) \tag{3.23}$$

where $\overline{\tau}$ is the average delay, given by

$$\overline{\tau} = \frac{\int_0^{\infty} q G_{\alpha}^{m}(q)dq}{\int_0^{\infty} G_{\alpha}^{m}(q)dq} = \frac{m+1}{\alpha} \tag{3.24}$$

In the limit in Eq. 3.23 we can write

$$z(t) = x(t - \overline{\tau}) \tag{3.25}$$

which is the retarded state variable of the fixed delay DDE. With the kernel of Eq. 3.22, we can define the following equations

$$\begin{aligned} y_0(t) &\equiv x(t) \\ y_i(t) &\equiv \int_{-\infty}^{t} G_{\alpha}^{i-1}(t-u)x(u)du \quad i = 1, 2, \cdots, m+1 \end{aligned} \tag{3.26}$$

The solutions $y_i(t)$ are obtained by computing dy_i/dt (using Leibniz's rule) and using the recursive relation

$$\frac{dG_\alpha^i(t-u)}{dt} = \alpha\{G_\alpha^{i-1}(t-u) - G_\alpha^i(t-u)\} \tag{3.27}$$

so the DDE can be transformed into an $(m+2)$-dimensional system of ordinary-differential equations (ODE's) [68, 69]

$$\begin{aligned} \frac{dy_0}{dt} &= f(y_0, y_{m+1}) = -by_0 + F(y_{m+1}) \\ \frac{dy_i}{dt} &= \alpha(y_{i-1} - y_i), \quad i = 1, 2, \cdots, m+1\,. \end{aligned} \tag{3.28}$$

When both m and α go to $+\infty$ keeping their ratio constant, the number of ODE's becomes infinite, so Eq. 3.28 and 3.1 will give exactly the same solution.

As in the DDE case, one can use linear stability analysis of Eq. 3.28 to understand the dynamics of the system near the fixed point y^*, and also multistability when the delay is increased. To a first order approximation, Eq. 3.28 can be written as

$$\begin{aligned} \frac{du_0}{dt} &= -bu_0 + F'(y^*, y^*)u_{m+1} \\ \frac{du_i}{dt} &= \alpha(u_{i-1} - u_i) \quad i = 1, 2, \cdots, m+1\,, \end{aligned} \tag{3.29}$$

where $u_k = y_k - y^*$, $k = 0, 1, \cdots, m+1$. This system of $m+2$ equations has $m+2$ eigenvalues, which are solutions of the characteristic equation

$$(s+b)(s+\alpha)^{m+1} - F'(y^*, y^*)\alpha^{m+1} = 0\,. \tag{3.30}$$

Eq. 3.30 can be written in the following form

$$(s+b)(1+\frac{s}{\alpha})^{\alpha\overline{\tau}} - F'(y^*, y^*) = 0\,. \tag{3.31}$$

As α goes to $+\infty$, the term $(1+\frac{s}{\alpha})^{\alpha\overline{\tau}}$ goes to $e^{s\overline{\tau}}$, and the characteristic equation of distributed delays becomes identical to the one with a single fixed delay $\overline{\tau}$,

$$s + b - F'(y^*, y^*)e^{-s\overline{\tau}} = 0, \tag{3.32}$$

where $F'(y^*, y^*)$ is equivalent to $F'(x^*)$ in a single delay equation. Numerical simulations of systems like Eq. 3.1 where a single time delay is replaced with a distribution of delays (Eq. 3.28) indicate that the qualitative behavior of solutions is largely unaffected by the addition of a distribution of delays for $m > 100$, as shown in figure 3.7. We will study this distributed delay system in more detail in the context of DDE attractor dimension in Sect.4.5.

3.6 Continuous-time difference-equation limit

If $R \equiv b\tau = \tau/t_r >> 1$ in Eq.3.1 and the initial function is piecewise constant, the continuous solutions then consist of "plateaus" linked together by short transitions of width proportional to $2t_r/\tau$ [9, 66], as shown in Fig.3.2c and 3.6a for period-2 and period-4 respectively. Each plateau evolves from its initial constant independently from the other plateaus. After transients, all plateaus cycle through the same set of values in the same order. In the singular limit $R \to \infty$ of Eq.3.1($\epsilon \to 0$ in Eq.3.3), these values are exactly given by the asymptotic solution of the continuous-time difference equation (CTDE)

$$x(t) = b^{-1}F(x(t-\tau))\,. \tag{3.33}$$

Such an equation has previously been used to study properties of DDE's like stability and bifurcations [9, 66] and the influence of noise [70]. In many studies, Eq.3.33 has been interpreted as evolving in discrete-time, but here we distinguish the discrete-time map from the difference equation. This is why we emphasize the qualifier "continuous-time". In the periodic regime, Eq.3.33 is of course multistable and adequately predicts the plateau values of the DDE even for values of R on the order of 30, as in this thesis. In the chaotic regime however, Eq.3.33 is still multistable and can predict the plateau values only in the singular limit $R \to \infty$ of the DDE. Figure 3.8 shows three multistable solutions of Eq.3.33 for $a = 0.1365$ similar to Figure 3.6, except for a short transition time at the end of the plateaus, due to the continuity and the differentiability of the solutions of the DDE. If one goes one step further and discretizes the continuous time in Eq. 3.33 in units of τ, the evolution of each point on $(-\tau, 0)$ is then governed by the one-dimensional map studied in Chapter 2,

$$x_n = b^{-1}F(x_{n-1}). \tag{3.34}$$

All points on $(-\tau, 0)$ are mapped in parallel from one delay interval to the next. These points evolve independently since, in this limit, the solution is not constrained to be continuous nor differentiable. We will study this continuous-time difference equation later in this thesis in the context of DDE attractor dimension, controllabiblity and synchronization.

3.7 Conclusion

We have shown that the stability of fixed points in delay-differential equations can be studied by linear stability analysis. We have also shown the different periodic and chaotic regimes of a DDE obtained by varying the delay and/or the feedback parameter. Multistability for both periodic and chaotic regimes at large delay is found to be related to the unstable modes revealed by a linear stability analysis. The solutions of distributed delay systems are found to be qualitatively very similar to those of a single delay for sufficiently large m. The continuous-time difference equation, obtained in the singular limit, is found also to be multistable and can be used to study the DDE at large delay.

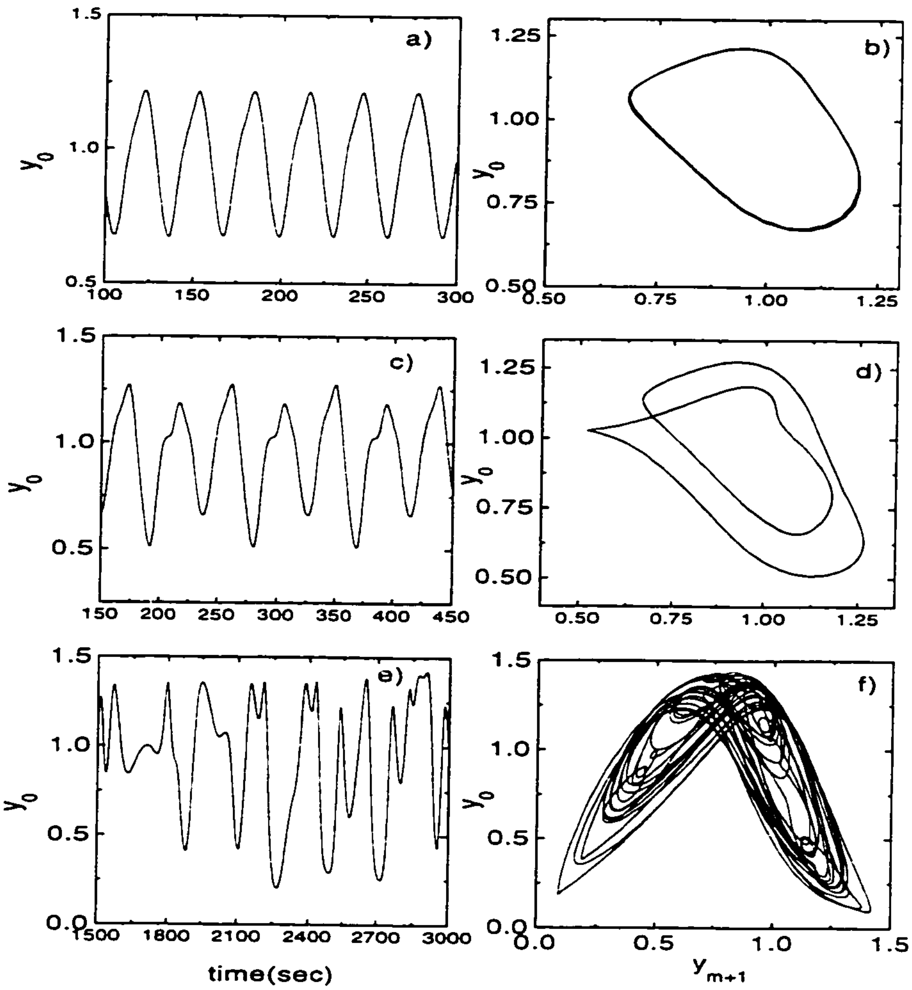

Figure 3.7: Numerical solutions of the distributed delay approximation (Eq.3.28) in the MG equation for $a = 0.2$, after transients have died out. The solutions are similar to the ones with a single fixed delay in Fig.3.3. a-b) Show y_0 vs t and a phase plot y_0 vs y_{m+1} for a period-2 orbit for $\alpha = 10, m = 99$ ($\overline{\tau} = 10$). c-d) Show y_0 vs t and a phase plot y_0 vs y_{m+1} for $\alpha = 10, m = 149$ ($\overline{\tau} = 15$) for a period-4 orbit. e-f) Show y_0 vs t and a phase plot y_0 vs y_{m+1} of a chaotic solution for $\alpha = 1, m = 299$ ($\overline{\tau} = 300$).

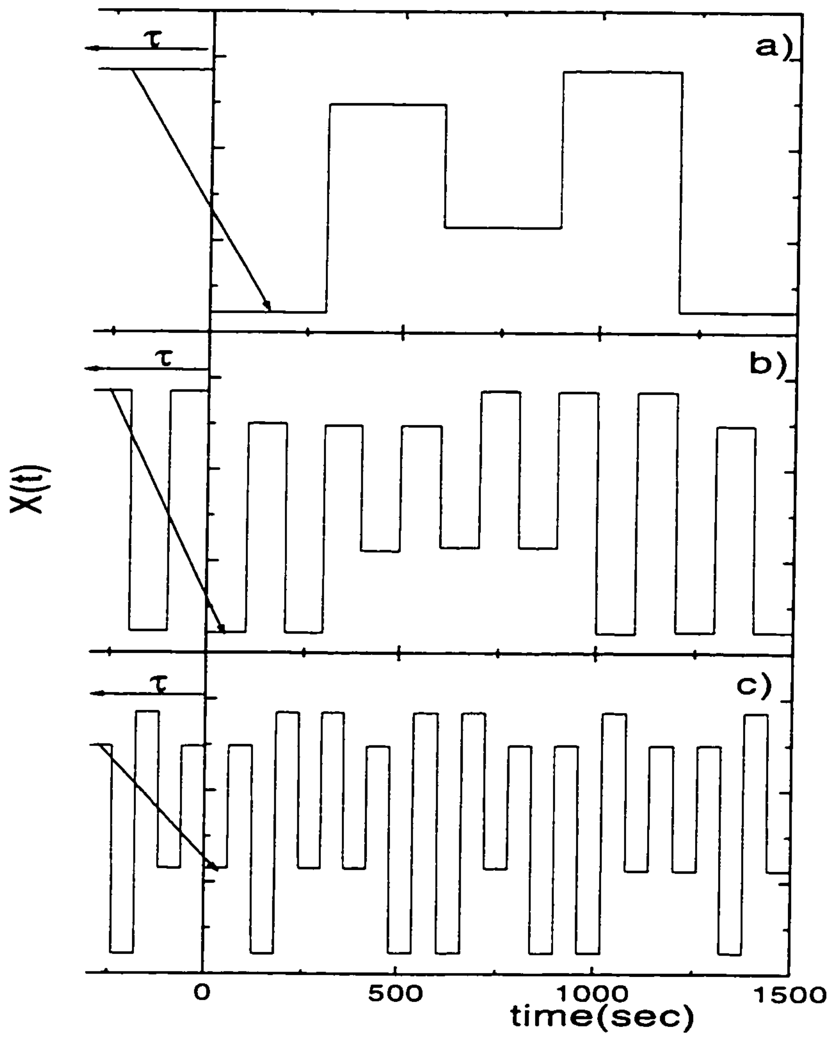

Figure 3.8: Three multistable solutions of Eq.3.33 are obtained with $a = 0.1365$ and $\tau = 300$ by varying the initial function as in Fig.3.6. a) The fundamental solution with one plateau ($n = 1$). b) The third harmonic solution with 3 plateaus ($n = 3$). c) The fifth harmonic solution with 5 plateaus ($n = 5$).

Chapter 4

Power spectra and dynamical invariants for delay and difference equations

4.1 Introduction

In this chapter, we show that properties of DDE's at large delays, such as dynamical invariants and multistability, can in fact be studied using linear stability analysis, power spectra of temporal solutions, and a discrete-time map obtained from the DDE. Some of our results complement those in a recent paper [24] which suggested a relationship between, on the one hand, the exponential decay rate of such spectra, and on the other, the sum of certain Lyapunov exponents and thus the Lyapunov dimension. Our study makes use of two classes of dynamical systems obtained in the singular perturbation limit of the DDE [8, 71]: the usual discrete-time one-dimensional map, as well as an infinite-dimensional continuous-time difference equation (CTDE) (see Sect.3.6). We find that the extreme multistability displayed by the CTDE, which is relevant to understanding memory storage and chaos control onto desired patterns in DDE's, can be exploited to explain features of large-delay spectra in DDE's, such as peak shapes. CTDE spectra can also be used to estimate attractor dimension in a corresponding DDE at mid-to-large delays.

The main advantage of working with spectra is that they are much simpler to calculate numerically compared to usual invariants, especially when the attractors are high-dimensional; the further advantage of working with CTDE's is that their spectra can be calculated analytically, once the spectrum of the aforementioned discrete-time map is determined (an even simpler numerical task).

An initial motivation for our work is an observation by Farmer in his seminal study of dynamical invariants of DDE's [7]. He noted in the power spectrum of the Mackey-Glass equation "a curious modulation" superimposed on an exponentially decaying envelope when the ratio R of delay to response time was large (30 in his study). We find that both the Ikeda and Mackey-Glass models exhibit such a near-periodic modulation when R is large, and that the peaks of this modulation are associated with the modes predicted by linear stability analysis of the dynamics around the fixed point. This correspondence in turn suggests new relationships between these linear modes, the spectral decay rate, the Lyapunov exponents and the Lyapunov dimension of the attractor. In particular we find that, at least for such first-order DDE's at large R values, the exponential decay rate observed at mid-to-high frequencies is more relevant to the characterization of dynamical invariants than the asymptotic spectrum (i.e. at very high frequency). This follows from the fact that most of the energy of the chaotic fluctuations lies in this frequency range, and is associated with the largest Lyapunov exponents and most unstable linear modes.

This Chapter is organized as follows. In Section 4.2, we discuss the properties of power spectra at different delays and over different frequency ranges. The spectra are further characterized using notions from linear filter theory. In Section 4.3, we calculate the frequencies of the modes using linear stability analysis around the fixed point and associate them with peaks in the power spectrum. Section 4.4 estimates the attractor dimension from the power spectrum. Section 4.5 investigates spectra for the distributed delay case where the DDE is approximated by a finite number of ODE's. Section 4.6 proposes an analytical investigation of solution spectra in the singular limit perturbation of the DDE. Section 4.7 gives a thorough derivation of spectral properties for the CTDE for arbitrary initial functions, and discusses the connection between such spectra, those of the singular limit map, and those of finite-delay DDE's. The Chapter concludes in Section 4.8.

4.2 Power spectra at different delays

4.2.1 Temporal and spectral behaviors

Our study focusses on Mackey-Glass delay-differential equation [2] (Eq.3.4) with parameters $a = 0.2, b = 0.1$ [7, 24]. A fourth-order Runge-Kutta method with linear interpolation on the delay variable has been used throughout our study. As the ratio $R = \tau/\tau_r$ of the delay to response time $\tau_r = 1/b$ increases, the chaotic solution loses some of its regularity, as can be seen on going from Fig.4.1a to Fig.4.1b. For very large R values (Fig.4.1c: $R = 500$), the solution which evolves from a constant initial condition exhibits plateaus, with a bit of chaotic fluctuations at the end of each plateau. In the singular limit $R \to \infty$, obtained throughout our paper by letting $\tau \to \infty$ and keeping b fixed, the evolution of these plateaus is given by the CTDE:

$$x(t) = \frac{F(x(t-\tau))}{b} \equiv G(x(t-\tau)) \ . \tag{4.1}$$

We note that time is still continuous in this difference equation. A further simplification of the dynamics in this singular limit results from discretizing time in units of one delay, and associating only one value of the state variable x with each time unit. The dynamics can then be cast in the form of a discrete time map (see e.g. [9]):

$$x_{n+1} = \frac{F(x_n)}{b} = G(x_n). \tag{4.2}$$

Hence, for a constant initial function on $(-\tau, 0)$, the values of the successive plateaus are predicted by this map.

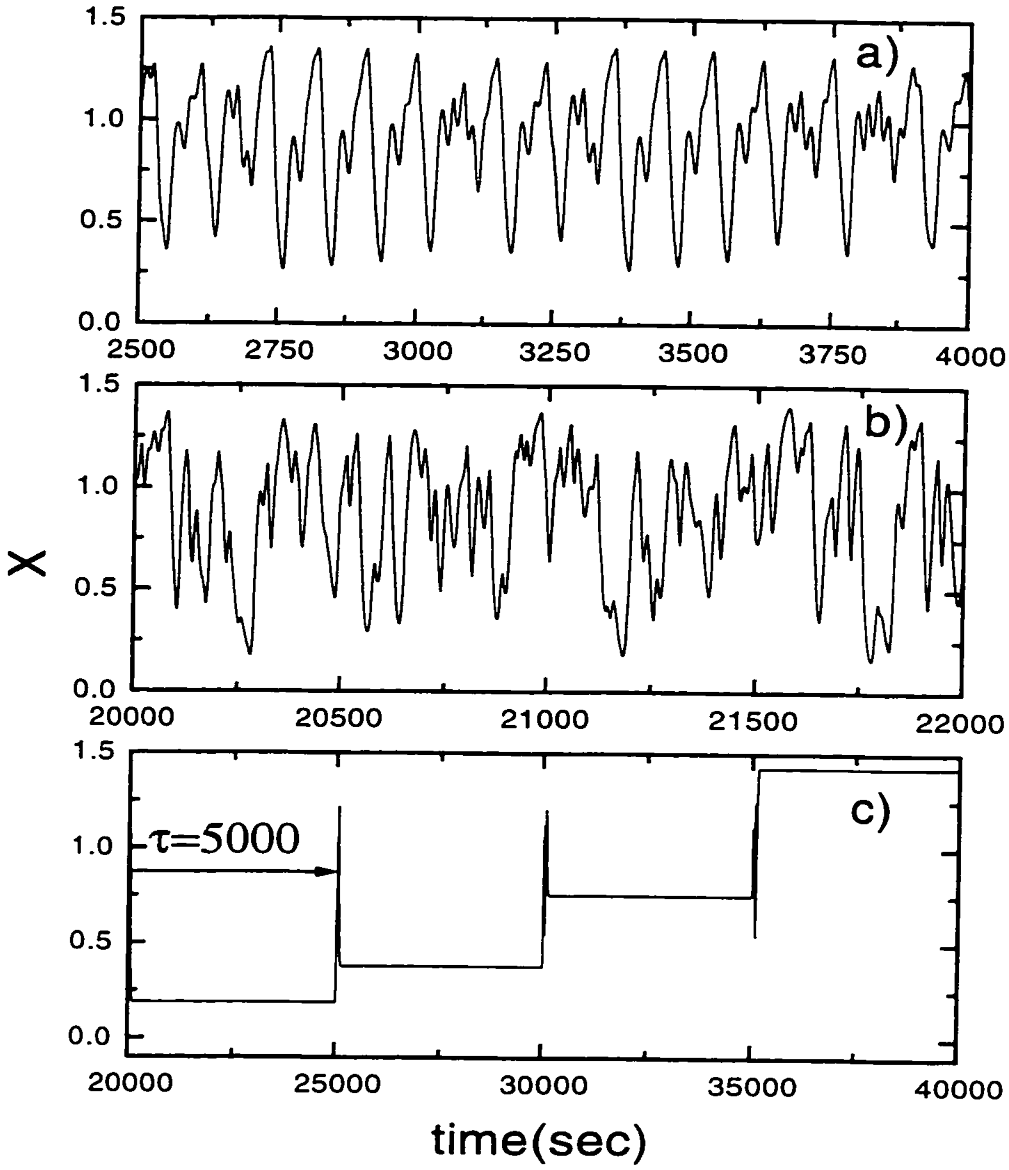

Figure 4.1: Solutions of the Mackey-Glass equation Eq.3.4 for delay values of a) $\tau = 25$, b) $\tau = 200$ and c) $\tau = 5000$. Other parameters are $a = 0.2$ and $b = 0.1$. A fixed step fourth-order Runge-Kutta method was used with integration time step 0.01. Linear interpolation was used for the required two midpoint evaluations of the delayed variable. The initial condition was a constant (0.8) on the delay interval $(-\tau, 0)$ in each case. The solution was found to be insensitive to the value of the constant initial condition (unless it is equal to 1, the unstable fixed point). Asymptotic solutions are shown in (a) and (b); the transients in (c) have not completely decayed, but remain confined to the small transition regions (boundary layers) between adjacent delay intervals.

To further investigate the properties of high-dimensional solutions of such first-order DDE's, we calculate the spectral properties of solutions. We numerically generate a long solution time series starting with a constant initial condition on $(-\tau, 0)$. This solution is divided into many adjacent pieces. The power spectrum for each piece is computed using the Fast Fourier Transform-periodogram method; the individual results are finally averaged to produce an "averaged" power spectrum.

Figure 4.2 shows power spectrafrom solutions of the Mackey-Glass equation for different delays using constant initial functions. We cannot exclude the possibility that different initial functions lead to different asymptotic chaotic solutions with different spectra and dynamical invariants, i.e. that the dynamics are multistable [60]. However, for a given delay, all constant initial functions tested yielded solutions having similar average power spectra.

When the delay is small (e.g. $\tau = 25$, as in Fig.4.2a), the spectrum is broadband with a few broad peaks, a familiar characteristic of chaotic motion. There does not appear to be any clear relationship between the position of these few peaks and the frequency of the solutions obtained from a linearization of the dynamics around the fixed point (see Sect.4.3).

However, if the delay is increased further to e.g., $\tau = 200$ (Fig.4.2b), a clear periodic modulation of the broadband background appears, as first noted in [7]. Further, the mean decay rate of this background no longer changes for larger delay values (the rate is the same in Fig.4.2b and 4.2c), and is well-fitted over a large range by an exponential (Fig.4.2c). The number of peaks in the power spectrum increases linearly with the delay, and for the accuracy used in our simulations, the modulation can no longer be seen when $\tau \geq 2000$, due to the finite frequency resolution in our spectra (see Fig.4.2c). Let us assume that two peaks can be resolved if their centers are separated by at least $2\Delta_f$, where Δ_f is the width of one peak. Estimating the width of each peak as $\Delta_f = 0.00025Hz$, we expect that neighboring peaks can be resolved if $\tau^{-1} \geq 2\Delta_f$, which agrees with our observation.

Figure 4.3 shows a power spectrum for $\tau = 200$, as in Fig.4.2b, but using a smaller sampling time of 1 sec rather than 3.75 sec (note that time in Eq.3.4 is not dimensinoless, and thus we choose an arbitrary time unit of 1 sec throughout our work). We find that the modulation seen in Fig.4.2b begins to die out past $c\delta^{-1}$, and disappears around $f = 0.14$ Hz. Here c is a system-dependent constant as discussed in Section 4.4.1, and δ is defined below. Also, the rate of decay seen in the range where the periodic modulation is present is the same as in Fig.4.2b. This suggests that aliasing effects, while potentially present because the solution is resampled with a time step larger than the integration time step, seem to slightly affect power estimates only at the very highest frequencies, i.e. those close to the Nyquist frequency used for the computation of a given spectrum. We have found behaviors with increasing delay similar to those in Figs.4.2-4.3 for spectra of the Ikeda equation. For example, Fig.4.4 shows a modulation as in Fig.4.2b for a ratio of decay to response time of $R = 20$. However, we note a difference in line shape between the Mackey-Glass and Ikeda cases, the line shape being much simpler in the latter case. This difference will be explained in Sect.4.7.

4.2.2 Insights from linear filter theory

Our spectra for large delays can be decomposed into three different ranges of frequencies: 1) the low frequency range $0 < f < b/2\pi$, 2) the mid-to-high frequency range $b/2\pi \leq f \leq c\delta^{-1}$ (δ being the correlation time of the feedback term - see below, plus Figs.4.2b,4.4,4.6 and 4.7), where the periodic modulation is clearly seen for large delays, and 3) the very high frequency range $f > c\delta^{-1}$; this latter range is shown only in Fig.4.3. In order to qualitatively compare the spectral features in each of those ranges, we compute the Laplace transform of Eq.3.1:

$$sX(s) - x(0) = -bX(s) + \tilde{F}(s) \quad , x(0) = 0 \tag{4.3}$$

where $\tilde{F}(s)$ is the Laplace transform of the nonlinear feedback function. This feedback term can be seen as a chaotic forcing or "input" term. A transfer function between the output

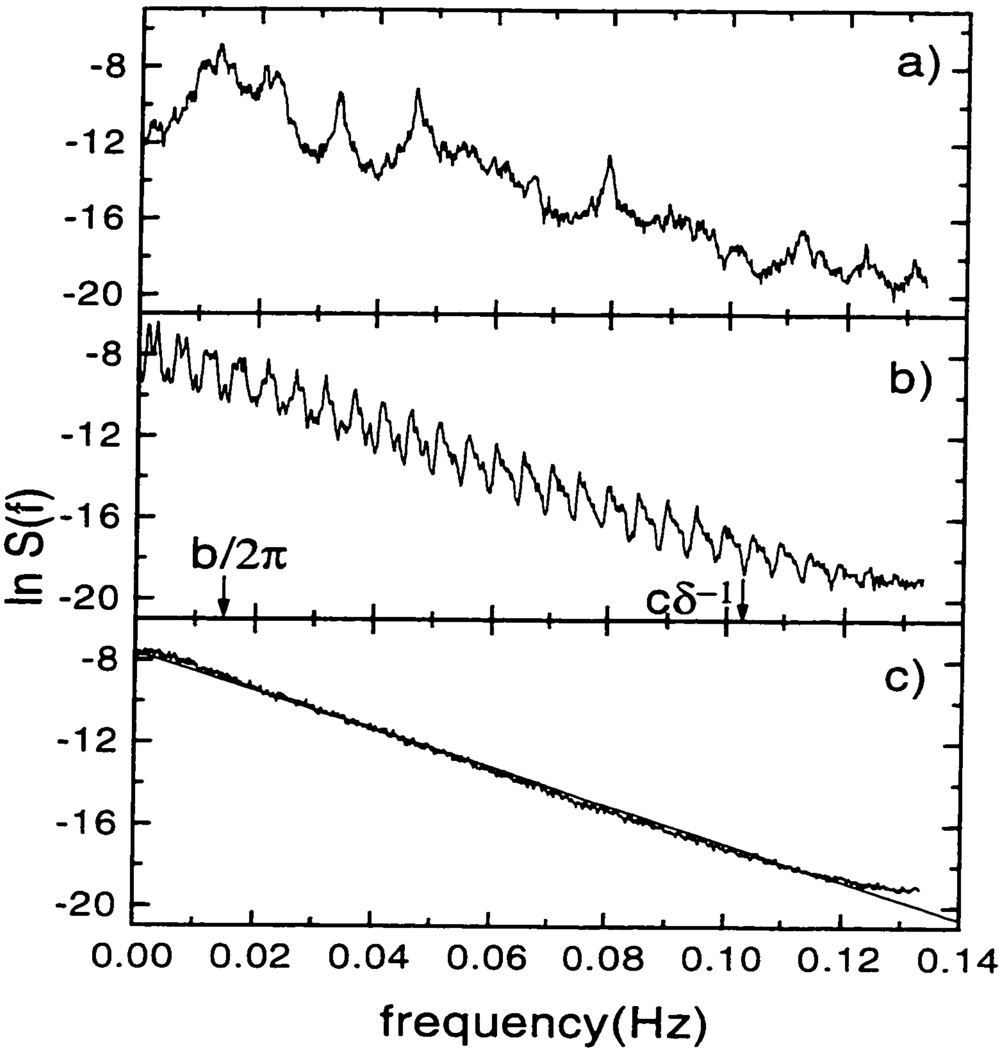

Figure 4.2: Power spectra of solutions of Eq.3.4 for the parameters used to generate the time series in Fig.4.1; a) τ = 25, b) τ = 200 and c) τ = 5000. The spectra are obtained using the FFT algorithm, and are averages of spectra from 100 consecutive 8192-point time series. The integration time step is 0.01 sec. The spectrum for $\tau = 5000$ is fitted to $y = C_1 + C_2 f$ with $C_1 = -7.6$ and $C_2 = -93.02$. The sampling time is 3.75 sec. A Hanning window was used for all spectra in our study.

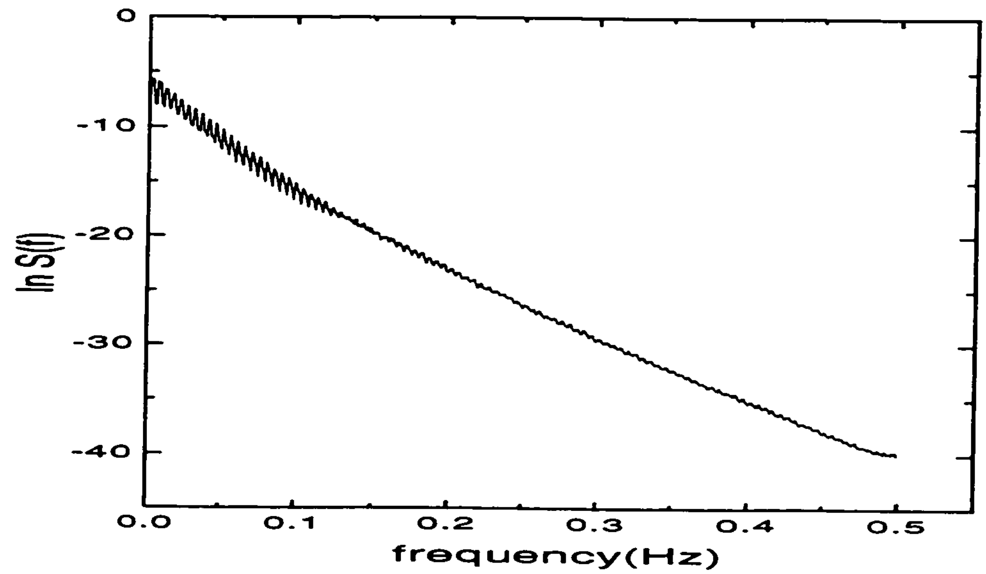

Figure 4.3: Power spectrum for $\tau = 200$, as in Fig.4.2b, but with a sampling time of 1, i.e. a Nyquist frequency of 0.5 Hz. The spectrum in $(0, 0.12)$ Hz was not changed (compare Fig.4.2b) by using this smaller sampling time.

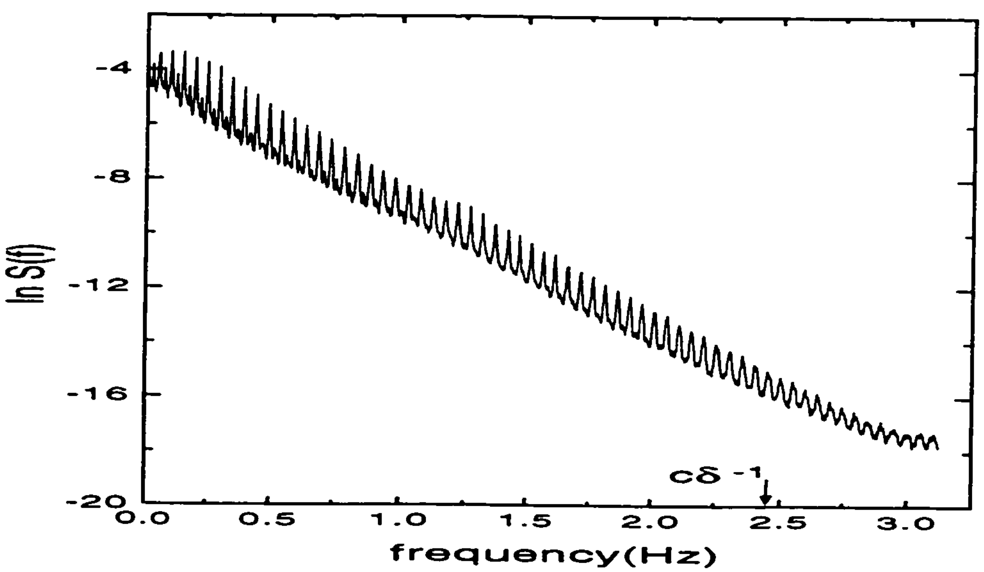

Figure 4.4: The power spectrum of the Ikeda equation, i.e. Eq.3.1 with $F(x(t-\tau)) = 2.1b^{-1}\pi\sin(x(t-\tau))$ with parameters $b = 1$ and $\tau = 20$. The spectrum is obtained from 100 consecutive 8192-point time series with an integration time step of 0.01 sec and a sampling time of 0.16 sec.

$X(s)$ and the input $\bar{F}(s)$ is then:

$$r(s) = \frac{X(s)}{\bar{F}(s)} = \frac{1}{b+s}. \tag{4.4}$$

The magnitude squared amplitude (MSA) response function is obtained by considering the steady state where $s = j2\pi f$ (i.e. by considering instead the Fourier transform):

$$|r(f)|^2 = \frac{|X(f)|^2}{|\bar{F}(f)|^2} = \frac{1}{b^2 + 4\pi^2 f^2}, \tag{4.5}$$

We numerically calculate the power spectrum of the output $x(t)$ and the input $F(x(t))$ for the Mackey-Glass equation and find that their ratio is close to that given by Eq.4.5. The magnitude of the Fourier transform of the nonlinear input is related to the magnitude of the output by Eq.4.5, as shown in Fig.4.5. From Eq.4.5, $\bar{F}(f)$ and $X(f)$ become equal when $b^2 + 4\pi^2 f^2 = 1$, i.e. at $f = 0.158$, which is approximately the case in Fig.4.5.

If $f << b/2\pi$, the MSA response function is $\approx 1/b^2$, so that in this leftmost part of region (1) fluctuations are amplified by $\approx 1/b^2$ from one delay interval to the next, in agreement with the difference equation 4.1 (see also [53]). As will be shown in Sect.4.7, the shape of the peaks in this low-frequency region are similar to those for the CTDE (Eq.4.1) (Figs.4.13,4.14), except that each main peak for the DDE is composed of two peaks rather than four in the CTDE, due to the limited resolution of our spectrum calculation for the DDE. The CTDE in fact can be used to relate the low-frequency spectral features of the DDE to those of the discrete time map (Eq.4.2). As we move towards $b/2\pi$, the frequency dependence of the denominator in Eq.4.5 comes into play, yielding a Lorentzian-type of decay which carries into the beginning of region (2). Region (1) can be assimilated with the "core range" in the terminology of Ikeda and Matsumoto [53], i.e. it contains the most dominant (i.e. most energetic) Fourier modes of the chaotic motion.

In region (2), the spectrum initially follows Eq.4.5, but quickly gives way to an exponential decay over the remainder of this range. In fact, most of region (2) is well-fitted by an exponential:

$$S(f) = Ae^{-\mu^{-1}f} \tag{4.6}$$

where A is a constant and μ^{-1} is a spectral decay rate (in seconds: see Fig.4.3). This region of exponential decay can be associated with the so-called dissipative range [53], characteristic of viscous dissipation at high frequency (or high wave number) in the context of turbulent flow. Region (3) is found to exhibit a slower decay, which is also to a good approximation exponential over a substantial part of its range ($0.2 < f < 0.4$ Hz).

For the Mackey-Glass equation, the integrated power S_I is found not to depend on the delay, provided this delay is larger than approximately 50, i.e. provided $R > 5$ (since $b = 0.1$). With negligible error, this integrated power can be approximated by

$$\begin{aligned} S_I &= \int_0^{c\delta^{-1}} S(f)df \\ &= \frac{A}{\mu^{-1}}\left(1 - e^{-\mu^{-1}c\delta^{-1}}\right) \simeq C(0) \end{aligned} \tag{4.7}$$

where $C(0)$ is the autocorrelation function of $x(t)$ at zero lag (by the Wiener-Khintchine theorem, the integrated power in the spectrum is equal to $C(0)$). Thus, past a certain delay, the power in the signal $x(t)$ is constant, and consequently, the variance $C(0)$ of $x(t)$ becomes constant.

4.2.3 Investigating the singular limit

In this study, we are particularly interested in the singular limit of Eq.3.1. The hope in studying this limit is that the properties of multistability in this limit will provide insight into attractor dimensionality for the DDE at arbitrary delays (see Sect.4.7). The behavior in this limit can also be studied in the frequency domain using the Laplace transform and the rescaled equation (Eq.3.3). The rescaling property is further useful to study the DDE in terms of an input-output response function as in the previous subsection. This function

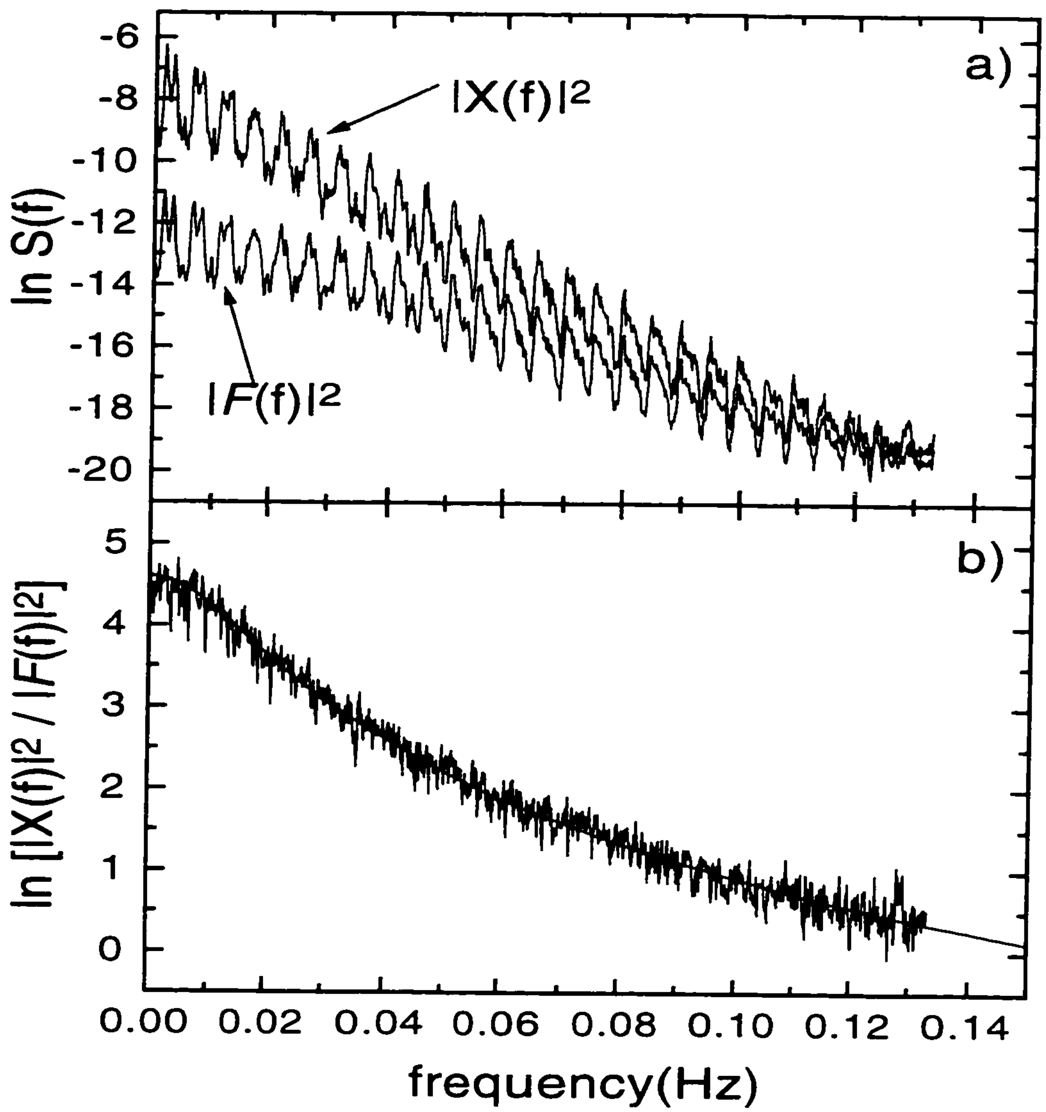

Figure 4.5: Power spectra from the Mackey-Glass equation Eq.3.4 for $\tau = 200$. a) Power spectrum of the solution $x(t)$ and of the feedback function $F(x(t))$. b) Logarithm of the ratio of the two spectra in (a), i.e. logarithm of the squared amplitude of the response function $|r(f)|^2$ in Eq.4.5 which relates the output $x(t)$ to the "input" $F(x(t-\tau))$ in the frequency domain. The sampling time is 3.75. The function fitted to the data in (b) is simply $(b^2 + 4\pi^2 f^2)^{-1}$ with $b = 0.1$, as predicted by Eq.4.5.

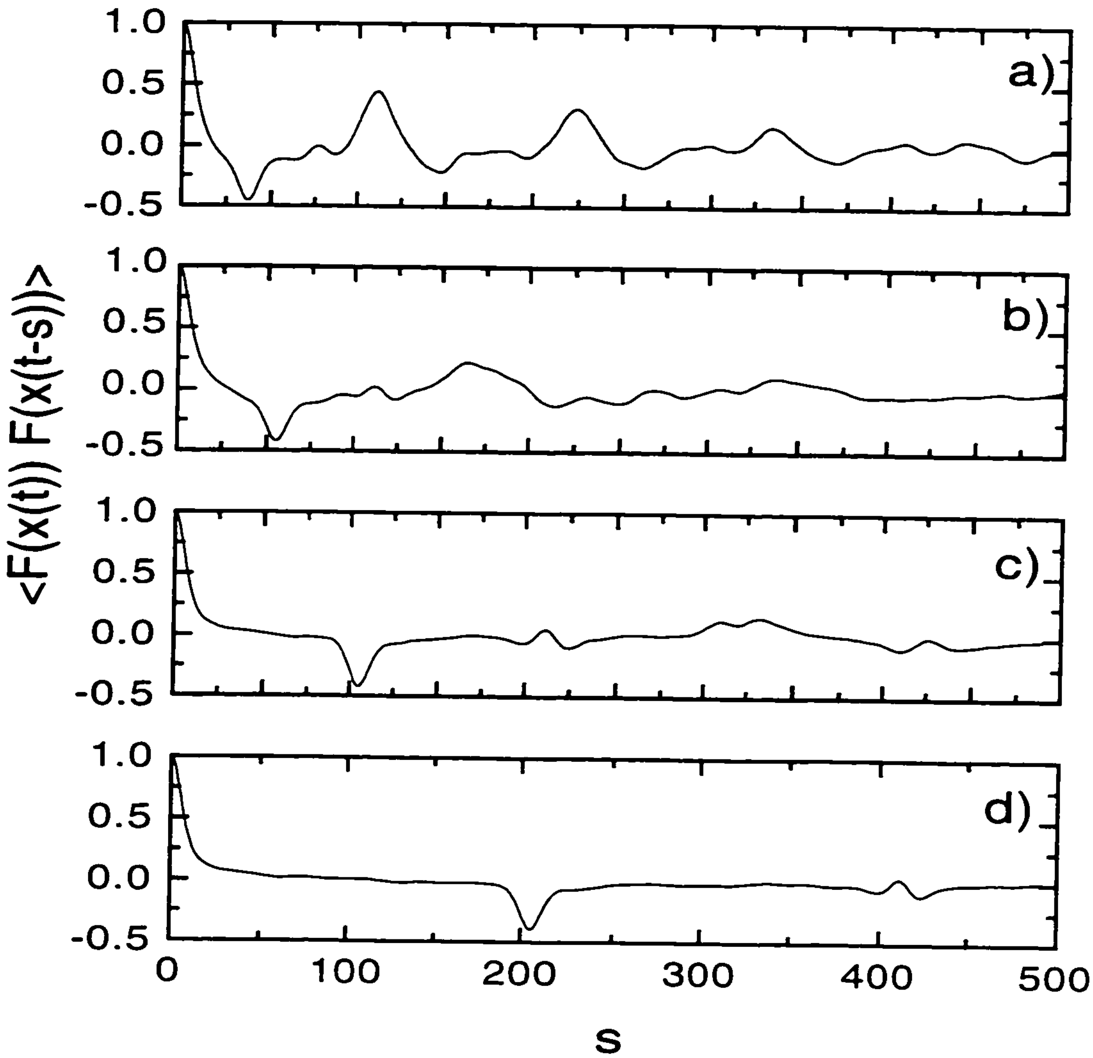

Figure 4.6: Autocorrelation function of the feedback term $F\ (x(t-\tau))$ for the Mackey-Glass equation (Eq.3.4) in the chaotic regime ($a = 0.2, b = 0.1$) for various delays: a) $\tau = 31.8$, b) $\tau = 50$, c) $\tau = 100$, d) $\tau = 200$. The correlation time δ, at which the autocorrelation decays to $1/e$ times its maximum value of 1 (at $t = 0$), is found to be 9.72 sec in all cases.

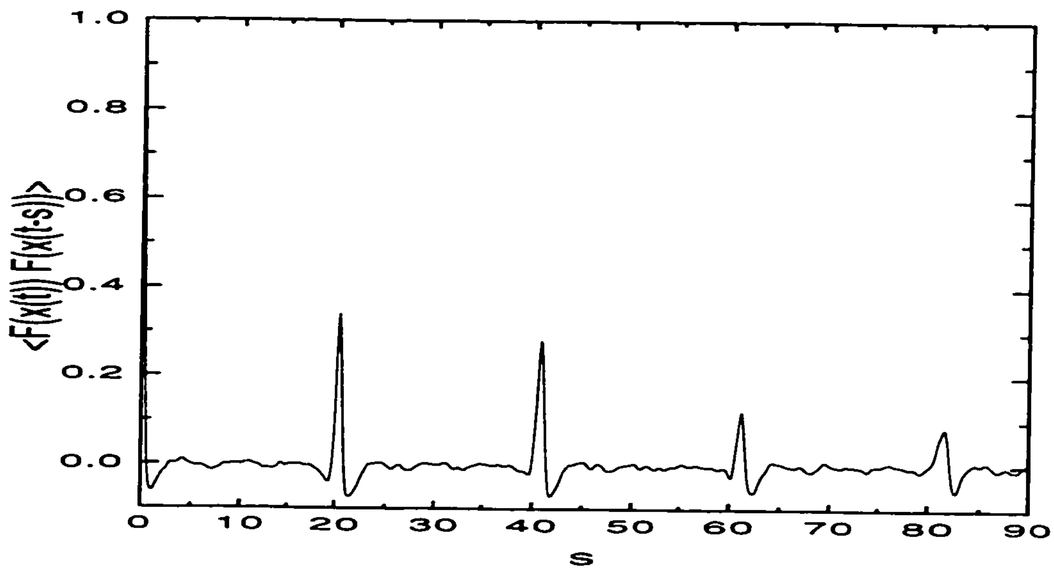

Figure 4.7: Autocorrelation function of the feedback term for the Ikeda equation (see Fig.4.4) with $\tau = 20$. The correlation time δ, at which the autocorrelation decays to $1/e$ times its maximum value, is found to be 0.35 sec.

is now given by

$$r(s) = \frac{X(s)}{\bar{F}(s)} = \frac{1}{b + \epsilon s}, \tag{4.8}$$

where we have labeled the Laplace transform of $y(t')$ in Eq.3.3 as $X(s)$. The MSA response function is then given by

$$|r(f)|^2 = \frac{|X(f)|^2}{|\bar{F}(f)|^2} = \frac{1}{b^2 + 4\pi^2\epsilon^2 f^2} \tag{4.9}$$

In the singular limit $\epsilon \rightarrow 0$, $|r(f)|^2 \rightarrow 1/b^2$, which is the MSA response function for the CTDE (Eq.4.1).

4.3 Linear stability analysis

We now show that the frequencies of the peaks that make up the modulated part of the power spectrum at large delays, such as for $\tau = 200$ in Fig.4.2b, agree very well with the frequencies of linear modes obtained by linear stability analysis of the DDE. These modes are determined by the characteristic equation Eq.3.9 of the DDE linearized around its fixed point x^* (which of course is unstable in the chaotic regime). Equation 3.9 has an infinite number of roots $s_n = \lambda_n \pm i2\pi f_n$, with f_n satisfying (see also [65])

$$\frac{(n-1/2)}{2\tau} < f_n < \frac{n}{2\tau} \qquad n = 1, 3, 5, \cdots \tag{4.10}$$

The mode associated with s_n goes unstable at $\lambda_n = 0$. If the delay is increased much beyond the response time b^{-1}, many modes cross the imaginary axis and thus become unstable with period close to $2\tau/n$ (see Sect.3.3).

All modes show up as clear peaks in the power spectrum at frequencies corresponding to those of the roots, with the most unstable ones being the dominant ones (Figs.4.2, 4.8). Some of the stable modes close to the imaginary axis appear also in the power spectrum because of nonlinear coupling to the unstable modes. In fact, due to nonlinearity, even the most unstable modes in the dissipative range appear in the power spectrum. It is as if all these eigenfrequencies are excited by the chaotic fluctuations, even though they are stable in the absence of these fluctuations. One can expect that the number of degrees of freedom in the system is directly related to these "spectrally visible" unstable and stable modes of the linearized system (see Sect.4.4).

Hence, each peak of this modulation corresponds to a mode of oscillation predicted by linear stability analysis around the fixed point. This one-to-one correspondance between the peaks in the power spectrum and the linear modes has, to our knowledge, been studied only for periodic systems [72], as well as for low-dimensional chaos [1] when the delay is not too large compared to the response time. In this latter case, the correspondance is not very good because the modes don't appear at the same frequencies as the spectral peaks. It is also clear from our results that most of the energy in the chaotic waveform lies in the low frequencies (the ordinate is logarithmic). This is similar to the case of fluid turbulence, where most of the energy lies in the long wavelength modes.

We also note that the real parts of the roots decrease with increasing delay (Fig.4.8). This explains why the peaks in the power spectrum decrease in amplitude with increasing delay. At the same time, the peaks become closer, since their spacing is proportional to $1/\tau$, until they can no longer be resolved using a given level of frequency resolution in the spectral calculation. An approximate expression for the frequencies of these modes can be obtained for $\lambda_n \approx 0$:

$$f_n = \frac{n}{2\tau}(1 - \frac{1}{b\tau}) \approx \frac{n}{2\tau} \qquad n = 1, 3, 5, \cdots \tag{4.11}$$

and for n large, these modes decay as

$$\lambda_n = -\frac{\ln(-2\pi f_n/\beta)}{\tau} \approx -\frac{1}{\tau}\ln n - \frac{1}{\tau}\ln\left(-\frac{\pi}{\beta\tau}\right) \tag{4.12}$$

This dependence of the real part of the eigenvalue on the logarithm of the root number has also been found for the Lyapunov exponents [7, 53]. Ikeda [53] further suggested (without showing it) that the Lyapunov exponents with larger negative values, for which this logarithmic scaling of exponents with exponent number is seen, in fact correspond to the linear modes. The reason for this is that the decay rates (as a function of n) of the real part of the roots and of the Lyapunov exponents are the same when n becomes large. Thus, these negative Lyapunov exponents λ^L can be estimated from the expression for the stable modes (Eq.4.12), i.e.

$$\lambda^L_{(n+1)/2} = \lambda_n \tag{4.13}$$

for n odd and sufficiently large. Comparing the Lyapunov exponents recently computed by Sigeti [24] with our roots of the characteristic equation, we find that the Lyapunov exponents indeed agree with the real parts for sufficiently large n. For example, for $\tau = 200$ in the Mackey-Glass equation, we find the following real parts λ_n and Lyapunov exponents λ^L_i (remember only odd numbered modes are seen in the spectrum): $(\lambda_{29} = -0.000695, \lambda^L_{15} = -0.00075), (\lambda_{31} = -0.00102, \lambda^L_{16} = -0.00102), (\lambda_{33} = -0.00132, \lambda^L_{17} = -0.00132), (\lambda_{35} =$

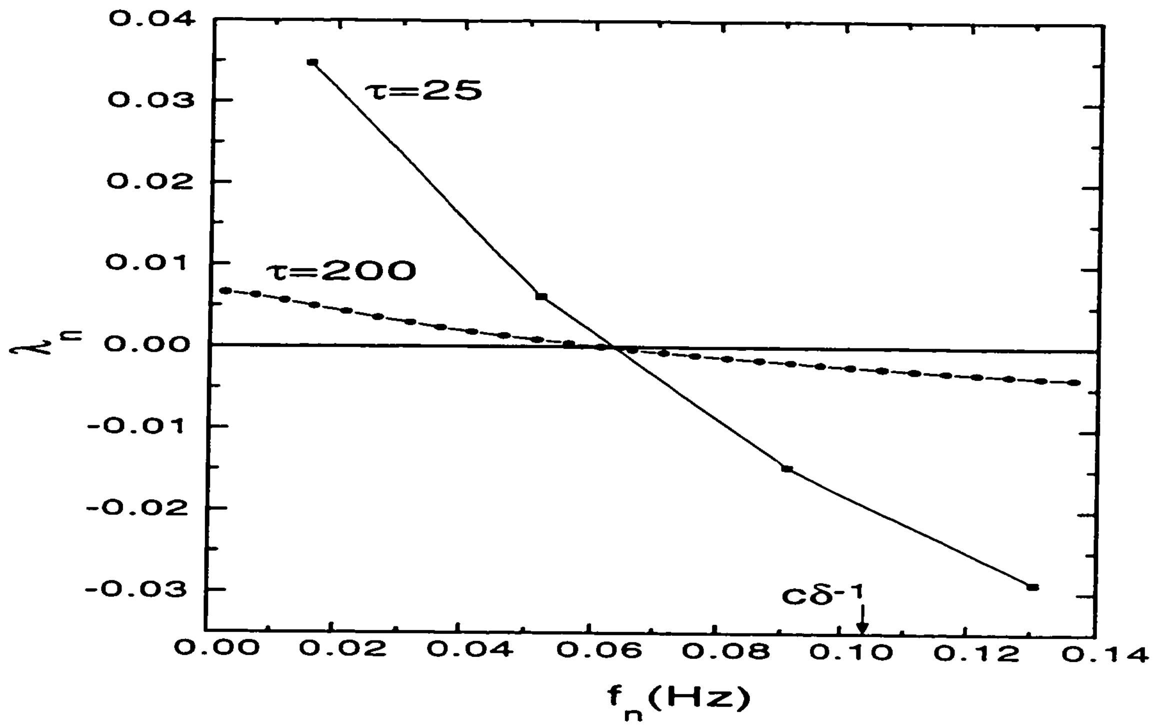

Figure 4.8: Roots of the characteristic equation Eq.3.9 obtained by linearizing the Mackey-Glass equation Eq.3.4 around the fixed point for $\tau = 25$ and $\tau = 200$. Note that the real part λ of the root (ordinate) is plotted against its imaginary part $\omega/(2\pi) = f$. Other parameters are $a = 0.2$ and $b = 0.1$.

$-0.00161, \lambda_{18}^{L} = -0.00162), (\lambda_{37} = -0.00188, \lambda_{19}^{L} = -0.00193), (\lambda_{39} = -0.00214, \lambda_{20}^{L} = -0.00222), (\lambda_{41} = -0.00238, \lambda_{21}^{L} = -0.00250)$.

These negative modes do not, a priori, provide information on attractor dimension (such as the Lyapunov dimension) and Kolmogorov-Sinai entropy, since one needs the positive exponents and the first few negative ones to estimate such quantities [47, 73]. Nevertheless, this agreement between modes and exponents shows that apparently nonlinear characteristics of DDE's, such as self-oscillation frequencies and negative Lyapunov exponents, are in fact closely related to simple linear characteristics. In the next section, we discuss how other linear properties of the DDE are related to dynamical invariants such as dimension and Lyapunov exponent spectrum.

4.4 Dynamical invariants from power spectra

4.4.1 Estimating the dimension

For the Mackey-Glass equation, the information dimension d of the motion on the attractor has been shown to increase linearly with the delay [7, 55]. The same applies to the Lyapunov dimension, since both dimensions were shown to be equal [7]. The proportionality constant between delay and dimension is closely governed by the autocorrelation time δ of the feedback function ([55]: see Figs.4.6 and 4.7). This time can be estimated as the $1/e$ decay time of the central peak in the autocorrelation function from its maximal value at zero lag, i.e. at $s = 0$ (the other symmetric half of this peak is at negative lags, which are not shown). A good estimate of the Lyapunov dimension is then $d = c\tau/\delta$, where c is a constant that depends on the particular feedback used. For example, in the Mackey-Glass equation c is close to one [7, 55]; for Ikeda equation, $c \approx 0.85$ [55].

We have found that d can be estimated from either the power spectrum or linear stability analysis. Since power spectra can be easily calculated with standard algorithms, and linear stability analysis is straightforward to carry out, estimating dimension in these ways clearly is advantageous in comparison with algorithms to compute, e.g., the correlation integral or the spectrum of Lyapunov exponents. In particular these latter methods, while standard tools, are particularly time consuming for high-dimensional systems such as those of interest in our study.

Our estimation method works as follows. From the spectral point of view, the attractor dimension can be estimated as the number of peaks within the frequency range $(0, c\delta^{-1})$. Since each peak corresponds to a mode, the dimension also represents the number of roots of the characteristic equation (Eq.3.9) within that range; this is the basis of the linear analysis estimate. For example, in the Mackey-Glass model with parameters (see [7]) $a = 0.2, b = 0.1, c = 10$, and a delay $\tau = 200$, we found $\delta \simeq 9.72$ (see Fig.4.6) and a dimension

$d = c\tau/\delta \simeq 21$ (see Table 4.1). The number of peaks in the power spectrum within the $(0, c\delta^{-1})$ frequency range is also found to be approximately 21, in good agreement with the Lyapunov dimension found in [7]. For the Ikeda model, the Lyapunov dimension found for the parameters $\tau = 20$ and $\tilde{\mu} = 2.1$ is $\simeq 42$ [8]. We compute $\delta = 0.35$ (see Fig.4.7), which yields a dimension $d = c\tau/\delta = 48$ (where $c \approx 0.85$ [55]), which is close to 42. Further, estimating dimension by counting the number of spectral peaks in the corrected range $(0, c\delta^{-1})$, as the results in [55] would suggest, yields approximalety 48 (see Fig.4.4), and thus there is agreement with the value obtained above.

We note that the spectra show a continuous variation of features as the delay increases: while the background converges to a constant mean slope, the number of modes increases smoothly and their amplitude decreases, following the behavior of the linear modes (more cross the imaginary axis and their real parts decrease); consequently, the fundamental frequency (roughly $1/2\tau$ as predicted by Eq.4.11) steadily decreases. Given the relationship found between the number of modes within the characteristic bandwidth $(0, c\delta^{-1})$ and the Lyapunov dimension, it is reasonable to assume that the attractor dimension also increases smoothly with the delay for high delays. As Farmer [7] found that dimension still increases in small jumps at high delays, more work is perhaps needed to verify whether these jumps really occur and what their origin is.

4.4.2 Lyapunov exponents and power spectrum decay

For the ring cavity laser, the Lyapunov dimension increases linearly with the delay, but the metric entropy stays constant past a certain delay value [54]. The fact that the metric entropy saturates but the dimension keeps increasing with delay implies that the Lyapunov exponents scale as $1/\tau$, as has been pointed out in various studies (see e.g. [7, 54]). The findings of Sect.4.3 support this dependence. Indeed, we found that the negative Lyapunov exponents are closely given by the real part of the roots of the linear characteristic equation.

τ	d_S	d_{KY}	$\sum\lambda_L^+$	$\sum\lambda_n^+$	μ	$\mu/\sum\lambda_L^+$	$\mu/\sum\lambda_n^+$
50	6	5.37	$8.99\ 10^{-3}$	$4.067\ 10^{-2}$	$1.075\ 10^{-2}$	1.196	0.264
100	11	10.34	$1.022\ 10^{-2}$	$4.062\ 10^{-2}$	$1.075\ 10^{-2}$	1.052	0.265
200	21	20.28	$1.041\ 10^{-2}$	$4.063\ 10^{-2}$	$1.075\ 10^{-2}$	1.033	0.265

Table 4.1: Numerical results at different delays for the Mackey-Glass equation. d_S is the dimension of the attractor estimated from the power spectrum by counting the number of peaks within the range $(0, c\delta^{-1} = 0.103)$ Hz (Fig.4.6), where $c = 1$. This dimension is approximately given by τ/δ. d_{KY} is the Kaplan-York dimension and λ_L^+ are the positive Lyapunov exponents, obtained from [24]. λ_n^+ are the real parts of solutions of the characteristic equation of the linearized system (Eq.3.9). μ^{-1} is the exponential decay constant of the power spectrum $S(f) = Ae^{-\mu^{-1}f}$, where A is a constant.

As shown in Eq.4.12, these real parts also scale as $1/\tau$.

Table 4.1 presents our attractor dimension estimates D_S based on the power spectrum. These values agree with estimates based on the Kaplan-Yorke conjecture D_{KY} using the Lyapunov exponent estimates in [24] (as well as other sources). The sum of positive Lyapunov exponents $\sum\lambda_L^+$ converges to a constant when the delay is increased, and can be related to the decay rate of the power spectrum μ^{-1} in the dissipative range as follows:

$$\mu \approx \sum\lambda_L^+ \tag{4.14}$$

This result is significant since the chaotic fluctuations of longer wavelengths are related to the positive Lyapunov exponents in that range. In region (3) beyond the dissipative range, the Lyapunov exponents are very negative, and therefore it is less likely that the decay rate in this range is governed by the positive Lyapunov exponents. We found that this decay rate μ^{-1} can also be related to the sum of the unstable linear modes by

$$\mu \approx \sum\lambda_n^+/4. \tag{4.15}$$

Hence, the relation between the positive Lyapunov exponents and the unstable linear modes is

$$\sum\lambda_L^+ \approx \sum\lambda_n^+/4 \tag{4.16}$$

This correspondance established using the decay rate in region (2) may be a peculiarity of the Mackey-Glass and Ikeda systems, i.e. of first-order DDE's with feedback dynamics; for other lower-dimensional ODE's, a correspondance can perhaps only be found at high frequency, as the results in [24] suggest. It is the modulation in the spectrum at mid-frequencies and large delays ($\tau > 100$) which initially drew our attention to a possible matching of the sum of Lyapunov exponents with the spectral decay rate in the region (2) containing much of the energy in the solution. This is the region where the modulation is present, i.e. where most of the dominant modes are fluctuating.

4.5 Power spectra of distributed delay systems

We have studied the more realistic case of distributed delays [68, 69] rather than fixed single delays. The hope is to obtain more insight into the origin of the exponential behavior of DDE spectra. It is also interesting to find conditions under which the distributed delay case, which as we will see is equivalent to a finite number of coupled ODE's, has solutions that are spectrally similar to those of the delay-differential equation.

In this distributed delay case, the system state in the present is affected by not one, but many values of the system state in the past via a memory kernel $K(t)$ in Eq.3.21. In the limit $(m, \alpha) \to \infty$ (keeping their ratio constant), the kernel becomes a delta-function, and this set of ODE's is equivalent to the DDE with the average delay given by Eq.3.24.

The power spectrum of solutions of this distributed delay dynamical system starts approaching the one for the DDE for $\overline{\tau} = 200$ when $m = 199$ ($\alpha = 1$), and in the limit $(m, \alpha) \to \infty$, these power spectra are identical. Figure 4.9 shows that for parameters $(m = 399, \alpha = 2)$, we can obtain a good approximation for the DDE with an average delay $\overline{\tau} = 200$. At this point, we can count the number of peaks in the power spectrum to estimate attractor dimension, as in the previous section, as well as estimate the center frequency of these peaks. As in the DDE, the frequencies of the Fourier modes are the roots of the characteristic equation obtained by linearizing the system (Eq.3.28) around the fixed point (see Sect.3.5)

$$(s + b)(s + \alpha)^{m+1} - F'(x^*)\alpha^{m+1} = 0\,. \tag{4.17}$$

This equation has $m + 2$ roots corresponding to $m + 2$ frequencies. In the limit $\alpha \to \infty$, the characteristic equation of the distributed delay system becomes identical to that for a DDE with fixed delay $\overline{\tau}$:

$$s + b - F'(x^*)e^{-s\overline{\tau}} = 0\,. \tag{4.18}$$

The results in this section indicate that the spectra for the finite-dimensional ODE approximation of the DDE shows some exponential scaling for all three large values of m, and that there is a convergence of this spectrum towards that of the DDE.

4.6 Power spectrum of solutions in the singular perturbation limit

In the limit ($R \to \infty$), the solution of the DDE approaches the continuous time difference equation (CTDE) (Eq.4.1), and clear plateaus are observed (see Fig.4.10). Their values are predicted by the map (Eq.4.2). In this case, the power spectrum can be calculated analytically using the Fourier transform of a non-periodic signal with an infinite period ($T \to \infty$) as follows:

$$X(f) = \lim_{T\to\infty} \frac{1}{T} \int_{-T/2}^{+T/2} x(t)e^{2\pi i f t}dt \tag{4.19}$$

We choose $T = N\tau$ (an integer multiple of the delay) with $N \to \infty$. Eq.(4.19) becomes

$$\begin{aligned} X(f) &= \lim_{N\to\infty} \frac{1}{N\tau} \int_{-N\tau/2}^{+N\tau/2} x(t)e^{2\pi i f t}dt \\ &= \lim_{N\to\infty} \frac{e^{-\pi i N f \tau}}{N\tau} \int_{0}^{+N\tau} x(t')e^{2\pi i f t'}dt' \end{aligned} \tag{4.20}$$

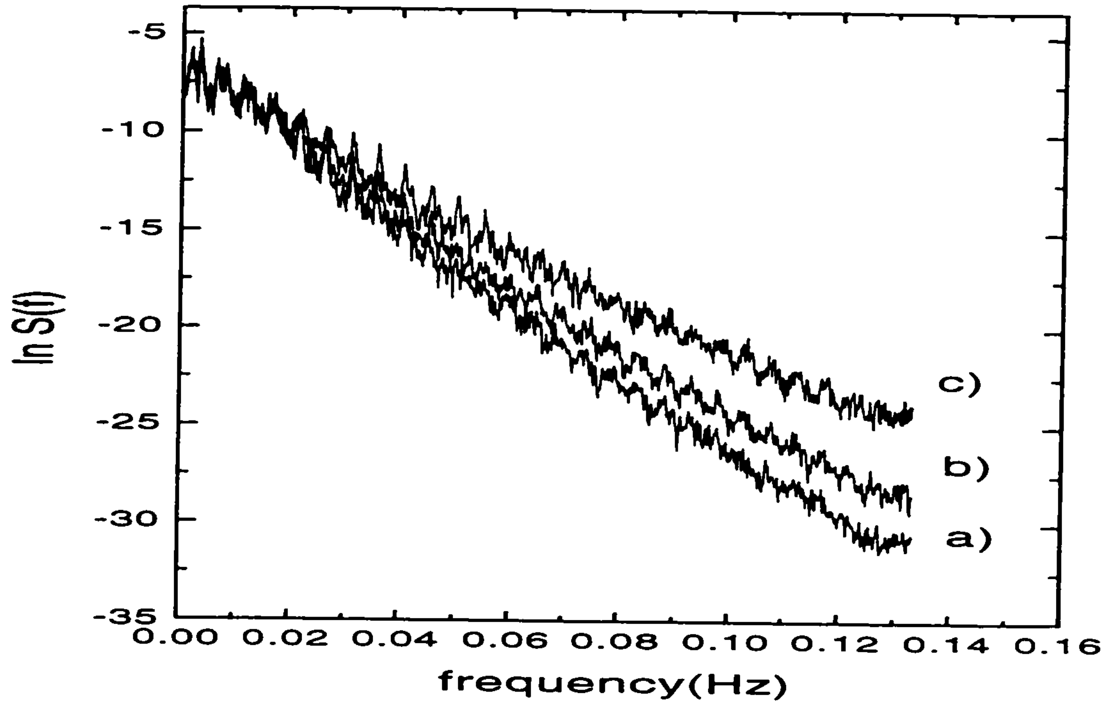

Figure 4.9: The power spectrum of the distributed delay approximation Eq.3.28 to the Mackey-Glass equation Eq.3.4 with an average delay $\bar{\tau} = (m+1)/\alpha = 200$. The parameters for the Gamma memory kernel are a) $m = 199$ and $\alpha = 1$, b) $m = 399$ and $\alpha = 2$, and c) $m = 799$ and $\alpha = 4$. The spectrum converges to that in Fig.2b as m in Eq.3.28 is increased, i.e. as the approximation to the DDE improves. The peaks, which are most prominent in (c), correspond to the frequencies of the modes obtained from linear stability analysis around the fixed point of the system of ODE's Eq.3.28. These peaks are equivalent to those obtained with the DDE for $\tau = 200$. The sampling time is 3.75.

For a constant initial function, the solution $x(t)$ is composed of plateaus of length τ, i.e. $x(t) = a_j$ for $j\tau < t < (j+1)\tau$, where $j = 0, 1, 2, \cdots (N-1)$ (the a_j's are constant). The above equation becomes:

$$\begin{aligned} X(f) &= \lim_{N\to\infty} \frac{e^{-\pi i N f\tau}}{N\tau} \sum_{j=0}^{N-1} a_j \int_{j\tau}^{(j+1)\tau} e^{2\pi i f t'} dt' \\ &= \lim_{N\to\infty} \frac{e^{-\pi i N f\tau}}{N\tau} \int_0^{\tau} e^{2\pi i f t'} dt' \sum_{j=0}^{N-1} a_j e^{2\pi i j f\tau} \\ &= \lim_{N\to\infty} \frac{e^{-\pi i (N-1) f\tau}}{N\tau} \frac{\sin(\pi f\tau)}{\pi f} \sum_{j=0}^{N-1} a_j e^{2\pi i j f\tau} \\ &= \lim_{N\to\infty} \frac{e^{-\pi i (N-1) f\tau}}{\tau} \frac{\sin(\pi f\tau)}{\pi f} X_1(f) \end{aligned} \tag{4.21}$$

where $X_1(f)$ is the Fourier transform of a series of points generated by the map (Eq.4.2). Using the transformation $f \to f\tau$ and the approximation $f/\tau \simeq \sin(f/\tau)$ at large delays, the power spectrum can then be written as

$$S(f) = |X(f)|^2 = \frac{1}{\tau^2} \frac{\sin^2(\pi f)}{\sin^2(\pi f/\tau)} S_1(f), \tag{4.22}$$

where $S_1(f) = |X_1(f)|^2$ is the power spectrum of the map(Eq.4.2). In Sect.4.7, we will show that a similar form can be obtained for the power spectrum using the discretization of the time in units of τ in Eq.4.1. Figure 4.11 shows the power spectrum of the DDE at very large delay ($\tau = 540000$) which is equivalent to the power spectrum of the CTDE in Fig.4.14.

4.7 Initial function dependence of spectra in the singular limit

4.7.1 The spectrum of M parallel maps

We now show how the discrete time map Eq.4.2 can explain the shape of the spectral peaks for the DDE at finite delay, and also be used to estimate attractor dimension. This method is even easier and faster than that in Sect.4.4, since it doesn't require a numerical integration

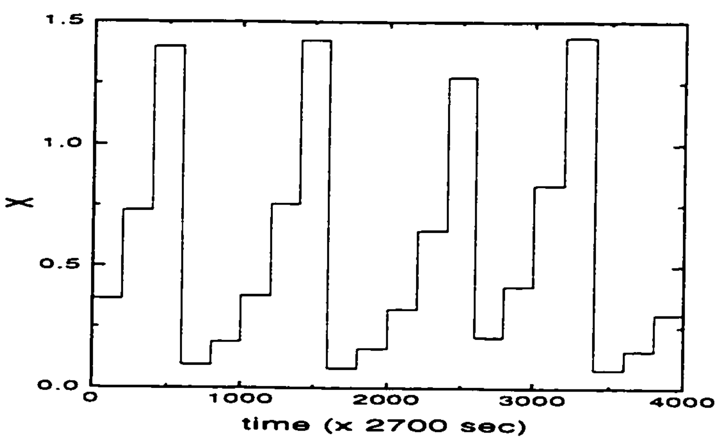

Figure 4.10: Solution of the Mackey-Glass equation Eq.3.4 at very large delay $\tau = 540000$. Other parameters are $a = 0.2$ and $b = 0.1$. This solution is equivalent to the one obtained with the continuous-time difference equation Eq.4.1. The integration time step is 0.001. The transformation given by Eq.3.3 with $\tau' = 200$ and $\epsilon = 1/2700$ was used.

algorithm (such an algorithm, along with an autocorrelation function estimator, are required however to obtain the correlation time δ). By discretizing the time delay τ in Eq.4.1 into M points, the CTDE is equivalent to M difference equations (or M mappings in parallel), as shown in Fig.4.12. We show below that the power spectrum of these M moving points is related to the power spectrum of the map (Eq.4.2) via a lowpass filter response function. In the following, we will consider the CTDE as M parallel ("decimated" is perhaps a better term) series of N points, each series of N points being generated by the map in Eq.4.2. Each series $x_m(t)$, $m = 1, 2, \cdots, M$ can be represented as

$$x_m(t) = \sum_{j=0}^{N-1} G^j(x_{0m})\, \delta[t - (j-1)M\Delta - (m-1)\Delta] \tag{4.23}$$

where Δ is the sampling time and δ is the Dirac delta function. The serie of $N * M$ points for the M moving points is given by

$$\begin{aligned} x(t) &= \sum_{m=1}^{M} x_m(t) && (4.24)\\ &= \sum_{m=1}^{M} \sum_{j=0}^{N-1} G^j(x_{0m})\, \delta[t - (j-1)M\Delta - (m-1)\Delta]\,. && (4.25)\end{aligned}$$

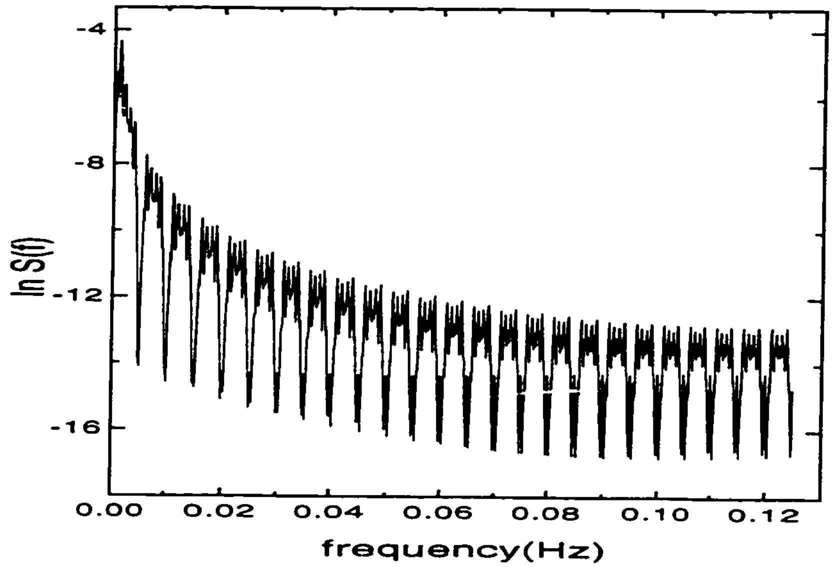

Figure 4.11: Power spectrum of the Mackey-Glass equation Eq.3.4 at very large delay $\tau = 540000$, for which the solutions are as shown in Fig.4.10. The initial condition was constant. Spectra were computed as in Fig.4.2 (sampling time is 3.75 sec) using the rescaled dynamics Eq.3.3 with $\tau' = 200$ and $\epsilon = 1/2700$. The spectrum is equivalent to the one obtained with the CTDE in Fig.4.14, even though the delay is finite.

The Fourier transform of these M parallel series is given by

$$\begin{aligned}
X(f) &= \frac{1}{N*M}\int_{-\infty}^{+\infty} x(t)e^{2\pi i f t}dt \\
&= \frac{1}{N*M}\sum_{m=1}^{M}\sum_{j=0}^{N-1} G^j(x_{0m})\int_{-\infty}^{+\infty} e^{2\pi i f t}\delta[t-(j-1)M\Delta-(m-1)\Delta]dt \\
&= \frac{1}{N*M}\sum_{m=1}^{M}\sum_{j=0}^{N-1} G^j(x_{0m})e^{2\pi i f[(j-1)M\Delta+(m-1)\Delta]} \\
&= \frac{e^{-2\pi i f M\Delta}}{N*M}\sum_{m=1}^{M} e^{2\pi i(m-1)f\Delta}\sum_{j=0}^{N-1} G^j(x_{0m})e^{2\pi i j f M\Delta}. \qquad (4.26)
\end{aligned}$$

Since $x(t)$ is discrete in time with time step Δ, its Fourier transform will be discrete in the frequency domain with frequency step $f_k = k/(M*N*\Delta)$, $k = 0, \cdots, (NM-1)$. Equation (4.26) becomes

$$X(f_k) = \frac{e^{-2\pi i k/N}}{N*M}\sum_{m=1}^{M} e^{2\pi i(m-1)k/(M*N)}\sum_{j=0}^{N-1} G^j(x_{0m})e^{2\pi i jk/N}$$

$$= \frac{e^{-2\pi i k/N}}{M} \sum_{m=1}^{M} e^{2\pi i(m-1)k/(M*N)} X_m(f_k) \tag{4.27}$$

where

$$X_m(f_k) = \frac{1}{N} \sum_{j=0}^{N-1} G^j(x_{0m}) e^{2\pi i jk/N} \tag{4.28}$$

is the Fourier transform of the m^{th} series of N points.

In the context of information storage in DDE's [11, 13, 62] (see Chap.5,6), the initial conditions of interest are piecewise constant functions on the interval $(-\tau, 0)$. This fact, along with the eventual goal of generalizing our results to arbitrary initial functions, lead us to pursue our calculation with initial functions made up of L constant plateaus in the interval $[-M\Delta, 0[$. We can then write for the Fourier transform of $N * M$ points from M parallel time series of N points:

$$\begin{aligned}
X(f_k) &= \frac{e^{-2\pi i k/N}}{M} \sum_{l=1}^{L} \sum_{m=(l-1)\frac{M}{L}+1}^{l\frac{M}{L}} e^{2\pi i(m-1)k/(M*N)} X_l(f_k) \\
&= \frac{e^{-2\pi i k/N}}{M} \sum_{l=1}^{L} e^{2\pi i(l-1)k/(L*N)} \sum_{m'=1}^{\frac{M}{L}} e^{2\pi i(m'-1)k/(M*N)} X_l(f_k) \\
&= \frac{e^{-2\pi i k/N}}{M} \sum_{m'=1}^{\frac{M}{L}} e^{2\pi i(m'-1)k/(M*N)} \sum_{l=1}^{L} e^{2\pi i(l-1)k/(L*N)} X_l(f_k) .
\end{aligned} \tag{4.29}$$

This assumes that all chosen initial values for the plateaus belong to the attractor of the map; in other words, each plateau evolves in an asymptotic regime, once the transients have died out. If the map is ergodic, we can expect identical power spectra for time series starting from typical initial conditions. Therefore we can expect that, for any l,

$$|X_l(f_k)|^2 = |X_1(f_k)|^2 . \tag{4.30}$$

Here $X_1(f_k)$ is the Fourier transform of the map (Eq.4.2). If the map has periodic solutions, then there is a finite number of attractor solutions, and each one can be obtained from any other one by a simple time shift. In this case, we can write

$$X_l(f_k) = X_1(f_k) e^{2\pi i \Psi_l} , \tag{4.31}$$

where $\Psi_l = \varphi_l - \varphi_1$ is the phase difference between $X_l(f_k)$ and $X_1(f_k)$. If the map is chaotic, the Fourier transforms will differ in phase at each frequency, but not in modulus since the spectra will be similar. In this case, one expects a more complicated relationship of the form $\Psi_l(k) = \varphi_l(k) - \varphi_1(k)$ where we have highlighted the frequency dependence. Hence we have the following general form for the Fourier transform of a CTDE solution with initial functions defined using L subintervals:

$$X(f_k) = \frac{e^{-2\pi ik/N}}{M} X_1(f_k) \sum_{m'=1}^{\frac{M}{L}} e^{2\pi i(m'-1)k/(M*N)} \sum_{l=1}^{L} e^{2\pi i[(l-1)k/(L*N)+\Psi_l(k)]}. \tag{4.32}$$

The power spectrum is

$$\begin{aligned} S(f_k) &= |X(f_k)|^2 \\ &= |H(k)|^2 S_1(f_k) \end{aligned} \tag{4.33}$$

where $S_1(f_k) = |X_1(f_k)|^2$ is the power spectrum of the map (Eq.4.2), $|H(k)|^2$ is the magnitude squared amplitude response

$$|H(k)|^2 = \frac{1}{M^2} \frac{sin^2(\pi k/(L*N))}{sin^2(\pi k/(M*N))} |Z(k)|^2 \tag{4.34}$$

with

$$Z(k) = \sum_{l=1}^{L} e^{2\pi i[(l-1)k/(L*N)+\Psi_l(k)]} \tag{4.35}$$

This spectrum $S(f_k)$ can be estimated using the periodogram for $N*M$ points generated by the M parallel maps (Fig.4.12). This periodogram is defined at $(N*M/2+1)$ frequencies as

$$\begin{aligned} S(0) &= |X(0)|^2 \\ S(f_k) &= \frac{1}{2}\left[|X(f_k)|^2 + |X(f_{N*M-k})|^2\right] \quad k = 1, 2, \cdots, \left(\frac{N*M}{2} - 1\right) \\ S(f_{N*M/2}) &= |X(f_{N*M/2})|^2 \end{aligned} \tag{4.36}$$

For M maps in parallel, f_k is defined for the following frequencies:

$$f_k = \frac{k}{M*N*\Delta} = 2f_c \frac{k}{M*N} \quad k = 0, 1, \cdots, \frac{N*M}{2} \tag{4.37}$$

where $f_c = 1/2\Delta$ is the Nyquist frequency.

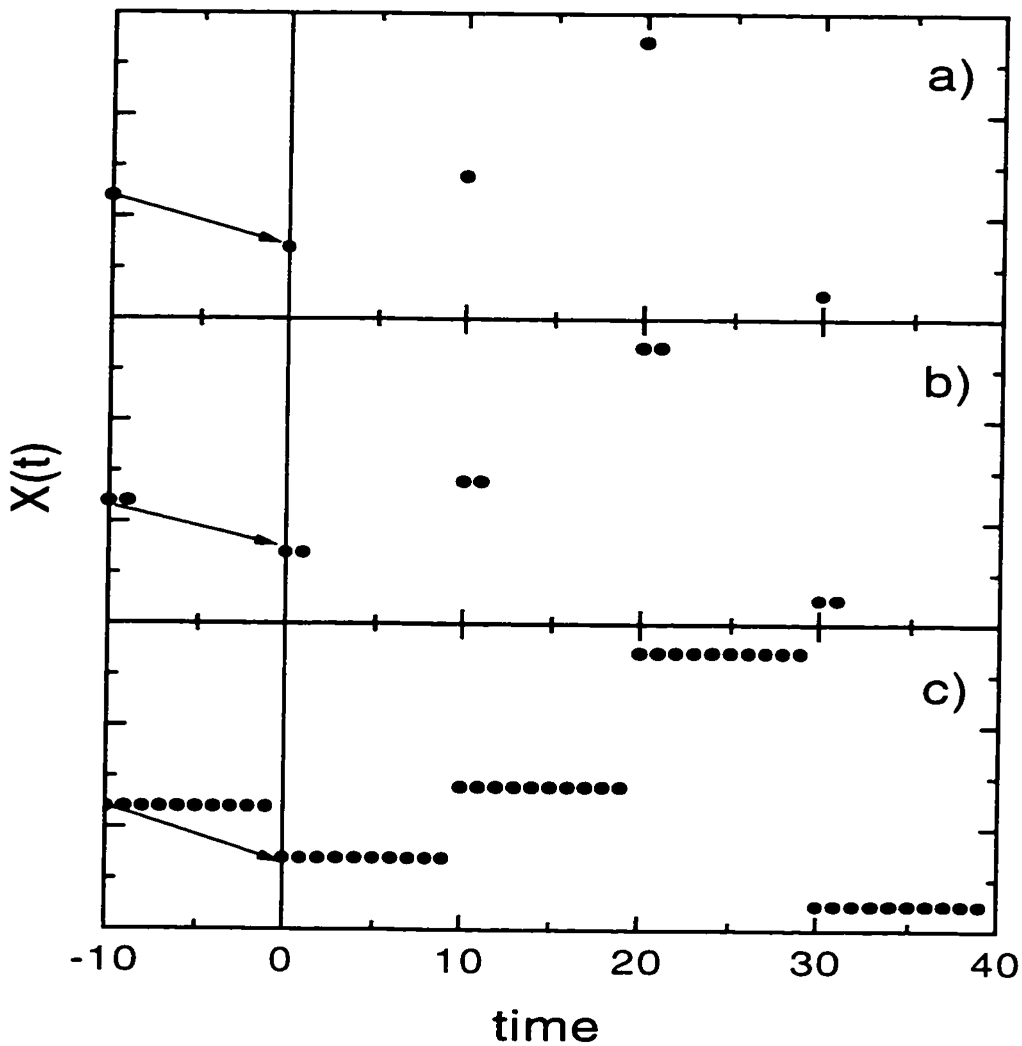

Figure 4.12: Transition from a map evolving in discrete time to M maps evolving in parallel in discrete time. The points on $(-\tau, 0)$ evolve independently from one interval to the next, and so are mapped in parallel according to the map $x(i) = G(x(i-1))$. As M goes to infinity, the system of parallel maps becomes equivalent to the continuous-time difference equation Eq.4.1.

4.7.2 The case of constant initial conditions

If $\Psi_l = 0,\ \ l = 1, 2, \cdots, L$ (same initial conditions), then

$$|Z(k)|^2 = \frac{sin^2(\pi k/N)}{sin^2(\pi k/(L * N)} \tag{4.38}$$

The power spectrum takes the form

$$S(f_k) = \frac{1}{M^2}\frac{sin^2(\pi k/N)}{sin^2(\pi k/(M * N))} S_1(f_k). \tag{4.39}$$

with zeros at $k = N, 2N, \cdots, M * N/2$. This form is equivalent to the one found in Sect.4.6 (see Eq.4.22) by replacing M with τ. Note that the maximum value of the denominator is one, and that for low frequencies Eq.4.39 decreases as $1/k^2$, i.e. as $1/f^2$. Figures 4.13 and 4.15 show parallel map power spectra for, respectively, the Mackey-Glass and Ikeda models for $M = 1$, $M = 2$, and $M = 10$. We note that, for illustration purposes, we have normalized our spectra in order to keep the Nyquist frequency at 0.5. In fact, if we were to compare actual spectra for, e.g., $M = 1$ and $M = 10$, we would find that the spectrum for $M = 10$ extends over ten times the frequency range of that for $M = 1$.

As M increases, more and more peaks are seen in the power spectrum. In fact, closer inspection reveals that the power estimates for higher frequency values for $M = 2$ are obtained by juxtaposing the spectrum for a single map (Figs.4.13a,4.15a) with its mirror image about the y-axis. This juxtaposition is then multiplied by the frequency-dependent filtering or "scaling" factor in Eq.4.39, i.e. the prefactor of $S_1(f_k)$ on the right-hand-side. Spectral estimates at higher values of M are similarly obtained by reflection, translation and scaling.

The filtering function $|H(k)|^2$ in Eq.4.39 (see also Eq.4.34) affects the amplitude of the power and determines its zeroes as well. The symmetries of the spectra can be seen to originate from the properties of the spectrum of M parallel maps without this filtering function. The spectral estimates over different frequency ranges are then related to each other by:

$$S(f_k) = S(f_{k+q*N}), \quad q = 1, \cdots, M-1; \quad k = 0, \cdots, N \; . \tag{4.40}$$

With the filtering function in place, the following translation and reflection relationships hold:

$$\begin{aligned} S(f_{k+(q-1)N}) &= |H(k+(q-1)N)|^2 S_1(f_k), \\ S(f_{k+(q-1/2)N}) &= |H(k+(q-1/2)N)|^2 S_1(f_{N/2-k}), \quad q = 1, \cdots, M/2; \quad k = 0, \cdots, \frac{N}{2} \; . \end{aligned} \tag{4.41}$$

Thus, one can construct piece by piece the whole power spectrum for M parallel maps.

Figures 4.14, 4.16 show spectra for $M = 54$, obtained from the FFT algorithm in (a) and from our analytical expression (Eq.4.39) in (b). The agreement is excellent when the FFT of the map (Eq.4.2) in (b) uses M times the number of points in the FFT in (a). The envelope of this power spectrum decays as $1/\sin^2 f_k$, as can be seen by setting the numerator in Eq.4.39 equal to one (see Figs.4.14, 4.16). The low-to-mid frequency part of these spectra, at which most of the energy of the chaotic fluctuations concentrates, then approximately follows a power law $P(f) \simeq 1/f^2$ (as can be seen by Taylor expansion of the denominator in Eq.4.39), a property usually associated with stochastic processes. The spectrum of M parallel maps thus appears as a collection of peaks, whose shape is determined by the spectrum of a single map, and these peaks are "superimposed" on a background similar to a noise background at low-to-mid frequencies.

We note that this decay rate does not depend on the specific map (Ikeda or Mackey-Glass) obtained in the singular limit. This map only determines the shape of the peaks in the CTDE limit.

There is also a correspondance, for large delays, between the peaks in these CTDE spectra with the mode frequencies in the DDE: $f_n^{DDE} = n/2\tau$ $(n = 1, 3, 5, \cdots, [\tau/\Delta] + 1)$ for the DDE, and $f_n^{CTDE} = n/2M\Delta(n = 1, 3, 5, \cdots, (M+1))$, where $M = [\tau/\Delta]$. [ ] stands for the integer part of τ/Δ. Δ is the sampling time in the DDE. In the CTDE the frequencies should be estimated in the middle of the main peaks. The attractor dimension can then be found from the CTDE by counting the number of peaks within $c\delta^{-1}\Delta$. For DDE's at large delay, these estimate agree with the $c\delta^{-1}\tau$ estimate proposed in [54].

4.7.3 Other special initial conditions

If $\Psi_l \neq 0,\ \ l = 1, 2, \cdots, L$, then $|Z(k)|^2$ rarely has zeroes. The only remaining zeros are in the power spectrum, namely at $k = L * N, 2 * L * N, \cdots, M * N/2$. In general, we expect that the sum $Z(k)$ will have no particular structure, and that the spectrum will be broadband. Further insight into the decay of spectra for CTDE's and even DDE's could perhaps be obtained by further analyzing the properties of the quantity $Z(k)$.

It is possible to make predictions of certain spectral features when the initial function has simplifying features. Here, we only give an example for the case where this function has periodicity p with an integer number of periods $n_p = L/p$. Then $Z(k)$ will have zeros

$$Z(f_k) = \sum_{m'=1}^{p} e^{2\pi i[(m'-1)k/(L*N)+\Psi_{m'}(k)]} \sum_{n'=1}^{n_p} e^{2\pi i[(n'-1)pk/(L*N)]} \tag{4.42}$$

The first summation rarely equals zero for $\Psi_{m'}(k) \neq 0$. The second summation can be rearranged into the following form

$$\sum_{n'=1}^{n_p} e^{2\pi i[(n'-1)pk/(L*N)]} = e^{\pi i(1-p/L)k/N} \frac{sin(\pi k/N)}{sin(\pi pk/(L*N))}. \tag{4.43}$$

Eq.4.34 has zeros, solutions of the following equation:

$$\sin(\pi k/(L*N)) \frac{sin(\pi k/N)}{sin(\pi pk/(L*N))} = 0 \tag{4.44}$$

Examples of spectra determined numerically for various initial conditions are shown in Fig.4.17. In this case the spectra also obey the relationship defined by Eqs.(4.34)-(4.36), but the presence of more zeroes gives these spectra an overall more complicated shape when compared to those for constant initial conditions. The spectra in Fig.4.17b-d-e have only

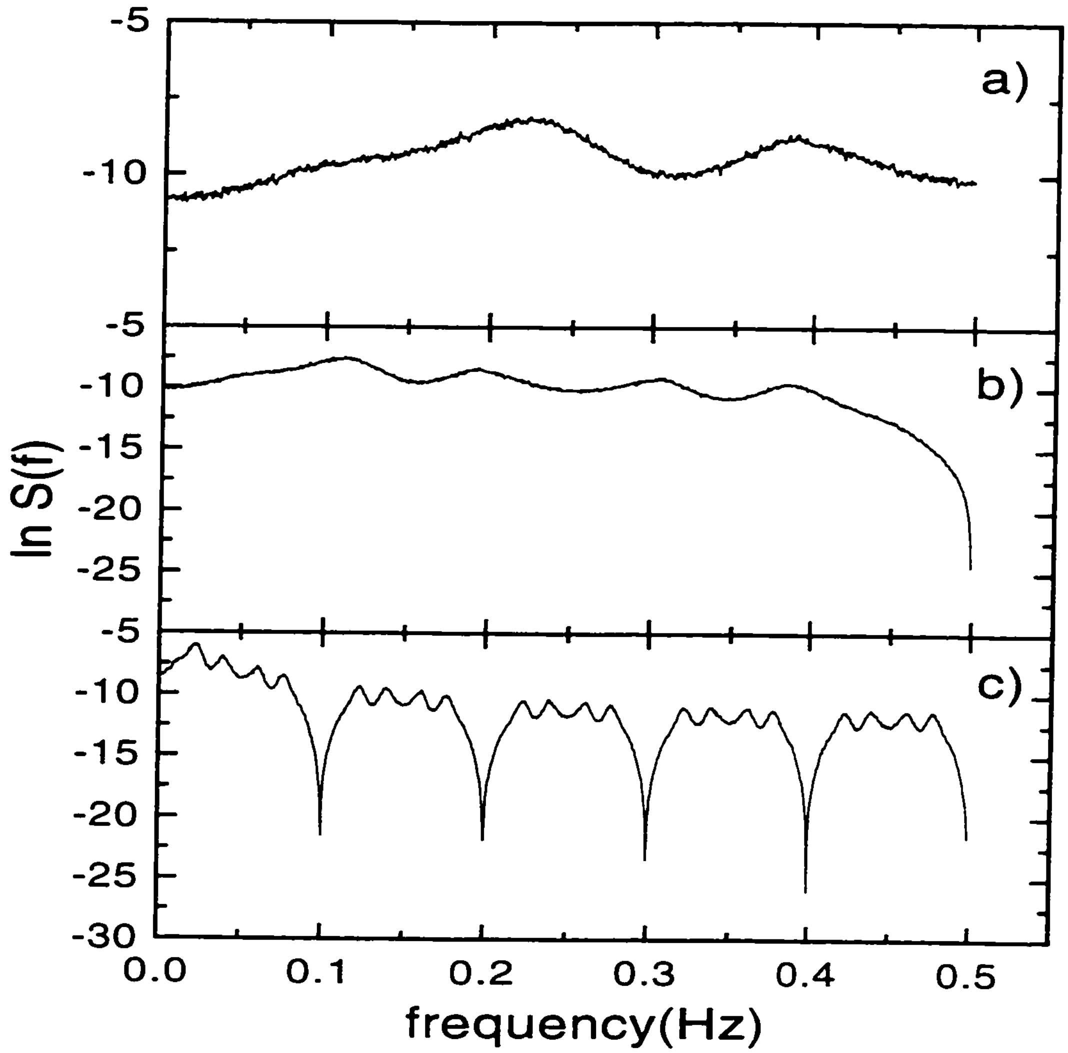

Figure 4.13: Power spectra of the Mackey-Glass continuous time difference equation (CTDE) Eq.4.1: $x(t) = G(x(t-\tau))$ (see Fig.4.12). a) Power spectrum of a single point evolving in time ($M = 1$). b) Same as is (a) but for $M = 2$ points on the delay interval evolving in time. c) Same as in (a) but for $M = 10$ points. The initial values for all points are the same in each case.

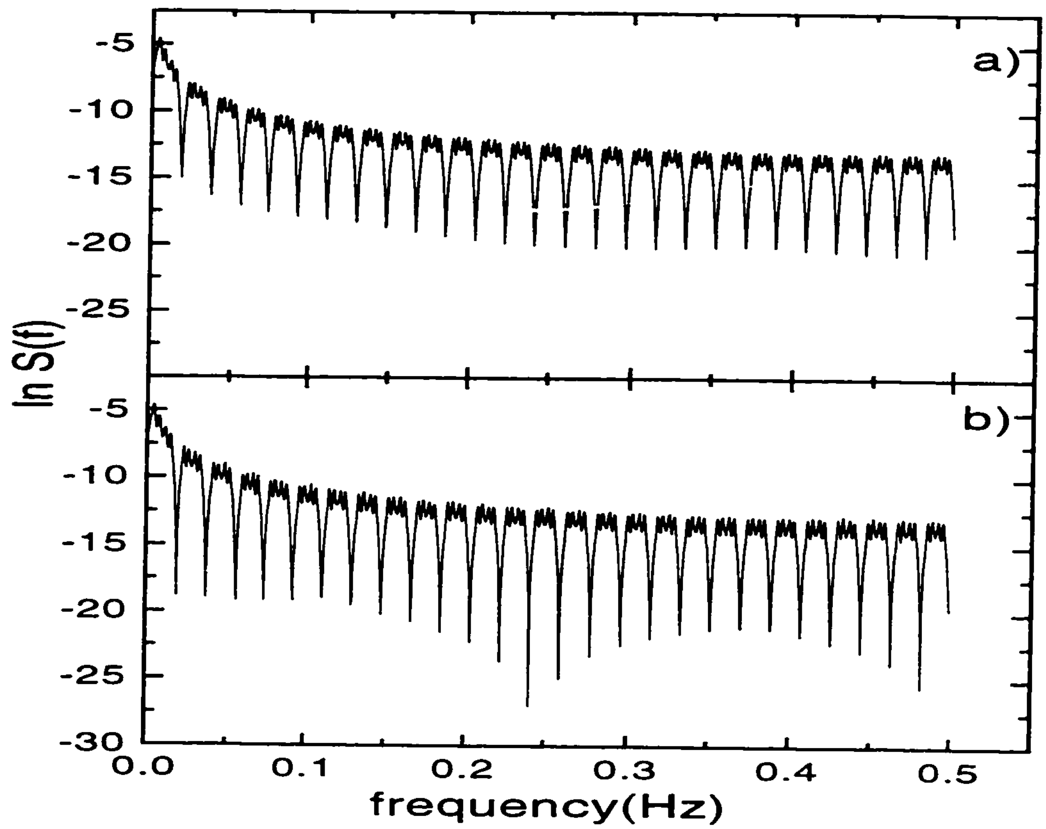

Figure 4.14: Power spectra of the Mackey-Glass CTDE Eq.4.1 for $M = 54$ points on a delay interval evolving in parallel forward in time, calculated a) from the time series generated by the CTDE, and b) analytically using Eq.4.39 in which $S_1(f_k)$ is the power spectrum computed numerically from the evolution of a single point ($M = 1$) following the map Eq.4.2 (shown in Fig.4.12a). The spectra are equivalent when the number of points used to calculate the FFT in b) is equal to M times the number of points in (a). If the number of points used to calculate the FFT is the same in (a) and (b), then we have to multiply the power spectrum in (b) by the factor M in order to get the agreement. The initial values for all points is the same in each case.

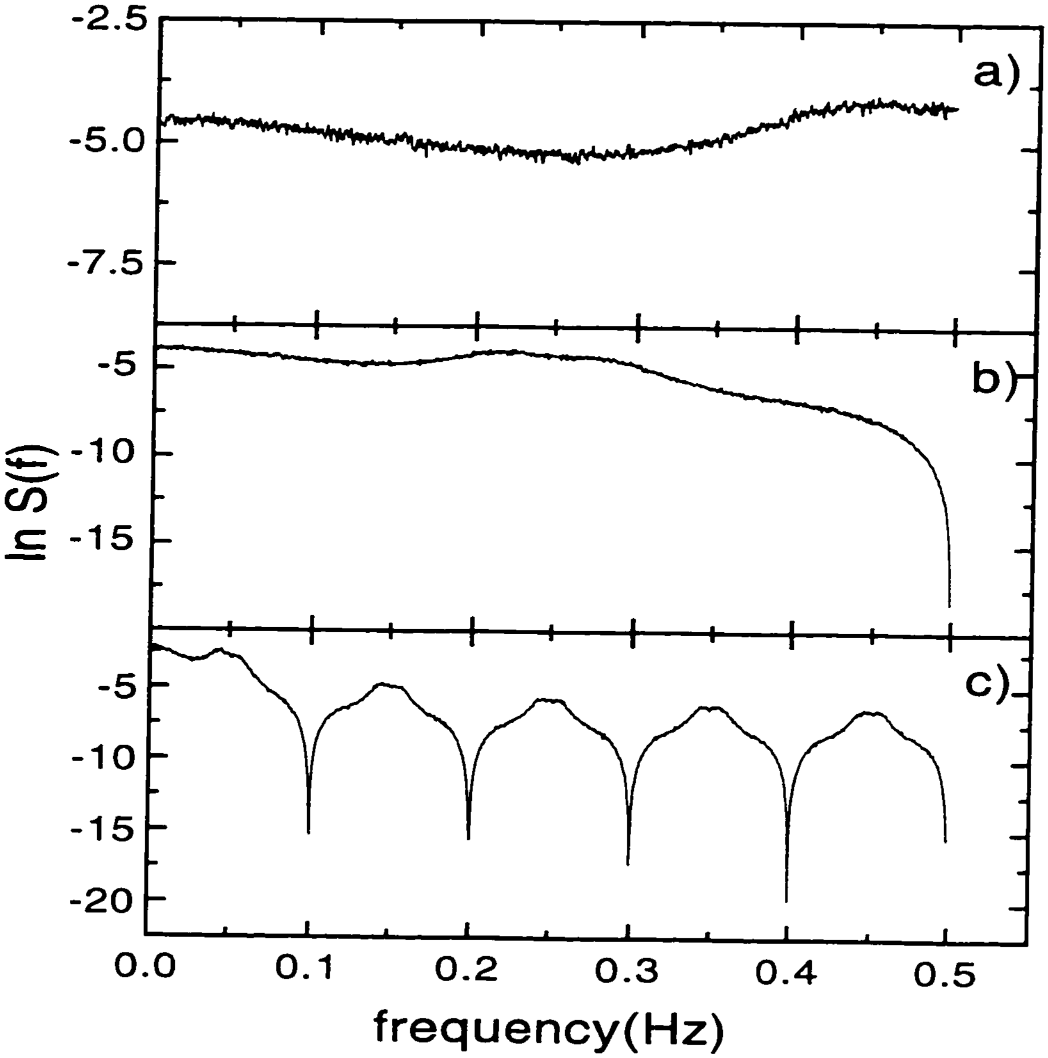

Figure 4.15: Power spectra of the Ikeda CTDE $x(t) = 2.1b^{-1}\pi\sin(x(t-\tau))$ with parameters $b = 1$ and $\tau = 20$. a) Power spectrum for $M = 1$, i.e. for a single point evolving according to the Ikeda map. b) Same as is (a) but $M = 2$. c) Same as in (a) but $M = 10$. The initial values for all points is the same in each case.

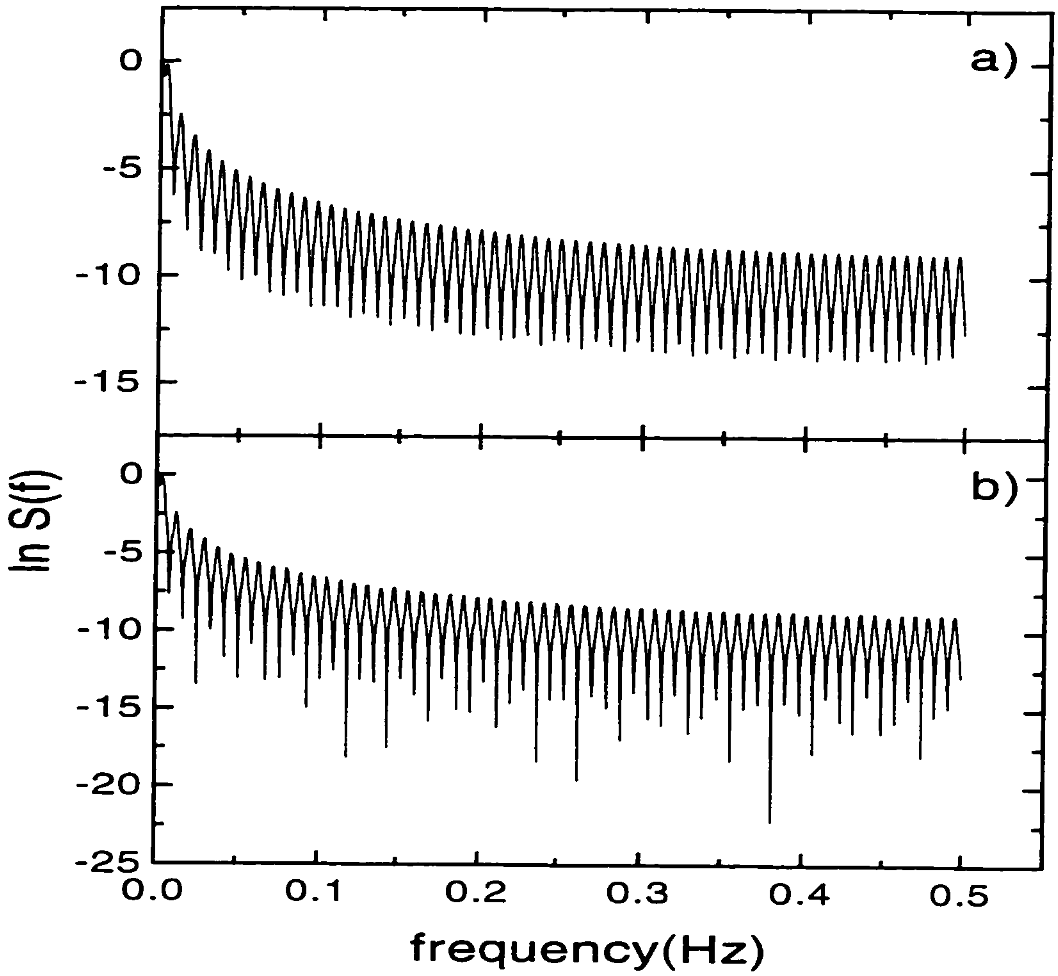

Figure 4.16: Power spectra of the Ikeda CTDE with $M = 118$, calculated a) from the time series generated by the CTDE, and b) analytically using Eq.4.39 in which $S_1(f_k)$ is the power spectrum computed numerically from the evolution of a single point ($M = 1$) (shown in Fig.4.15a). The initial values for all points is the same in each case.

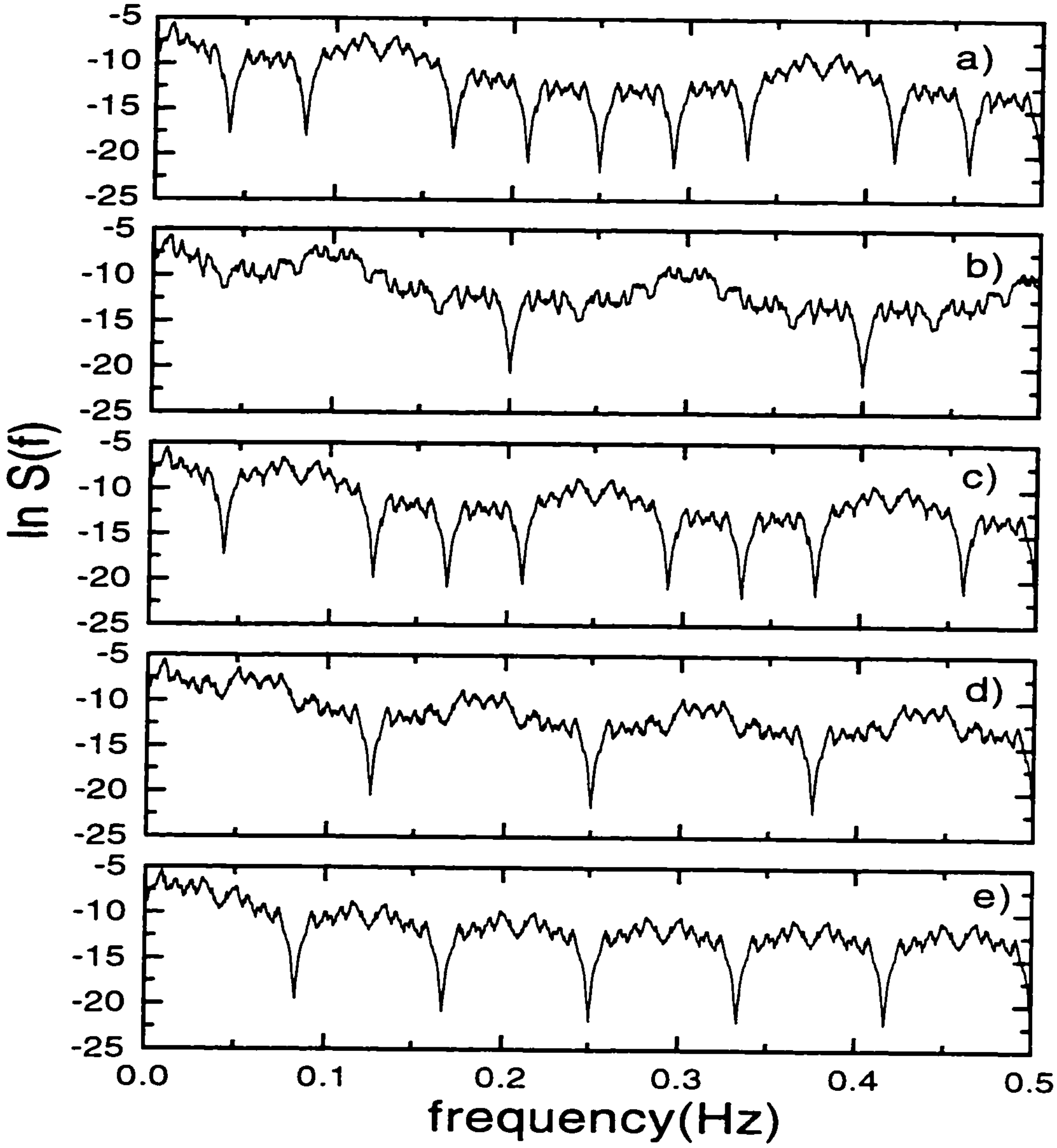

Figure 4.17: Power spectra of the Mackey-Glass CTDE calculated numerically using initial functions with and without periodicity. The initial function is divided into L plateaus evolving independently from one interval to the next. The pronounced negative-going peaks in the power spectrum correspond to the zeros of the response function in Eq.4.34. a) $L = 6$ (c1, c2, c1, c2, c1, c2); b) $L = 5$ (c1, c2, c1, c2, c1); c) $L = 4$ (c1, c2, c1, c2); d) $L = 3$ (c1, c2, c1); e) $L = 2$ (c1, c2). The values of $c1$ and $c2$ are 1.2 and 0.2 respectively.

zeroes at the zeroes of the first sine term in Eq.(4.44) since they do not have a periodic initial function; those in (a) and (c) have more zeroes due to the other terms in Eq.(4.44), arising from the periodicity of the initial function. The shape of the spectrum in these latter cases is basically independent of the values of C1 and C2, and are determined by the symmetry of the initial condition.

4.8 Conclusion

In conclusion, the peaks in the power spectra of the Mackey-Glass and Ikeda models at large delays are found to agree with the frequencies of the linear modes obtained through linear stability analysis of the dynamics around the fixed point. The attractor dimension can be estimated from the power spectrum of the DDE using these peaks; it can also be estimated using the CTDE approach (Eq.4.39) combined with the numerically determined spectrum from a single map (Eq.4.2); hence our approach to calculating dimension (and metric entropy) for these DDE's with high-dimensional attractors is simpler than the one based on the computation of Lyapunov exponents or the correlation integral. We anticipate that our results may be applicable to DDE's other than the simple first-order ones of the type studied here.

The map (Eq.4.2) obtained in the singular limit of the Mackey-Glass DDE explains many properties of the DDE. For example, this map exhibits a period-doubling cascade to chaos like the DDE. This is not the case for all DDE's. LeBerre *et al.*[54] have shown that the bifurcation sequence to chaos in the ring-cavity delay-differential equation is different from that of the 2D map obtained in its singular limit, even though the Lyapunov dimension increases linearly with the delay as for the Mackey-Glass equation. In particular, they show that the dimension of attractors in the "map" description is bounded by the dimension of the map, i.e. 2. Our approach here suggests that the CTDE is perhaps a better system with which to compare attractor dimensions of DDE's. The CTDE is in fact infinite-dimensional. as is the DDE from which it is derived as the delay (or more precisely, the ratio R) becomes infinite.

Farmer [7] suggested that the number of degrees of freedom in the DDE is likely to be related to the embedding dimension of the attractor rather than to its Lyapunov or information dimension [7]. Alternately, LeBerre *et al.* [54] have proposed that the number of degrees of freedom in a laser system such as the ring-cavity system is roughly given by the delay-to-response time ratio $R = \gamma\tau$ for that system (γ is the linewidth). Our findings for the class of first order DDE's studied here show that the number of modes within the characteristic time δ/c is close to previously reported Lyapunov dimensions, a result in the same spirit as [54].

We summarize our findings as follows:

1. Many properties of the DDE at large delay, such as its dynamical invariants and its power spectra, are related to the roots of the characteristic equation of the DDE, obtained by linearizing its dynamics around the fixed point.

2. The almost-periodic peaks in the power spectrum seen e.g. for $\tau = 200$ ($R = 20$), first observed by Farmer [7], correspond to the frequencies of the roots of the linearized dynamics. The correspondence becomes perfect as $R \rightarrow \infty$. These peaks, corresponding to modes of oscillation, are located at odd integer multiples of the reciprocal of the fundamental period, which is on the order of 2τ.

3. The disappearance of the modulation in the power spectrum at very large R values follows from the accompanying decrease of the real part of the eigenvalues of the linearized problem.

4. The Lyapunov dimension of the attractor agrees with the number of peaks in the

power spectrum between zero frequency and the reciprocal of the correlation time of the feedback function.

5. The sum of the positive Lyapunov exponents equals the rate of decay of the power spectrum in the mid-to-high frequency region (2). This metric entropy stays approximately constant for $R > 5$.

6. Systems with a distribution of delays rather than a single fixed delay exhibit spectral behaviors similar to those of DDE's when their memory kernel becomes sharply localized in time. In particular, when they are equivalent to 200 or more coupled ordinary differential equations, the decay rate of their power spectrum is very close to that for the corresponding DDE. Hence our study with distributed delays shows that the decay rates, and thus the attractor dimensions, match only when the system of ODE's for the distributed delay case has sufficient (and very high) dimensionality.

7. The spectra of CTDE can be calculated analytically for arbitrary initial functions, provided the spectrum of the map obtained in the singular limit is known. This latter spectrum can be obtained numerically. The CTDE spectrum is in fact constructed by translations of the basic spectrum of the map, as well as of mirror symmetric images of this basic spectrum. These basic "units" are then put end to end and multiplied by a filtering function Eq.4.34. As for the DDE at very large delay, the peaks in the CTDE spectrum obtained using a large number of plateaus (i.e. for M large) merge, and their fine structure becomes washed out.

8. CTDE spectra for constant initial functions have a particularly simple form (Eq.4.39: see Figs.4.14,4.16), with the basic peak structure similar to that seen in DDE's at low frequency (see e.g. Fig.4.1b). That such a correspondence should exist at low-frequency is expected since that is where the behavior of finite-delay DDE's is most similar to that of the CTDE (see Sect.4.2.1).

9. The peak structure mentioned in the previous item is determined by the spectrum of the map (see Fig.13a for Mackey-Glass and Fig.15a for Ikeda) obtained in the singular limit of the DDE. It is in fact composed of that spectrum alongside its mirror image. This explains why the peaks in the spectrum of the Ikeda DDE are sharp, while those for the Mackey-Glass DDE are broader and have more than one extremum.

10. The more negative Lyapunov exponents can be estimated from the analytic expression for the stable modes, as suggested by Ikeda [53].

11. At very large delays, there is a transition from an exponential to a $1/\sin^2(f)$-type spectrum decay, which approximates a $1/f^2$-type at low-to-mid frequencies.

Chapter 5

Encoding information in stable limit cycles of feedback systems

5.1 Introduction

We showed in Chapter 3 that nonlinear delay-differential equations can exhibit an important property known as multistability. In this Chapter we show how to use this property for the storage of information in recurrent neural feedback circuits modeled by nonlinear delay-differential equations.

Multistability is a mechanism for memory storage and temporal pattern recognition in both artificial [14, 74, 75, 76, 77] and living neural networks [15, 16, 78, 79]. In a living nervous system, recurrent loops involving two or more neurons are ubiquitous and are particularly prevalent in cortical regions important for memory, e.g., the hippocampal-mesial temporal lobe complex [80, 81]. The time required for activity to propagate around the loop is an important determinant of the dynamical behavior of such circuits, especially if this delay is large compared to the neuron response times. Here we show that time-delayed recurrent loops have a potentially large capacity to encode information in a periodic temporal pattern of membrane voltage or spiking activity. The possibility that some forms of memory in the living nervous system may be encoded into a temporal patterning of neural spike trains has been well recognized [82, 83, 84, 85]. Thus, besides exhibiting multistability, these systems can also generate a variety of temporal spike train patterns.

The models studied here are cast in terms of delay-differential equations (DDE's). The storage property originates in the multistability which arises from the combination of non-linearity and delays [58]. The idea of using DDE's as memory devices was first suggested by Ikeda and Matsumoto [8] and implemented on a hybrid laser diode by Aida and Davis [11]. A finite string of bits was encoded directly into the initial function (IF) for this device, as we will see in Sect.5.3. The state variable evolved from its IF into a periodic waveform uniquely specified by this string. As the time delay increases much beyond the system response time, the number of multistable solutions increases. This number, which is equal to the number of unstable modes for a certain value of the feedback parameter (see Sect.3.4), is related to the maximum storage capacity of the system.

In this Chapter, we discuss the application of this idea to physiologically-based models of recurrent inhibition (RI) and recurrent excitation (RE) with non-spiking neurons such as the Mackey-an der Heiden model [5], and spiking neurons such as the Plant and Hodgkin-Huxley models [4, 12]. By focusing on the temporal features of DDE's, our approach is complementary to the growing body of work on physiologically-based neural-network models of active short-term memory, involving neural activity recirculating among neurons in a recurrent configuration with fixed connections [15, 16, 86]. It is also complementary to studies of networks capable of a Hebbian-type learning of temporal sequences (see e.g. [87, 88]).

Our results also provide insight into multistability in simple DDE models of neural feedback [4] and in control systems, physiological and other, involving multiple delayed feedback loops [26]. Our method further provides an alternative to models of temporal pattern storage based on networks of many coupled neurons [6, 14, 75, 87].

This Chapter is organized as follows: Section 5.2 discusses the dynamics of recurrent inhibition and excitation between two populations of neurons. Section 5.3 explains the principle of coding and illustrates it using the Mackey-Glass equation. Section 5.4 shows how an RI circuit with non-spiking neurons can store information in its patterns of voltages and spikes. Section 5.5 looks at an RI model based on the Fitzhugh-Nagumo equation. We find that its solutions are encodable despite the presence of spiking dynamics. Section 5.6 shows the storage of information in a more realistic model: the Hodgkin-Huxley model with a feedback current. The Chapter concludes in Section 5.7.

5.2 Dynamics of recurrent excitation and inhibition

Recurrent excitation and inhibition between isolated cells or cell populations is ubiquitous in the nervous system. From the Renshaw cells of the spinal cord to the hippocampus, one sees excitatory groups of neurons giving off collateral axonal branches which excite interneuron groups. In turn, these neurons either excite or inhibit the firing of the first neurons (see Fig.5.1). In certain instances, this type of circuitry can involve only one or two neurons, rather than groups.

In the following, we denote by E the excitatory neuron, and I the inhibitory interneuron. Neurons E and I thus are involved in an inhibitory feedback loop. We will also consider the recurrent excitation case where neuron E excites itself after a certain delay τ. The excitatory or inhibitory influence of I on E depends on the activity of E at time τ in the past. This time delay represents the sum of the conduction time along the axon and dendrites, the time required for quantal release of neurotransmitters at synapses, processing times in the interneuron, and the rise time of the excitatory or inhibitory potential. Recurrent inhibition is commonly observed in the spinal motoneurons, in pyramidal cells of the hippocampus, in the cerebellum, thalamus and neocortex, and in the retina and olfactory bulb [4, 5]. Recurrent excitation is postulated to be involved in the genesis of behavior in the hippocampus. The behavior of RI or RE circuits is most naturally formulated in terms of DDE's [4, 5, 89, 90], when delay times are considered to be significant:

$$\begin{aligned} C\frac{dV(t)}{dt} &= -I_{ion}(V, W_1, W_2, \cdots, W_n) + F(V(t-\tau)) + I_0, \\ \frac{dW_i(t)}{dt} &= \beta\frac{[\hat{W}_i(V) - W_i]}{\Gamma(V)}, \end{aligned} \tag{5.1}$$

where $V(t), V(t-\tau)$ is the membrane potential at, respectively, times t and $t-\tau$, Γ is a voltage-dependent time constant, C is the membrane capacitance, I_{ion} is the sum of V- and τ-dependent currents through the various ionic channel types, I_0 is the applied current, W_i describes the fraction of channels of type "i" that are in various conducting states (e.g., open versus closed), $\hat{W}_i(V)$ describes the equilibrium functions, and β is a temperature-like time scale factor. The function F describes the effects of the inhibitory neuron on the membrane potential of the excitatory neuron.

This is a very simplified model of recurrent feedback currents in which the time-course of the current has the same shape (but different sign and amplitude) as the action potential itself. This is an idealized case for real neuronal circuits, since the excitatory postsynaptic potentials (EPSP's) and inhibitory postsynaptic potentials (IPSP's) are very narrow in time. It is thus a first step towards studying multistability in such biological circuits. Our approach is even more relevant to the design of spiking neural networks in which the biological details are less important.

When $F(V(t-\tau)) = 0$, there is no recurrent input, and the choice of I_0 determines whether the neuron is excitable (firing only when sufficiently stimulated) or periodically firing [91, 92]. In this thesis, we will consider only the first mechanism where both excitatory and inhibitory pulses can cause a neuron to produce an action potential. The other case has been treated by our colleagues [13]. When the membrane potential V of the neuron is depolarized to a certain critical level, called the *threshold*, the neuron fires and V returns to its resting potential V_0 after a brief hyperpolarization. The firing of the neuron excites the

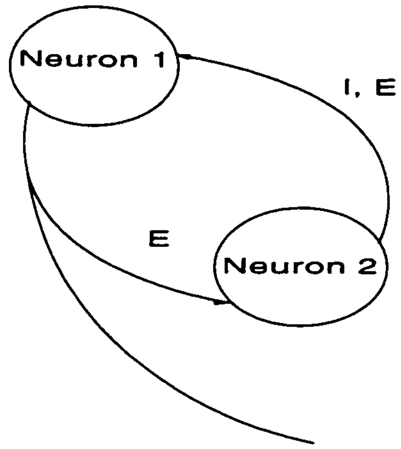

Figure 5.1: Recurrent excitation and inhibition between two neurons. Neuron 1 fires an action potential and excites (E) neuron 2. In turn neuron 2 either stimulates (E) or inhibits (I) the firing of neuron 1.

inhibitory interneuron, which in turn at time τ later, either delivers an EPSP or an IPSP to the excitatory neuron. The effect of the IPSP will be to move the membrane potential away from the threshold for firing an action potential. In this case, normally, the postsynaptic cell is "inhibited". However, if the inhibition is sufficiently strong, an action potential can result once the IPSP stops. The IPSP changes the timing of the next neuronal firing by an amount δ [93, 94, 95, 96, 97]. This phenomenon, known as anode break excitation or "rebound", is paradoxical, although well-documented and thought to be important in firing pattern generation [98]. It arises because the IPSP brings the system state across the curved threshold separatrix, and an action potential follows upon release of the inhibition (see Fig.5.2). Assume that in the absence of input the neuron is at rest. If the neuron fires at time t_0 then it must, as a consequence of rebound, also fire at $t_0 + \tau + \delta$ ($\delta = 0$ in the case of RE). The condition for permissible, periodic spike train patterns containing n spikes occuring at times t_i is simply $t_{i+1} - t_i \geq T_r + \delta$, $i = 1, \cdots, n$, where T_r is the absolute refractory period of the neuron, i.e. the interval of time during which a second action potential cannot be initiated. The condition that qualitatively different, temporally patterned spike trains can occur is $\tau > 2(T_r + \delta)$. Under this condition an infinite number of patterns can be stored; however, these are neutrally stable since a small perturbation in the timing of a spike is perpetuated. This behavior is similar to that of singularly perturbed DDE's [10] seen in Sect.3.6.

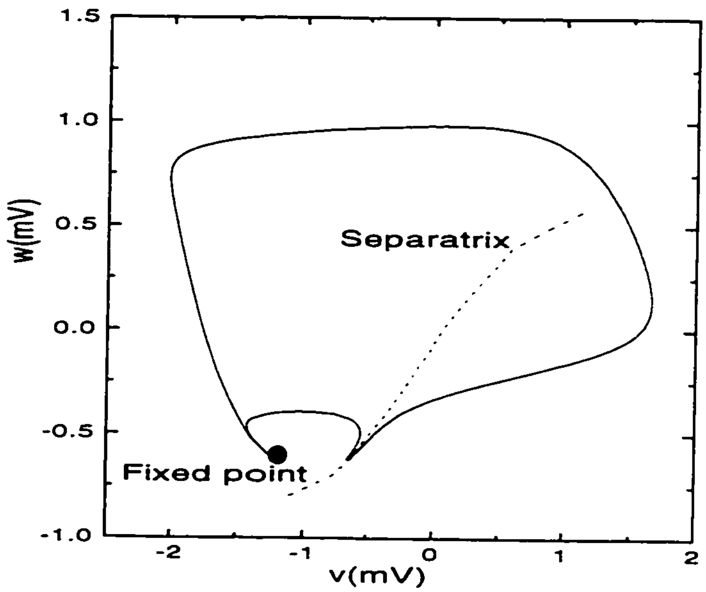

Figure 5.2: W vs V in Plant's model (Eq.5.4). The parameters used are $a = 0.7$, $b = 0.8$, $\rho = 0.08$, and $\mu = 0$. If the threshold separatrix (dashed line) is not crossed, the system goes to the resting potential (the fixed point). If the threshold separatrix is crossed however, the system goes around the loop, thereby generating an action potential (solid line).

5.3 Principle of coding for Mackey-Glass equation

Ikeda and Matsumoto [8] studied the bifurcation structure and multistability properties of the Ikeda equation describing the oscillatory modes of an optical cavity, and suggested its application as a memory device when the ratio R of delay to response time is large. Aida and Davis [11] proposed a method called "seeded bifurcation" for coding finite messages into these multistable oscillation modes for large R, and implemented this procedure on a laser. Their principle of information storage will be illustrated here using the Mackey-Glass equation (MG) [2] (Eq.3.4) which is closer to one of the models of RI investigated below. If $R \gg 1$ and the IF is a constant, the solutions exhibit "plateaus" as in Fig.5.3b. The values of these plateaus are approximately given by the iterations, from one delay interval to the next, of the CTDE (Eq.3.33). The map, obtained by discretizing the time in unit of τ in Eq.3.33 (see Eq.3.34), is shown in Fig.5.3a, and for the parameters used in Fig.5.3b, has a period of 4. Note that the solution of the CTDE has a period of 4τ, but the DDE has period slightly larger than 4τ, because of the finite time for the solution to jump from one plateau to another. Thus the plateaus in Fig.5.3b follow the succession given by the CTDE (Eq.3.33). If the plateaus are wide enough, i.e. if R is large enough, the IF can be subdivided into n bins. The plateau value in each bin evolves independently of its neighboring bins (except for a small transition layer between the bins) according to Eq.3.33 (see Fig.5.4).

The bifurcation parameter a is chosen to yield a periodic orbit for the map; this orbit has $l = 2^m$ values, where m is the bifurcation order. For example, a period-2 orbit ($m = 1$) has 2 values, a period-4 orbit ($m = 2$) has 4 values, and so on. The solutions with n bins in the interval $(-\tau, 0)$ are here called (n, l) isomers and represent the different memory states of the system. There are l^n different initial functions or "messages" which can be stored into a solution of period $l\tau$. For example, in Fig.5.4b, for which $R \rightarrow \infty$, the IF on $(-\tau, 0)$ is divided into 3 bins, the map has period 4, and the resulting solution of the DDE has period close to 4τ. The mapping of the plateaus in a cyclic manner is indicated by the slanted arrow.

A binary signal can be encoded into the IF by assigning a binary number to each of the l values, in a ranked fashion with the lowest binary number corresponding to the lowest of the l values as indicated in Fig.5.3b. The number of bits for each value is m. Fig.5.4a gives a solution of MG with the same parameters as in Fig.5.4b, but $\tau = 300$, and thus $R = 30$.

This solution has period $T \approx 4\tau$. While this ($n = 3, l = 4$) isomer is more rounded, the mean values of the four kinds of plateaus still follow Eq.3.33(see Fig.5.4b). The coding for peak and valley levels is indicated on the solution. To minimize the transients, the values of the plateaus in the IF were chosen from the map in Fig.5.3a.

For $\tau = 300$ (i.e. $R = 30$) and $a = 0.1365$, a solution with more than three bins is not stable. The bins merge and the solution converges to the fundamental in Fig.5.3b. If we increase a however, solutions up to seven bins can be stored (see Fig.3.4). This implies that only four modes are independent (ω_1, ω_3, ω_5, and ω_7) as discussed in Sect.3.4. The number of unstable modes, obtained from the linear stability analysis for a bifurcation parameter a, at which the fundamental solution is a perfect square-wave, is a measure of the number of bins or "memory buffers" that can be used. This connection between the unstable modes and the memory buffers has not been mentioned in earlier studies [8, 11]. The maximum storage capacity is achieved when the initial function has the maximum number of plateaus that can evolve without merging; it is given by $l^{n_{max}}$ ($n_{max} = 7$ in this case). For example, if the number of plateaus is $l = 4$, this number is 4^7.

5.4 Mackey an der Heiden model of recurrent inhibition

The Mackey-an der Heiden [5] model (MH) has been proposed to study the dynamics of the hippocampal circuit formed by the presynaptic mossy fibres, which are excitatory to the postsynaptic CA3 pyramidal cells, and the basket cell interneurons. The interneurons are activated by axon collaterals from the postsynaptic cells and, in turn, produce inhibitory inputs to the postsynaptic cells. The nonlinearities of transmitter-receptor interaction and the delays yield a DDE model for the total inhibitory potential $i(t)$ at the postsynaptic

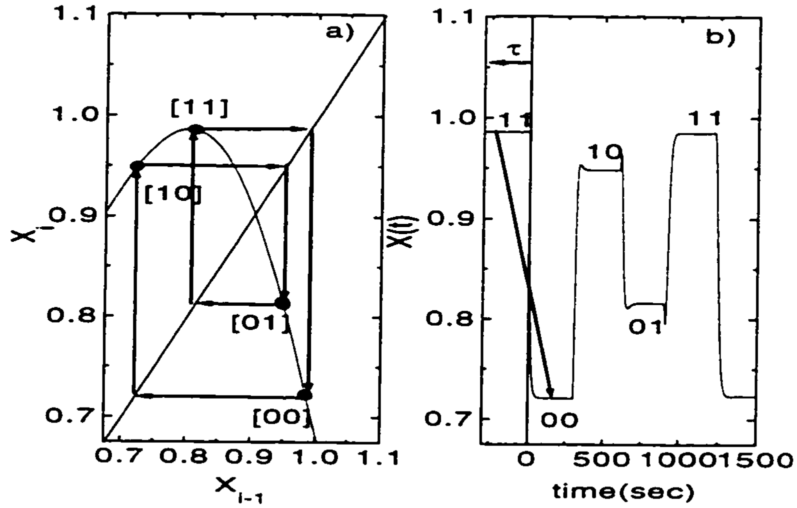

Figure 5.3: Coding with period-4 orbit in Mackey-Glass DDE for $a = 0.1365$, which has only one multistable solution, the third harmonic (see Fig.3.4). a) Discrete-time map $x_i = b^{-1}F(x_{i-1})$ obtained by letting $R \to \infty$ and discretizing the time in units of τ in Eq.3.4. The map has period-4 orbit (shown on the map), cycling through the values: [11], [00], [10], [01]. b) Period-4 oscillation waveform for $\tau = 300$, solution of the DDE (Eq.3.4) for a constant initial function.

"average" neuron:

$$\frac{di(t)}{dt} = -\gamma i(t) + F(i(t-\tau)) = -\gamma i(t) + \beta \frac{f(t-\tau)}{1 + f^3(t-\tau)} \tag{5.2}$$

$\gamma = 0.1$ is the decay rate of the IPSP (i.e. the reciprocal of the response time), and $\beta = 0.6\ 10^{-3}T$ where T is the average number of inhibitory receptors per CA3 cell. This model was modified slightly by replacing the unbounded linear firing function in [5] by a sigmoidal firing function. In the first case, the neuron fires if $e(t) - i(t) > 1mV$, and the firing function f is linear for $e(t) - i(t) > 1mV$. $e(t)$ is the total excitatory bias to the potential; it is chosen as $e(t) = e = 1.6mV$. In our case the firing function is instead given by

$$f(t) = \frac{H}{(1 + e^{-\alpha(e(t) - i(t) - 1)})} \tag{5.3}$$

The steepness of the firing function with $\alpha = 5$ gives reasonable results for the inhibitory potential current in comparison with the linear firing function; in fact, for parameters equiv-

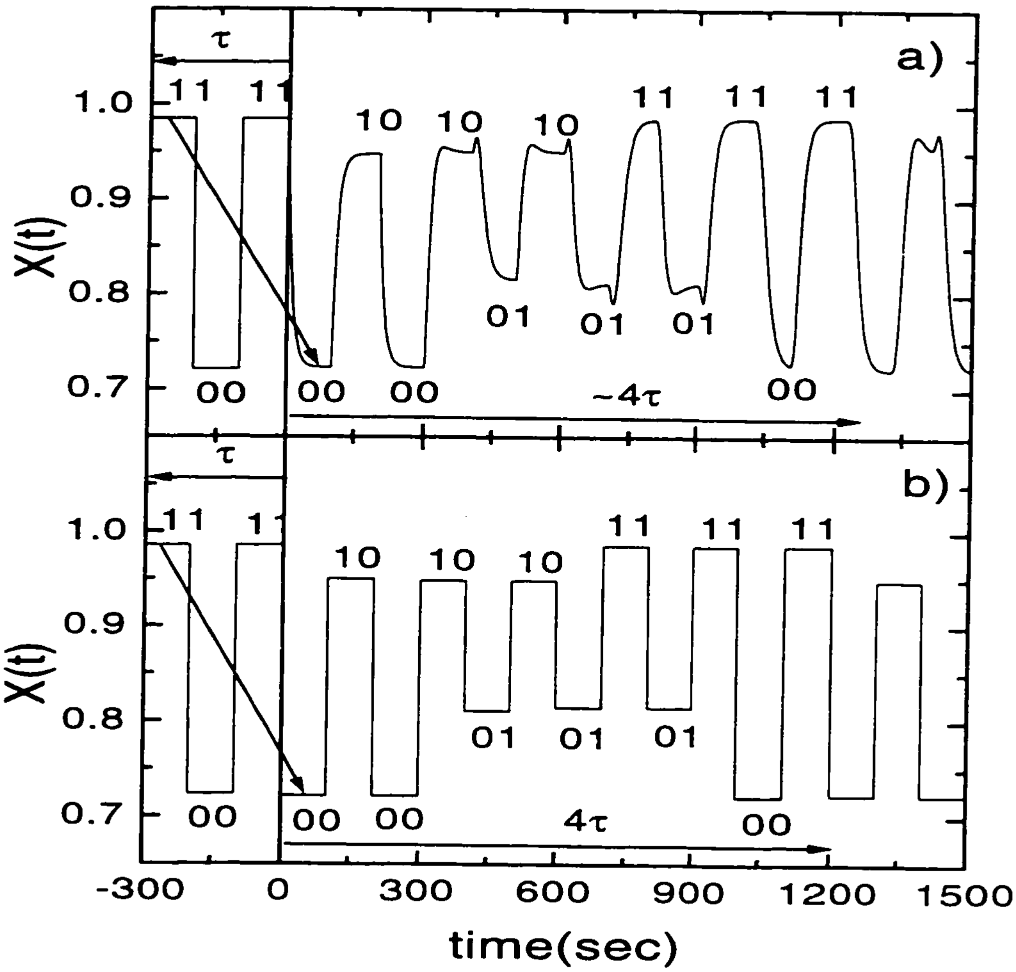

Figure 5.4: Isomers of the Mackey-Glass equation and their encoding for $a = 0.1365$. The initial function on $(-\tau, 0)$ is chosen to be piecewise constant, with each constant being equal to one of the four values in Fig.5.3. a) Isomer ($n = 3, l = 4$), resulting from storing the sequence [11,00,11] within a delay $\tau = 300$ into the solution of the DDE (Eq.3.4). This is the only solution which coexists with the fundamental for $a = 0.1365$ (see Fig.3.4). Isomers with $n > 3$ will merge and the solution will converge to the fundamental. b) Same as in (a) but for the CTDE (Eq.3.33).

alent to those used by MH, it more readily yields solutions with well-defined plateaus at large delays. Period-doubling bifurcations, chaos, and periodic windows with period $3\tau, 5\tau, 7\tau, \cdots$ are similarly observed as H and T vary, as in the original paper with the linear unbounded firing function. The importance of using the sigmoidal firing function is that in the limit $\alpha \to \infty$, this function reduces to the step function with values 0 and H. The latter has been widely used in discrete networks. Also, saturation of the firing rate is more physiologically plausible. We have investigated this model in the case where R is large, in order to gain insight on how multistability can arise in recurrent inhibition models for lower R.

Figure 5.5a shows the voltage and spike patterns for the period 3 oscillation with constant IF (i.e. it is a ($n = 1, l = 3$) isomer), for $H = 4.2$, $T = 1900$ and $\tau = 300$ ($R = 30$). Clear plateaus are observed, indicating that this DDE can also be approximated by a map, and thus that its solutions are encodable. The spikes are obtained from the values given by the firing function when the voltage threshold $(e - i(t))_{th} = 1mV$ is crossed. The isomer ($n = 3, l = 3$) in Fig.5.5b can be observed by injecting the IF shown, formed of 3 bins with two plateau values chosen among the three found in the solution in Fig.5.5a (for clarity we have not shown the transients, and plotted the periodic solution directly after the IF). We note that the interpretation of the IF in this context is that it represents the temporal pattern of spikes propagating around the loop at time zero.

5.5 Plant's model of recurrent inhibition or excitation

Plant's model of RI and RE [4] is based on the Fitzhugh-Nagumo equations, a two-dimensional approximation of the Hodgkin-Huxley model of nerve firing [12]. The model simulates recurrent inhibition or excitation between two populations of cells. The membrane voltage $v(t)$ of an average excitatory cell is governed by

$$\frac{dv(t)}{dt} = v(t) - \frac{1}{3}v^3(t) - w(t) + \mu[v(t-\tau) - v_0],$$

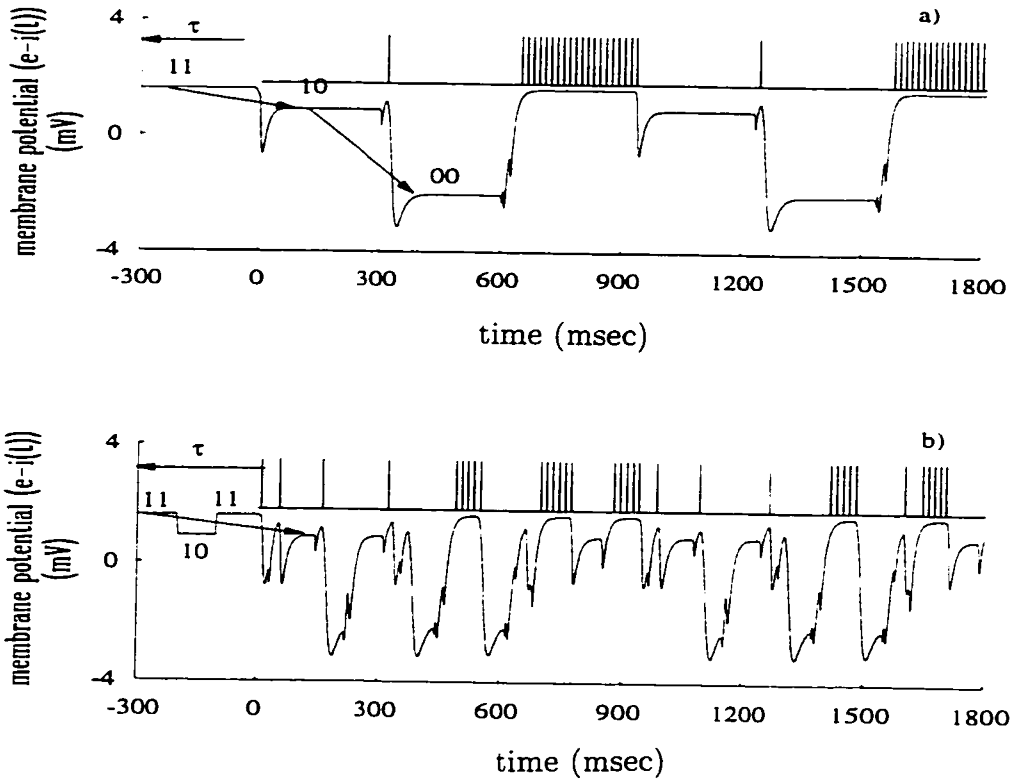

Figure 5.5: Storing information in the temporal pattern of voltage and spiking activity in the Mackey-an der Heiden model (Eq.5.2) with period 3τ for $\tau = 300$ and $\gamma = 0.1$. a) Membrane potential versus time, and its associated spike train. This is an $(n = 1, l = 3)$ isomer. b) An $(n = 3, l = 3)$ isomer and its spike train, resulting from storing the sequence [11,10,11] into the solution in (a). The spikes are generated each time the membrane voltage $e - i(t)$ crosses the threshold of 1mV.

$$\frac{dw(t)}{dt} = \rho[v(t) + a - bw(t)], \tag{5.4}$$

where $a = 0.7$, $b = 0.8$ and $\rho = 0.08$ [4]; μ is the feedback control parameter, τ is the synaptic delay, and w is the recovery variable. This model has a refractory period T_r which depends non-trivially on the equation parameters: spikes must be at least one T_r apart. Periodic spiking solutions are obtained for both excitatory ($\mu = +0.1$) and inhibitory ($\mu = -0.1$) feedback. Increasing the delay increases the interval between spikes. The basic dynamics are bistable if only constant-valued IF's are considered. Some constants lead to the stable fixed point, while others lead to coexisting spiking periodic solutions.

We find that many isomers can be generated using special IF's. Here, in fact, any solution consists only of spikes and plateaus between the spikes. The spikes used in the IF's can be real spikes obtained from the solution when the transients have died out, as shown in Fig.5.6, or piecewise constant spikes, as shown in Fig.5.7. In the latter case, the spikes propagate independently without merging if they are at least $4ms$ in duration and separated by at least $32ms$ for the excitatory case with $\mu = 0.1$. For the inhibitory case with $\mu = -0.1$, the corresponding values are larger than for the excitatory case by an amount $\delta = 15ms$, due to the "rebound" (see Sect.5.2). These values are $18ms(\approx 4 + \delta)$ and $45ms(\approx 32 + \delta)$.

In the case of real spikes, the minimum size of a bin must be equal to $T_r + \delta$ ($\delta = 0$ for excitatory feedback). A bit (1) is assigned to a bin containing a spike, otherwise it is assigned (0). The number of different IF's is thus $2^{[\tau/(T_r+\delta)]}$, where $[\tau/(T_r + \delta)]$ stands for the integer part of $\tau/(T_r + \delta)$. This represents the number of different memory states, each of which propagates into its specific periodic function. Figure 5.6a and b shows the coding of the signals [10101] and [10110] into a "spiking" isomer ($n = \tau/(T_r + \delta), l = 2$) with respectively $\mu = -0.1$ and $\mu = 0.1$. We obtain similar solutions if we use piecewise constant spikes as in Fig.5.7.

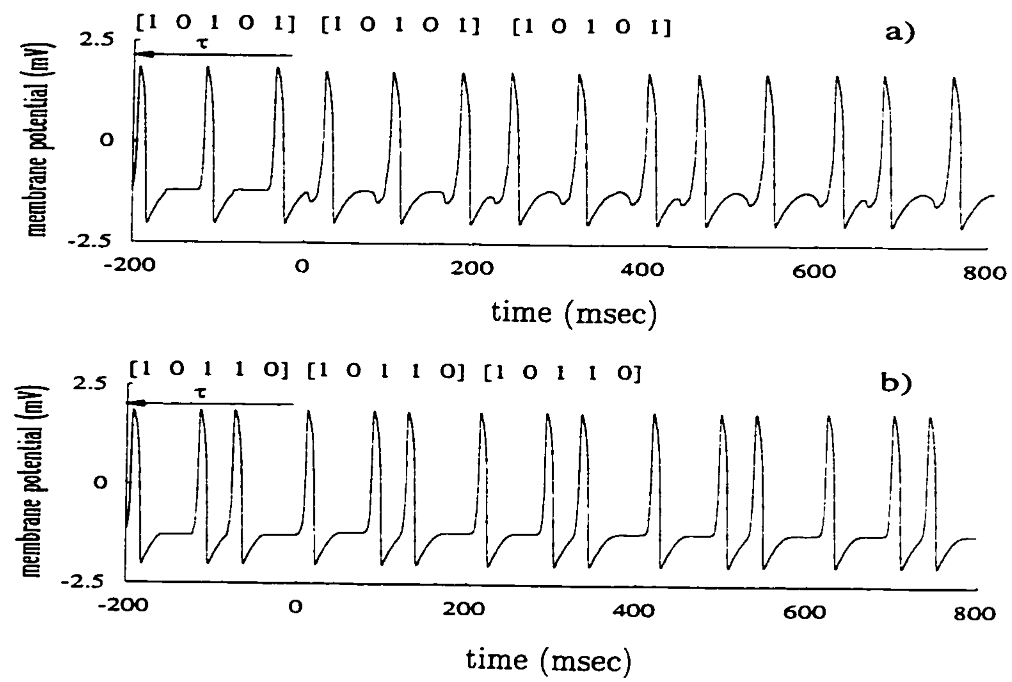

Figure 5.6: Coding with spikes (τ = 200) using Plant's model (Eq.5.4) with three spikes per delay in the initial function. The spikes are $40ms$ in duration, including the refractory period T_r and the time δ for a rebound to occur after release of inhibition. Since δ is zero for the excitatory case, the duration of the spikes in (b) including the refractory period, can be less than $40ms$. The values of the plateaus between the spikes correspond to the resting potential $v_0 = -1.19$. a) Coding with spikes in recurrent inhibition ($\mu = -0.1$), using the IF [1 0 1 0 1]. The spikes are separated by $40ms$. b) Coding with spikes in recurrent excitation ($\mu = +0.1$), using the initial function [1 0 1 1 0]. The first two spikes are separated by $40ms$ and the last two by $0ms$. The refractory period T_r has already been included in the duration of the spikes. For example, the last two spikes in (b) are in reality separated by T_r.

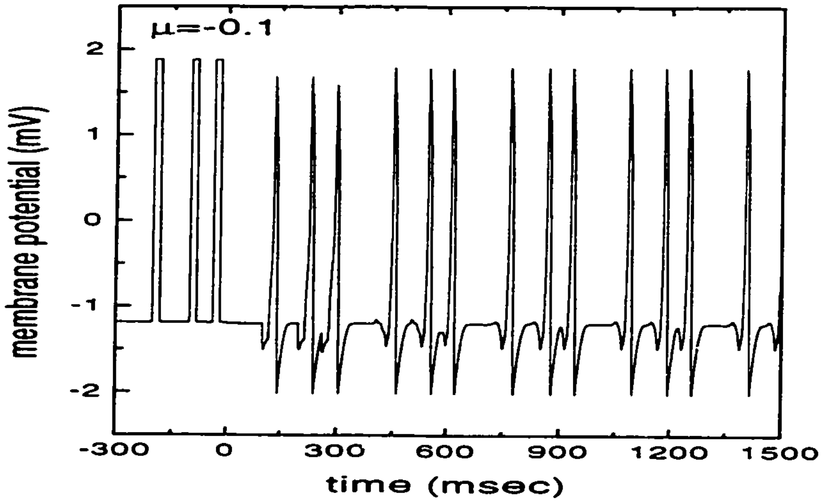

Figure 5.7: Similar results as in Fig.5.6 can be obtained when coding with piecewise constant initial conditions for $\tau = 300$ and $\mu = -0.1$ in Plant's model (Eq.5.4). The spikes in the initial function on $(-\tau, 0)$ are 18 ms in duration. The first two spikes are separated by $80ms$ and the last two by $45ms$.

5.6 Hodgkin-Huxley model of recurrent inhibition or excitation

This model is a four-dimensional system of ordinary differential equations [12] that describes the three main currents underlying the action potential in the squid axon. The fast inward sodium current (V_{Na}) is the current responsible for generating the upstroke of an action potential, while the potassium current (V_K) repolarizes the membrane. The leakage current (V_L) is much smaller than the two other currents. We modified this model by adding a negative feedback current $\mu V(t-\tau)$ [13]:

$$\begin{aligned} C\frac{dV(t)}{dt} &= -g_{Na}m^3h(V - V_{Na}) - g_K n^4(V - V_K) \\ &\quad -g_L(V - V_L) - \mu V(t-\tau) + I_0, \\ \frac{dm(t)}{dt} &= \alpha_m(V)(1-m) - \beta_m(V)m, \end{aligned}$$

$$\frac{dn(t)}{dt} = \alpha_n(V)(1-n) - \beta_n(V)n, \tag{5.5}$$
$$\frac{dh(t)}{dt} = \alpha_h(V)(1-h) - \beta_h(V)h,$$

where $g_{Na} = 120mScm^{-2}, g_K = 36mScm^{-2}, g_L = 0.3mScm^{-2}, V_{Na} = -115mV. V_K = 12mV, V_L = -10.613mV$, and $C = 1\mu Fcm^{-2}$. The voltage-dependent rate constants are given by [12]:

$$\begin{aligned}
\alpha_m &= \frac{0.1(V+25)}{e^{0.1(V+25)}-1} \\
\beta_m &= 4e^{V/18} \\
\alpha_n &= \frac{0.01(V+10)}{e^{0.1(V+10)}-1} \\
\beta_n &= 0.125e^{V/80} \\
\alpha_h &= 0.07e^{V/20} \\
\beta_h &= \frac{1}{e^{0.1(V+30)}+1}
\end{aligned} \tag{5.6}$$

We have taken the original sign convention of Hodgkin and Huxley [12], in which an action potential is a negative spike. Thus a negative (positive) μ corresponds to recurrent excitation (inhibition). In Eq.5.5, the action potential and the postsynaptic potentials are replicas of one another, as in [4, 89]. Figure 5.8 shows the effect of changing the initial function for Eq.5.5 when $I_0 = 0$ (excitable regime). Qualitatively different solutions occur as the IF is varied. These solutions can be seen to be formed from repeating identical segments of length τ. Provided that the IF satisfies the condition given in Section 5.2, there is a 1:1 correspondence between the IF and the solution of Eq.5.5. If the spikes in the IF are sufficiently separated, they will propagate without merging. However, if two spikes are too close, their relative separation can change, or merging can occur after which a stable pattern is obtained.

For the excitatory case, spikes propagate independently if separated by $11.6ms$ for $\mu = -0.1$ or by $7.5ms$ for $\mu = -0.2$. In the inhibitory case, the corresponding values are $17ms$ for

$\mu = 0.1$ and $4.5ms$ for $\mu = 0.2$. These values are governed by the phase resetting properties of Eq.5.5 as a function of amplitude and duration of the IPSP's. When $\mu = 0.2$, there is not necessarly a one-to-one mapping between spike positions from one delay to the next (see Fig. 5.8c). This behavior at higher μ values is expected in the Plant model as well. Many different asymptotic patterns are then possible, depending on the number and position of the initial spikes in the loop. It would be interesting to investigate the details of this dependence in future work.

5.7 Conclusion

We have shown that the multistability, which arises from taking delays into account in the dynamics of simple neural feedback circuits, can be used to store information contained in finite bit strings. The storage capacity increases with the ratio of loop delay to response time of the cell (i.e. to the membrane time constant). The result applies to both non-spiking neurons (i.e. whose response is an analog instantaneous firing frequency) and spiking neurons. Preliminary results suggest that our approach can be extended to the more realistic case of distributions of delays rather than single fixed delays.

From a neurobiological viewpoint, the possibility of storing finite bit strings is perhaps secondary in importance compared to the realization that multistability exists in the first place. One then expects that such recurrent circuits, when time delays are important, can generate a variety of patterns depending on their initial conditions and on the perturbations which they receive.

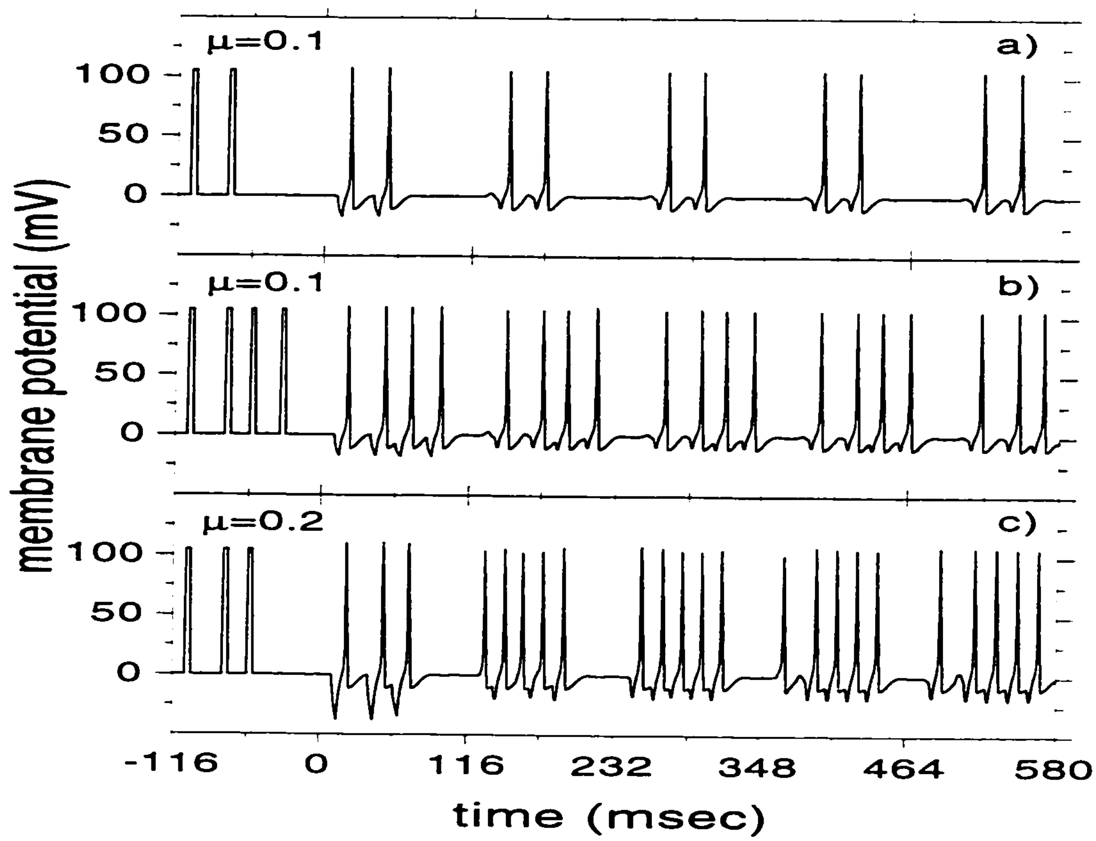

Figure 5.8: Three spike train patterns generated by Eq.5.5 for three choices of IF (left hand side) when $I_0 = 0$ (excitable regime) and $\tau = 116msec$. The spikes in the initial function on $(-\tau, 0)$ are $4msec$ in duration. The first two spikes in (a), (b), and (c) are separated by $25ms$, the middle two in (b) and (c) by $17ms$ and the last two in (b) by $20ms$. For $\mu = 0.2$ in (c), two other extra spikes are added to the solution. The initial conditions for all variables (including $V(0)$ between the spikes) correspond to the fixed point when $\mu = 0$.

Chapter 6

Storing information in unstable limit cycles

6.1 Introduction

The dynamics of delay-differential equations (DDE's) such as the Mackey-Glass or the Ikeda equations [1, 2] become chaotic when e.g. the strength of the feedback and/or the delay are increased [7, 60]. The exponential divergence of trajectories does not allow the memory storage strategy discussed in Chapter 5 to work in the chaotic regime. The memory of a constant initial function is lost in the chaotic evolution, as shown in Fig.6.1a for the Mackey-Glass equation, but multistability still exists at large delay (see Sect.3.4). In the chaotic regime, an infinite number of unstable periodic orbits (UPO's) coexist with one or more chaotic attractors [8, 58, 60, 99]. These periodic solutions are not visible for typical initial conditions, although chaotic trajectories can spend time near them before being repelled away.

In this Chapter, we show that UPO's of the Mackey-Glass DDE [2] can be observed using a recently proposed chaos-control technique [17], and more importantly, that memory storage is also possible in these controlled waveforms [62]. This chaos-control technique has previously been applied to DDE's that describe cortical activity in a network of excitatory and inhibitory neurons [25]. However, the delay used wasn't large enough to warrant the study of memory storage. It is possible that some multistability with respect to initial functions, as discussed in this Section, may be present in that model.

We find that the chaotic regime allows for an enhanced versatility of memory storage since, for fixed parameters in the uncontrolled system, UPO's of different periods can be controlled by tuning one control parameter. Further, we present a theoretical analysis of the controllability of the UPO's in such infinite-dimensional dynamical systems using a low-dimensional discrete-time map. This map arises in the singular limit of the DDE in which the delay to response time ratio R goes to infinity (see Sect.3.6). The controllability is found to be predictable by the Lyapunov exponents and other characteristics of this map.

The large number of UPO's and the sensitivity to small perturbations endow chaotic systems with a flexibility to produce different patterns using minimal perturbations and without changing system parameters [101]. Our method benefits from this flexibility.

The control of UPO's in other high-dimensional systems such as partial differential equations [100] has been reported. There have also been recent studies of chaos-control in the context of message encryption and transmission, as in seminal papers [102, 21] where this is achieved using the synchronization of chaotic systems. Also, Hayes *et al.* [103] have shown that the oscillations of a chaotic system can be made to follow, using small perturbations, a desired sequence of symbols, thus encoding an arbitrary long message into a waveform. It was further experimentally demonstrated in [104] that this encoding technique can be used for digital communication, where a message is encoded and then transmitted using a nonlinear chaotic oscillator.

In contrast to that of Hayes *et al.* [103], our method involves the storage of finite messages. However, it relies on multistability, rather than on the system's symbolic dynamics which preclude certain symbol sequences. Consequently, in our method, messages are directly encodable without the necessity of a "grammar" as in [103]. Furthermore, our method can also be used for analog as well as digital secure communication, where a message is encoded on a controlled UPO, masked by or modulated with a chaotic signal, and then transmitted, as we will see in Chapter 8.

This Chapter is organized as follows: In Section 6.2, we describe the method of controlling unstable periodic orbits for the Mackey-Glass DDE and its corresponding CTDE equations. In Section 6.3, we show how to store finite messages using piecewise constant initial functions. In Section 6.4, we study the stability of UPO's in the Mackey-Glass DDE, using the dispersion and the Lyapunov exponents of the map obtained in the singular perturbation limit. In Section 6.5, we present and discuss the spectral properties of the dispersion in a neural network model described by DDE's. Finally, we conclude in Section 6.6.

6.2 Controlling unstable periodic orbits at large delays

Our study focusses on numerical simulations of the Mackey-Glass equation (Eq.3.4). With parameters (constant throughout our study) $a = 0.145, b = 0.1, c = 10$, Eq.3.4 exhibits aperiodic behavior when the delay time $\tau > 42$ (see Fig.6.1a). Although we have not analyzed this motion in detail using e.g. dimension or Lyapunov spectrum calculations (see Chap.4), this aperiodicity is consistent with earlier reports of deterministic chaos in this parameter range [2, 7, 1]; the behavior is thus assumed here to be chaotic. The multistability of this DDE is easily characterized (see e.g. [11]) when 1) the parameters yield a stable periodic solution (e.g. for $a < a_\infty = 0.138$) and 2) the feedback delay τ is much greater than the system response time $t_r = b^{-1}$ (see Sect.5.3). The initial functions of interest here are piecewise constant, each constant corresponding to a binary number in a code. Unstable periodic orbits in Eq.3.4 are controlled using a delayed negative feedback of the form $D(t) \equiv K\,[x(t-T) - x(t)]$ following the method of [17] for ordinary differential equations.

T is the period of the selected UPO and K is the control parameter. The dynamics then become

$$\frac{dx(t)}{dt} = -bx(t) + F(x(t-\tau)) + K\left[x(t-T) - x(t)\right], \tag{6.1}$$

where $F(x(t)) = ax(t)/(1 + x(t)^c)$. For a piecewise constant initial function, the plateaus in the solution of Eq.6.1 (see Fig.6.1b) cycle through values approximately given by the orbits of the difference equation obtained in the singular limit ($R \to \infty$) of Eq.6.1 (see Sect.3.6):

$$x(t) = (b + K)^{-1}[F(x(t-\tau)) + Kx(t-T)]. \tag{6.2}$$

Note that this is a continuous-time difference equation like Eq.3.33. Figure 6.2a illustrates this stable periodic orbit on the discrete-time map associated with Eq.3.4, to avoid the three-dimensional representation using the variables $x(t)$, $x(t-\tau)$ and $x(t-T)$ from Eq.6.2. The period-4 orbit in Fig.6.2a is unstable without the second delayed feedback, since without this term the dynamics are chaotic with $a = 0.145$.

Figure 6.2b shows the solution of Eq.6.2 corresponding to the "stabilized" period-4 orbit in Fig.6.2a. The perturbation $D(t) \equiv K[x(t-T) - x(t)]$ is small when the trajectory lies close to an UPO of the uncontrolled system. We focus here on these UPO's rather than on new orbits created by the control. This second delayed feedback can be switched on at any time; control occurs after transients have died out.

We have found that a plot of the limit cycle amplitude versus τ for Eq.6.1 can be used to estimate the maximum number of plateaus, in one delay τ, which can evolve in time without merging. This is another way of estimating the number of multistable solutions, discussed in Sect.3.4, for controlled systems. For the parameters chosen, a Hopf bifurcation occurs at $\tau = 11.2$, and for $\tau > \tau_c \approx 43$ this amplitude saturates, as shown in Fig.6.3. τ_c, which is defined as 95% of the maximum amplitude of the limit cycle, can be seen as the minimum delay needed to distinguish two plateaus, since for that delay, the limit cycle has two clearly defined plateaus. The approximate number of plateaus is found to be $\tau/\tau_c \approx 7$

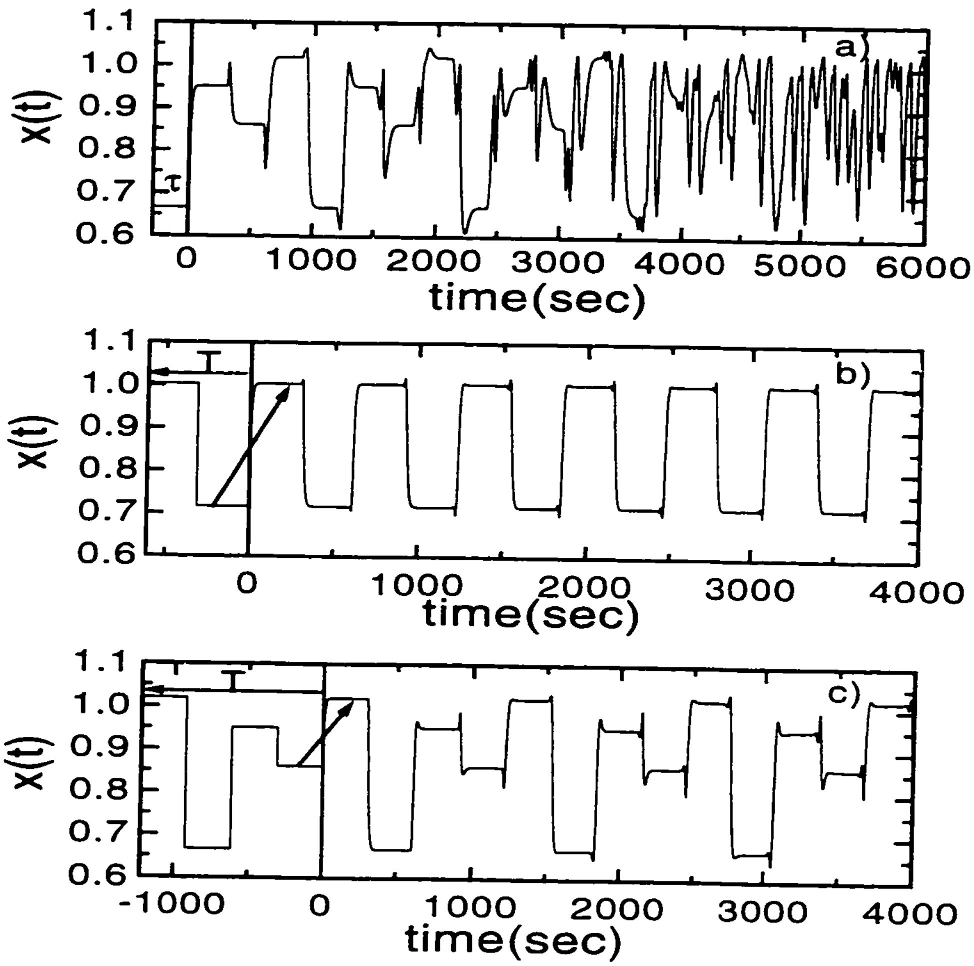

Figure 6.1: Numerical solutions of Eq.3.4 for a ratio of delay to system response time $R = 30$. Other parameters are $\tau = 300$, $a = 0.145$, $b = 0.1$ and $c = 10$. a) Chaotic regime. The constant initial function on $(-\tau, 0)$ evolves into a solution whose plateaus shrink and finally disappear, leaving no trace of this initial condition. b) A second feedback term with delay T (see. Eq.6.1) is used to stabilize the unstable periodic orbit P_2 (see text). The initial function is a constant on $(-T, 0)$. The solution oscillates between two values determined by Eq.6.2, and reflects the value of the initial function. The control parameters are $K = 0.05$ and $T = 616.4$. c) Same as in (b) but $T = 1225.4$. This allows the control of the unstable periodic orbit P_4 which cycles between four values determined by Eq.6.2.

since $\tau = 300$ in our study. This holds over the wide range of K values for which this limit cycle can be controlled (without control, the first period-doubling occurs at $\tau = 28.1$). If an initial function with more than seven plateaus is used, the transition time between plateaus becomes comparable with the width of one plateau, and merging occurs. This result agrees with the multistability discussed in Sect.3.4, for which harmonic solutions with $n > 7$ are not stable and merge for $\tau = 300$.

We showed in Sect.3.4 that multistability exists between stable periodic solutions, stable chaotic solutions or both, and depends on the feedback parameter a (see Fig.3.4). For $a \geq 0.149$, the multistable solutions are unstable and are not visible to a particular initial function. If the control in Eq.6.1 is applied however, these solutions become stable and coexist for the same value of the parameter a, as shown in Fig.6.4 for $a = 0.15$. The initial condition in the interval $-T < t < 0$ is split into $2n$ equal plateaus (n is an odd integer representing the harmonic order). The values of these plateaus are chosen from the unstable fundamental solution in Fig.6.4a. Small perturbations around these initial values yield the same controlled solution.

A desired UPO can be stabilized by substituting either 1) the fixed point x^*, or 2) $x(t-\tau)$ for $x(t-T)$ in Eq.6.1. The linear stability analysis of the map in the singular limit of Eq.6.1 (see Eq.6.2, or Eq.6.4 below) shows that the fixed point is stable for $K > -[F'(x^*) + b]$ in the first case, and if $K > -[F'(x^*) + b]/2$ in the second. If K is smaller than these values, it is possible to control period-doubled solutions, which have more states and thus are more interesting for memory storage. Our discussion will focus on controlling P_2, the limit cycle arising through a Hopf bifurcation, and P_4, its first period-doubled solution. Here P_N means there are N values of plateaus in the solution, which are approximately given by the N values in a periodic orbit of the map obtained in the singular limit of the DDE. Note that in the singular limit, the Hopf bifurcation becomes the first period-doubling bifurcation of the map [9, 66, 70].

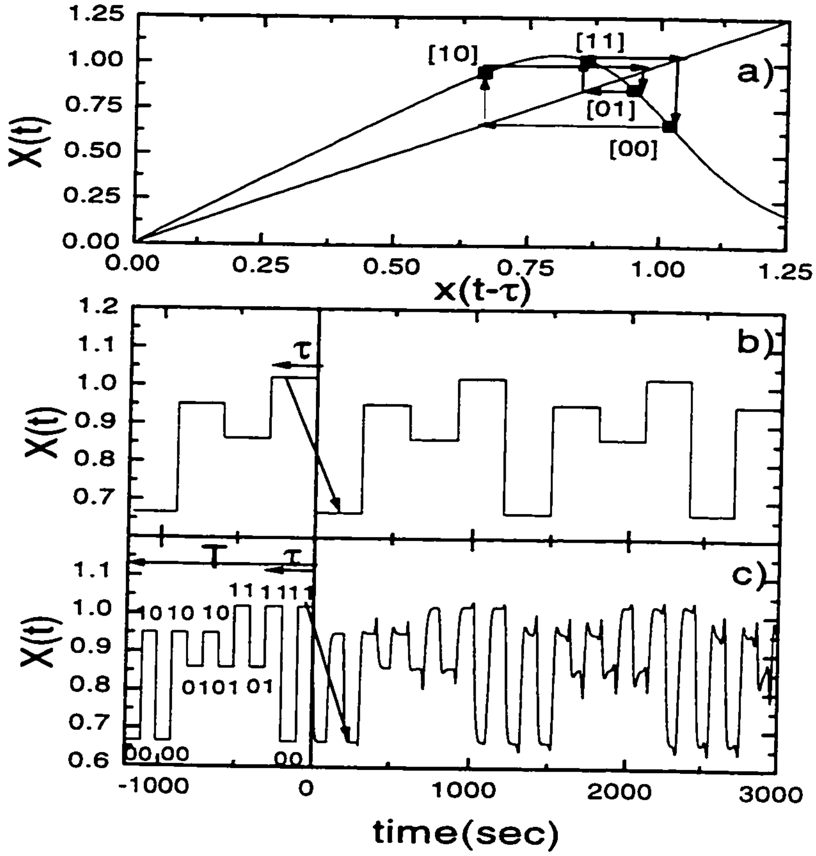

Figure 6.2: Storage of a finite message into the controlled periodic waveform P_4 with $K = 0.05$. a) Discrete-time map $x(i) = b^{-1}F(x(i-1))$ obtained by letting $R \to \infty$ in Eq.6.1 to obtain Eq.6.2, and discretizing time in units of τ. Without control, this map has an unstable period-4 orbit (shown on the map), cycling through [11], [01], [10], [00]. With control ($T = 4\tau = 1200$) this same period-4 orbit, governed by Eq.6.4, is stable. b) Solution of the difference equation Eq.6.2 obtained in the singular limit of Eq.6.1, with $T = 4\tau$. The initial function on $(-T, 0)$ is chosen to be piecewise constant, with constants equal to one of the four values of the controlled period-4 orbit in (a). This periodic waveform has period T. (c) Storing the sequence $[11, 00, 11]$ within a delay τ into the solution of the controlled delay-differential equation (Eq.6.1). The control delay is $T = 1225.4$, which is also the period of the waveform, close to the value of $4\tau = 1200$ in (b). To minimize transients, the plateaus on $(-T, -\tau)$ were chosen such that the perturbation $D(t) = K[x(t-T) - x(t)]$ is close to zero. This is achieved by choosing these plateaus as the three pre-images, dictated by the map in (a), of the message on $(-\tau, 0)$.

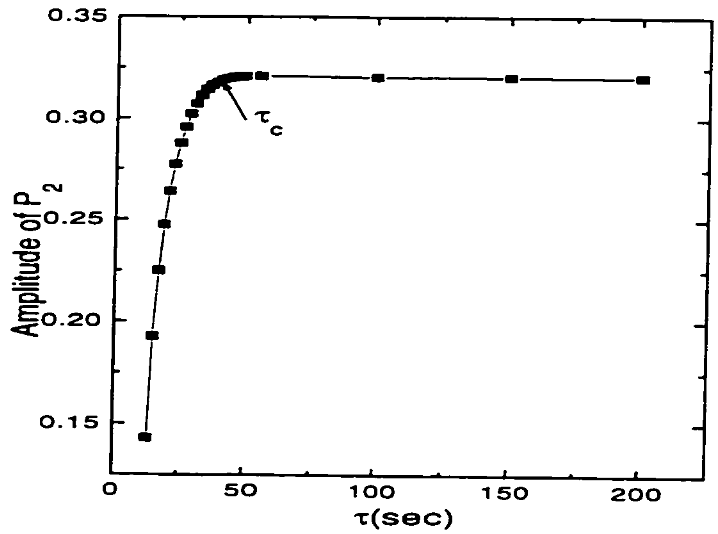

Figure 6.3: Amplitude of the limit cycle of the controlled DDE Eq.6.1 as a function of τ. A Hopf bifurcation occurs at $\tau = 11.2$.

Substituting x^* or $x(t-\tau)$ for $x(t-T)$, one numerically observes a solution with approximately the right period, but the wrong amplitude. This measured period is very close to that of the desired UPO; it can then be used for T in Eq.6.1 to properly control the amplitude of the UPO. For P_2 and P_4, a fine-tuning as in Figs.6.5a and 6.5b will further decrease $D(t)$ until P_2 or P_4 are optimally controlled. The range of parameter K for which an UPO is stable is called *controllability*. For constant R, the controllability of P_4 is much narrower than that for P_2. Higher P_N's are increasingly difficult to control. The resulting controlled P_4 is shown in Fig.6.1c. This method enabled us to also control UPO's in the Ikeda equation (not shown).

6.3 Storing finite messages using piecewise constant initial functions.

We now show how a sequence of binary numbers can be encoded into one of the many possible waveforms of an UPO of a given period. Again, this multistability in Eq.6.1 arises because the delay is large. Following [11] (see also Sect. 5.3), we define a "(n, l) isomer" as a solution with n plateaus in one delay τ, each cycling through the l values of a P_N-type solution. There are l^n different initial functions or "messages" which can be stored. The maximum storage capacity is achieved when the initial function has the maximum number of plateaus that can evolve without merging; it is given by l^{τ/τ_c}. A binary number can be assigned to each of the l values, in a ranked fashion with the lowest binary number corresponding to the lowest of the l values. The number of bits for each value is given by $log_2(l)$. For example, P_4 cycles through four values; thus, a 2-bit code can be assigned to each of the 4 values: [00], [01], [10], or [11].

The controlled singular limit map obtained by discretizing time in units of τ in Eq.6.1 is given by

$$x(i) = b^{-1}F(x(i-1)) + b^{-1}K[x(i-l) - x(i)] \tag{6.3}$$

which can be rewritten as

$$x(i) = (b+K)^{-1}[F(x(i-1)) + Kx(i-l)]\,. \tag{6.4}$$

For a certain range of K, an orbit of period l can be controlled. As the perturbation $K[x(i-l) - x(i)]$ in Eq.6.3 vanishes when the control is achieved, the orbit cycles between l points on the map $x(i) = b^{-1}F(x(i-1))$. If, for example, $K = 0$, this map is chaotic; however, if $K = 0.05$, a controlled P_4 orbit cycling between four values is obtained, as shown in Fig.6.2a. An $(n = 3, l = 4)$ isomer for the DDE carrying the information [11,00,11] in a solution of period 1225.4 (which is approximately $l\tau = 4\tau = 1200$) is shown in Fig.6.2c. The map in Eq.6.3 accurately predicts the evolution of the mean values of the plateaus for this

DDE. Comparing Fig.6.2c to the singular limit case in Fig.6.2b, one sees small spikes near the transition points, which the control can not eliminate. Nevertheless, this waveform is stable and preserves the memory of the initial function.

6.4 Stability and controllability of orbits

The map Eq.6.4 can also be used to assess the range of K values for which a desired UPO can be controlled. Figure 6.6a plots the dispersion $< |x(t-T)-x(t)| >$ (similar to the dispersion in Fig.6.5) versus K for the DDE and for Eq.6.2, its associated difference equation. For Eq.6.2, this dispersion is zero when control is achieved. Figure 6.6a shows that the difference equation approximation of the DDE is justified, even for $R = 30$, since both dispersions have a similar dependence on K over the range of K where P_4 is controllable.

The Lyapunov exponents for Eq.6.4 can also be used to study the stability of the orbits. This l-dimensional map is first converted into l coupled one-dimensional maps,

$$\begin{aligned} y_0(i) &= \frac{1}{b+K}[F(y_0(i-1)) + K y_1(i-1)] \\ y_j(i) &= y_{j+1}(i-1) \qquad j = 1, 2, ..., l-2 \\ y_{l-1}(i) &= y_0(i-1) \end{aligned} \tag{6.5}$$

The Lyapunov exponents are then calculated using the QR decomposition method [32] in the implementation of [50]. Figures 6.6b and 6.6c show the maximum Lyapunov exponent λ_{max} for, respectively, P_4 and P_2 as a function of K. Comparing the regions where $\lambda_{max} < 0$, we see that P_2 has a larger range of stability than P_4. The K-range for P_4 decreases when a in Eq.6.1 increases until it vanishes for $a > 0.151$ and we are unable to control this orbit (not shown). However if we then increase K, control can be achieved but for a limited time only, as λ_{max} is close to zero. Good agreement is found between the stability domains based on the dispersion $< |x(t-T) - x(t)| >$ and λ_{max}. Figure 6.6 clearly indicates that P_4 is stable only in the range $K \in [0.04, 0.11]$, while P_2 is stable for any value of $K > 0.035$. We will

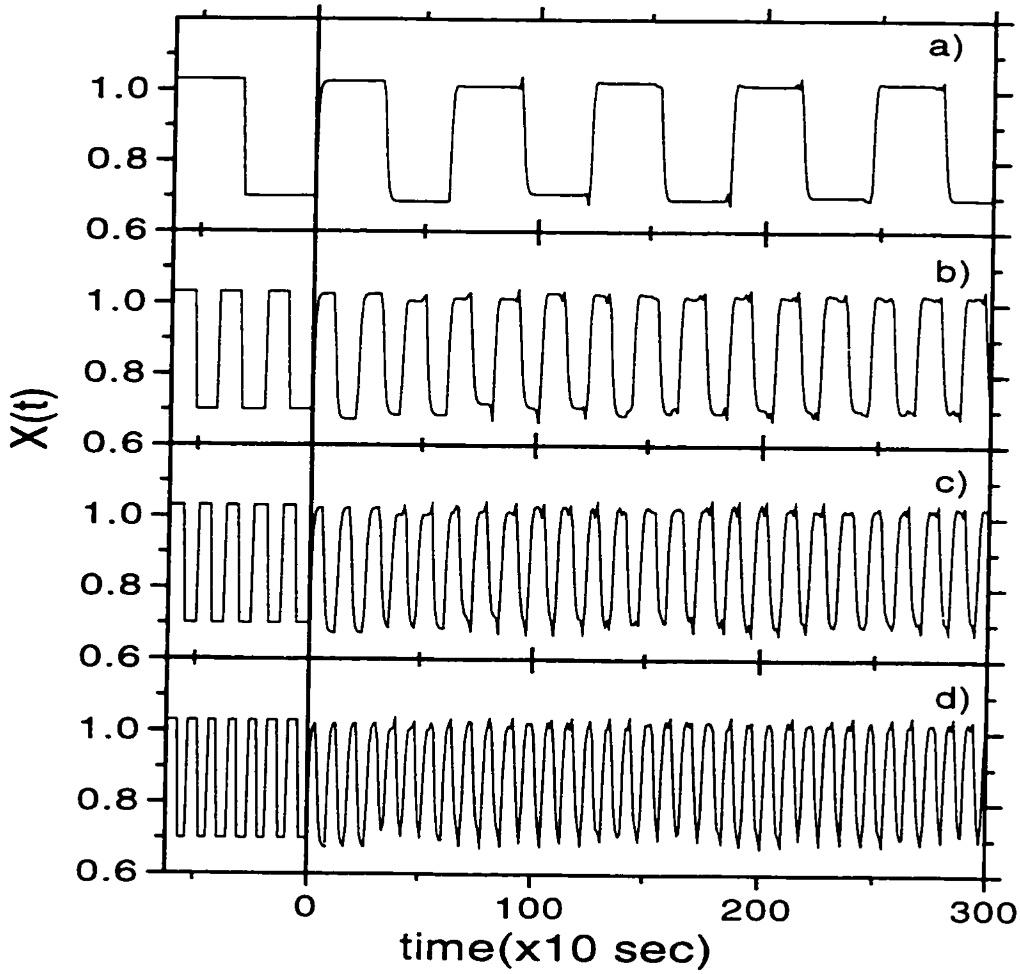

Figure 6.4: Controlling the multistable solutions in Fig.3.5 for $a = 0.15$, $K = 0.05$, using a fourth-order Runge-Kutta integration algorithm with step $\Delta t = 0.01$. The initial condition on $-T < t < 0$ is subdivided into $2n$ plateaus, where n is the harmonic order. The period T in each case is chosen slightly different from the period of the UPO P_2 ($T = 615.9$), for which the perturbation $D(t)$ is almost zero. The reason is that the ratio $T/(n\Delta t)$ should be an integer in order to allow the integration. This procedure doesn't affect our result. a) The controlled P_2 orbit ($T = 615.8$). b) The controlled third harmonic with $T = 615.6$. c) The controlled fifth harmonic with $T = 616.0$. d) The controlled seventh harmonic with $T = 614.6$.

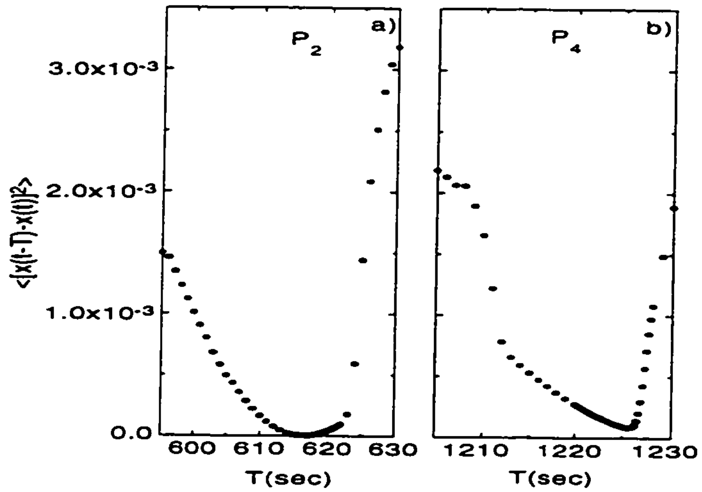

Figure 6.5: Plot of the dependence of the dispersion $< [x(t-T) - x(t)]^2 >$ on the delay T of the second feedback loop in Eq.6.1 with $K = 0.05$ and $\tau = 300$. The quality of the control is inversely proportional to this dispersion. a) P_2 with $T = 616.4$; b) P_4 with $T = 1225.4$.

see in Chapter 7 that the control of higher orbits can be enhanced when using the extended control method proposed by Socolar *et al.* [18]. This method uses many previous states of the system instead of just one as in Eq.6.1.

6.5 Spectral properties of dispersion in neural networks

Recently, Laurenço and Babloyantz [25] used the restricted perturbation proposed by Pyragas [17] (see Eq.6.11 below) to control UPO's in a network that describes cortical activity. They claim that a $15msec$ oscillation is observed in the x dispersion $< [x(t-T) - x(t)]^2 >$ versus T and is related to the major peak in the power spectrum. Our analysis of their control procedure shows that there is a periodic structure in the dispersion with peaks at every $15msec$, but there is no "oscillation". This periodic structure can be understood from the temporal solution of x, in which a fast oscillation of $15msec$ is superimposed on a slow oscil-

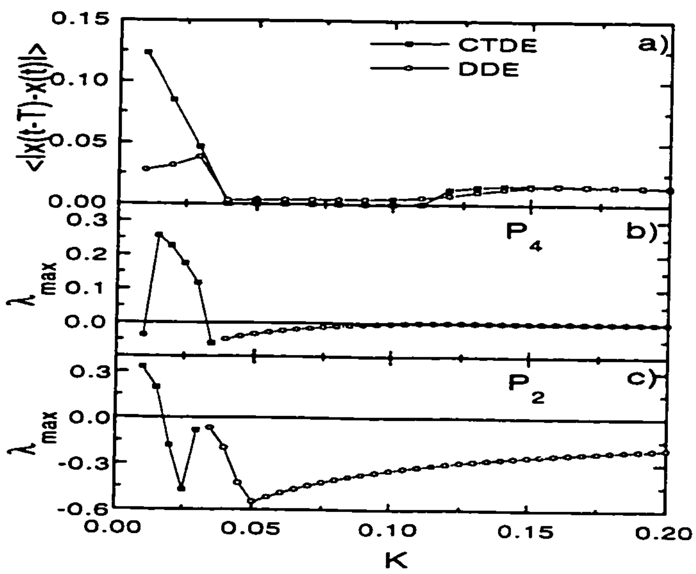

Figure 6.6: Investigating the controllability of UPO's as a function of the control parameter K. a) Dispersion $< |x(t-T) - x(t)| >$ of P_4 for the continuous-time difference equation Eq.6.2 (CTDE) with $T = 1200$ and for the DDE Eq.6.1 with $T = 1225.4$. b) Maximal Lyapunov exponent of the map Eq.6.4 for P_4. c) Same as in (b) but for P_2. The filled squares at low K with $\lambda_{max} < 0$ in (b) and (c) correspond to other orbits of higher period.

lation of 105.3$msec$, as shown in Fig.6.7a, and b. The 15$msec$ oscillation is in fact observed as a sharp peak every 15$msec$ interval when the perturbation is unrestricted (see Fig.6.9a). If the perturbation is restricted as in [25] however, the only peaks that can be observed are those corresponding to the UPO of 105.3$msec$. Further, the unrestricted perturbation also allows us to observe peaks corresponding to fixed points, as shown in Figure 6.9a.

The controlled model of cortical activity is described in terms of DDE's as follows [25]:

$$\begin{aligned}\frac{dx}{dt} &= -\gamma(x - V_L) - (x - E_1)\Omega_1 F_x(x(t-\tau)) - (x - E_2)\Omega_2 F_y(y(t-\tau)) + D_x(t)\,, \\ \frac{dy}{dt} &= -\gamma(y - V_L) - (y - E_1)\Omega_3 F_x(x(t-\tau)) - (y - E_2)\Omega_4 F_y(y(t-\tau)) + D_y(t)\,,\end{aligned} \tag{6.6}$$

where $F_x(x)$ and $F_y(y)$ are the sigmoidal firing functions given by

$$F_x(x) = \frac{1}{1 + e^{-0.09(x+25)}}\,, \quad F_y(y) = \frac{1}{1 + e^{-0.2(y+25)}}\,. \tag{6.7}$$

$D_x(t)$ and $D_y(t)$ are the control terms given by

$$D_x(t) = K[x(t-T) - x(t)]\,, \quad D_y(t) = K[y(t-T) - y(t)]\,. \tag{6.8}$$

The parameter values are the same as in [25], i.e. $\gamma = 0.25msec^{-1}$, $E_1 = 50mV$, $E_2 = -80mV$, $\Omega_1 = 6.3$, $\Omega_2 = \Omega_3 = 5$, $\Omega_4 = 0$, and $\tau = 16msec$.

6.5.1 Linear stability analysis

We examine the behavior near the fixed point $x(t) = x^* + \delta x(t)$ and $y(t) = y^* + \delta y(t)$. By taking solutions of the form $\delta x(t) = e^{st}$ and $\delta y(t) = \beta e^{st}$, we obtain the following characteristic equation:

$$s^2 + as + bse^{-s\tau} + ce^{-s\tau} - de^{-2s\tau} + e = 0\,, \tag{6.9}$$

where

$$a = 2\gamma + (\Omega_1 + \Omega_2)F_x(x^*) + \Omega_2 F_y(y^*)\,,$$

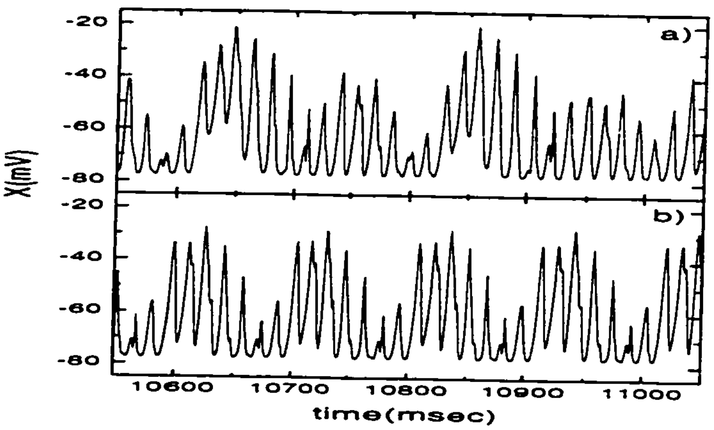

Figure 6.7: Numerical solutions of Eq.6.6 for $\tau = 16msec$, using a fourth-order Runge-Kutta integration algorithm with integration time step 0.01. a) X vs t without control ($K = 0$). b) X vs t with control ($K = 0.275msec^{-1}$ and $T = 105.3msec$), using unrestricted perturbations $D_x(t) = K[x(t-T) - x(t)]$ and $D_y(t) = K[y(t-T) - y(t)]$ in Eq.6.6.

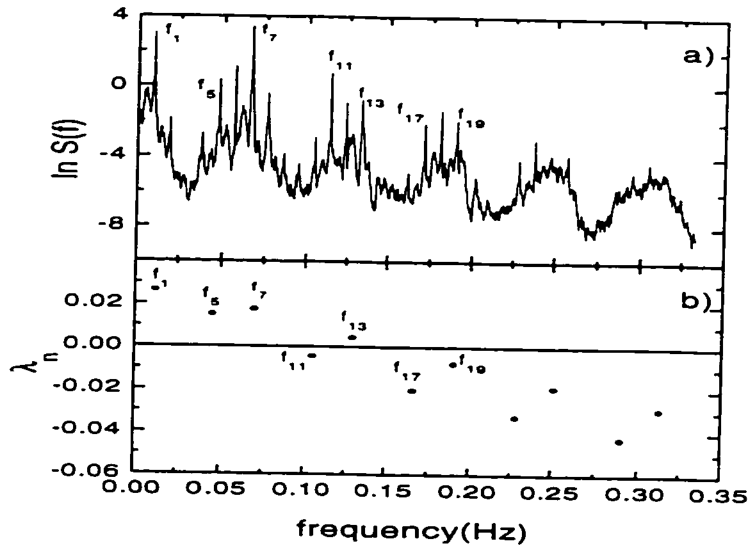

Figure 6.8: Spectral properties of the cortical activity model (Eq.6.6) for $\tau = 16msec$. a) Power spectrum of X obtained from 30 consecutive 8192-point time series with an integration time step of $0.01msec$ and a sampling time of $1.5msec$. Aliasing effects, which are due to resampling the solution with a time step larger than the integration time step, affect the power spectrum only at very high frequencies. b) Real parts vs imaginary parts of the linear modes, solutions of Eq.6.9.

$$
\begin{aligned}
b &= \Omega_1(x^* - E_1)F_x'(x^*)\,, \\
c &= \Omega_1(x^* - E_1)F_x'(x^*)(\gamma + \Omega_2 F_x(x^*))\,, \\
d &= \Omega_2^2(x^* - E_2)(y^* - E_1)F_x'(x^*)F_y'(y^*)\,, \\
e &= [\gamma + \Omega_2 F_x(x^*)][\gamma + \Omega_1 F_x(x^*) + \Omega_2 F_y(y^*)]\,.
\end{aligned}
\tag{6.10}
$$

This equation has an infinite number of complex conjugate roots $s_n = \lambda_n + i2\pi f_n$. We associate, as in Sect.3.3, to each pair of complex conjugate eigenvalues s_n a "mode". These modes can predict the peaks in the power spectrum, as in Chapter 4, even though the delay is small ($\tau = 16msec$ in this case). However, the one-to-one correspondence between the modes and the peaks is not quite exact because the modes do not appear at the same frequencies as the spectral peaks (see Sect.4.3). Figures 6.8a and b show the power spectrum of x for the unperturbed system ($K = 0$ in Eq.6.6), and its corresponding linear modes, solutions of Eq.6.9. The large bumps correspond to the fundamental and harmonics of the fast $15msec$ oscillation in the solution. The power spectrum is composed of the fundamental oscillation P_2 of period $T \approx 105.3msec$, which corresponds to the most unstable mode, and its odd harmonics, which correspond to the other unstable and stable modes. The even modes also show up in the power spectrum for small delay but they cannot be predicted by linear stability analysis (see Fig.6.8). The major peak in the power spectrum (shown as f_7 in Fig.6.8a) is associated with both the seventh harmonic f_7 of the slow oscillation solution of period $105.3msec$, and the fast oscillation solution of period $\approx 15msec$. This peak shows up in the dispersion $< [x(t-T) - x(t)]^2 >$ versus T as a sharp dip at every $15msec$ interval, and thus is not really a $15msec$ oscillation as suggested in [25] (see Fig.6.9). Numerical simulations show that the oscillation of $15msec$ observed in the dispersion by [25], appears only when the perturbations $D_x(t)$ and $D_y(t)$ in Eq.6.8 are restricted (see [17]):

$$
\begin{aligned}
D_x(t) &= -D_0\,, \quad K[x(t-T) - x(t)] \leq -D_0\,, \\
&= K[x(t-T) - x(t)]\,, \quad -D_0 < K[x(t-T) - x(t)] < D_0\,, \\
&= D_0\,, \quad K[x(t-T) - x(t)] \geq D_0\,;
\end{aligned}
\tag{6.11}
$$

$D_y(t)$ is defined similarly. The limitation of the perturbation eliminates the sharp dips in the dispersion that are related to fixed points as well as the major peak in the power spectrum, and introduce an apparent $15msec$ oscillation which is, in fact, a periodic structure that comes from the temporal solution of x as a fast oscillation (see Fig.6.7a, and b).

6.6 Conclusion

We have shown that the multistability of controlled unstable periodic orbits of the Mackey-Glass delay-differential equation at large delay can be exploited to store finite messages into periodic waveforms. Our method is based on the chaotic rather than periodic regime, for which a broader range of waveforms of different shapes and periods can be accessed by tuning the control delay. Our analysis shows that the properties of this high-dimensional dynamical system, and in particular, the controllability of its UPO's (as measured by the maximal Lyapunov exponent and the dispersion), can be predicted by a low-dimensional map obtained in a singular limit of this DDE. Increasing the ratio of delay to response time in the uncontrolled system allows isomers of increasing complexity to be controlled. We have found (not shown) that a moderate-to-high noise level increases the amplitude of the perturbation $D(t)$; this can cause the solution to jump from one basin of attraction to another, and thus degradation of the memory. However, a small amount of noise merely adds a bit of fluctuations on the plateaus, without altering the basic period and message content of the waveform. Finally, we have studied the spectral properties of the dispersion in a cortical oscillation model and have found that while the linear stability analysis can predict most of the peaks in the power spectrum, the dispersion can predict only the highest peaks f_1 and f_7 in Fig.6.8a.

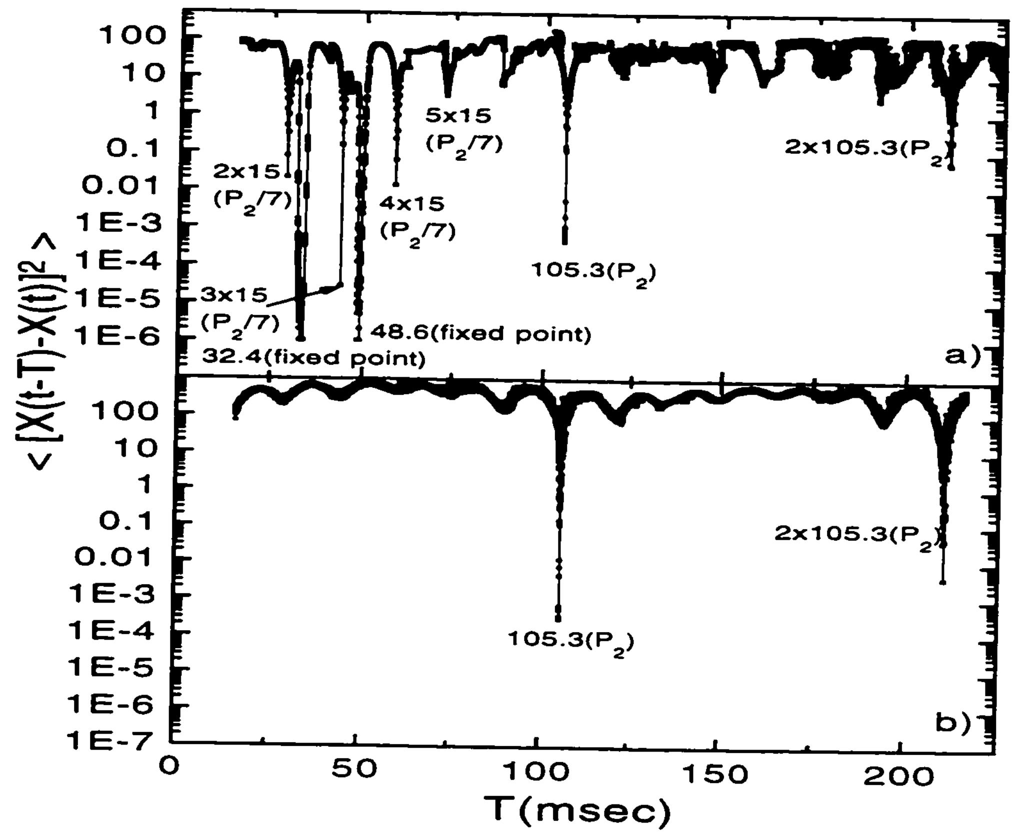

Figure 6.9: Dispersion $< [x(t-T) - x(t)]^2 >$ vs T. a) With the unrestricted perturbations $D_x(t) = K[x(t-T) - x(t)]$ and $D_y(t) = K[y(t-T) - y(t)]$ for $K = 0.275$. The peaks represent the different unstable orbits such as the fixed points, the $15msec$ oscillation, and the fundamental solution P_2 of period $T = 105.3msec$ (shown as f_1 in Fig.6.8a). b) With the restricted perturbations (Eq.6.11) for $K = 0.275$ and $D_0 = 0.3$. There are only peaks corresponding to the fundamental solution of period $T = 105.3msec$.

Chapter 7

Controlling chaos in discrete dynamical systems

7.1 Introduction

Models of excitable cells such as those of Hodgkin-Huxley [12] or FitzHugh-Nagumo [105, 106] can generate complex periodic as well as chaotic patterns of action potentials in the presence of periodic forcing. Such behaviors have also been observed in experimental preparations modeled by such equations [107]. The concepts of chaos-control described in Chapter 6, or more generally, of unstable periodic orbit control, can be applied to such systems to stabilize their responses to more desirable fixed point or periodic patterns. For example, these have been applied to assemblies of heart cells [108] and nerve cells [109, 110] which, the authors claim, were likely to be firing in a chaotic regime. The hope of such efforts is to develop techniques to control disorders such as, e.g., epilepsy or heart arrhythmias.

Models of such cell assemblies usually rest on a simplified description of the single cell dynamics, as compared to Hodgkin-Huxley dynamics. For example, Courtemanche *et al.* couple many Fitzhugh-Nagumo models to simulate cardiac cells in a a two-dimensional geometry [111]. Even in such simplified cases, the simulations can be very long. Single-cell models based on discrete-time maps are then useful, since their use reduces computation time, while keeping many of the essential nonlinearities of the firing dynamics. These have been used for example as the fundamental computational elements of artificial neural networks (see e.g., Nagumo and Sato [19], Aihara *et al.* [20]).

We present here an improved technique of controlling chaos in single maps. It can eventually be applied to problems where many such maps are coupled, such as in the examples mentioned above. Our technique is inspired from our application of the chaos-control method of Pyragas [17] to DDE's described in Chapter 6. It is in fact suggested by consideration of the controlled dynamics in "discrete time" that results from taking the singular perturbation limit $R \to \infty$ of the DDE. As we saw in Chapter 4, that map could be used to explain certain spectral features of the power spectra as well as the attractor dimension of the DDE at large but finite delay. Also in this limit, the study of the "controlled map" yielded information about the stability and controllability of orbits in the DDE, as shown in Sect.6.4.

We illustrate the method by controlling chaos in the Mackey-Glass and the Logistic maps, and in a neural network model known as the Nagumo-Sato model [19] (see also [20]). We also improve our method by using extended control as in [18], i.e. by using feedback from values of the state variable at several times in the past. With this improvement, orbits of even higher periodicity can be stabilized. Our method is found to allow the control of unstable periodic orbits in these maps over larger parameter ranges than those found with existing methods [17, 18, 112].

This Chapter is organized as follows. In Section 7.2, we present the "extended control" method of Socolar *et al.* [18] and apply it to the Mackey-Glass equation. In Section 7.3, we present our improved method of controlling discrete-time maps. In Section 7.4, we show an application of this method to a small chaotic neural network based on the Nagumo-Sato model [19] (see also [20]). The Chapter concludes in Section 7.5.

7.2 Controlling large delay solutions in MG DDE using extended control

The Mackey-Glass equation (Eq.3.1) has one delayed feedback control term. In the absence of other delayed feedback terms, its solutions at large delay is chaotic over a wide range of parameters (see Fig.7.1a). As $R \to \infty$, the continuous-time difference equation (CTDE) (Eq.3.33 or Eq.7.5 below for $r = 0$ and $K = 0$) and the associated discrete-time map (Eq.3.34 or Eq.7.6 below for $r = 0$ and $K = 0$), are also chaotic (see Figs.7.1b, and c). We will show that if a second delayed feedback control is properly applied, and beter still, if an " extended control" (see [113]) is properly applied, the solutions to the DDE, CTDE and map become periodic, as shown in Fig.7.2a, b, and c for a period-4 orbit (the map cycles between four values, and the DDE oscillates between four plateaus connected by abrupt transitions or "boundary layers" in which the derivative is of order R^{-1}).

Higher periodic orbits are found to be difficult to control with only one added delayed feedback term, i.e. the term $D(t) = K[x(t-T) - x(t)]$ discussed in Chap.6 and which depends on only one previous state. To improve the situation, Socolar *et al.* [18] have recently proposed the generalization of the feedback term in Eq.6.1 to many previous states as follows:

$$D(t) = K[(1-r)\sum_{m=1}^{\infty} r^{m-1}x(t-mT) - x(t)] \tag{7.1}$$

which can be rewritten as

$$D(t) = K[x(t-T) - x(t)] + rD(t-T)\,. \tag{7.2}$$

In that equation, $0 \le r < 1$ is an adjustable parameter. The parameter r can be tuned to yield the largest interval of K values over which an UPO is controllable. We have to note here that contrary to Socolar *et al.*'s method [18], our method when combined with the extended control term is much better (see Fig.7.4 for the control of a fixed point).

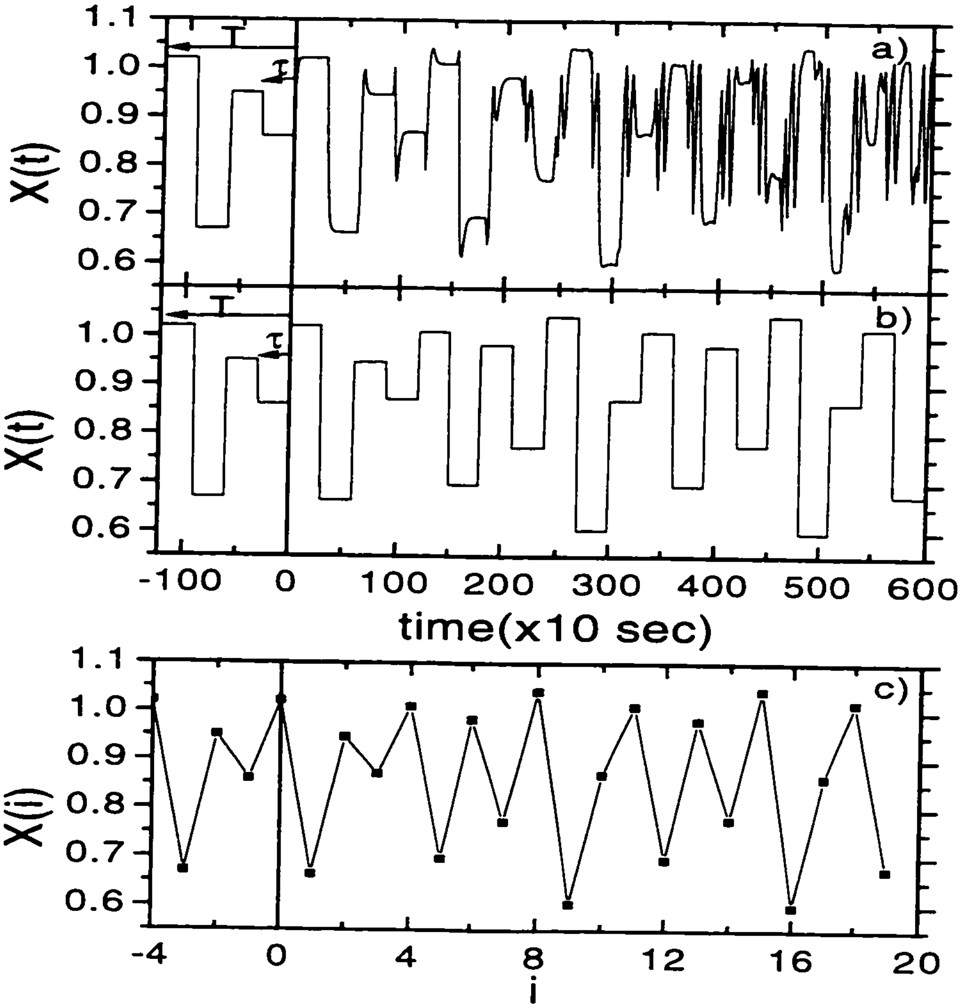

Figure 7.1: Numerical solutions of Eq.3.4 and its corresponding CTDE and map for $a = 0.145$ without control ($K = 0$, $r = 0$) using piecewise constant initial conditions. We used a fourth-order Runge-Kutta integration algorithm with step 0.01 and the scaling property (Eq.3.2). a) Chaotic solution of the DDE (Eq.7.3) for $\tau = 300$ and $T = 1225.6$. b) Chaotic solution of the CTDE ($b\tau \to \infty$) (Eq.7.5) for $\tau = 300$ and $T = 1200$. c) Chaotic solution of the map (Eq.7.6). Note that the solutions in (b) and (c) look periodic because the initial function makes them initially follow and UPO.

The dynamics of the DDE in the presence of extended control thus become:

$$\begin{aligned}\dot{x}(t) &= -bx(t) + F(x(t-\tau)) + D(t) \\ D(t) &= K[x(t-T) - x(t)] + rD(t-T)\end{aligned} \tag{7.3}$$

This system of equations can be solved by specifying the initial function for $x(t)$ and $D(t)$ in the interval $-T < t < 0$. To minimize transients, $x(t)$ is given its average asymptotic values on each plateau predicted by the map (Eq.7.6) and $D(t)$ is given its asymptotic value 0. Figure 7.2 shows the control of the P_4 orbit in the MG DDE (Eq.7.3) for $a = 0.145$ and $\tau = 300$. The interval of controllability, e.g. for $r = 0.8$, is $0.07 \leq K \leq 0.53$, which is larger compared to $0.04 \leq K \leq 0.11$ with $r = 0$ (see Fig.7.6).

Denoting by N_{max} the maximum period of plateau values through which the stabilized UPO can cycle in one period, and by n_{max} the maximum number of plateaus on $(-\tau, 0)$ that can evolve without merging. The latter is associated with the number of the highest harmonic solution that can exist for those values of τ and a (see Sect.6.2). The maximum number of patterns which can be stored in the solutions due to multistability, is $(N_{max})^{n_{max}}$. This is the number of coexisting solutions. Our storage method (see Chap.6) allows us to control and store only one pattern at a time. The possibility of using more than one of the coexisting solutions at a time will be left for future work. We illustrate this notion of storage capacity with an example. For $\tau = 300$, n_{max} is 7. If $r = 0$, N_{max} is 4, but if $r = 0.9$, N_{max} is 8 (see Fig.7.3). The storage capacity is then increased by a factor of 1.5 using extended control. Higher UPO's with $N > 8$ are very difficult to control in the DDE due to the continuity of the solution imposed by the dynamical equations. In the map and CTDE however (see Section below), such solutions can be controlled up to $N = 16$ for $a = 0.145$. More work is needed to develop a control technique that can stabilize UPO's with higher N.

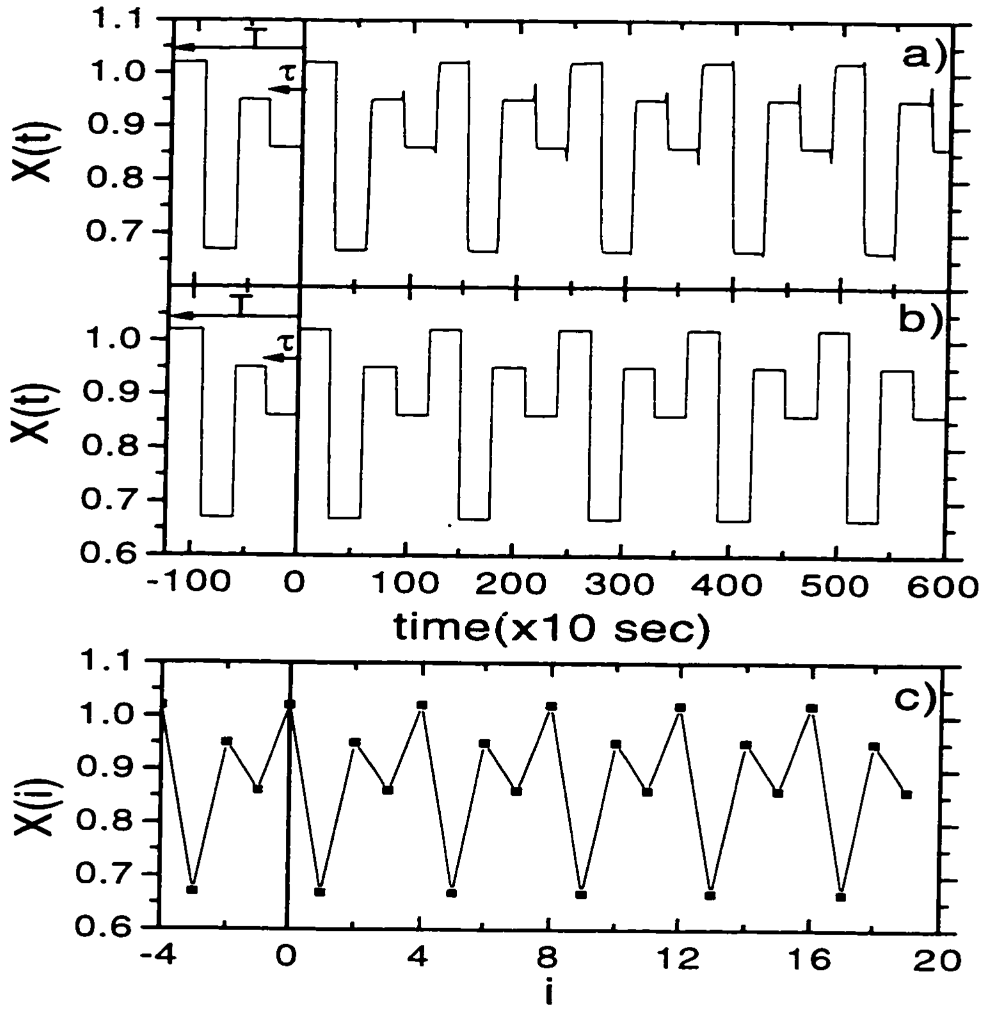

Figure 7.2: Numerical solutions of Eq.3.4 and its corresponding CTDE and map for $a = 0.145$ with control according to Eq.(): $K = 0.2$, and $r = 0.8$ using piecewise constant initial conditions. a) Controlled P_4 orbit for the DDE (Eqs.3.2 and 7.3) for $\tau = 300$ and $T = 1225.6$. b) Controlled P_4 orbit for the CTDE ($b\tau \rightarrow \infty$) (Eqs.3.2 and 7.5) for $\tau = 300$ and $T = 1200$. c) Controlled P_4 orbit for the map (Eq.7.6).

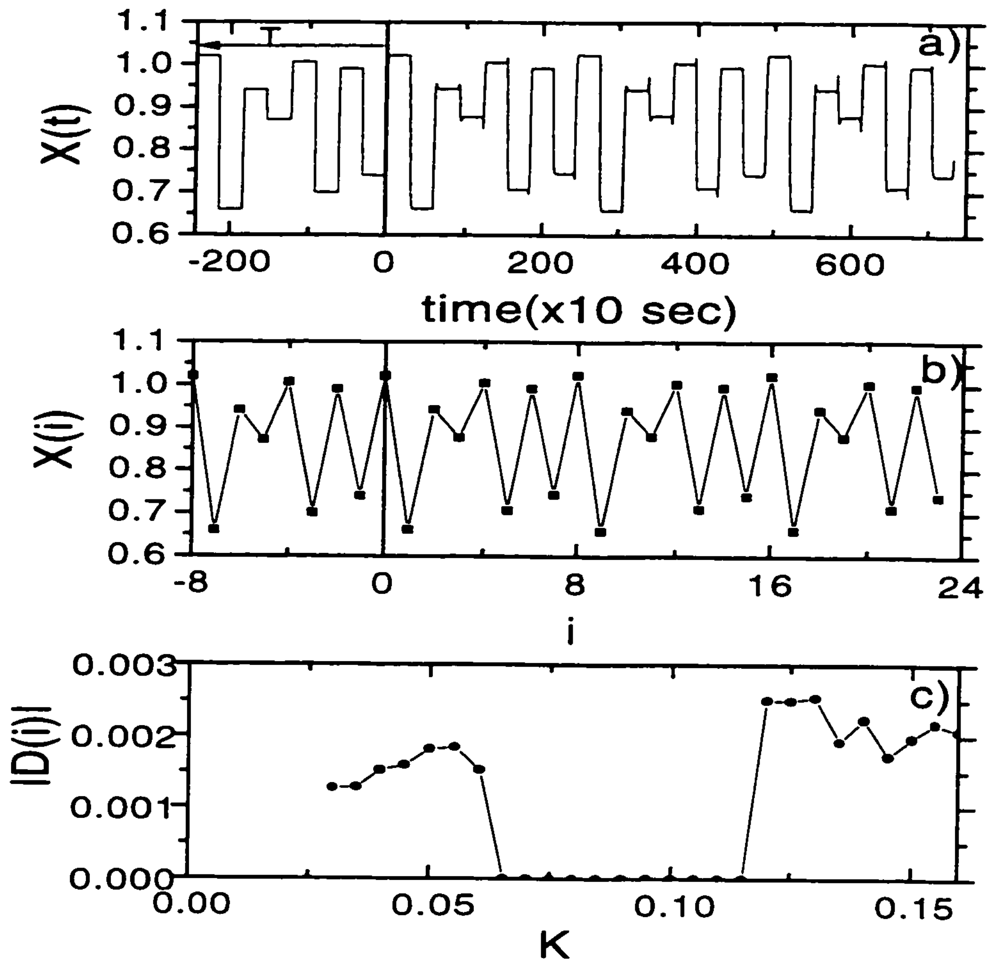

Figure 7.3: Controlling P_8 orbit in MG for $a = 0.145$, $K = 0.08$, and $r = 0.9$. a) The DDE (Eq.7.3) with $\tau = 300$ and $T = 2447.2$. The initial condition on $-T < t < 0$ is a piecewise constant corresponding to P_8, which is predicted by the map (Eq.7.6). b) The map (Eq.7.6) with $l = 8$. c) Dispersion $|D(i)|$ vs K for P_8 orbit, using Eq.7.6. Transients of about 5000 periods have been discarded.

7.3 New method for discrete-time chaos control

We now show that the asymptotic solution and the controllability of the DDE for large but finite delay can be predicted by the map in the singular perturbation limit ($b\tau \rightarrow \infty$) as shown in Fig.7.6. In this limit, the controlled DDE (Eq.7.3) becomes equivalent to a controlled CTDE,

$$\begin{aligned} x(t) &= b^{-1}[F(x(t-\tau)) + D(t)] \\ D(t) &= K[x(t-T) - x(t)] + rD(t-T)\,, \end{aligned} \tag{7.4}$$

which can be rewritten as

$$\begin{aligned} x(t) &= (b+K)^{-1}[F(x(t-\tau)) + Kx(t-T) + rD(t-T)] \\ D(t) &= K[x(t-T) - x(t)] + rD(t-T)\,. \end{aligned} \tag{7.5}$$

For constant initial conditions, the solutions are composed of plateaus. The points on each plateau are uncorrelated and evolve independently from one delay to the next. The evolution of each point on the plateau is given by the map obtained by discretizing the time in units of τ in Eq.7.5,

$$\begin{aligned} x(i) &= (b+K)^{-1}[F(x(i-1)) + Kx(i-l) + rD(i-l)]\,, \\ D(i) &= K[x(i-l) - x(i)] + rD(i-l)\,, \end{aligned} \tag{7.6}$$

where l is an integer that represents the period of the UPO on the map. The initial condition is specified in the interval $-l < i < 0$. When the control for a selected UPO is achieved, the perturbation $D(i)$ becomes exactly zero in this case (in contrast to the differential dynamics case where it is small but finite). The behavior of $D(i)$ for this map predicts the controllability of the DDE at large R (Fig.7.3c and Fig.7.6 below).

This method of controlling maps, inspired by the singular limit of the controlled DDE, is to our knowledge more efficient than other methods discussed in the literature, since it allows more complicated orbits to be controlled, and allows control of a given solution over a broader range of parameters. It is also practical since it can access a large range of the control parameter K and intrinsic feedback parameter a. Its efficiency stems from the timing of the applied perturbation. For example, in the method of Socolar *et al.* [18], Eq.7.1 is discretized and used to control UPO's in the Logistic map $x(i) = \mu x(i-1)[1 - x(i-1)]$. That method adds a feedback of the form $d(i-1) = K[x(i-1) - x(i-1-l)] + rd(i-1-l)$ to the feedback parameter μ, which depends on the previous time $x(i-1)$ instead of the present time $x(i)$ as in our method (Eq.7.6).

7.3.1 Range of control

In order to compare Socolar *et al.*'s method with our improved version of their algorithm, we investigate the control of the fixed point of the Logistic map, using additive feedback control. The dynamics of the Logistic map with extended control [18] are then:

$$\begin{aligned} x(i) &= \mu x(i-1)[1 - x(i-1)] + d(i-1) \\ d(i) &= K[x(i) - x(i-1)] + rd(i-1)\,, \end{aligned} \tag{7.7}$$

which can be rewritten as

$$\begin{aligned} x(i) &= \mu x(i-1)[1 - x(i-1)] + d(i-1) \\ d(i) &= Kx(i-1)[\mu(1 - x(i-1)) - 1] + (K + r)d(i-1)\,. \end{aligned} \tag{7.8}$$

The controlled map has a fixed point at $(x^*, d^*) = ((\mu - 1)/\mu, 0)$ which is unstable for $\mu > 3$. By linearizing the controlled map around this fixed point, and letting $y(i) = x(i) - x^*$ and $e(i) = d(i) - d^*$, the above equations yield

$$\begin{pmatrix} y(i) \\ e(i) \end{pmatrix} = \begin{pmatrix} \nu & 1 \\ K(\nu - 1) & K + r \end{pmatrix} \begin{pmatrix} y(i-1) \\ e(i-1) \end{pmatrix} \tag{7.9}$$

where $\nu = \mu(1 - 2x^*) = 2 - \mu$. The stable control is obtained by finding the eigenvalues of the matrix in Eq.7.9, which are given by

$$\lambda_\pm = \frac{1}{2}\left[\nu + K + r \pm \sqrt{(\nu + K + r)^2 - 4(\nu r + K)}\right] . \tag{7.10}$$

The control is stable if $|\lambda_\pm| < 1$. This yields the domain of stability: $\nu < 1$ (i.e. $\mu > 1$), $K > (1 + r)(3 - \mu)/2$, and $K < 1 + (\mu - 2)r$. Here the domain of stable control increases with increasing r as shown in Fig.7.4a.

Now, we use instead our control term in Eq.7.6, and apply the resulting control method to the Logistic map. The dynamics become:

$$\begin{aligned} x(i) &= (1 + K)^{-1}[\mu x(i - 1)[1 - x(i - 1)] + Kx(i - 1) + rD(i - 1)] , \\ D(i) &= K[x(i - 1) - x(i)] + rD(i - 1). \end{aligned} \tag{7.11}$$

The linearization around the fixed point $(x^*, D^*) = ((\mu - 1)/\mu, 0)$ with $y(i) = x(i) - x^*$ and $e(i) = D(i) - D^*$ yields the following dynamics:

$$\begin{pmatrix} y(i) \\ e(i) \end{pmatrix} = \frac{1}{1 + K}\begin{pmatrix} \nu + K & r \\ K(1 - \nu) & r \end{pmatrix}\begin{pmatrix} y(i - 1) \\ e(i - 1) \end{pmatrix} . \tag{7.12}$$

The eigenvalues that determine the stable control are given by,

$$\lambda_\pm = \frac{1}{2(1 + K)}\left[\nu + K + r \pm \sqrt{(\nu + K + r)^2 - 4\nu r(1 + K)}\right] . \tag{7.13}$$

The stable control is bounded by the following curves: $\nu < 1$ (i.e. $\mu > 1$), $K > -(1 + r)(3 - \mu)/2$, and $K > r(2 - \mu) - 1$. As r increases, the stable control increases for $\mu < 3$ and decreases for $\mu > 3$. The range of stability in the (K, μ) plane is much larger than that in the previous case (see Fig.7.4b). In that previous case, the stable control is found to increase with r. In the case of period-4 orbit of the Logistic map for example, which becomes unstable at $\mu = 3.54$, the control is maintained up to $\mu \approx 3.62$ for $r = 0$. However, using our method (Eq.7.6) for $r = 0$, the control of this orbit can be maintained up to $\mu = 3.97$ and the allowable range of K is much larger. This range decreases with increasing l, so higher-periodic orbits are very difficult to control using both methods for $r = 0$.

Our method improves even more if $r \neq 0$ (see Fig.7.5), allowing control of higher period UPO's and enhanced parameter ranges. For example, with $r = 0.9$ the control of the period-4 orbit can be maintained up to $\mu = 4.5$ while with the other method the controls up to $\mu = 3.75$. Figures 7.5, and 7.6 show how the range of controllability is enhanced with Eq.7.6 for P_4 of the Logistic map ($\mu = 3.95$), and the MG map ($a = 0.145$) for $r = 0.9$. and 0.8 respectively.

7.3.2 Prediction of controllability of the DDE

The absolute value of the feedback perturbation, or "dispersion" $|D(i)|$, and the Lyapunov exponents of the map are two important quantities for predicting the controllability of the DDE at large but finite delays as that of the map itself. Calculating dispersion is straightforward. However, we have found that the Lyapunov exponents estimation must be done carefully, e.g. using QR decomposition as we do below [32, 50]. The Jacobian matrices may have singularities for higher period orbits because of finite numerical precision. The more negative a Lyapunov exponent is, the more stable is the orbit (see Fig.7.6b).

To calculate the Lyapunov exponents, we proceed as follows. We rewrite Eq.7.6 as

$$\begin{aligned} x(i) &= (b+K)^{-1}[F(x(i-1)) + Kx(i-l) + rD(i-l)] \\ D(i) &= (b+K)^{-1}[-KF(x(i-1)) + bKx(i-l) + brD(i-l)]\,. \end{aligned} \tag{7.14}$$

We convert this $2l$-dimensional map into $2l$-coupled one-dimensional maps,

$$\begin{aligned} y_0(i) &= (b+K)^{-1}[F(y_0(i-1)) + Ky_1(i-1) + rz_1(i-1)] \\ z_0(i) &= (b+K)^{-1}[-KF(y_0(i-1)) + bKy_1(i-1) + brz_1(i-1)] \\ y_j(i) &= y_{j+1}(i-1), \quad j = 1, 2, \cdots, l-2 \\ z_j(i) &= z_{j+1}(i-1), \quad j = 1, 2, \cdots, l-2 \\ y_{l-1}(i) &= y_0(i-1) \end{aligned}$$

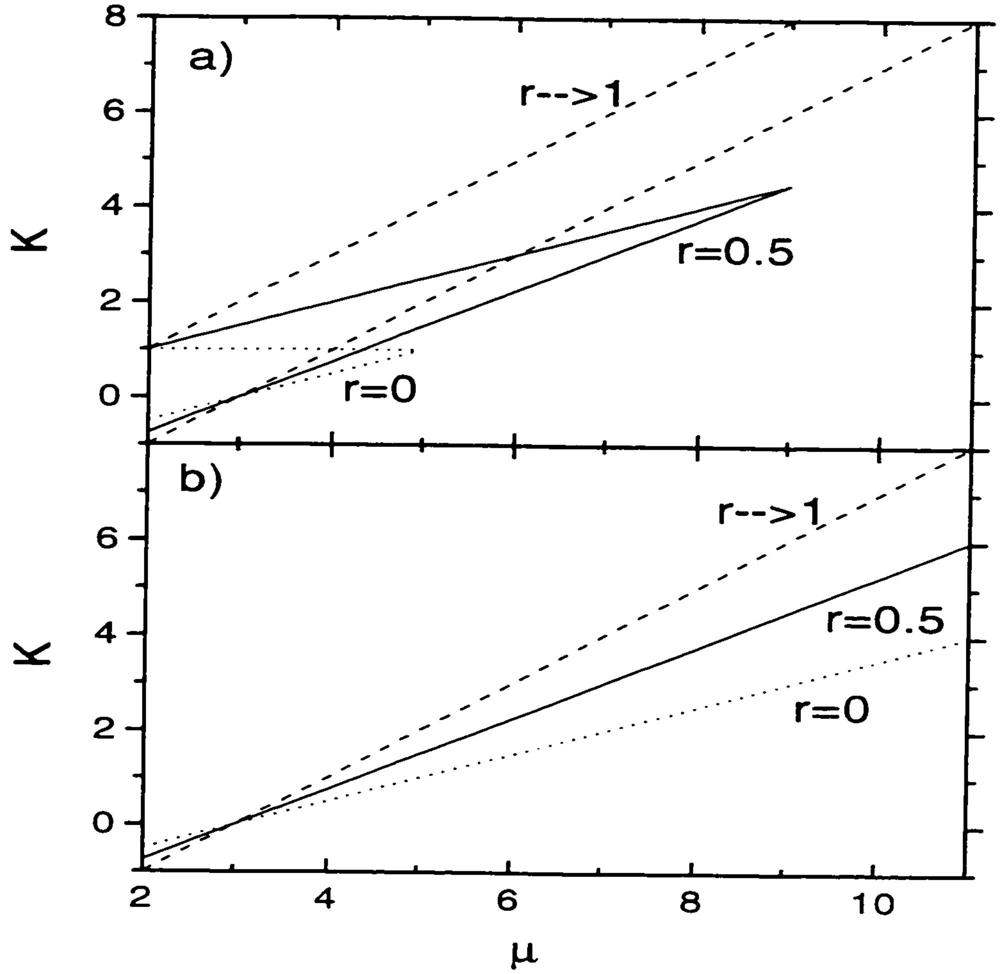

Figure 7.4: Boundaries in the (K, μ) plane for stable control of the fixed point in the Logistic map. Dotted lines are for $r = 0$, solid lines for $r = 0.5$, and dashed lines for $r \to 1$. a) The range of stable control (between lines) increases with increasing r using Eq.7.7. b) The range of stable control (in the upper-half-planes limited by the stability lines $K > -(1+r)(3-\mu)/2$) increases with increasing r for $\mu < 3$ and decreases with increasing r for $\mu > 3$ using Eq.7.11. We haven't represented the stability lines $K > r(2-\mu)-1$, since their range of stable control is already included in the upper-half-planes of the first stability lines for $\mu \geq 2$.

$$z_{l-1}(i) = z_0(i-1) \tag{7.15}$$

The Lyapunov exponents are the sum of the logarithm of the diagonal elements in the R matrices of the Jacobian in Eq.7.15, obtained by the QR decomposition method proposed in [32] and applied to time series in [50] (see Sect.2.6.2). Only a few QR decompositions are needed for Q to converge to the identity matrix. The result is shown in Fig.7.6b. It can be seen that there is very good agreement between the behaviors of the maximum Lyapunov exponent and the dispersion $|D(i)|$.

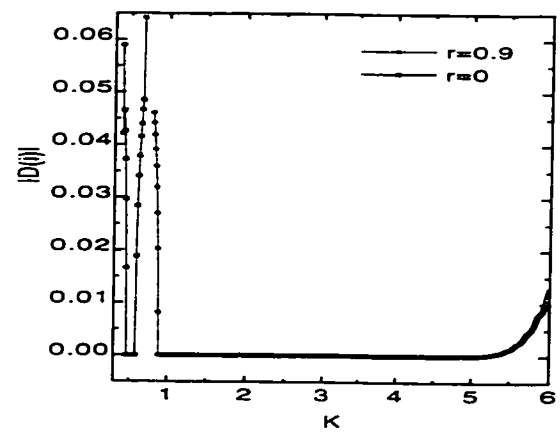

Figure 7.5: Dispersion $|D(i)|$ vs K for P_4 orbit in the Logistic map $x(i) = \mu x(i-1)[1 - x(i-1)]$, using Eq.7.6 for $\mu = 3.95$ with $r = 0$, and $r = 0.9$. The range of controllability with $r = 0.9$ is much larger than the one with $r = 0$.

7.4 Application of our method to neural networks

The control method discussed above is now applied to a small chaotic neural network evolving in discrete time [19, 20]. The dynamics of the nth neuron in a network of M chaotic neurons is given by

$$x_n(i) = f_n\left\{ \sum_{m=1}^{M} W_{nm} \sum_{q=0}^{i-1} k^q h_m(x_m(i-1-q))\right.$$

$$
\begin{aligned}
&+ \quad \sum_{m=1}^{N} V_{nm} \sum_{q=0}^{i-1} k^q I_m(i-1-q) \\
&- \quad \alpha \sum_{q=0}^{i-1} k^q g_n[x_n(i-1-q)] - \theta_n \Bigg\} \\
&= \quad f_n(y_n(i))
\end{aligned} \tag{7.16}
$$

where $x_n(i)$ is the output of the nth neuron at timke i. In the original model [19], the output function $f(y)$ was a unit step function; we have used instead a sigmoidal function, as in [20] whose steepness can be adjusted: $f(y_n(i)) = 1/(1+e^{-y_n(i)/0.02})$. Thus, the output of a given neuron is an analog value between 0 and 1. The threshold for firing is θ. The coupling parameters W_{nm}, V_{nm}, α and activity functions h_m, I_m and g_n are described in [20]. We apply the control to the first chaotic neuron in a network of three neurons ($M = 3$) with parameters as in [20]. The dynamics are then:

$$
\begin{aligned}
y_1(i) &= (1+K)^{-1}[ky_1(i-1) - f(y_1(i-1)) + 0.5f(y_2(i-1)) \\
&+ Ky_1(i-l) + rD(i-l)] \\
D(i) &= K[y_1(i-l) - y_1(i)] + rD(i-l) \\
x_1(i) &= f(y_1(i)) \\
y_2(i) &= ky_2(i-1) - f(y_2(i-1)) + 0.5f(y_3(i-1)) \\
x_2(i) &= f(y_2(i)) \\
y_3(i) &= ky_3(i-1) - f(y_3(i-1)) + 0.5f(y_1(i-1)) \\
x_3(i) &= f(y_3(i)),
\end{aligned} \tag{7.17}
$$

$k = 0.769231$ is a bifurcation parameter. Without chaos-control, the response of this neural circuit of three neurons is chaotic (see Fig.7.7a). The sharp spikes correspond to neuron firings. If our control technique is applied to the first neuron in Eq.7.17, the network response behaves periodically, as shown in Figs.7.7b and c for $l = 15$ and $l = 16$, respectively. Our method is thus applicable to real world models of activity in networks of neurons.

7.5 Conclusion

We have studied the singular perturbation limit of the DDE and shown that the map obtained in this limit can be used to predict the asymptotic solutions, and the range of controllability of the DDE at large delays. The control dynamics in this limit suggest an improved method of controlling discrete-time systems. Its power relates to the fact that the control, extended or not, is applied to system states using information on where from the immediate past. The method can be applied to a variety of discrete systems used to model systems in the physical sciences, medicine and engineering. Our method was illustrated here on a chaotic neural network, since there is much interest in being able to control such aperiodic dynamics in real systems of e.g. nerve or cardiac cells.

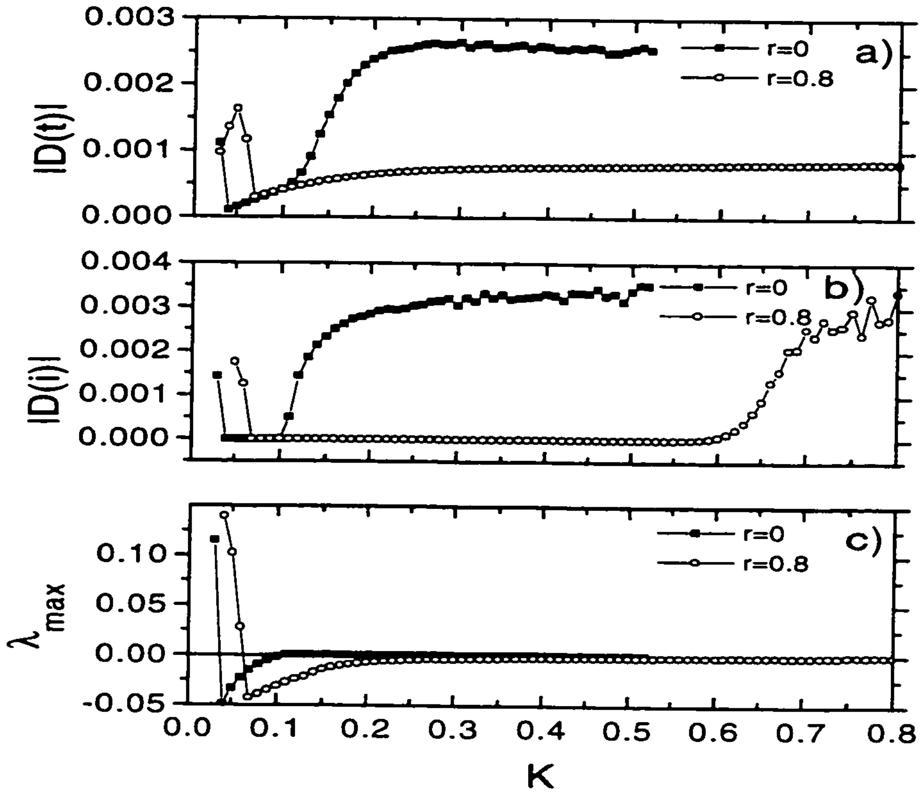

Figure 7.6: Range of controllability of P_4 orbit in the MG map for $a = 0.145$ with $r = 0$, and $r = 0.8$. a) Dispersion $|D(t)|$ vs K of the DDE using Eq.7.3. b) Dispersion $|D(i)|$ vs K of the map using Eq.7.6. c)) Maximum Lyapunov exponent λ_{max} vs K of the map using Eq.7.15 and the QR decomposition method with $L = 3000$ and $k = 3$ (see Sect.2.6.2). Transients of about 5000 periods have been discarded. In (a), the period of the UPO varies slightly with K according to $T = 1208.34 + 13.87exp[(0.07 - K)/0.1]$ obtained from fitted data. This variation was taken into account for the calculation of $D(t)$ vs K..

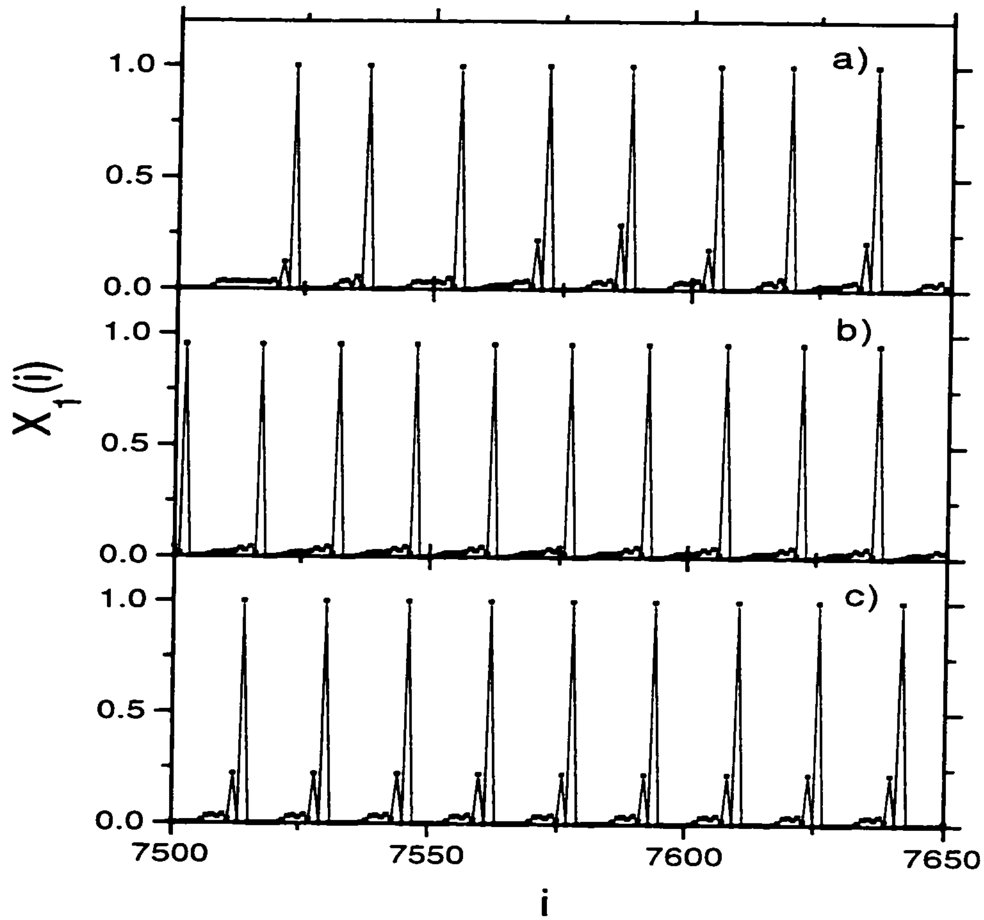

Figure 7.7: Controlling chaos in a Nagumo-Sato network composed of three neurons. $X_1(i)$ is the output of the first chaotic neuron, which takes value between 0 and 1. a) The chaotic solution of the first neuron $X_1(i)$ vs i for $K = 0$ and $r = 0$. b) Controlled solution using Eq.7.6 with $l = 15$, $K = 0.38$ and $r = 0.5$. c) Same as in (b) but for $l = 16$, $K = 0.2$, and $r = 0.5$.

Chapter 8

Synchronization of delay-differential equations with applications to communications

8.1 Introduction

Synchronization of chaotic systems have received a lot of attention in the last few years because of its potential application to private communication and signal processing [21, 22, 23, 127]. The basic principle of synchronization is to recover the message at the receiver end, at which the initial conditions are not known. The principle of secure communication is to hide this message with chaos before sending it. Chaotic signals have much wider spectra compared to information signals and are very difficult to predict. These properties make them interesting to use as broadband carriers for secure communication purposes; they can be used for masking or modulation as in spread spectrum communication [124].

The information signal, which has low probability of being detected, is recovered at the receiver end using synchronization techniques. Two type of synchronization techniques have widely been used in the literature. The first one, developed by Pecora and Carroll [102, 118], consists of decomposing the system into two identical subsystems: a master system (transmitter), which has some positive Lyapunov exponents, is used to drive the slave system (receiver), which has only negative Lyapunov exponents, into synchronization. In this manner, synchronization has been achieved in various electrical circuits [21, 22, 23, 119]. The second synchronization method is based on a negative feedback perturbation, proportional to the difference between the outputs of the two chaotic systems. This method of synchronization is an extension of the method of control discussed in Chapters 6 and 7, where the control is applied to aperiodic orbits instead of unstable periodic orbits (UPO's) (see [116]). By varying the strength of the feedback perturbation, the Lyapunov exponents of the driven system can be made negative, causing distances between the orbits of the coupled systems to decrease to zero. This method of synchronization has also been realized experimentally using different electrical circuits [114, 121, 122].

This synchronization of chaotic systems can be used for secure communication, in which chaos plays the role of a masking signal or of an aperiodic carrier signal. Most investigations of such communication have focused on the problem of transmitting signals by using low-dimensional chaotic systems, such as Rossler and Lorenz systems, as transmitters and receivers. Transmission of information is less secure in this case than with high-dimensional chaotic systems. It is thus desirable to use high-dimensional chaotic carriers in order to make the signal detection and decoding as difficult as possible. Xiao *et al.* [120] have discussed how high-dimensional spatiotemporal chaos can be used for transmitting and receiving a large number of informative signals simultaneously. Also, Parlitz and Kocarev [22, 23] have constructed a high-dimensional system using a series of low-dimensional "building blocks" of Rossler systems (each Rossler system has dimension three). This method has many advantages, but some limitations in its implementation since the attractor dimension is proportional to the number of blocks.

Delay-differential equations present an alternative simpler and efficient way of transmitting and receiving messages with low detectability (high privacy) and very low distorsion.

Delay-differential equations are simple yet infinite-dimensional dynamical systems that generate high-dimensional chaotic attractors. The latter are further interesting because of the multistability they exhibit at large delays. The high-dimensional chaos they exhibit, when used as a broadband carrier, makes the information carrying signal very difficult to detect.

Thus in this Chapter, we show that DDE's are synchronizable and are very interesting for private communication. They are also easily implementable electronically [58, 115]. The principle of our method can be summarized as follows: a message contained in a finite string of bits is first encoded onto a multistable solution of a selected unstable periodic orbit (UPO), using a specific piecewise constant initial function and a feedback control (see Chap.6). The message is then transmitted using a chaotic DDE carrier, and recovered using synchronization of the chaotic behavior between the transmitter and receiver (see Fig.8.4). The detection of the message is thus very difficult without knowledge about the dynamical system used to generate the carrier signal. Both methods of synchronization mentioned above can be applied to DDE's and distributed delay systems (see Sect.3.5). While the feedback-method is applied directly to the receiver as a small perturbation, the master-slave method requires that a master-slave decomposition must be found in order to achieve synchronization.

The map obtained in the singular perturbation limit discussed in Sect.3.6 can be used to find the range of synchronization parameters. For example, it can be used to calculate the dispersion relation and the Lyapunov exponents of the two outputs. If the synchronization is achieved, the diffference between the two outputs vanishes. As for the control technique (see Sect.7.3), the method of synchronization of the map obtained in this limit can also be applied to synchronize any discrete system to transmit digital signals.

This Chapter is organized as follows: In Section 8.2 we explain the method of synchronization of the Mackey-Glass DDE and of its singular limit map. In Section 8.3 we present the method of synchronization of distributed delay systems. In Section 8.4 we discuss the application of chaotic synchronization with DDE's to secure communication. The Chapter concludes in Section 8.5.

8.2 Synchronization of Mackey-Glass DDE

At least two types of chaotic synchronization schemes can be applied to DDE's such as the Mackey-Glass or the Ikeda equations. The first scheme is straightforward. It consists of supplying the drive variable $x(t-\tau)$ or $x(t)$ from the driving DDE,

$$\frac{dx(t)}{dt} = -bx(t) + F(x(t-\tau)), \tag{8.1}$$

to the feedback function of the second "response" DDE to be synchronized,

$$\frac{dy(t)}{dt} = -by(t) + F(x(t-\tau)) \tag{8.2}$$

or

$$\frac{dy(t)}{dt} = -by(t) + F(x(t)) . \tag{8.3}$$

In both cases, the response system synchronizes very rapidly as time increases. When driving with $x(t)$ however, the two outputs are shifted from one another in time by τ. Synchronization is expected in both cases since $x(t-\tau)$ or $x(t)$ are driving (through the static nonlinearity F) a linearly stable response system $\dot{y} = -by$, i.e. this response system has a negative conditional Lyapunov exponent. This kind of synchronization would apply to identical systems which respond to essentially the same feedback variable.

A second type of synchronization consists of applying a feedback perturbation proportional to the difference between the two outputs as follows:

$$\begin{aligned} \frac{dx(t)}{dt} &= -bx(t) + F(x(t-\tau)) \\ \frac{dy(t)}{dt} &= -by(t) + F(y(t-\tau)) + K[x(t) - y(t)] . \end{aligned} \tag{8.4}$$

The second DDE is identical to the first DDE, except for its coupling to the first via the perturbation $D(t) \equiv K\,[x(t) - y(t)]$. This could apply to situations where one feedback system is linearly coupled to another identical feedback system, perhaps through some form of crosstalk. We focus here on this second type of synchronization in the Mackey-Glass DDE (Eq.3.4). The synchronization (i.e. coupling) term is similar to the control term used in [17, 25, 62], i.e. the dynamics are similar to

$$\frac{dx(t)}{dt} = -bx(t) + F(x(t-\tau)) + K\left[x(t-T) - x(t)\right] , \tag{8.5}$$

where T is the UPO period. However, aperiodic orbits are now synchronized, as in [116] rather than UPO's. The aperiodic orbits are generated by two similar DDE's evolving from different initial functions. We note that $x(t)$ can have many positive Lyapunov exponents.

By varying the strength of the perturbation, the Lyapunov exponents of the second equation can be made negative, causing distances between the orbits of the two systems to decay to zero. The system is then synchronized and the outputs $y(t)$ and $x(t)$ become identical (i.e. within a very small distance of one another). Figures 8.1a, and b show the synchronization of two chaotic MG DDE's (Eq.8.4) for $a = 0.2$ and $\tau = 300$, each of which starts from a different initial function. Without perfect synchronization, the two orbits can still remain close; without the coupling however, the two trajectories diverge exponentially. Figure 8.1c shows the asymptotic time behavior of $|x - y|$ for different values of K. Synchronization occurs for $K > 0.08$.

The map obtained in the singular perturbation limit $R = b\tau \to \infty$ of the DDE can be used to study synchronization of the DDE's Eq.8.4 at large R. First, this limit yields synchronized continuous-time difference equation's (CTDE's):

$$\begin{aligned} x(t) &= b^{-1}F(x(t-\tau)) \\ y(t) &= (b+K)^{-1}[F(y(t-\tau)) + Kx(t)] \end{aligned} \tag{8.6}$$

If time is discretized in units of τ in Eq.8.6, synchronization is governed by the following map dynamics:

$$x(i) = b^{-1}F(x(i-1))$$

$$
\begin{aligned}
y(i) &= (b+K)^{-1}[F(y(i-1)) + Kx(i)] \\
&= (b+K)^{-1}[F(y(i-1)) + Kb^{-1}F(x(i-1))] \,. \qquad (8.7)
\end{aligned}
$$

Figures 8.1d, and e show the distance (the "dispersion relation") $|x(i) - y(i)|$ and the maximum Lyapunov exponent λ_{max} for the map (Eq.8.7) as a function of K. The maximum Lyapunov exponent is calculated using the QR decomposition method [32, 50]. Synchronization is achieved if $K \geq 0.07$, close to the actual value found for the DDE (Fig.8.1c). We note that the dispersion goes to zero and λ_{max} goes negative (indicating synchronization) at similar values of K. This is true even though this analysis is based on the map, rather than on the DDE itself. This discrete method of synchronization can of course be applied to a variety of discrete dynamical systems.

8.3 Synchronization of distributed delay systems

Synchronization can also be studied in the context of systems with a distribution of delays rather than a single fixed delay. Such systems are actually the norm in specific applications. Mathematically, the infinite-dimensional DDE can be approximated by an integro-differential equation with a smooth memory kernel, which can be converted into a (m+2)-dimensional system of ordinary differential equations (ODE's) such as Eq.8.8 below [68, 69]. The method of Pecora and Carroll [102] for synchronizing ODE's can be used here, and one possible decomposition is into a master subsystem governed by

$$
\begin{aligned}
\dot{y}_0 &= f(y_0, y_{m+1}) = -by_0 + F(y_{m+1}) \\
\dot{y}_i &= -\alpha(y_i - y_{i-1}) \qquad i = 1, \cdots, m+1 \,, \qquad (8.8)
\end{aligned}
$$

and a slave subsystem governed by

$$
\begin{aligned}
y_0' &= y_0 \qquad (8.9) \\
\dot{y}_1' &= -\alpha(y_1' - y_0)
\end{aligned}
$$

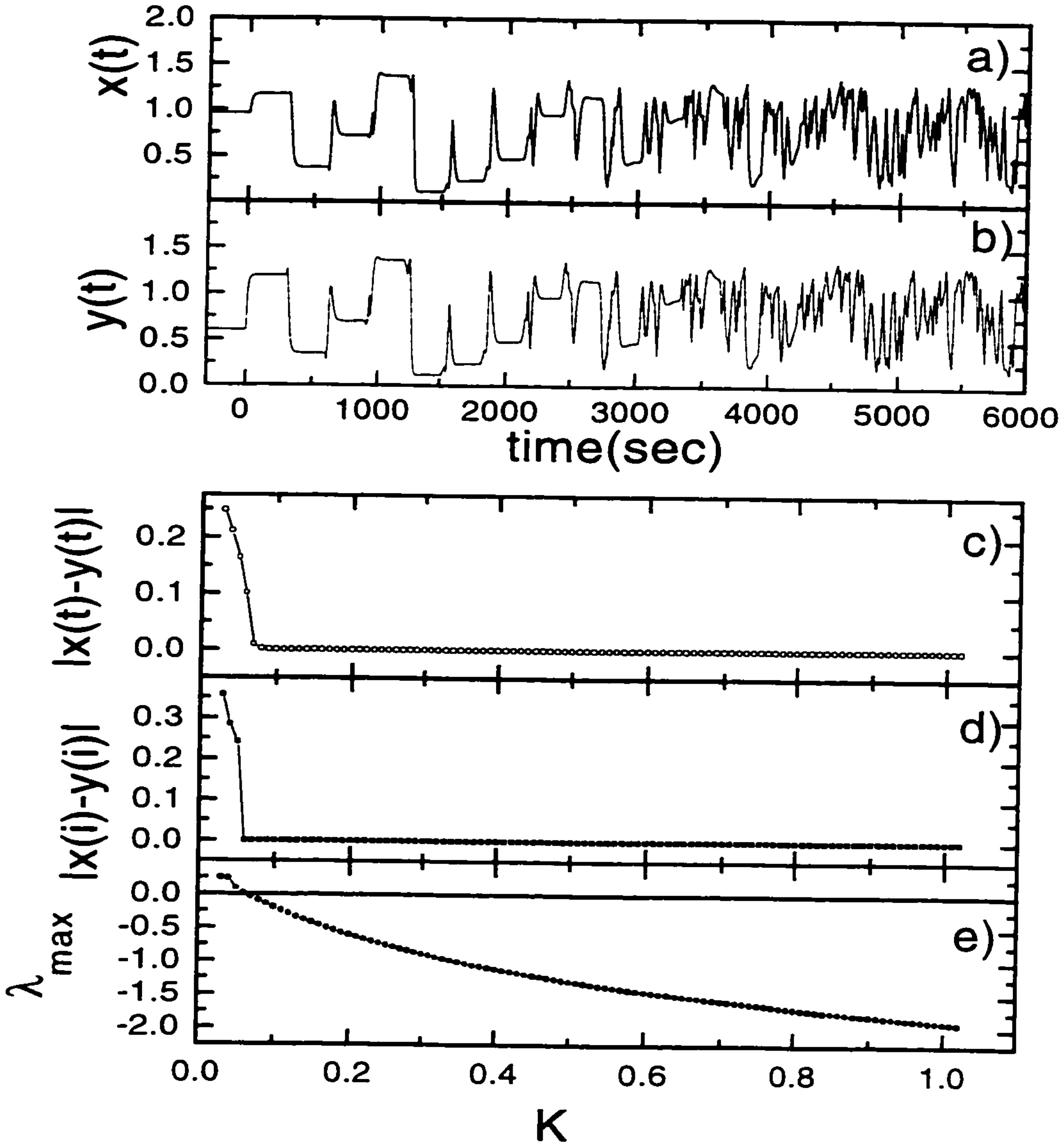

Figure 8.1: Synchronization of two MG chaotic DDE's ($a = 0.2, \tau = 300$). a-b) x vs t and y vs t using Eq.8.4 with two different initial conditions. c) The dispersion $|x(t) - y(t)|$ as a function of K for the DDE (Eq.8.4). d) The dispersion $|x(i) - y(i)|$ as a function of K for the map (Eq.8.7). e) The maximum Lyapunov exponent λ_{max} as a function of K for the map (Eq.8.7). We used a fourth-order Runge-Kutta integration algorithm with time step 0.01.

$$\dot{y}_i' = -\alpha(y_i' - y_{i-1}') \qquad i = 2, \cdots, m+1 . \tag{8.10}$$

Here, the master system drives the slave system through the component y_0. The other components $y_1', y_2', \cdots, y_{m+1}'$ are allowed to have different arbitrary initial conditions. There is of course a finite number of possible decompositions, many of which are expected to yield synchronization [118, 23] due to the conditional Lyapunov exponents of the subsystem (see below). The asymptotic stability of the slave subsystem that underlies synchronization can be established by finding a Lyapunov function [21, 117]. Let y_i^* be the difference between the desired value y_i and the actual value of the slave variable y_i': $y_i^* = y_i - y_i'$. The y_i^* dynamics are governed by:

$$\begin{aligned} \dot{y}_1^* &= -\alpha y_1^* \\ \dot{y}_i^* &= -\alpha(y_i^* - y_{i-1}^*) \quad i = 2, \cdots, m+1 . \end{aligned} \tag{8.11}$$

The y_i^* dynamics are globally asymptotically stable at the origin. This result follows by considering the (m+1)-dimensional Lyapunov function defined by

$$E(t) = \frac{1}{2}(y_1^{*2} + y_2^{*2} + \cdots + y_{m+1}^{*2}) . \tag{8.12}$$

The time rate of change of $E(t)$ along a trajectory is given by

$$\begin{aligned} \dot{E}(t) &= y_1^*\dot{y}_1^* + y_2^*\dot{y}_2^* + \ldots + y_{m+1}^*\dot{y}_{m+1}^* \\ &= -\frac{\alpha}{2}[y_1^{*2} + (y_1^* - y_2^*)^2 + \ldots + (y_m^* - y_{m+1}^*)^2 + y_{m+1}^{*2}] \leq 0 \end{aligned} \tag{8.13}$$

The Lyapunov function $E(t)$ decreases for all $y \neq 0$. Lyapunov's theorem [123] (see also [117]) implies that $E(t) \to 0$ as $t \to \infty$. Therefore, the distances y_i^*, along with Eq.8.12, go to zero and synchronization occurs as $t \to \infty$ (see Fig.8.2).

Synchronization also follows here from the fact that the conditional Lyapunov exponents of the response system are negative. It is straightforward to show that those exponents are the roots of $(-\alpha - \lambda)^{m+1} = 0$. Thus there is only one $(m+1)$-fold degenerate exponent

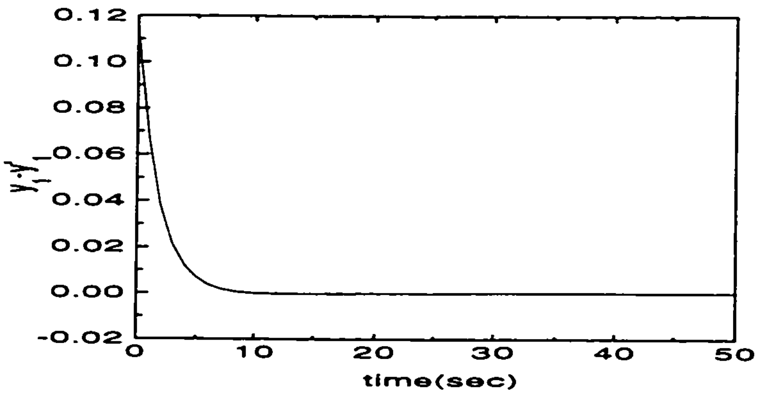

Figure 8.2: Synchronization of two MG distributed delay systems ($\alpha = 0.55, m = 54$). The master subsystem drives the slave subsystem with the component y_0. The difference between the two outputs, $y_i - y_i'$ ($i = 1, 2, \cdots, m+1$), shown here for $y_1 - y_1'$, vanishes as $t \to \infty$.

$\lambda = -\alpha$. This exponent is in fact the exponential relaxation rate seen in Fig.8.2. We can extend this calculation to arbitrary values of m. In the limit $m \to \infty$ the distributed delay system becomes identical with the original DDE, and the synchronization is of the simple type seen in Eq.8.2 .

8.4 Application to secure communication

8.4.1 Generalities

An information signal $m(t)$ containing a message can be transmitted by using a chaotic signal $x(t)$ as a broadband carrier which masks or modulates the signal. Chaos synchronization can then be used to extract the message at the receiver end. Different strategies can be used to make the transmitted signal $s(t)$ as "noisy" as possible (i.e. with a broadband power spectrum) such that the signal has low power and is difficult to distinguish from the background (low detection probability). One is signal masking, where $s(t) = x(t) + \epsilon m(t)$; another is modulation: $T(t) = x(t)m(t)$ (widely used in spread spectrum communication

[124]), or some combination of masking and modulation, such as $s(t) = x(t)[1 + \epsilon m(t)]$.

High-dimensional chaos in DDE's can be obtained by increasing the product of relaxation rate and the delay $b\tau$ (see [125] and references therein). In particular, the spectrum of such trajectories contains many modes superimposed on a broad background. The detection of a transmitted message using such a chaotic carrier is thus very difficult using spectral techniques.

8.4.2 Communication using signal masking

We propose the following masking technique. A message $\epsilon m(t)$ $(0 < \epsilon \ll 1)$ drives the chaotic "DDE transmitter" as follows:

$$\frac{dx(t)}{dt} = -bx(t) + F(x(t-\tau)) + b\epsilon m(t) \tag{8.14}$$

This can be rewritten in terms of the actual signal $s(t) = x(t) + \epsilon m(t)$ which is being transmitted:

$$\frac{dx(t)}{dt} = -b[2x(t) - s(t)] + F(x(t-\tau)) \; . \tag{8.15}$$

A receiver with an identical copy of the transmitter is used to generate an output $y(t)$ which is synchronized to $x(t)$ using proportional feedback control:

$$\frac{dy(t)}{dt} = -by(t) + F(y(t-\tau)) + b[s(t) - y(t)] \; . \tag{8.16}$$

Since x and y are synchronized, the message $m(t)$ can be recovered as $m(t) = [s(t) - y(t)]/\epsilon$. Figures 8.3 shows the power spectrum of the recovered sine wave signal $m(t) = \sin(2\pi t/100) + 1.5$ after being masked by a MG chaotic carrier. The power spectrum of the transmitted signal (8.3b) shows only a small peak at $f = 0.01Hz$, of the same order of magnitude as other peaks in the chaotic broadband.

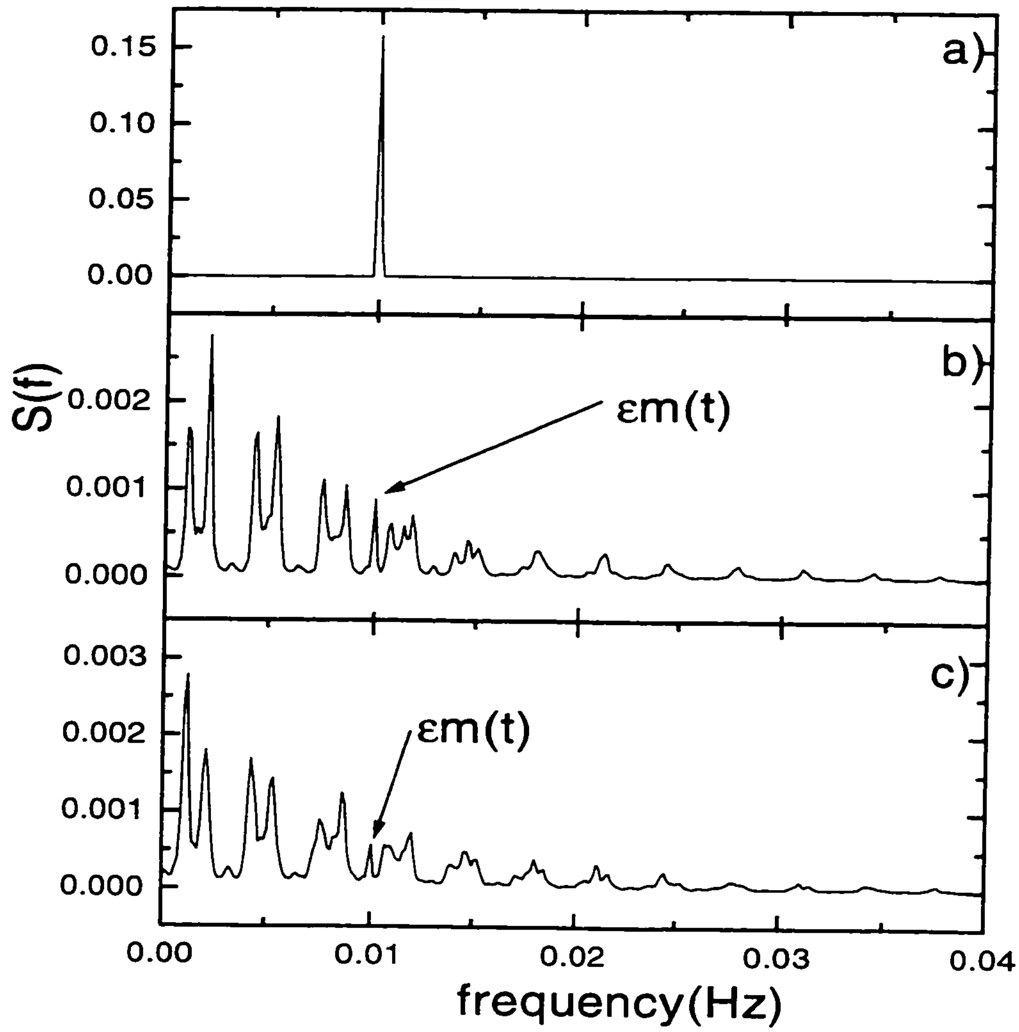

Figure 8.3: Transmitting a sine wave signal $m(t) = \sin(2\pi t/100) + 1.5$ with $\epsilon = 0.05$, using an MG carrier with $a = 0.2$ and $\tau = 300$. a) Power spectrum of the recovered sine wave signal using the masking technique Eq.8.15. b) Power spectrum of the transmitted signal using masking $s(t) = x(t) + 0.05m(t)$ where x is the chaotic carrier. c) Same as (b) but using masking-modulation $s(t) = x(t)[1 + 0.05m(t)]$, yielding an even smaller power for the sinusoid. Spectra are averages over 20 samples of 4096 points each with sampling time 3.75.

8.4.3 Communication using chaotic masking-modulation

We now study masking-modulation of the message by a broadband carrier $x(t)$ using $s(t) = x(t)[1+\epsilon m(t)]$ as the transmitted signal. This masking-modulation technique is used to drive the transmitter in Eq.8.15 in the same way as for the masking technique. by synchronizing the receiver to the transmitter, the message can be recovered exactly as $m(t) = [s(t)/y(t) - 1]/\epsilon$. The spectral peak corresponding to the simple "sine wave" message is even smaller in comparison with the masking technique (see Fig.8.3c).

8.4.4 Encoding messages onto UPO's of DDE's

The use of UPO's for private communication has been demonstrated in [126] using the P_4 orbit of the Hénon map. That method requires an attractor dominated by a few UPO's, near which the system spends more time. We now present a method which suffers less from this contraint and allows a more secure transmission. It applies to the transmission of short messages.

One such message is encoded directly onto an UPO of the DDE which is first stabilized by chaos control of the type in Eq.8.5 (see [62]). Such controlled UPO's are multistable, and they can be given, using a suitable initial function, a precise form determined by the short message to be transmitted. The message can be encoded onto any UPO if it can be controlled. Also, different messages can be transmitted and received by simply changing the UPO or the initial condition. Since the encoding uses UPO's embedded in the chaotic attractor, the transmitted message will have frequencies that match those of the chaotic trajectories. In other words, these frequencies will not stand out in the spectrum, and the message has low detectability.

A block diagram of the method is shown in Fig.8.4. The message encoded onto a controlled UPO in the "encoder" is then modulated with a chaotic carrier of a DDE similar to the one in the encoder before being transmitted. This second DDE can have the same or different feedback parameters. At the receiver, which contains the exact copy of the transmitter system, the message is extracted using synchronization. Figures 8.5a and b show a controlled UPO of a period four orbit P_4 orbit of the MG DDE Eq.3.4 containing the message [10,01,11,01,11,00,11,00,10,00,10,01] and its power spectrum. This P_4 orbit is determined essentially by the period-four orbit of the singular limit map of the encoder DDE [62]. The transmitted signal in Figures 8.5c (masking) and 5d (masking-modulation) is now extremely difficult to distinguish in spectra from the chaotic DDE carrier.

8.4.5 Digital communication

We now show that the continuous-time difference equation (CTDE) obtained in the singular perturbation limit $R \to \infty$ of Eqs.8.15 and 8.16 can be used to securely transmit and receive digital messages instead of the analog-type messages studied uup to now (although in practice the short messages discussed in the previous section can be considered as digital). For constant initial conditions, such CTDE's exhibit a series of plateaus which go chaotically between different values. These plateaus are highly unstable (for example, they will not remain "plateaus" in the presence of even minute perturbations) unless they are stabilized by some UPO control. For example, the dynamics of the masking-modulation technique can be written as:

$$\begin{aligned} x(t) &= \frac{b^{-1}F(x(t-\tau))}{1-\epsilon m(t)} \\ y(t) &= \frac{1}{2}[b^{-1}F(y(t-\tau))+s(t)]\,, \end{aligned} \tag{8.17}$$

with $s(t) = x(t)[1 + \epsilon m(t)]$. The dynamics for the masking technique can be obtained similarly. Figure 8.6 shows the transmission of a digital message using masking-modulation technique (Eq.8.17). The digital message is a controlled multistable P_4 solution obtained in the singular limit.

8.5 Conclusion

In summary, we have shown that the chaotic behavior of delay-differential and distributed delay systems can be synchronized and can be used as a broadband carrier for secure communication. Mixing their high-dimensional chaos to a message signal makes this signal very difficult to detect, especially when the message is encoded onto UPO's of the DDE or of the distributed delay system. It remains to be seen just how sensitive the transmission and decoding to noise. Preliminary results for Gaussian white noise indicate thet the quality of the transmission is substantially degraded when its standard deviation is on the order of the amplitude of the information signal $\epsilon m(t)$ (not shown).

Our results here also suggest that response subsystems will tend to synchroniza to noise as well as any chaotic behavior present in a "drive" system. Thus aperiodic behavior of deterministic or stochastic origin in one feedback system can entrain the motion of similar systems to which it is unidirectionally coupled. This is relevant to the study of single or multi-loop feedback systems with fixed or distributed delays, such as those occuring in control systems engineering, optoelectronics, physiology [26], and especially in neurobiology [25, 13]. Future work will include extending our result to bi-directional synchronization of mutually coupled delayed feedback systems.

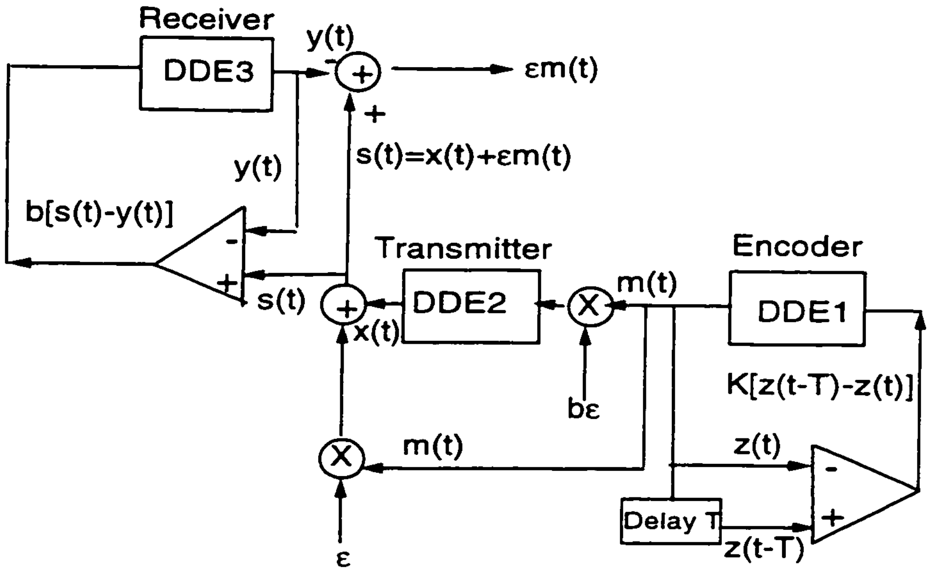

Figure 8.4: Block diagram of a chaotic communication system based on the masking technique and unstable periodic orbits of a DDE. A finite message is stored on an unstable periodic orbit of a DDE stabilized by delayed feedback control. This waveform is then masked by the chaotic behavior of a similar but uncontrolled DDE (transmitter), and decoded by another similar DDE with a synchronizing perturbation as in Eq.8.4.

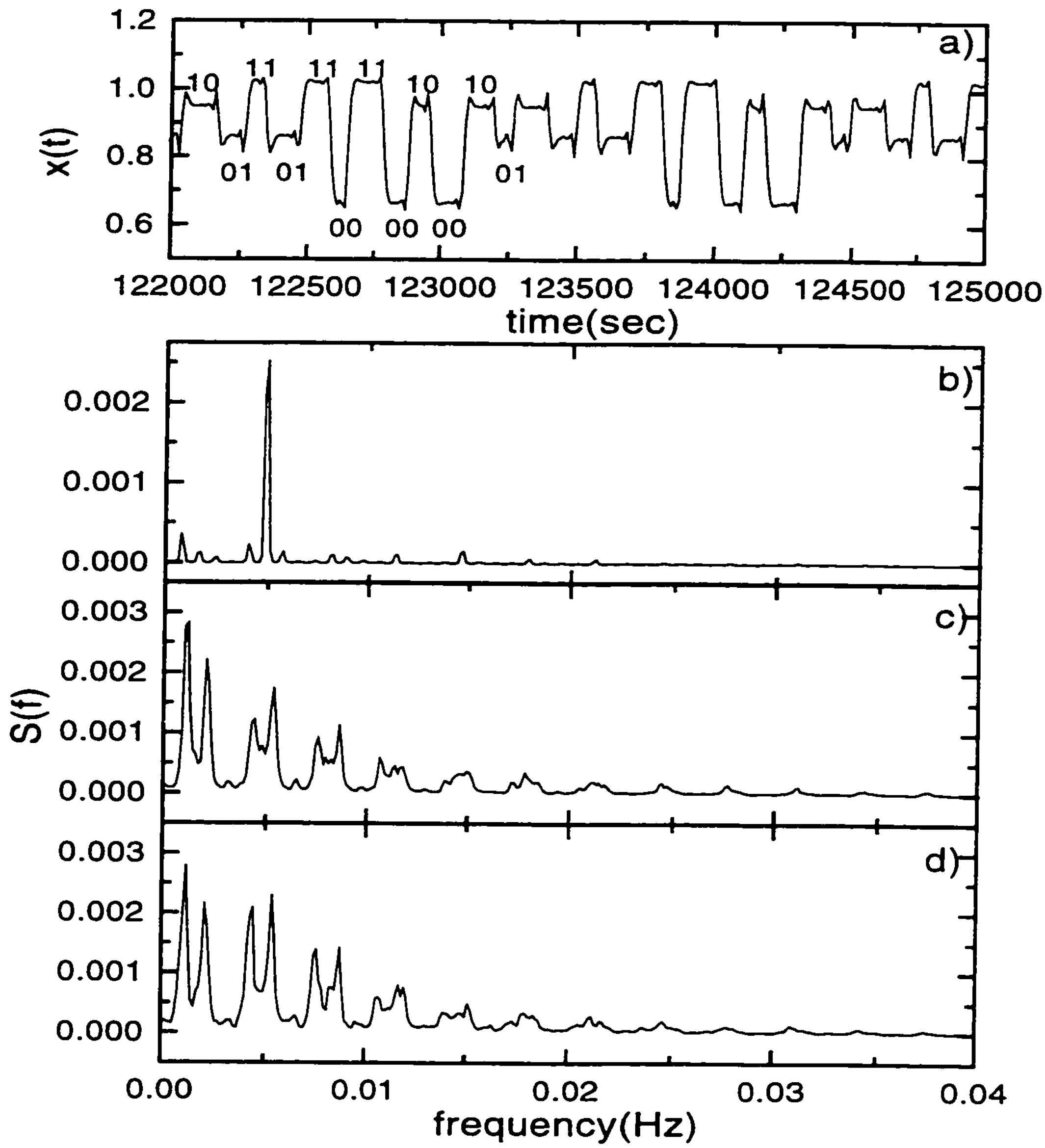

Figure 8.5: A message is encoded onto a multistable solution of a controlled P_4 orbit, masked or modulated with a chaotic carrier $x(t)$ using Eqs.8.15-8.16 (a = 0.2, τ = 300), and then transmitted. a) The controlled multistable solution of P_4 in the DDE obtained from Eq.6.1 with a = 0.145, τ = 300 and K = 0.05, on which the message [10,01,11,01,11,00,11,00,10,00,10,01] has been encoded [62]. b) Power spectrum of the waveform in (a). c) Power spectrum of the masked signal $s(t) = x(t) + 0.1m(t)$. d) Power spectrum of the masked-modulated signal $s(t) = x(t)[1 + 0.1m(t)]$. Spectra are averages over 20 samples of 4096 points each with sampling time 3.75.

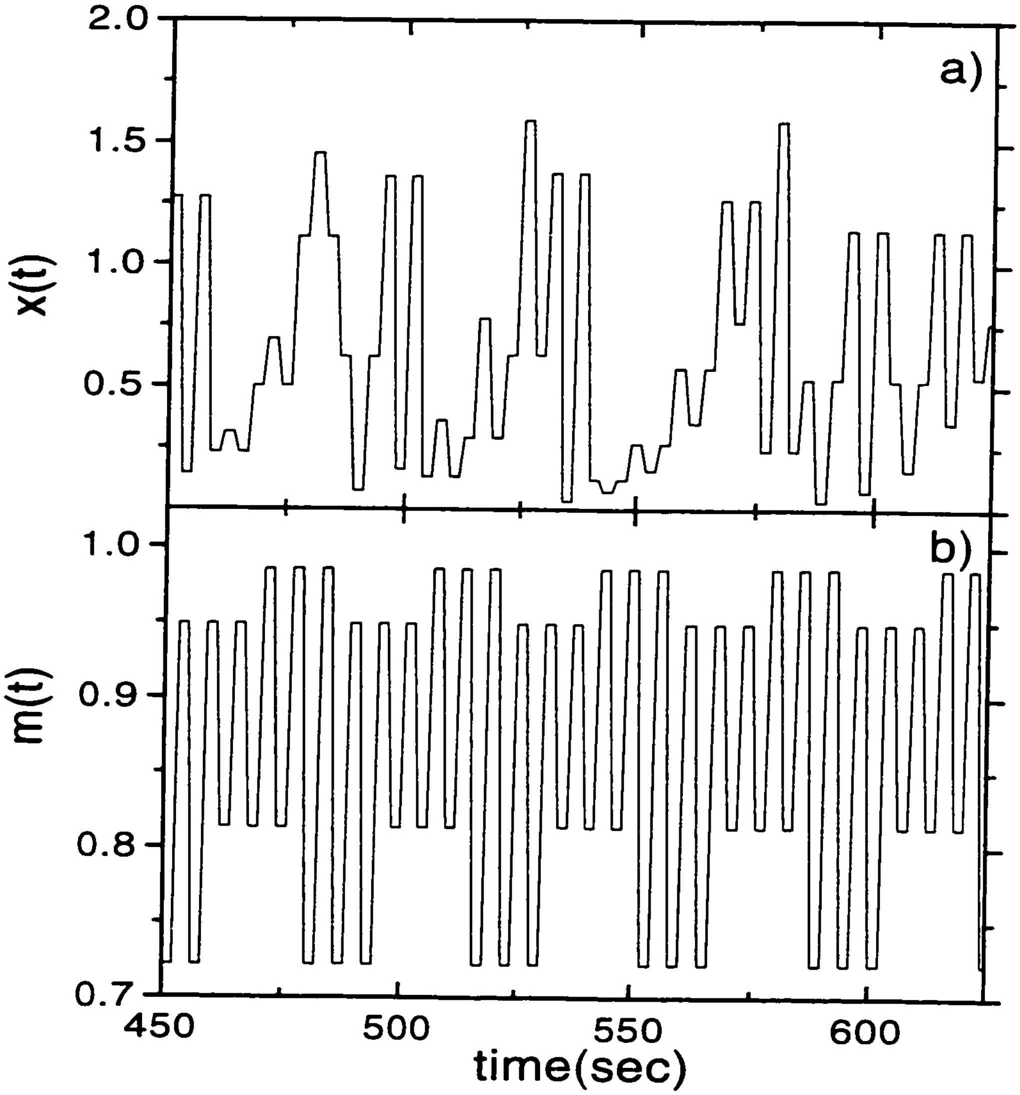

Figure 8.6: Transmission of a digital message using chaotic synchronization of CTDE's with masking-modulation Eq.8.17 ($\epsilon = 0.1$). a) The transmitted signal. b) The recovered message.

Chapter 9

Conclusion

We have studied nonlinear systems with time-delayed feedback, whose dynamics are governed by delay-differential equations (DDE's). These systems exhibit multistability when the delay in the feedback loop is much greater than the response time of the system. We have shown the potential applicability of this property in storing and transmitting information in neural, optical, and control feedback systems in general. In neural feedback circuits for example, the information is stored into a periodic temporal pattern of membrane voltage or spiking activity. Further, we have shown that the chaotic regime yields a more versatile memory device than the periodic regime because of the infinite number of unstable periodic orbits (UPO's) that coexist with one or more chaotic attrators.

We have first stabilized these UPO's with a chaos-control technique proposed by Pyragas [17] in order to encode information in their waveforms. However, the number of UPO's that can be stabilized with this technique is limited since higher periodic orbits (i.e. periodic orbits with a large number of plateaus) are very difficult to control. Thus, the storage capacity is also limited. The improved chaos-control technique introduced in [18], can stabilize orbits with higher periodicity. More work is needed to develop a control technique that can stabilize a larger number of UPO's including ones of higher periodicity, and thus increase the storage capacity of such systems. Such work would also benefit from a better understanding of the transients in such controlled systems.

We have shown that many properties of delay-differential and difference equations at large delay can be studied using simpler techniques such as linear stability analysis, power spectra, and the map obtained in the singular limit. These properties are: dynamical invariants, multistability, and controllability. The relevance of linear stability analysis is surprising because these are usually considered highly nonlinear properties, and are relevant to motion which is very different from fixed point motion. Multistability is found to be related to the unstable modes in the linearized system. The singular limit map is found to exhibit a period-doubling cascade to chaos similar to the DDE as in [9]. Stability and controllability of orbits are studied using the dispersion and the Lyapunov exponents for the map. The periodic peak structure in the power spectrum is found to be related to the modes of oscillations at odd integer multiples of the fundamental, predicted by linear stability analysis. The structure of these peaks is determined by the spectrum of the map using mirror images and translations of the basic map spectrum, along with a filtering function.

The Lyapunov dimension of the attractor is found to agree both with the number of peaks in the DDE or the CTDE and with the number of roots of the linearized dynamics, seen between zero frequency and the reciprocal of the correlation time of the feedback function. The sum of positive Lyapunov exponents, which is found to converge to the sum of unstable modes for $R > 5$, is a constant equal to the inverse rate of decay of the power spectrum in the mid-to-high frequency range.

The different properties discussed above for a single fixed delay have also been studied in systems with a distribution of delays. These properties are found to be the same only when the system of ordinary-differential equations for the distributed delay case is sufficiently high-dimensional. This means that the dimension has to be sufficiently high to see similar decay in the power spectrum, and to have peaks at the same locations as for the DDE.

The spectrum of the CTDE explains the structure of the peaks in the DDE at large delays. However, we have not explained the transition from an exponential decay in the DDE to a $1/f^2$-type decay at low frequency in the CTDE. It is also unclear whether or not there exists a mathematical relationship between the amplitude of the modulation in the power spectrum and the real parts of the eigenvalues of the linearized problem. This will be left for future investigations.

Although DDE's have many important properties such as high-dimensionality and multistability observed by simply increasing the delay, they may be too complicated for elements of large scale artificial optical or neural networks. The complexity comes from the fact that we need to synthesize the delays in the network with optic fibers, or in electronic circuits, using analog delay lines [58]. Further, the numerical calculations are often very difficult and time-consuming. Discrete neural network systems however, besides being simpler and easier to implement experimentally, can reproduce many properties of the DDE's at large delays. These systems are widely used as models of real structures from small networks of neurons to large scale neurodynamics. We presented in Chapter 7 an improved chaos-control technique that we believe can be used to stabilize the complex temporal patterns of these systems, and potentially make these patterns encodable.

The synchronization discussed in Chapter 8 is another area where the DDE's can play an important role, especially for secure communication. These systems, besides being easier to implement experimentally compared to series of low-dimensional "building blocks" systems, can use their own attractors for encoding, sending and receiving information with high security. The reason for this is that they exhibit high-dimensional chaos and multistability when the delay-to-response time ratio is large. The signal is very difficult to recover since it does not stand out from the background in the chaotic power spectrum. Such properties are difficult to realize in low-dimensional systems such as the Lorenz or Rossler systems.

In the future, multistability in neural recurrent loops should be studied with more realistic feedback coupling, either through synapses or with a standard form of current pulse, rather than one which mimics the intracellular potential during a spike. Our goal with studying multistability by reflecting the neuron's output to its input (as in Plant's model [4]) was to show elementary multistability properties of such circuits. Even though there is much work to be done to find the full implications of our results for real neuronal circuits, they are immediately useful for the artificial neural network community, since recent years have seen the development of, e.g., nets with delayed pulse-coupled neurons.

In summary, we believe that the results presented in this thesis on dynamical invariants, multistability, controllability, and synchronization of DDE's at large delays can be used for future developments in control systems, physiological and other, involving single or multiple feedback loops [128].

Bibliography

[1] K. Ikeda, H. Daido, and O. Akimoto, *Phys. Rev. Lett.* **45**, 709 (1980).

[2] M.C. Mackey and L. Glass, *Science* **197**, 287 (1977).

[3] A. Longtin, J.G. Milton, J.E. Bos, and M.C. Mackey, *Phys. Rev. A* **41**, 6992 (1990).

[4] R.E. Plant, *SIAM J. Appl. Math.* **40** (1), 150 (1981).

[5] M.C. Mackey and U. an der Heiden, *J. Math. Biology* **19**, 211 (1984).

[6] C.M. Marcus and R.M. Westervelt, *Phys. Rev. A* **39**, 347 (1989).

[7] J.D. Farmer, *Physica* **4D**, 366 (1982).

[8] K. Ikeda and K. Matsumoto, *Physica* **29D**, 223 (1987).

[9] S.N. Chow and J. Mallet-Paret, in: " Coupled Nonlinear Oscillators, Singularly Perturbed Delay-Differential Equations", J. Chandra and A. C. Scott, eds. p.7 (North-Holland, Amesterdam, 1983).

[10] A.F. Ivanov and A.N. Sharkovskii, in: "Dynamics Reported", Vol. **3** eds. p.165, H.O. Walther and U. Kirchgraber (Springer-Verlag, Berlin, 1991).

[11] T. Aida and P. Davis, *IEEE J. Quantum Electron.* **28**, 686 (1992).

[12] A.L. Hodgkin and A.F. Huxley, *J. Physiol.* **117**, 500 (1952).

[13] J. Foss, A. Longtin, B. Mensour and J. Milton, *Phys. Rev. Lett.* **76**, 708 (1996).

[14] D. Kleinfeld, Proc. Nat. Acad. Sci. USA **83**, 9469 (1986).

[15] D. Zipser, *Neural Comput.* **3**, 179 (1991).

[16] D. Zipser, B. Kehoe, G. Littlewort and J. Fuster, *J. Neurosci.* **13**, 3406 (1993).

[17] K. Pyragas, *Phys. Lett. A* **170**, 421 (1992).

[18] J.E.S. Socolar, D.W. Sukow, and D.J. Gauthier, *Phys. Rev. E* **50**, 3245 (1994).

[19] J. Nagumo and S. Sato, *Kybernetik* **10**, 155 (1972).

[20] K. Aihara, T. Takabe and M. Toyota, *Phys. Lett. A* **144**, 333 (1990).

[21] K.M. Cuomo and A.V. Oppenheim, *Phys. Rev. Lett.* **71**, 65 (1993).

[22] L. Kocarev and U. Parlitz, *Phys. Rev. Lett.* **74**, 5028 (1995).

[23] U. Parlitz, L. Kocarev, T. Stojanovski, and H. Preckel, *Phys. Rev. E* **53**, 4351 (1996).

[24] D.E. Sigeti, *Physica* **82D**, 136 (1995).

[25] C. Laurenço and A. Babloyantz, *Neural Computation* **6**, 1141 (1994).

[26] L. Glass and C.P. Malta, *J. Theor. Biol.* **145**, 217 (1990).

[27] R.C. Hilborn, in: "Chaos and Nonlinear Dynamics", Oxford University Press, New York (1994).

[28] M.W. Hirsch and S. Smale, "Differential Equations, Dynamical Systems, and Linear Algebra", Academic Press, New York (1974).

[29] E. Ott, "Chaos in Dynamical Systems", Cambridge University Press, New York (1993).

[30] H.G. Schuster, "Deterministic Chaos", Physik-Verlag, Germany (1994).

[31] A.S. Weigend and N.A. Gershenfeld, "Time Series Prediction: Forecasting the Future and Understanding the Past", Addison-Wesley Publishing Company, Massachusetts (1994).

[32] J.P. Eckmann and D. Ruelle, *Rev. Mod. Phys.* **57**, 617 (1985).

[33] E.N. Lorenz, *J. Atmos. Sci.* **20**, 130 (1963).

[34] D. Singer, *SIAM J. Appl. Math.* **35**, 260 (1978).

[35] J. Guckenheimer and P. Holmes, "Nonlinear Oscillations, Dynamical Systems, and Bifurcations of Vector Fields", Springer-Verlag, New York (1990).

[36] M.J. Feigenbaum, *Los Alamos Science* **1**, 4 (1980).

[37] R.L. Devaney, "An Introduction to Chaotic Dynamical Systems", Benjamin-Cumming, Menlo Park, CA (1986).

[38] Y. Pomeau and P. Manneville, *Comm. Math. Phys.* **74** 189 (1980).

[39] C. Grebogi, E. Ott and J.A. Yorke, *Phys. Rev. Lett.* **48**, 1507 (1982).

[40] C. Grebogi, E. Ott and J.A. Yorke, *Physica D* **7**, 181 (1983).

[41] C. Grebogi, E. Ott, F. Romeiras and J.A. Yorke, *Phys. Rev. A* **36**, 5365 (1987).

[42] D. Ruelle and F. Takens, *Comm. Math. Phys.* **20**, 167 (1971).

[43] J. Theiler, *J. Opt. Soc. Am. A* **7**, 1055 (1990).

[44] B.B. Mandelbrot, "The Fractal Geometry of Nature", Freeman, San Francisco (1982).

[45] P. Grassberger and I. Procaccia, *Phys. Rev. Lett.* **50**, 346 (1983).

[46] J.L. Kaplan and J.A. Yorke, *Springer Lecture Notes in Mathematics* **730**, 204 (1979).

[47] Ya.B. Pesin, *Russ. Math. Surveys* **32**, 55 (1977).

[48] D. Ruelle, *Bol. Soc. Bras. Mat.* **9**, 83 (1978).

[49] V.I. Oseledec, *Moscow Math. Soc.* **19**, 197 (1968).

[50] H.D.I. Abarbanel, R. Brown and M.B. Kennel, *J. Nonlinear Sci.* **2**, 343 (1992).

[51] J. Stoer and R. Burlisch, "Introduction to Numerical Analysis", Springer-Verlag, New York (1980).

[52] V. Kolmanovskii and A. Myshkis, "Applied Theory of Functional Differential Equations", *Mathematics and its Applications* Vol. **85**, (Kluwer Academic Publishers, Dordrecht, 1992).

[53] K. Ikeda and K. Matsumoto, *J. Statist. Phys.* **44**, 955 (1986).

[54] M. LeBerre, E. Ressayre, A. Tallet and H.M. Gibbs, *Phys. Rev. Lett.* **56**, 274 (1986).

[55] M. Le Berre, E. Ressayre, A. Tallet, H.M. Gibbs, D.L. Kaplan, and M.H. Rose, *Phys. Rev. A* **35**, 4020 (1987).

[56] S. Lepri, G. Giacomelli, A. Politi and F.T. Arecchi, *Physica D* **70**, 235 (1993).

[57] J. Losson and M.C. Mackey, *J. Stat. Phys.* **69**, 1025 (1992).

[58] J. Losson, M.C. Mackey, and A. Longtin, *Chaos* **3**, 167 (1993).

[59] G. Giacomelli, R. Meucci, A. Politi and F.T. Arecchi, *Phys. Rev. Lett.* **73**, 1099 (1994).

[60] K. Ikeda, K. Kondo, and O. Akimoto, *Phys. Rev. Lett.* **49**, 1467 (1982).

[61] B. Mensour and A. Longtin, IEEE 17^{th} Ann. Intern. Conf. of the Engineering in Medicine and Biology Society & 21^{st} Canadian Medical and Biological Engineering Conference, Montreal, Canada (Sept. 1995).

[62] B. Mensour, A. Longtin, *Phys. Lett. A* **205**, 18 (1995).

[63] J.G. Milton, U. an der Heiden, A. Longtin and M.C. Mackey, *Biomed. Biochem. Acta* **49**, 697 (1990).

[64] H.M. Gibbs, F.A. Hopf, D.L. Kaplan and R.L. Shoemaker, *Phys. Rev. Lett.* **46**, 474 (1981).

[65] P. Nardone, P. Mandel and R. Kapral, *Phys. Rev. A* **33**, 2465 (1986).

[66] J. Mallet-Paret and R.D. Nussbaum, in: "Chaotic Dynamics and Fractals", eds. M.F. Barnsley and S.G. Demko (Academic Press, New York, 1986).

[67] A.T. Winfree, "The Geometry of Biological Time" (Springer-Verlag, New York, 1990).

[68] D. Fargue, *C.R. Acad. Sci. Paris* **T.277**, No.**17** (Série B, 2e semestre), 471 (1973).

[69] K.L. Cooke and Z. Grossman, *J. Math. Anal. Appl.* **86**, 592 (1982).

[70] A. Longtin, *Phys. Rev. A* **44**, 4801 (1991).

[71] C.G. Lange and R.M. Miura, *SIAM J. Appl. Math.* **42**, 502 (1982).

[72] J.Y. Gao, L.M. Narducci, L.S. Schulman, M. Squicciarini, and J. M. Yuan, *Phys. Rev. A* **28**, 2910 (1983).

[73] D. Ruelle, "Chaotic Evolution and Strange Attractors", (Cambridge University Press, Cambridge, UK, 1989).

[74] J. Hertz, A. Krogh and R. G. Palmer, "Introduction to the Theory of Neural Computation", (Addison–Wesley, New York, 1991).

[75] H. Sompolinsky and I. Kanter, *Phys. Rev. Lett.* **57**, 2861 (1986).

[76] A.C.C. Coolen and C.C.A.M. Gielen, *Europhys. Lett.* **7**, 281 (1988).

[77] J.J. Hopfield and D.W. Tank, in: *Neural Models of Plasticity*, edited by J.H. Byrne and W.O. Berry (Academic Press, San Diego,1989), p.363.

[78] C.C. Canavier, D.A. Baxter, J.W. Clark and J.H. Byrne, *J. Neurophysiol.* **69**, 2252 (1993).

[79] H.R. Wilson and J.D. Cowan, *Biophys. J.* **12**, 1 (1972).

[80] R.S. y Cayal, "Histologie du Systéme Nerveux de l'Homme et des Vertébrés" (Volume 1, Malöine, Paris, 1909).

[81] R.D. Traub and R. Miles, "Neuronal Networks of the Hippocampus", (Cambridge University Press: New York, 1991).

[82] D.H. Perkel and T.H. Bullock, *Neurosci. Res. Prog. Bull.* **6**, 221 (1968).

[83] J.C. Middlebrooks, A.E. Clock, L. Xu and D.M. Green, *Science* **264**, 842 (1994).

[84] L.M. Optican and B.J. Richmond, *J. Neurophysiol.* **57**, 162 (1987); *ibid*, *J. Neurophysiol.* **64**, 370 (1990).

[85] C.A.G. Wiersma and R.T. Adams, *Physiol. Comp. et Oecol.* **2**, 20 (1950).

[86] J.D. Cowan, "Stochastic Models of Neuroelectric Activity. In: Statistical Mechanics", edited by S.A. Rice, K.F. Fread and J.C. Light (University of Chicago Press, Chicago) p.181.

[87] A.V.M. Herz, Z. Li and J.L. van Hemmen, "Statistical Mechanics of Temporal Association in Neural Networks with Delayed Interactions". In: Advances in Neural Information Processing Systems 5, edited by S.J. Hanson, J.D. Cowan and C.L. Giles (Morgan-Kaufmann, San Mateo, Ca) p.176 (1991).

[88] B. de Vries and J.C. Principe, "A Theory of Neural Networks with Time Delays". In: Advances in Neural Information Processing Systems 5, edited by S.J. Hanson, J.D. Cowan and C.L. Giles (Morgan-Kaufmann, San Mateo, Ca) p.162 (1991).

[89] A.M. Castelfranco and H.W. Stech, *SIAM J. Appl. Math.* **47**, 573 (1987).

[90] U. Ernst, K. Pawelzik and T. Giesel, *Phys. Rev. Lett.* **74**, 1570 (1995).

[91] J. Rinzel and R.N. Miller, *Math. Biosc.* **49**, 27 (1980).

[92] J. Cronin, " Mathematical Aspects of Hodgkin-Huxley Neural Theory", (Camdridge University Press, New York, 1987).

[93] H.M. Pinsker, *J. Neurophysiol.* **40**, 527 (1977).

[94] E.N. Best, *Biophys. J.* **27**, 87 (1979).

[95] J.F. Vibert, M. Davis and J.P. Segundo, *Biol. Cybern.* **33**, 167 (1979).

[96] A.F. Kohn, A. Frietas da Rocha and J.P. Segundo, *Biol. Cybern.* **41**, 5 (1981).

[97] O. Diez Martinez and J.P. Segundo, *Biol. Cybern.* **47**, 33 (1983).

[98] D.H. Perkel and B. Mulloney, *Science* **185**, 181 (1974).

[99] J.N. Li and B.L. Hao, *Commun. Theor. Phys.* **11**, 265 (1989).

[100] H. Gang and H. Kaifen, *Phys. Rev. Lett.* **71**, 3794 (1993).

[101] T. Shinbrot, C. Grebogi, E. Ott, and J. Yorke, *Nature* **363**, 411 (1993).

[102] L.M. Pecora and T.L. Carroll, *Phys. Rev. Lett.* **64**, 821 (1990).

[103] S. Hayes, C. Grebogi, and E. Ott, *Phys. Rev. Lett.* **70**, 3031 (1993).

[104] S. Hayes, C. Grebogi, E. Ott, and A. Mark, *Phys. Rev. Lett.* **73**, 1781 (1994).

[105] R.A. FitzHugh, *Biophys. J.* **1**, 445 (1961).

[106] J.S. Nagumo, S. Arimoto, and S. Yoshizawa, *Proc. IRE.* **50**, 2061 (1962).

[107] L. Glass and M.C. Mackey, "From Clocks to Chaos: The Rhythms of Life", Princeton University Press, Princeton, 1988.

[108] A. Garfinkel, M. Spano, W.L. Ditto, J.N. Weiss, *Science* **257**, 1230 (1992).

[109] J. Glanz, *Science* **265**, 1174 (1994).

[110] S.J. Schiff, K. Jerger, D.H. Duong, T. Chang, M.L. Spano, and W. Ditto, *Nature* **370**, 615 (1994).

[111] M. Courtemanche, J.P. Keener, and L. Glass, *SIAM J. Appl. Math.* **56**, 119 (1996).

[112] K. Konishi, M. Ishii, and H. Kokame, *Phys. Rev. E* **54**, 3455 (1996).

[113] K. Pyragas, *Phys. Lett. A* **206**, 323 (1995).

[114] A. Kittel, K. Pyragas, and R. Richter, *Phys. Rev. E* **50**, 262 (1995).

[115] A. Namajunas, K. Pyragas, and A. Tamasevicius, *Phys. lett. A* **201**, 42 (1995).

[116] K. Pyragas, *Phys. Lett. A* **181**, 203 (1993).

[117] R. He and P.G. Vaidya, *Phys. Rev. A* **46**, 7387 (1992).

[118] L.M. Pecora and T.L. Carroll, *Phys. Rev. A* **44**, 2374 (1991).

[119] N.F. Rul'kov, A.R. Volkovskii, A. Rodriguez-Lozano, E. Del Rio and M.G. Velarde, *Int. J. Bif. Chaos* **2**, 669 (1992).

[120] J.H. Xiao, G. Hu, and Zhilin Qu, *Phys. Rev. Lett.* **77**, 4162 (1996).

[121] T.C. Newell, P.M. Alsing, A. Gavrieldes, and V. Kovanis, *Phys. Rev. E* **49**, 313 (1994).

[122] Y. Hun Yu, K. Kwak, T.K. Lim, *Phys. Lett. A* **191**, 233 (1994).

[123] D.W. Jordon and P. Smith, "Nonlinear Ordinary Differential Equations", 2nd ed. New York: Oxford University Press (1987).

[124] M.K. Simon *et al.*, "Spread Spectrum Communications Handbook", McGraw-Hill, New York (1994).

[125] B. Mensour and A. Longtin *Physica D* **1786**, 1 (1997).

[126] H.D.I. Abarbanel and P.S. Linsay, *IEEE Trans. Circuits Syst. II* **40**, 643 (1993).

[127] N. Gershenfeld and G. Grinstein, *Phys. Rev. Lett.* **74**, 5024 (1995).

[128] W. Gerstner, *Phys. Rev. Lett.* **76**, 1755 (1996).

IMAGE EVALUATION TEST TARGET (QA-3)

150mm

6″

APPLIED IMAGE . Inc
1653 East Main Street
Rochester, NY 14609 USA
Phone: 716/482-0300
Fax: 716/288-5989

© 1993, Applied Image, Inc., All Rights Reserved